Spectroscopic Considerations on Molecular Adsorption at the Solid/Liquid Interface

Thesis submitted in accordance with the requirements of the
University of Liverpool for the degree of Doctor in Philosophy

by

Andrew Francis Bowfield

Department of Physics

July 2009

If the facts don't fit the theory, change the facts

Albert Einstein

for Sandra, Frank and Charlotte

Abstract

This thesis mainly focuses on the adsorption behaviour of various molecules at the solid/liquid interface. The variation in adsorption kinetics are studied as a function of concentration, pH, applied electrode potential and surrounding environment by the surface sensitive analytical techniques of Reflection Anisotropy Spectroscopy and X-ray Photoelectron Spectroscopy.

An electrochemical investigation into the surface reconstructions of Au(110) and their associated RA profiles is undertaken. The spectral profiles of Au(110) in 0.1 M H_2SO_4/Na_2SO_4, $NaClO_4/HClO_4$ and $NaClO_4$ electrolytes were observed as a function of potential and spectral signatures of the different reconstructions are assigned.

The adsorption of adenine and its monophosphate (AMP) on Au(110) was studied using RAS. It is shown that both molecules adsorb in a vertical orientation through sites common to the base through formation of base stacked layers. Application of a phenomenological Lorentzian transition model and rotations about the polarisation direction of the incident light suggest that the molecules align along the $[1\bar{1}0]$ principal axis of the substrate. Linear simulations show that the orientation of adenine at sub-saturation coverage is the same as that when a monolayer is adsorbed and that adenine does not adsorb on the surface at sufficiently alkaline pH.

The attachment of thiolated ss-DNA on a functionalised diamond surface and the subsequent detection of hybridisation are discussed. High resolution XPS spectra are used to characterise both the integrity and structure of the organic thin film and its modification to precipitate DNA adsorption.

The sensitivity of RAS to the orientation of the alkyl backbone of decanethiol is displayed through alteration to the surrounding environment of the molecule. It is suggested that orientation of the hydrophobic backbone varies as the surrounding environment is changed from ethanol to air and finally to phosphate buffer.

Acknowledgements

I would firstly like to thank Professor Peter Weightman for providing me with the opportunity to be a part of his research group. His wit, generosity, knowledge and endless enthusiasm will forever accompany me. Not just a good scientist, a good man.

Of course, I would never have gotten this far without Caroline 'time for tea' Smith and her invaluable help and advice. I would also like to thank Trevor Farrell and Paul Harrison whose technical expertise is second to none. Indeed, Paul Unsworth deserves a mention for all the guidance he has shown on the ever dependable XPS kit. Thanks also go to fellow PhD students Gerard Dolan, Nick Almond, Gareth Holder and James Convery. To Chelo Cuqeurella and Amy Schofield also thanks.

On a personal note, it is often close friends who amplify what an enjoyably tough PhD is really about. The following people have not only encouraged me to consume far too much alcohol, but also discuss life, the universe and physicists over many lost hours: Michael 'two socks' Cormack, Alex Brownrigg, Dan Poulter, Abdi Noor, Craig Wiglesworth, Joe Parle, Chris Mansley, Joe Croft, Craig Gray-Jones, Alex Grint, David Scraggs and Richard Miller. And not forgetting the girls Ella Morley, Katherine Elliott and Pauline Gallon.

A very special thank you must be extended to an extraordinary person who has accompanied me throughout these last four long years; Nina Morley. Love, laughter and support have always been in endless supply when submission seemed so far away. My gratitude to her is boundless. Her embracing approach to life is truly unique.

I would never have reached such an enviable position were it not for the influence of my family. Their unwavering confidence in my ability has gotten me through the toughest of times. To my mum, Sandra, I will never forget your sacrifices. To my dad, Frank, you will always make me laugh. And finally a very simple message to my sister, Charlotte: you are the best. I live to make them proud. This thesis is dedicated to you.

Acronyms

Adenosine 5′-monophosphate:	**AMP**
Atomic force microscopy:	**AFM**
Chemical vapour deposition:	**CVD**
Circular dichroism:	**CD**
Complete active space with second-order perturbation theory:	**CASPT2**
Complete neglect of differential overlap:	**CNDO**
Configuration interaction perturbing a multi-configurational zeroth-order wave function selected iteratively:	**CIPSI**
Cyclic voltammetry:	**CV**
Cytidine 5'-monophosphate:	**CMP**
Decanethiol:	**DCNT**
Deoxyribonucleic acid:	**DNA**
Intermediate neglect of differential overlap/screened approximation:	**INDO/S**
Linear dichroism:	**LD**
Low energy electron diffraction:	**LEED**
Low energy helium atom diffraction:	**LEAD**
Photoelastic modulator:	**PEM**
Photomultiplier tube:	**PMT**
Scanning tunnelling microscopy:	**STM**
Self-assembled monolayer:	**SAM**
Spectroscopic ellipsometry:	**SE**
Saturated calomel electrode:	**SCE**
Surface enhanced raman spectroscopy:	**SERS**
Time dependant density functional theory:	**TDDFT**
Ultra high vacuum:	**UHV**
X-ray diffraction:	**XRD**
X-ray photoelectron spectroscopy:	**XPS**

Contents

Abstract ... i
Acknowledgements ... ii
Acronyms ... iii

Chapter 1: Introduction ... 1
- 1.1: Emergence of Interdisciplinary Approaches ... 2
- 1.2: Surface Science and the Solid/Liquid Interface ... 3
- 1.3: Importance of Electrochemistry ... 4
- 1.4: Thesis Aims ... 4
- 1.5: Thesis Structure ... 5
- 1.6: References ... 7

Chapter 2: Experimental Techniques and Components ... 8
- 2.1: Reflection Anisotropy Spectroscopy ... 9
  - 2.1.1: The RA Spectrometer and its Optical and Electronic Components ... 11
- 2.2: The Propagation of Light Through the System ... 16
  - 2.2.1: The Jones Matrix Formalism ... 21
  - 2.2.2: Errors ... 28
- 2.3: Electrochemistry ... 29
  - 2.3.1: Measuring Electrode Potentials ... 32
  - 2.3.2: The Electrochemical Cell ... 33
  - 2.3.3: Cyclic Voltammetry ... 34
- 2.4: X-ray Photoelectron Spectroscopy ... 36
  - 2.4.1: The VSW ESCA Instrument ... 40
  - 2.4.2: Monochromated X-ray Source ... 41
  - 2.4.3: Analysis of Photoelectron Energies ... 42

2.5: References 44

Chapter 3: The Au(110) Surface 46

3.1: Introduction 47

3.2: Surface Phase Transitions 47

3.3: Physical Structure of the Au(110) Surface 48

3.3.1: Au(110) in UHV 49

3.3.2: Electrochemistry of Au(110) 53

3.4: Electronic Structure of Au(110) 55

3.5: RAS of Au(110): Origin of Spectral Features 57

3.6: The Three-Phase Model 62

3.6.1: The Dielectric Function 63

3.6.2: The Lorentzian Transition Model 64

3.7: Crystal Preparation 66

3.8: Simulations Using the Three-Phase Model 67

3.9: Spectral Signatures of the Different Reconstructions of Au(110): An Electrochemical Investigation 68

3.9.1: Au(110) in 0.1 M H_2SO_4/Na_2SO_4 at pH 1.36 69

3.9.2: Au(110) in 0.1 M $NaClO_4/HClO_4$ at pH 1.18 82

3.9.3: Au(110) in 0.1 M $NaClO_4$ at pH 6.14 88

3.10: Comparison of the (1x1), (1x2) and (1x3) Reconstructions in Different Electrolytes and Varying pH. 98

3.11: Simulation of (1x2) 102

3.12: Summary 104

3.13: References 105

Chapter 4: Determination of the Structure of Adenine Monolayers Adsorbed at Au(110)/electrolyte Interfaces 110

4.1: Introduction 111

4.2: Concentration Effect of Adenine Adsorption 113
4.3: Azimuth-Dependent RAS 118
4.4: Electronic Spectrum of Adenine 124
4.5: Simulation of Au & Au + Adenine RA spectra 130
4.6: Simulation of Sub-Saturation Adenine Spectrum 141
4.7: The Effect of Electrode Potential on Adenine Adsorption 142
4.8: Effect of pH Variation in the Supporting Electrolyte 148
4.9: Summary 151
4.10: References 152

Chapter 5: RAS of Alkanethiol Adsorption at Au(110)/liquid Interfaces 157

5.1: Introduction 158
5.2: Experimental Procedure 160
5.3: The Orientation of DCNT as a Function of Coverage 162
5.4: Azimuth Dependent RAS as a Function of Surrounding Environment 168
5.5: Summary 173
5.6: References 174

Chapter 6: Detection of DNA Hybridisation on a Functionalised Diamond Surface 177

6.1: Introduction 178
6.2: Experimental Procedure 180
6.3: XPS of Amine Functionalised TFAAD Protected Diamond 184
6.4: Determination of Elemental Ratios: 190
6.5: Structure of the Monolayer Films 191
6.6: XPS of Amine Terminated Deprotected Diamond 194
6.7: RAS of Thiol-Modified ss-DNA Attached to Diamond 198

6.8: Detection of DNA Hybridisation 201
6.9: Summary 202
6.10: References 202

Chapter 7: Conclusions 205

7.1: Summary of Findings 206
    7.1.1: The Au(110) Surface 206
    7.1.2: Adenine 206
    7.1.3: Decanethiol 207
    7.1.4: DNA on Diamond 208
7.2: Future work 209

Appendix 211

A.1: XPS of Amine Terminated Deprotected Diamond (II) 212

Publications 216

Chapter 1: Introduction

There follows a brief introduction as to the importance and aims of the research undertaken along with its relevance within a wider context.

1.1: Emergence of Interdisciplinary Approaches

"Now I am become Death, the destroyer of worlds" J. Robert Oppenheimer famously quoted as he witnessed the first detonation of an atomic bomb at the Manhattan Project headquarters at Los Alamos National Laboratory in New Mexico thereby capturing in a rather astonishingly morbid statement the impact of the physical sciences on the twentieth century. Of course, this is not to suggest that this was the *only* impact of a post relativity science community on the wider world, although it was without doubt the most noticeable. After Einstein had revolutionised physics thinking with his famous ruminations on mass-energy equivalence in 1905, the natural sciences became questions of the minute and how they impacted the large and visible world which humans inhabit. Advances in quantum mechanics, harnessing nuclear fission as a platform for safe, effective electricity generation and the immunisation programmes which rendered many diseases all but extinct gave us a far deeper understanding of not just our world but the universe as a whole. The latter half of the previous century bore witness to the semiconductor revolution which heralded the age of the computer microchip and altered the course of human history irrevocably. The problem with most of these discoveries is that their full ramifications were often only felt in solitary scientific communities. The first years of the twenty-first century confined this approach to science research to the dustbin.

The Human Genome Project is but one example of the major advances occurring in the life sciences as higher volumes of research grant funds are focused on discoveries which either aid the health of the ageing western populations or enable the first bio-electronic devices to be fabricated. It is the need to detail interactions at the molecular and atomic scale which has resulted in bioscientists turning to physical methodologies to provide accurate analysis on which valid conclusions can be drawn. The development of powerful tools, from desktop spectrometers to vast particle accelerators, has allowed scientists from all fields to delve further into the structure of matter.

One such area where physical approaches can be applied to biological systems is the interaction and adsorption kinetics of molecules at surfaces. This field is already well established [1] with an array of techniques available with which to study various properties [2]. It is only in a truly interdisciplinary and collaborative approach to science that solutions to many of mans immediate ailments lie.

1.2: Surface Science and the Solid/Liquid Interface

Surface science has developed at a fast pace since its inception over forty years ago. The ability to maintain UHV has allowed techniques such as LEED, XPS and STM, which exploit the short mean free path of electrons and require contaminants from air to be kept at a minimum, to flourish with abandon and have become essential surface sensitive diagnostic tools. While these approaches are still important they cannot be applied to a solid/liquid interface, for example STM being susceptible to surface tip effects, and since there is an increasing need to study biological molecules *in situ* so as to appropriately re-create an environment in which biological activity and functionality remains at a maximum, there is also a need for more versatile techniques. Hence understanding of the solid/liquid interface is a critical area of study for many scientists, however cataloguing the interactions occurring at this boundary is made difficult, rather ironically, by the presence of a supporting electrolyte or liquid.

The requirement to study biological systems *in situ* has led to the development of versatile optical probes such as RAS which can operate in UHV, ambient and electrochemical environments and thus avoids the problems associated with other techniques. RAS has a promising future in the field of biophysics with a proven sensitivity to the adsorption of nucleic acid bases and their orientations in 3-dimensions once adsorbed at the Au(110)/electrolyte interface [3,4].

1.3: Importance of Electrochemistry

Electrochemistry is increasingly pivotal to the study of interfacial systems and coupled with the development of optical probes has applications in both scientific and industrial sectors [3,5,6]. Recently, it has been shown that the change in optical response of metal surfaces and molecular and chemical adsorbates can provide a wealth of information which can be used to further the understanding of these systems [5]. The interface between electrode surface and electrolyte is crucially important since it provides the site of the majority of interactions which have scientific and industrial applications. These include the development of DNA labelled nanoparticles, bioarray technology and the exploitation of surface plasmon resonance and heterogeneous catalysis [6]. Other electrochemical techniques such as CV do not provide enough surface structural information alone to gain a full understanding of the interface.

1.4: Thesis Aims

The body of work presented in this thesis comprises several studies designed to investigate the adsorption of important molecules on to different substrates in an attempt to elucidate the adsorption kinetics at play at different interfacial boundaries. Analysis of these systems focuses on and also offers explanations of the organisation and/or preferential ordering of such molecules in realisation that this process is fundamental to the ability to fabricate bio-electronic devices and interfaces. Further, since the Au(110) surface features quite heavily in this thesis, owing to its inherent anisotropy, itself a requirement of the RAS technique, a chapter is dedicated to explaining the effect of potential and anion induced reconstruction on its optical response in an effort to understand the complex morphological variations in differing environments.

1.5: Thesis Structure

Chapter 2 Instrumentation and Theory

RAS is introduced and the experimental components described in detail. The layout of the spectrometer and a theoretical treatment of the passage of light through the system are considered. The current model of the solid/liquid interface at electrode surfaces is discussed along with how electrochemical control is maintained in the electrochemical cell. Also included is an introduction to cyclic voltammetry and its importance in investigating interfacial behaviours.

A detailed description of the X-ray photoelectron spectrometer employed is also included. The principles underpinning the technique, its components and an explanation of a typical XPS spectrum, including where the background signal originates, are detailed.

Chapter 3 The Au(110) Surface

The structure of the Au(110) surface is known to be sensitive to the environment in which it is studied and this section gives an overview of the physical configuration and previous RAS of the surface in both UHV and electrolyte in order to provide a basis upon which surface atomic arrangement can be explained. A Lorentzian transition model is described in an attempt to understand the changes in spectral profiles induced by molecular adsorption.

The organisation of surface atoms on Au(110) crystals are known to be sensitive to variations in external parameters such as applied electrode potential, pH and anion identity. These changes are accompanied by detailed modifications to the optical response of the system and this chapter attempts to distinguish between the different causal factors. Characteristic reflection anisotropy profiles of the various surface structures are assigned and detailed tabulated parameters used to simulate profiles using the three-phase model and Lorentzian transition model are discussed to quantitatively describe simulated optical profiles.

Chapter 4 The Adsorption of Adenine at the Au(110)/electrolyte Interface

The orientation of biologically important molecules such as nucleic acid bases once adsorbed at an interface is important in the production of bio-electronics. The three-dimensional structure of adsorbed adenine on Au(110) is determined using rotations of the crystal through a plane perpendicular to the incident light in conjunction with a Lorentzian transition model and studied as a function of surface coverage, potential and pH.

Chapter 5 Alkanethiol Adsorption at Au(110)/liquid Interfaces

The gold/sulphur bond is known to be very strong and thiolated species with a hydrophobic backbone should self-assemble in such a fashion so as to try and exclude hydrogen bonding between separate molecules. The formation of a SAM is investigated as a function of coverage along with changes to the surrounding environment to determine variations in the back-bone orientation.

Chapter 6 DNA Hybridisation on a Functionalised Diamond Surface

RAS is shown to be sensitive to the hybridisation of single stranded DNA on an amine functionalised diamond surface. XPS data is fitted to highlight the removal of a protecting group originally attached to the amine and also to prove functionalisation has occurred in an ordered fashion across the surface.

Appendix

Fitted XPS spectra of a diamond sample deprotected at the University of Liverpool are included to show that the process of deprotection resulted in the diamond samples having the same surface chemistry as those samples deprotected in the USA included in Chapter 6.

1.6: References

[1] Surface Science: The First Thirty Years, *Surf. Sci.* **299 – 300**, 1-1054 (1994)

[2] *Introduction to Surface Physics*, M. Prutton (Oxford University Press, 1998)

[3] P. Weightman, G. J. Dolan, C. I. Smith, M. C. Cuquerella, N. J. Almond, T. Farrell, D. G. Fernig, C. Edwards and D. S. Martin, *Phys. Rev. Lett.* **96**, 086102 (2006)

[4] C. I. Smith, A. Bowfield, G. J. Dolan, M. C. Cuquerella, C. P. Mansley, D. G. Fernig, C. Edwards and P. Weightman, *J. Chem. Phys.* **130**, 044702 (2009)

[5] R. LeParc, C. I. Smith, M. C. Cuquerella, R. L. Williams, D. G. Fernig, C. Edwards, D. S. Martin and P. Weightman, *Langmuir* **22**, 3413 (2006)

[6] *The Chemical Physics of Solid Surfaces,* Vol. **10**, edited by D. P. Woodruff (Elsevier Science, Amsterdam, 2002)

Chapter 2: Experimental Techniques and Components

The aim of this chapter is to inform the reader of both the theoretical considerations underpinning the techniques employed along with the electrical and optical components which comprise the experimental apparatus.

2.1: Reflection Anisotropy Spectroscopy

Reflection anisotropy spectroscopy is a non-destructive optical probe developed from SE [1,2] which can be used to investigate surface structure by exploiting the anisotropy found at some of the surfaces of cubic crystals. Optical probes are generally strongly influenced by the optical response of the bulk specimen due to light penetration many atomic layers into the material. This lack of sensitivity is not shared by certain techniques such as XPS and LEED, conducted in UHV environments, which exploit the low mean free path of electrons to obtain surface sensitivity. A comparison between the electron escape depth vs light penetration into a solid is shown in Figure 2.1 and it is immediately clear that contributions from bulk layers would dominate the optical response of the system thereby preventing surface sensitivity.

Crystalline materials such as gold have a cubic cell structure in which each atom in the material can be considered to occupy a position either at the corner of a cube or at the centre of each face of the cube (Figure 2.2). If one considers an infinite arrangement of these cubes, as is the situation when engaged in experimentation, the optical response of the bulk material at near normal incidence will be symmetrical in all

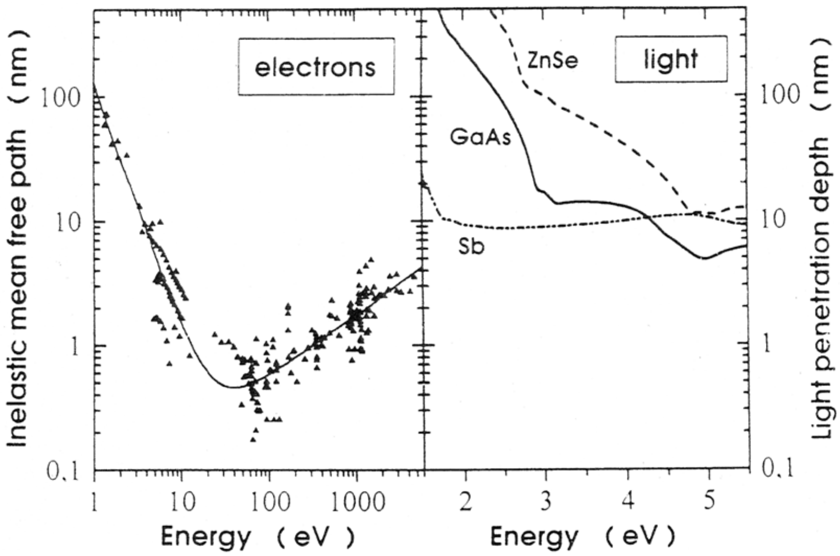

Figure 2.1: Comparison of electron escape depth vs light penetration depth in solids [3].

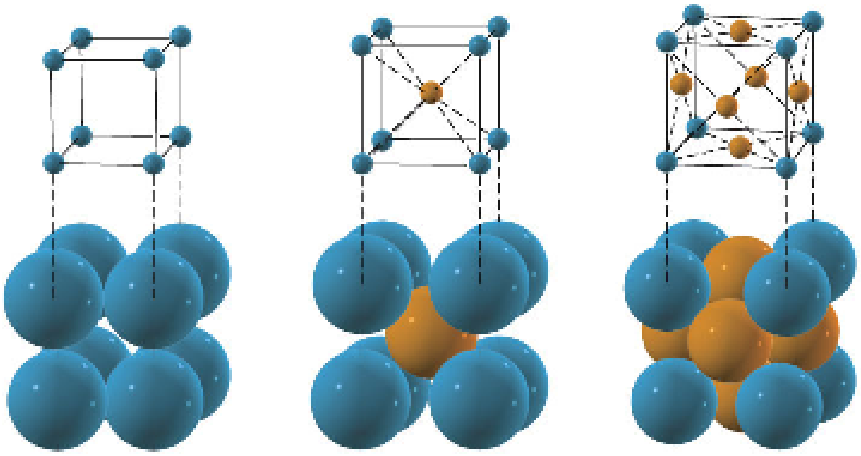

Figure 2.2: Examples of the three main cubic cell structures: primitive (left), body-centred cubic (BCC, centre) and face-centred cubic (FCC, right).

directions (isotropic) as all planes of atoms will contribute to the signal equally. As a consequence, any reflections dominated by a particular plane/crystal axis (anisotropic) will arise solely from the surface. RAS is therefore able to provide a characteristic diagnosis of the surface electronic structure with the added benefit of versatility in the range of environments in which experiments can be conducted. Since these environments must consist of optically transparent media, an application to electrode surfaces in electrochemical surroundings becomes possible. RAS is therefore a useful addition to a somewhat limited group of techniques with the ability to function in these electrochemical conditions.

RAS is able to achieve surface sensitivity by measuring the difference in reflectance (Δr) of normal incidence linearly-polarised light between two orthogonal directions in the surface plane (r_x,r_y) normalised to the mean reflectance (r) [Figure 2.3]:

$$\frac{\Delta r}{r} = \frac{2(r_x - r_y)}{r_x + r_y}$$

where the reflectances r_x and r_y are the complex Fresnel reflection coefficients of the two surface directions respectively.

2.1.1: The RA Spectrometer and its Optical and Electronic Components

RAS uses a similar experimental set-up to SE but with some significant differences. SE illuminates the sample with linearly polarised light near to the Brewster angle [4] whereas RAS illuminates the sample with linearly polarised light at near normal incidence (≤ 5°). Originally labelled reflection difference spectroscopy (RDS), the technique was initially created by the need for a real-time monitor of III-IV semi-conductor growth at near atmospheric pressure [5]. Developed in the 1980s by Aspnes and co-workers [6], RAS has recently been applied to the study of metal surfaces in UHV and air [7], the metal/liquid interface in the electrochemical environment [8] and the adsorption of biological molecules onto electrode surfaces [9-13]. The individual components of the spectrometer are displayed in Figure 2.3. Each of the components is described in the order in which light passes through the system. Mirrors, not pictured in the schematic, are placed before and after the polariser and analyser to facilitate the position of the focal length of the light. The axes of the gold substrate are defined as: $[1\bar{1}0] = r_x$ and $[001] = r_y$.

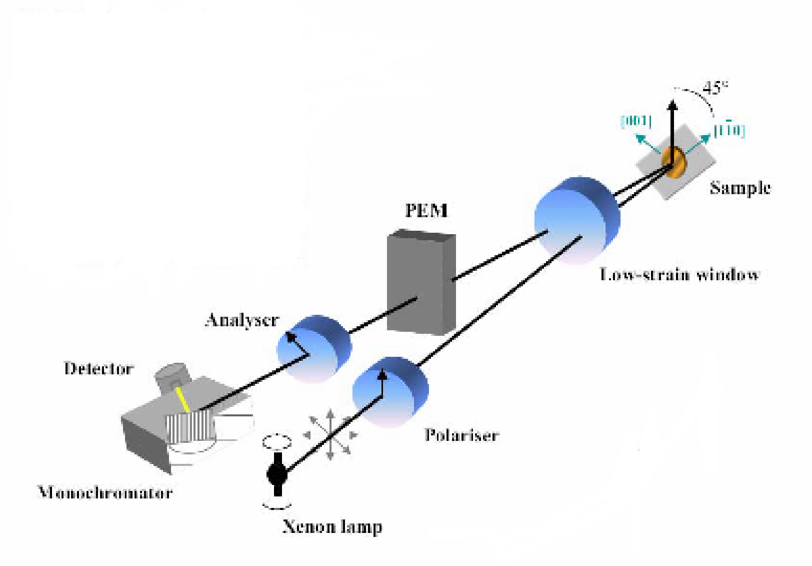

Figure 2.3: Schematic of the basic components of the RA spectrometer reproduced from [7].

Xenon Lamp

A 75 Watt Super-Quiet 9 short arc xenon discharge lamp (Hamamatsu), in conjunction with a stabilised power source (Hamamatsu C4621-02) which minimises fluctuations from the mains supply by removing spikes, provides a high intensity point source of light. The lamp functions by means of an arc discharge when high voltages are applied across the anode to a high performance cathode in a xenon gas environment. Such a light source is desirable for RAS studies due its reliable and stable output of a continuous spectrum in the infrared to ultraviolet range (1.5 – 5.5 eV). Owing to the fact that xenon gas pressure in the lamp varies for up to 1 hour after power up and does not reach thermal equilibrium and thus a maximal radiant intensity until after this point, care must be taken to only begin experimentation at least 1 hour after the lamp is switched on so as to ensure an unchanging photonic flux can be obtained with confidence.

Mirrors

Concave mirrors are employed to produce a parallel beam of focused light from the incident diverging light emitted by the Xe-lamp and, utilising the intrinsic astigmatism of the mirrors, to re-focus the light reflected from the sample surface onto the monochromator entry slit after it has passed through the photo-elastic modulator and analyser. The input of the monochromator is a narrow vertical slit; it is therefore possible to use the tangential focus as the image at the input slit and so reduce any sagittal component from the analyser. These mirrors are front coated aluminium on glass, with a thin silica coating to prevent mechanical abrasion.

Polariser

Since the differences in reflection between the r_x and r_y directions are often small, the polariser and analyser should have an extinction ratio typically greater than 10^5. There are two main categories of prism type polarisers which are particularly useful due to this consideration. Rochon and Wollaston type are beam splitting polarisers which consist of two attached quartz prisms that separate the ordinary and extraordinary polarised beams which are polarised perpendicular to each other. Glan prism polarisers separate the two polarised beams by total internal reflection and consequently a single beam emerges. A single beam is often preferable when used with UHV apparatus since they pose no restrictions on geometry to avoid the 2nd beam thereby allowing a more compact experimental layout. The RAS instrument detailed in this thesis makes use of Rochon type prisms due to a more efficient transmission of light in the UV region. This is a reasonable choice since UHV RAS measurements are not conducted in this body of work. Nevertheless, care must be taken to ensure the two beams which exit the polariser do not overlap.

Low-Strain window

After the light has been polarised, it next encounters a low-strain silica window prior to entering the electrochemical cell. This window itself will make a small contribution to the detected RAS signal as it will inherently possess some inhomogeneous birefringence. This contribution can be removed by subtracting a correction spectrum from all raw experimental data.

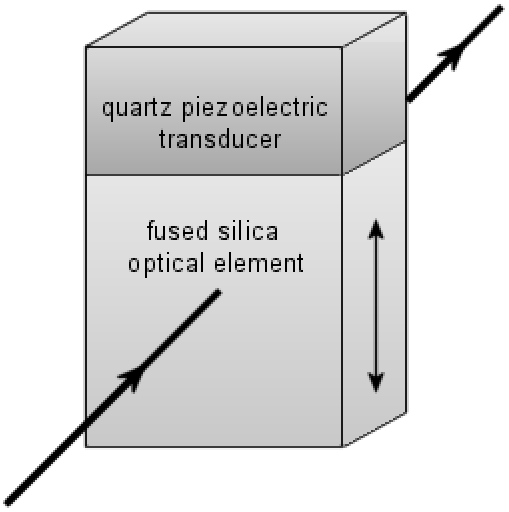

Figure 2.4: The Photo-Elastic Modulator reproduced from [14].

Photoelastic Modulator

The PEM (Hinds Instruments Inc., PEM90 Quartz) is crucial to how RAS is able to attain surface specificity and is displayed in Figure 2.4. Sir David Brewster discovered in 1816 that applying a mechanical stress to a normally transparent isotropic substance could induce an optical anisotropy in that same material. In some materials, namely fused silica in this instance, this mechanical effect manifests itself in the form of a stress-induced birefringence (photoelasticity).

The PEM is in effect a tuneable wave-plate which modulates the polarisation ellipse of the light reflected from the surface by exploiting the aforementioned process. This is to ensure collection of both real and imaginary elements of the light wave by driving a quartz piezoelectric transducer at 50 kHz, which is the natural resonant frequency of the coupled fused silica optical element. One can effectively consider the incident ellipse as having two orthonormal components polarised parallel and perpendicular to the modulation axis of the PEM. The PEM introduces an oscillating birefringence into the centre of the optical element and acts solely on the parallel component thus, as the silica is compressed the component polarised parallel to the axis of modulation travels faster than the perpendicular component and vice-a-versa when the optical element is stretched. The phase difference between the components at any instant is called the retardation (Γ) where the peak retardation is defined as the amplitude of the sinusoidal retardation as a function of time. Consequently, as elliptically polarised light impinges, the PEM introduces a phase modulation dependent upon the polarisation state.

Analyser

The analyser serves to convert the phase-modulated signal from the PEM into an amplitude modulated signal ready for detection. The analyser, orientated at an angle of 45° with respect to the polariser to produce a modulated signal switching between two linearly polarised states, is of the same design as the polariser.

Monochromator

To enable a spectroscopic analysis of the reflected light, it is necessary to split the light into its constituent wavelengths. A Jobin Yvon monochromator (H10), consisting of a holographic grating with 1200 grooves mm^{-1}, with a spectral range of 1.5 - 6.2 eV (200 to 800 nm) is utilised to this end. The position of the grating and hence the wavelength of light entering the detector is determined using a computer controlled stepper motor.

Detection

Located immediately behind the exit slit of the monochromator is a Hamamatsu multi-alkali cathode photomultiplier tube (PMT Hamamatsu R955). The PMT measures the intensity of the light and converts the intensity-modulated waveform into a current. This current is often minute (of the order of nA) and is therefore in need of amplification. The amplified signal is then converted to a potential relative to the initial intensity of the incoming light. The signal consists of an AC component, related to the surface anisotropy, superimposed on a DC offset, which is related to the reflectivity. These two components then need to be analysed separately which requires the use of a lock-in amplifier.

Silicon photodiodes are another type of detector which can also be used in RAS set-ups which are optimised for longer wavelength detection (200 - 1100 nm). The spectral range over which these types of detectors function does not extend into UV, however detection in this region can be attained through the application of an appropriately chosen coating which converts UV photons for detection within the visible range. This process ultimately results in a loss of sensitivity in the visible range and to avoid this occurrence a PMT was chosen for this instrument.

Lock-in Amplifier

A EG&G model 5210 (dual-phase) lock-in amplifier manufactured by PerkinElmer Instruments, which operates in a frequency range of 0 – 120 kHz, was used to analyse the resulting AC and DC voltage signals produced from the PMT by measuring the

Fourier coefficients of the first and second harmonics of the signal which carries the real and imaginary parts of the RA response respectively. Since such instruments are able to detect signals at very specific frequencies that would otherwise be obscured by noise, they are critical to the successful detection of the RA signal.

So as to produce accurate measurements and correct identification of the signal of interest, the lock-in is supplied with a reference voltage of the same frequency and phase relationship as that of the signal. Any differences between the frequencies of the signal of interest compared to this locked in signal will then be tracked. In this case the locked in reference signal is taken from the PEM.

2.2: The Propagation of Light Through the System

Thus far, only the optical considerations and signal analysis components of the spectrometer have been discussed. This section describes the theoretical applications to RAS in a quantitative manner using a highly successful mathematical formalism.

The accurate measurement of a RA signal requires a comprehensive method of determining the state of polarisation of the light reflected from the surface. It is pertinent to initially define the electric field vector, E, of a light wave which can be represented as a superposition of two orthogonal states.

$$E(z,t) = E_x(z,t) + E_y(z,t)$$

where

$$E_x(z,t) = E_{0x}\cos(kz - \omega t + \phi_x)$$

and

$$E_y(z,t) = E_{0y}\cos(kz - \omega t + \phi_y)$$

The resulting wave, $\boldsymbol{E}$, is therefore the vector sum of components, and may be written

$$\boldsymbol{E}(\mathrm{z,t}) = \hat{\mathrm{x}}E_{0\mathrm{x}}\cos(\mathrm{kz}-\omega\mathrm{t}) + \hat{\mathrm{y}}E_{0\mathrm{y}}\cos(\mathrm{kz}-\omega\mathrm{t}+\delta)$$

where $\delta = \phi_y - \phi_x$ and is the relative phase between the two components. The direction of polarisation of the resultant wave depends on both its relative projection along each axis and δ. When $\delta = m\pi$ for m = 0, ±1, ±2, ±3,… the wave is confined to a solitary plane and is said to be linearly polarised. If either E_{0y} or $E_{0x} = 0$, the wave is limited to vibrations along the x or y axes respectively. For non-zero magnitudes of both components, the linearly polarised light is inclined at an angle α to the x axis defined as [Figure 2.5]:

$$\alpha = \tan^{-1}\left(\frac{E_{0x}}{E_{0y}}\right)$$

The polarisation of the resultant wave will be restricted to the positive x axis if $\delta = 0$ whereas if the phase difference is $\pm\pi$, polarisation will lie along the negative x axis. If a phase lag of an integer multiple of $\pm\pi/2$ exists between the two components but they possess equal magnitudes ($E_{0x} = E_{0y}$), a state of circular polarisation is achieved. In this polarisation state the magnitude remains constant as the wave propagates through space, but the direction of $\boldsymbol{E}$ fluctuates with time following a circular path with angular frequency ω. If the resultant vector not only rotates in this fashion but is also accompanied by variations in magnitude, the result is a state of elliptical polarisation. Elliptical polarisation occurs when either $E_{0x} \neq E_{0y}$ and δ is a multiple of $\pm\pi/2$ or when $E_{0x} = E_{0y}$ but δ is an arbitrary angle.

In the RAS set-up, light which is initially linearly polarised on contact with a surface will emerge elliptically polarised due to surface anisotropy whereas light reflected from the bulk of the cubic material will be in a circularly polarised state. The PEM induces a retardation in the elliptically polarised light in different directions which then goes on to become an amplitude modulation as the light passes through the

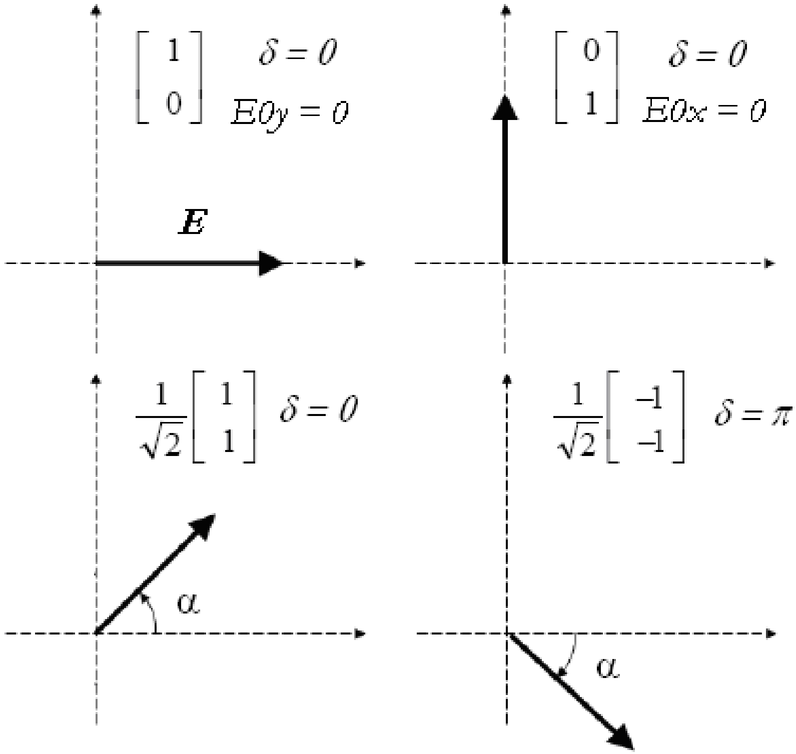
$\begin{bmatrix}1\\0\end{bmatrix}$
$\delta = 0$
$E0y = 0$
E
$\begin{bmatrix}0\\1\end{bmatrix}$
$\delta = 0$
$E0x = 0$
$\frac{1}{\sqrt{2}}\begin{bmatrix}1\\1\end{bmatrix}$
$\delta = 0$
α
$\frac{1}{\sqrt{2}}\begin{bmatrix}-1\\-1\end{bmatrix}$
$\delta = \pi$
α

Figure 2.5: Linear polarisation states determined from the magnitudes and phases of E_{0x} and E_{0y} [15].

analyser. As this action is only impacted upon elliptically polarised light, it is possible to extract harmonics from the amplitude modulation giving information deriving exclusively from the surface anisotropy. Circularly polarised light originating from the bulk response will pass through the modulator unaffected as the intensity of the resultant vector is the same in all phases.

The effect of δ on the linear, circular and elliptical polarisation states are displayed in Figures 2.5 – 2.7 and are shown alongside their respective normalised Jones vector representations. The matrix formalism of describing the polarisation state of light in terms of the electric field vector was created by R. Clark Jones in 1941 and will now be used to describe the propagation of the light through the RAS set-up.

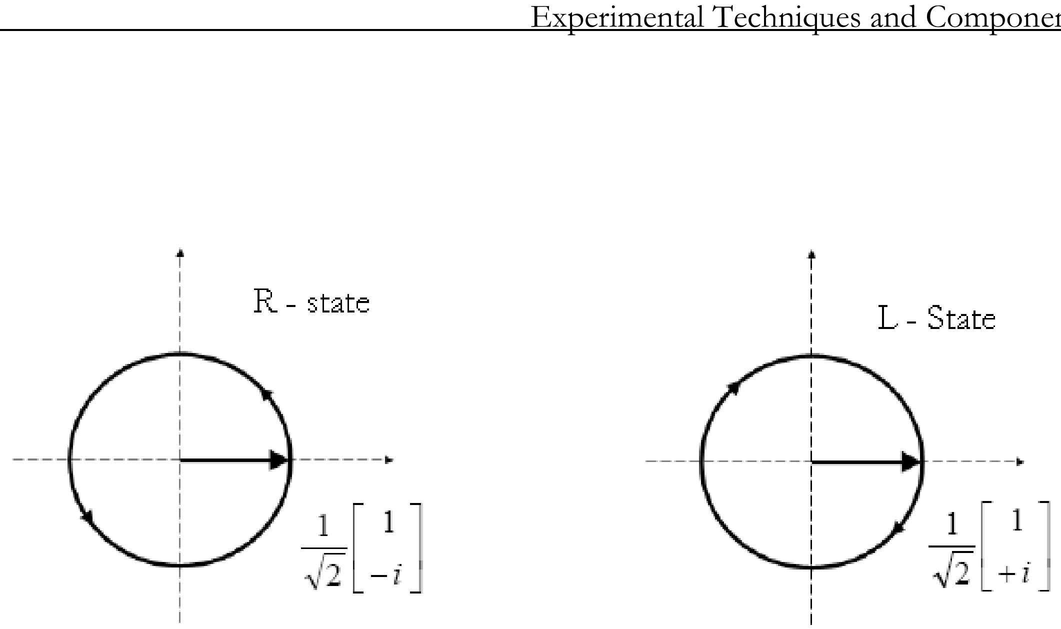
R - state
$\frac{1}{\sqrt{2}}\begin{bmatrix}1\\-i\end{bmatrix}$
L - State
$\frac{1}{\sqrt{2}}\begin{bmatrix}1\\+i\end{bmatrix}$

Figure 2.6: Circular polarisation states [15].

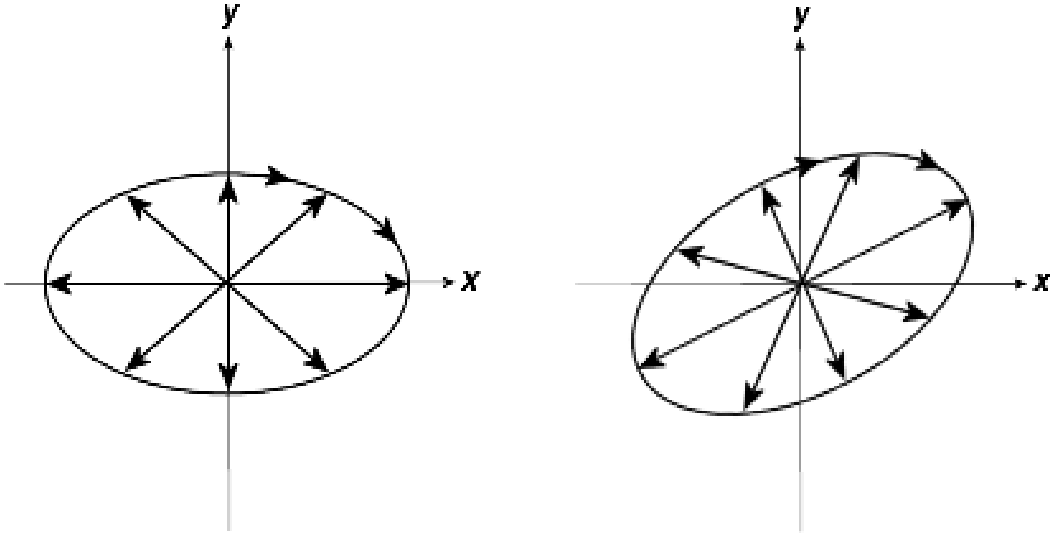

Figure 2.7: Elliptically polarised light. Left: Phase difference of ± $\frac{\pi}{2}$ and $E_{0x} \neq E_{0y}$. Right: $E_{0x} = E_{0y}$ and phase difference not equal to ± $\frac{\pi}{2}$ [15].

As Jones Calculus is applicable in this instance the resulting wave, ***E***, can now be described much more concisely as:

$$\boldsymbol{E}(z,t) = \left[\frac{\mathrm{E}_{0\mathrm{x}}\mathrm{e}^{\mathrm{i}\delta\mathrm{x}}}{\mathrm{E}_{0\mathrm{y}}\mathrm{e}^{\mathrm{i}\delta\mathrm{y}}}\right]$$

The implementation of the Jones vector (*M*) allows the polarisation state of the light, from its initial polarisation (E_i) emerging from the polariser to its final polarisation (E_f) arriving at the detector, to be determined as the light traverses the RAS instrument due to its ability to fully detail the effect on the light of the optical components.

$$E_f = ME_i \tag{2.1}$$

The Jones matrix *M* is formed by combining in sequence the 2 x 2 matrices which describe the effect that each of the optical components has on the polarisation state of the light. Each component has its own set of optical axes - the polariser and analyser have transmission *(t)* and extinction *(e)* axes while the PEM has fast *(f)* and slow *(s)* axes. The axes of the sample (*x,y*) are taken to be in the $[1\bar{1}0]$ and [001] surface directions and define the reference frame for each component thus rotation matrices, labelled *R*, are used to convert the Jones vector representing the polarisation state of the light to those of the optical component with which it is interacting.

$$R(\theta) = \begin{bmatrix} \cos(\theta) & -\sin(\theta) \\ \sin(\theta) & \cos(\theta) \end{bmatrix}$$

The azimuth angles P, M and A are shown in Figure 2.8 and denote the orientations of the reference frames of the polariser, modulator and analyser respectively. The azimuths correlate to the transmission axes for the polariser and analyser and the fast

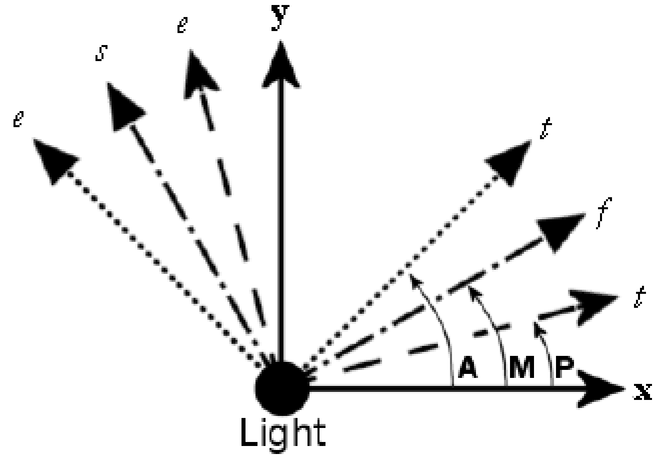

Figure 2.8: The orientation of the reference frames for each optical component relative to the *xy* frame. All angles are positive in the anticlockwise direction [14].

axis of the modulator. P, M and A are referenced to the *x* direction of the sample and are characterised as positive for an anti-clockwise rotation.

2.2.1: The Jones Matrix Formalism

Light emerging from the xenon lamp is unpolarised so it cannot be assigned an appropriate Jones matrix. However, after passing through the polariser it is in a definable polarisation state for the remainder of its journey through the instrument. Once through the polariser, it can be assigned the Jones matrix T_P^{te}, since it is in the *te* reference frame of that component.

$$T_P^{te} = \begin{bmatrix} 1 & 0 \\ 0 & 0 \end{bmatrix}$$

Next, to ensure the light is in the *xy* plane of the sample, T_P^{te} must be multiplied by the rotation matrix *R(P)*:

$$R(P)T_P^{te} = \begin{bmatrix} \cos P & \sin P \\ -\sin P & \cos P \end{bmatrix} \begin{bmatrix} 1 & 0 \\ 0 & 0 \end{bmatrix} = \begin{bmatrix} \cos P & 0 \\ -\sin P & 0 \end{bmatrix} \tag{2.2}$$

Before reflecting from the surface, the light will encounter a strain-free window as it enters the electrochemical cell. The orientation of the window axes are unknown and as such are assumed to be commensurate with those of the *xy* frame of the sample. It is likely the window will contain some birefringence (fast and slow axes) and hence some retardation of the incident light beam will occur. The effect of this action can be captured by:

$$T_{WI}^{xy} = \begin{bmatrix} 1 & 0 \\ 0 & e^{i\delta_{WI}} \end{bmatrix} \tag{2.3}$$

where, δ_{WI} is the retardation of the incident beam by the window. δ is defined as:

$$\delta = \frac{4\pi \mathrm{d}}{\lambda}\left(\mathrm{n_e} - \mathrm{n_o}\right) \tag{2.4}$$

where, d is the thickness of the material, λ is the wavelength of the light, and $\mathrm{n_e}$, $\mathrm{n_o}$, are the refractive indices of the extraordinary and ordinary directions of the material respectively. The light then impinges upon the surface and after reflection will pass through the window as it exits the cell. The light will leave via a different part of the window with an associated retardation δ_{WO}. The Jones matrix for the surface is:

$$T_S^{xy} = \begin{bmatrix} r_x & 0 \\ 0 & r_y \end{bmatrix} \tag{2.5}$$

After exiting the cell, the light meets the PEM. To change the lights' reference frame from that of the surface to that of the PEM, the rotation matrix must once again be utilised:

$$T_S^{fs} R(M) = \begin{bmatrix} 1 & 0 \\ 0 & \mathrm{e}^{\mathrm{i}\delta_\mathrm{M}} \end{bmatrix} \begin{bmatrix} \cos \mathrm{M} & -\sin \mathrm{M} \\ \sin \mathrm{M} & \cos \mathrm{M} \end{bmatrix} = \begin{bmatrix} \cos \mathrm{M} & -\sin \mathrm{M} \\ \left(\mathrm{e}^{\mathrm{i}\delta_\mathrm{M}} \sin \mathrm{M}\right) & \left(\mathrm{e}^{\mathrm{i}\delta_\mathrm{M}} \cos \mathrm{M}\right) \end{bmatrix} \tag{2.6}$$

The analyser then converts the light from phase-modulated to an amplitude-modulated signal, requiring the same matrix as that applied for the polariser and the rotation matrix.

$$\begin{aligned} T_A^{te} R(A-M) &= \begin{bmatrix} 1 & 0 \\ 0 & 0 \end{bmatrix} \begin{bmatrix} \cos(A-M) & -\sin(A-M) \\ \sin(A-M) & \cos(A-M) \end{bmatrix} \\ &= \begin{bmatrix} \cos(A-M) & -\sin(A-M) \\ 0 & 0 \end{bmatrix} \end{aligned} \tag{2.7}$$

The complete matrix representing the final polarisation state of the fully propagated light, *M*, is obtained by combining the matrices of each element. Matrices are non-commutative and as such the matrix for each component must operate in the order in which the light interacts with them. Combining Equations (2.2), (2.3), (2.5), (2.6) and (2.7) in order, the Jones matrix for the system becomes:

$$M = T_A^{te} R(A-M) T_M^{fs} R(M) T_{WO}^{xy} T_S^{xy} T_{WI}^{xy} R(P) T_P^{te}$$

Evaluating *M* from the above expression gives:

$$M = \begin{bmatrix} a_{11} & 0 \\ 0 & 0 \end{bmatrix}$$

where:

$$\begin{aligned} a_{11} &= (\cos(\mathrm{A}-\mathrm{M})\cos\mathrm{M} - \sin(\mathrm{A}-\mathrm{M})(\mathrm{e}^{\mathrm{i}\delta_\mathrm{M}}\sin\mathrm{M}))(\mathrm{r_x}\cos\mathrm{P}) - \\ &(-\cos(\mathrm{A}-\mathrm{M})\sin\mathrm{M} - \sin(\mathrm{A}-\mathrm{M})(\mathrm{e}^{\mathrm{i}\delta_\mathrm{M}}\cos\mathrm{M}))(\mathrm{r_y}\mathrm{e}^{\mathrm{i}\delta_\mathrm{WO}}\mathrm{e}^{\mathrm{i}\delta_\mathrm{WI}}\sin\mathrm{P}) \end{aligned} \tag{2.8}$$

The values of the angles P, A and M used are -45°, 0°, and 45° respectively [Figure 2.8]. Thus:

$$\sin(\pm 45°) = \pm\frac{1}{\sqrt{2}}, \qquad \cos(\pm 45°) = \frac{1}{\sqrt{2}}, \qquad \sin(0°) = 0, \qquad \cos(0°) = 1$$

Putting the above values into Equation (2.8) gives:

$$a_{11} = \frac{\mathrm{r_x}}{2\sqrt{2}}(1 + \mathrm{e}^{\mathrm{i}\delta_\mathrm{M}}) + \frac{\mathrm{r_y}\mathrm{e}^{\mathrm{i}\delta_\mathrm{WO}}\mathrm{e}^{\mathrm{i}\delta_\mathrm{WI}}}{2\sqrt{2}}(\mathrm{e}^{\mathrm{i}\delta_\mathrm{M}} - 1) \tag{2.9}$$

As a_{11} is the solitary non-zero term in the total system matrix, *M*, Equation (2.1) now becomes

$$E_f = \begin{bmatrix} a_{11} & 0 \\ 0 & 0 \end{bmatrix}\begin{bmatrix} 1 \\ 0 \end{bmatrix} = \begin{bmatrix} a_{11} \\ 0 \end{bmatrix} \tag{2.10}$$

The window terms can also be simplified:

$$e^{i\delta_{WO}}e^{i\delta_{WI}} = e^{i(\delta_{WO}+\delta_{WI})} = e^{i\delta_W}$$

It is possible to expand the exponential in terms of a power series since the total retardation induced by the low-strain window, although finite, is small:

$$e^{i\delta_W} = 1 + i\delta_W + \frac{(i\delta_W)^2}{2!} + \frac{(i\delta_W)^3}{3!} + \ldots \approx 1 + i\delta_W$$

Using the above simplifications, Equation (2.9) is now:

$$a_{11} = \frac{1}{2\sqrt{2}}[(r_x - r_y) + (r_x - r_y)e^{i\delta_M} - i\delta_W r_y(1 - e^{i\delta_M})] \tag{2.11}$$

r_x and r_y in Equation (2.11) represent the complex Fresnel reflection coefficients and can therefore be written in terms of their real and imaginary components:

$$r_x = a + ib,\ r_y = c + id$$

De Moivre's theorem can be applied to express the term relating to the retardation of the modulator as:

$$e^{i\delta_M} = \cos(\delta_M) + i\sin(\delta_M)$$

After some trivial manipulation a_{11} becomes:

$$\left(2\sqrt{2}\right)a_{11} = \alpha + i\beta \tag{2.12}$$

where α and β constitute the real and imaginary parts of a_{11}. If one assumes that the detector and monochromator are polarisation independent, then light beyond the analyser is no longer transformed and the detector would only measure the time dependent intensity at each wavelength. The measured intensity, I, is proportional to the square of E_f, which is dependent upon a_{11}, thus:

$$I \propto \left|\left(2\sqrt{2}\right)a_{11}\right|^2 = \alpha^2 + \beta^2$$

After some extensive algebraic manipulation, this becomes:

$$\begin{aligned} I \propto \left|a_{11}\right|^2 &= \frac{1}{4}\left[\left(a^2 + b^2\right) + \left(c^2 + d^2\right) + \left(c^2 + d^2\right)\delta_W{}^2\right] \\ &+ \frac{1}{4}\left[\left(a^2 + b^2\right) - \left(c^2 - d^2\right) - \left(c^2 + d^2\right)\delta_W{}^2\right]\cos\left(\delta_M\right) \\ &+ \frac{1}{2}\left[\left(ad - dc\right) - \left(ac + bd\right)\delta_W\right]\sin\left(\delta_M\right) \end{aligned} \tag{2.13}$$

Which can also be written in the form:

$$I = I_{dc} + I_{\omega}\sin\left(\delta_M\right) + I_{2\omega}\cos\left(\delta_M\right) \tag{2.14}$$

The PEM varies the retardation (δ_M) sinusoidally:

$$\delta_M = \alpha(\lambda)\sin(\omega t)$$

where ω is the resonant angular frequency of the modulator. $\alpha(\lambda)$ is the modulation amplitude, which is proportional to the applied excitation voltage and is a function of the wavelength of light. Fourier expansions of both $\cos(\delta_M)$ and $\sin(\delta_M)$ terms determine the frequency components of the signal and this introduces Bessel functions of the first kind:

$$\cos(\alpha\sin(\omega t)) = J_0(\alpha) + 2\sum_{n=1}^{\infty} J_{2n}(\alpha)\cos(2n\omega t)$$

$$\sin(\alpha\sin(\omega t)) = 2\sum_{n=1}^{\infty} J_{2n-1}(\alpha)\sin((2n-1)\omega t)$$

Where $J_n(\alpha)$ is the Bessel function of argument α and of order *n*. For the case of $J_0(\alpha) = 0$, achieved by adjusting the voltage applied to the PEM, Equation (2.14) becomes:

$$I = I_{dc} + I_{\omega} 2J_1(\alpha)\sin(\omega t) + I_{2\omega} 2J_2(\alpha)\cos(2\omega t) + \ldots \qquad (2.15)$$

The first term of Equation (2.15) is time-independent, and can be considered as a DC component. By comparing the terms in Equations (2.13) and (2.15), the intensity coefficients can be determined. It is assumed that for small surface anisotropies $r_x \sim r_y$ for additive terms. If one considers only the first order terms of window strain, the normalised frequency terms are found to be:

$$I_{dc} \sim \frac{\left\langle |r_x|^2 + |r_y|^2 \right\rangle}{2} = R \qquad (2.16)$$

$$\frac{I_{\omega}}{I_{dc}} \sim \mathrm{Im}\left(\frac{\Delta r}{r}\right) - \delta_W \qquad (2.17)$$

$$\frac{I_{2\omega}}{I_{dc}} \sim \mathrm{Re}\left(\frac{\Delta r}{r}\right) \qquad (2.18)$$

The I_{dc} is therefore a measure of the reflectivity of the subject material. The imaginary component of ($\Delta r/r$) is measured at frequency ω, and is found to be dependent on the first-order window strain term, whereas the signal at 2ω measures the real part of ($\Delta r/r$) and is only sensitive to window strain terms of the second order. In order to reduce the total contribution to the detected RA signal of remnant artefacts originating from non-optical components, the vast majority of published RAS measurements are of the real part of the RA spectral profile since window strain effects are substantial for imaginary constituents and make the analysis of the results non trivial. Experimentally, the real and imaginary parts of the signal are separated by their frequency dependence.

2.2.2: Errors

The major sources of error in the RAS experimental set-up are the relative misalignments of the polariser, PEM and analyser, azimuthal misalignment of the sample relative to the incident polarisation vector and insufficient linear polarisation of the beam emitted by the Xe lamp. Misalignment results in an offset of the measured Re($\Delta r/r$), but does not introduce new spectral features. Such offsets create problems when quoting the absolute values of Re($\Delta r/r$) as defining a zero level would require careful subtraction of the background. However, variations in line-shape between measured spectra can be investigated more accurately. A. Maunder conducted a thorough investigation on the effects of misalignment in his thesis [16] and it was found that the relationship between the polariser and modulator is very sensitive to misalignment, whereas analyser misalignment has less impact. RA spectra were also found to be sensitive to the anisotropy introduced by the window. Although this effect is small it is significant and accordingly a window correction is subtracted from all RA spectra to remove this influence. A typical spectrum detailing a small anisotropy attributed to the low-strain window can be observed in Figure 2.9.

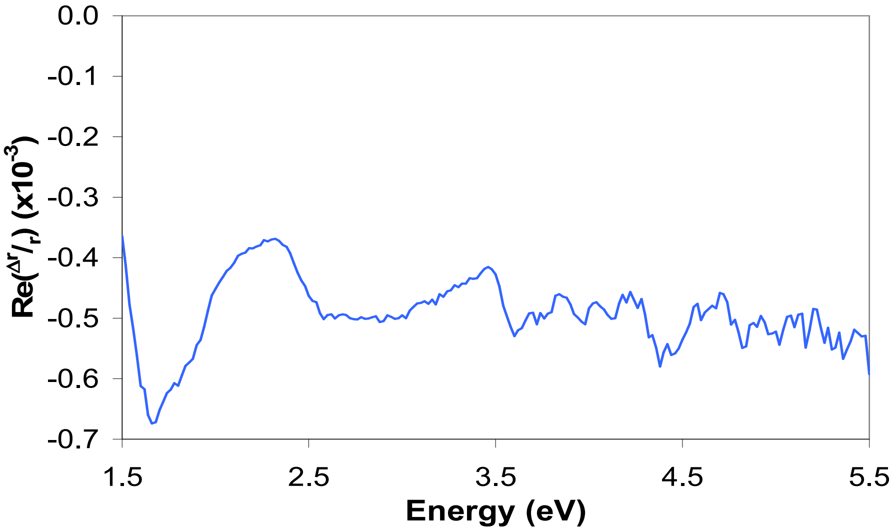

Figure 2.9: RA spectrum of the low-strain window correction.

2.3: Electrochemistry

Chemical reactions that relate to the transfer of electric charge between chemical species and an electrode come under an umbrella of research called electrochemistry. The existence of a potential gradient at the electrode surface drives the transfer of negatively charged species between electrode and solution at the molecular scale. Since only a minute distance exists at the interface, the potential gradient can be substantial (of the order of 10^{10} Vm^{-1}) [17]. Comprehension of the interfacial region requires a functional knowledge of the electrostatic consequences of the potential field and the kinetics of electron transfer specifically in the movement of ions towards the surface through electrostatic attraction and the effect the structure of the adsorbed species then has on the potential field in that expanse [18].

In 1853 Helmholtz coined the term “electric double layer” to describe the solid/liquid interface and proposed a model based on the assumption that no Faradic processes occur at the interfacial boundary. Electrical neutrality is preserved across the electrode surface due to an induced charge density which is balanced by the equal and opposite charge density of the electrolyte. The opposing charge of the solution is instigated by a migration of electrolyte ions to the electrode surface where the distance of closest approach is determined by the solvation shell of the ion. The principles underpinning the theory are analogous to those of a molecular scale parallel plate capacitor with a linear potential drop separating two plates of equal and opposite charge. The two plates are defined as a metal electrode which has its own surface excess charge and a plane which travels through the centre of fully solvated ions at their closest approach. This is labelled the Outer Helmholtz Plane (OHP).

A comprehensive depiction of the accepted model of the interfacial region [19], with the associated Helmholtz planes and potential drop, is given in Figure 2.10. Since Brownian motion dictates that excess charge must be dispersed, the charge in the electrolyte is not concentrated at the OHP and is instead spread over a diffuse layer with the majority at locations close to the electrode surface and some extending beyond the OHP due to the lack of a homogeneous charge distribution.

The interfacial region is made more complex by the existence of two kinds of adsorption at the interface: specific and non-specific. Non-specifically adsorbed solvated ions are held in position entirely by electrostatic forces and are accompanied by a linear drop in potential across the interface [red curve, Figure 2.10]. Specifically adsorbed ions (such as Cl^-, Br^-) are categorised by their weakly bound solvation shells and release part of those shells so as to form a chemical bond with the electrode surface. The Inner Helmholtz plane (IHP) is defined as a plane which runs through the centres of these ions. A steeper potential drop at the surface [purple curve, Figure 2.10] and an over-shooting of the potential with respect to the bulk electrolyte value is the typical behaviour observed with those anions that are specifically adsorbed. The potentials φ_m, φ_s, φ_1 and φ_2 correspond to potentials inside the metal, the electrolyte, the IHP at Z_1 and the OHP at Z_2 respectively.

When the electrode is immersed in electrolyte and a potential applied to it, its surface becomes charged away from its neutral state. The value of this surface charge is fundamentally dependent upon the electrode material, the electrolyte used and the

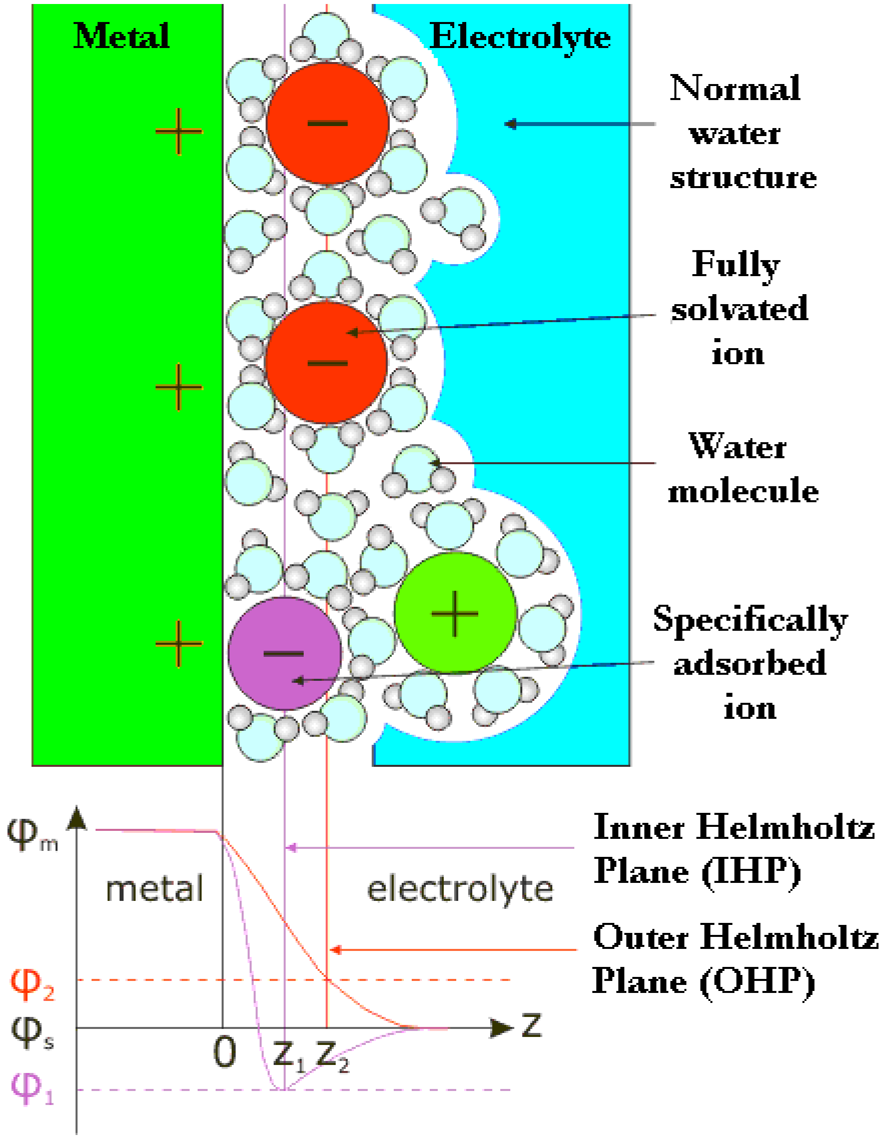
Metal
Electrolyte
Normal water structure
Fully solvated ion
Water molecule
Specifically adsorbed ion
Inner Helmholtz Plane (IHP)
Outer Helmholtz Plane (OHP)
φ_m
φ_2
φ_s
φ_1
metal
electrolyte
0
z_1 z_2
Z

Figure 2.10: A schematic interpretation of the metal/electrolyte interface and the electrochemical double layer. Also shown is a plot of the potential drop across the interface as a function of increasing distance Z. Adapted from [20].

potential applied. If a positive potential is applied, electrons will move out of the surface towards the electrolyte and its charge will become less negative and eventually positive. On the contrary, if the applied potential is negative, electrons will flow towards the electrode resulting in a negatively shifting surface charge. Consequently, a particular electrode/electrolyte combination will have a specific applied potential at which no electron transfer occurs. This leads to the concept of the potential of zero charge (PZC) and is described accurately by the above model.

2.3.1: Measuring Electrode Potentials

It is essential to be able to accurately control the potential drop across the working-electrode/solution interface $\left(\Phi_W - \Phi_{Solution}\right)$ as this is where the majority of reactions of interest in electrochemical systems occur. However, direct measurement of the absolute potential-difference across this interface is not possible. In a one-electrode cell measurements of the potential drop attempted with a digital volt meter (DVM), for example, fail since free-electrons will not flow from the DVM to the solution. If a second electrode is introduced to the cell the potential difference can be measured between these two electrodes. Still, this is an indirect method and is in effect a potential difference between two different metal/solution interfaces:

$$\begin{aligned}\Delta\Phi &= (\Phi_{(MetalA)} - \Phi_{(Solution)}) - (\Phi_{(MetalB)} - \Phi_{(Solution)}) \\ &= \Phi_{(MetalA)} - \Phi_{(MetalB)}\end{aligned}$$

The potential difference can be re-written if one of the electrodes represents a test system and the other a reference system:

$$\Delta\Phi = (\Phi_{(Test)} - \Phi_{(Solution)}) - (\Phi_{(Reference)} - \Phi_{(Solution)})$$

The potential drop across a reference electrode/solution interface remains constant, and the potential drop can now be written:

$$\Delta\Phi = (\Phi_{(Test)} - \Phi_{(Solution)}) - constant$$

The absolute value of $\Phi_{(Test)} - \Phi_{(Solution)}$ can still not be directly probed, but the changes in this value can be determined. The use of a reference electrode is thus an important introduction to electrochemistry experiments. The potential dependent experiments carried out in the current work involve the application of an external potential difference across the working electrode/solution interface. Large currents can alter the ionic concentration in the solution and therefore the contribution to the difference between the reference electrode and the measured potential will no longer be constant. As such two electrode set-ups are not applicable here since the current is sufficiently large to make the relative contributions an issue. The introduction of a third 'counter electrode' bypasses this problem by allowing the passage of current between it and the working electrode. This is different from the two electrode set-up where the passage of current is between the working and reference electrodes. For measurements in this thesis the counter electrode is a piece of platinum gauze due to its inert nature and large surface area.

2.3.2: The Electrochemical Cell

A purpose built three electrode spectro-electrochemical cell is employed for all potential controlled RAS experiments documented in this thesis [Figure 2.11]. The reference electrode is a SCE, consisting of Hg/Hg_2SO_4 in saturated aqueous KCl, whose role is to provide a fixed potential reference while a platinum gauze is used as the counter electrode. Also present is a luggin capillary to minimise the distance between the working and reference electrodes to avoid any potential drop while the SCE is separated from the electrochemical cell by a closed cap Teflon tap to prevent chloride contamination. All quoted potentials are versus SCE. Argon gas is bubbled into the electrochemical cell to de-gas and prevent oxygen contamination of the electrolyte.

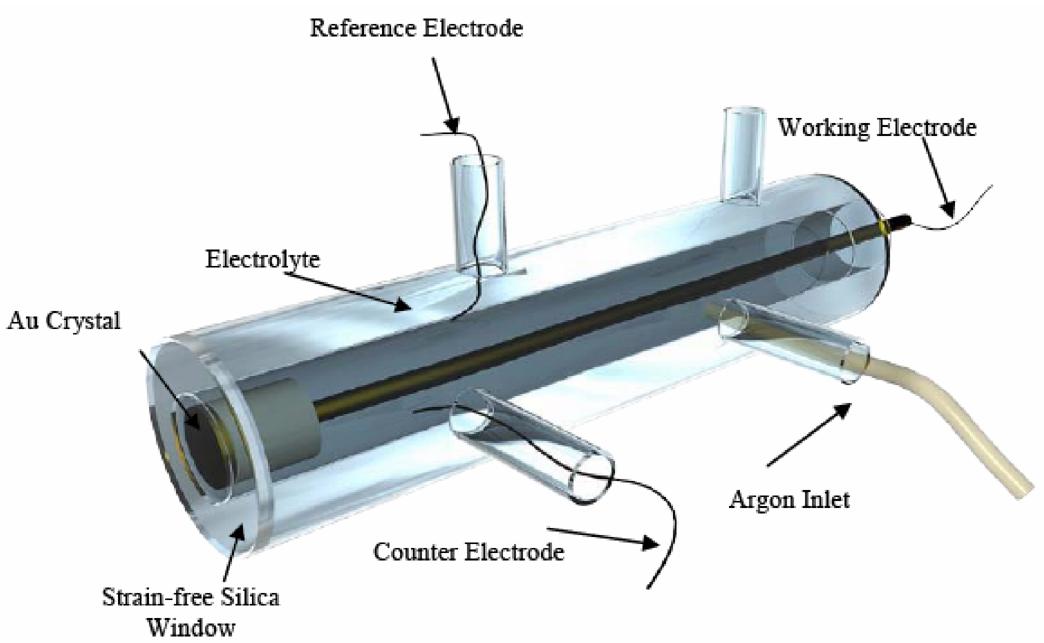

Figure 2.11: Schematic of the electrochemical cell used in all potential controlled experiments. Reproduced with permission from N. Almond [21].

2.3.3: Cyclic Voltammetry

Interpretation of current/voltage graphs are the classical method of studying electrochemical reactions and CV in particular is a very common technique for such endeavours. CV monitors the current between two electrodes as a function of applied potential, which is varied with a precise constant sweep rate of dV/dt. During experimentation, the applied potential is controlled with the use of a potentiostat. A potentiostat is in essence a feedback circuit based on an operational amplifier which ensures that zero current flows through the reference electrode. Peaks in CV profiles, otherwise known as 'cyclic voltamogramms', can arise from a number of electron transfer dependent reactions including; the formation or breaking of bonds, surface processes such as ionic adsorption/desorption and orientational variations in adsorbate layers. The range through which the potential traverses is chosen to correlate with an expected electrode reaction before the direction of the scan is reversed in order to determine whether the products of electron transfer are stable, intermediates or electroactive. Structural modifications to the electrode surface itself, such as surface reconstructions, are detectable on some electrode surfaces. Nonetheless, CVs are a measurement of electron transfer only and information regarding structural or chemical specificity cannot be substantiated directly. It is for this reason why it is very useful to use CV in conjunction with other *in situ* techniques such as RAS.

2.4: X-ray Photoelectron Spectroscopy

XPS is employed in this thesis as a sensitive diagnostic tool for the elemental and chemical analysis of adlayers on both Au(110) and CVD grown diamond surfaces. This technique harnesses the phenomena known as the photoelectric effect first detected by Heinrich Hertz in the latter part of the nineteenth century [22] which the eminent physicist James Clerk Maxwell had theorised some fifteen years previously. Einstein, through his famous Nobel prize winning paper of 1905 [23], placed the photoelectric effect in the common conscience by utilising Planck's quantum theory of black body radiation to propose that if and only if the frequency (ν) of the incident electromagnetic radiation had reached a specific threshold, could an electron spontaneously absorb a quantum of energy and hence be emitted from the material with a measurable kinetic energy (E_K). The technique is used extensively as it produces high quality re-producible results which can be interpreted in terms of the elemental composition and electronic structure of the subject sample.

Measurement of E_K together with knowing the work function ϕ of the analyser specific to each XPS instrument enables one to determine the binding energy (E_B) of the emitted electrons according to the photoelectric equation:

$$E_K = h\nu - \phi - E_B \tag{2.35}$$

thereby allowing identification of the characteristic energy levels of individual elements to be established.

The binding energy of an electron in a quantised atomic energy level is defined as the amount of energy required for that electron to escape the attractive electrostatic force provided by the atom's positive nucleus. The work function is defined as the difference in potential energy of an electron between two energy levels described as the Fermi level (E_F) and vacuum level (E_{vac}) as shown in Figure 2.12.

The nomenclature for core energy levels is *nlj* where *n* is the principal quantum number, *l* is the orbital angular momentum quantum number and *j* is the total angular momentum quantum number, $j = (l + s)$ where *s* is the spin angular momentum quantum number (± ½). Hence *s* levels ($l = 0$) are singlets but all other levels ($l > 0$) give rise to doublets.

In a recorded kinetic energy spectrum, the signals from core levels which one expects to be very sharp are broadened into peaks. There are two contributory factors which cause this broadening: (a) the lifetime of the core hole itself as it is governed by the processes that follow photoemission by which the excess energy of the ion state decays [24] (explained below) and takes the form of a Lorentzian contribution while more importantly (b) the instrumental Gaussian resolution function (Γ_I) whose origin arises from a combination of broadening effects from both the analyser (Γ_A) and monochromator (Γ_M) during measurement. The analyser resolution can be calculated from a well characterised feature such as the Fermi edge of Ag whilst the monochromator resolution is dependent upon how well the impingent radiation is focused. The relationship between these contributions is succinctly captured in Equation (2.36):

$$\Gamma_I^2 = \Gamma_A^2 + \Gamma_M^2 \tag{2.36}$$

K. Williams [25] has recently conducted calibration studies on the equipment used in the current work. A reproduction of the tabulated instrumental Gaussian resolution as a function of entrance slit width and pass energy is shown in Table 2.1.

The process of de-excitation of the electronic structure of the illuminated sample after photoelectron emission can occur via two decay paths; Auger electron processes [26] or X-ray fluorescence. The energy of the emitted Auger electron is dependent only upon the electronic structure of the subject atomic species and is independent of the energy of the incident electromagnetic radiation, in contrast to photoemission. The Auger decay path involves the creation of a core hole through either photoionisation or interaction with a high energy electron. This hole is filled by

Table 2.1: Gaussian resolution as a function of entrance slit width and pass energy.

	6mm slit	4mm slit	2mm slit	1mm circular aperture	5mm circular aperture
Analyser standard deviation Resolution at a pass energy of 10 eV	0.200	0.133	0.067	0.033	0.167
Analyser standard deviation Resolution at a pass energy of 20 eV	0.400	0.267	0.133	0.037	0.333
Analyser standard deviation Resolution at a pass energy of 50 eV	0.884	0.589	0.295	0.147	0.737
Analyser standard deviation Resolution at a pass energy of 100 eV	2.000	1.333	0.667	0.333	1.667

an electron from a less strongly bound energy level which liberates its excess energy in the form of the kinetic energy of a further (Auger) electron which is excited out of the atom. This process is explained schematically in Figure 2.12 for the case where an L-shell electron minimises the energy of the atom by dropping to the K-shell to fill the core hole. The energy released through this action, $E_B(K) – E_B(L)$, causes the electron remaining in the L-shell to be emitted and for the purposes of this specific case can be described in X-ray notation as a KLL Auger electron. The kinetic energy of the KLL Auger electron is:

$$E_K = E_B(K) - E_B(LL)$$

where $E_B(LL)$ is slightly larger than twice $E_B(L)$ since it also includes electron correlation and relaxation effects. The dominant decay pathway varies as a function of the atomic mass of the subject atom as displayed in Figure 2.13. For those species with $Z < Z_{Cu}$, Auger decay of K-shell holes is predominantly favoured whereas fluorescence has the highest yield for atoms with $Z > Z_{Cu}$.

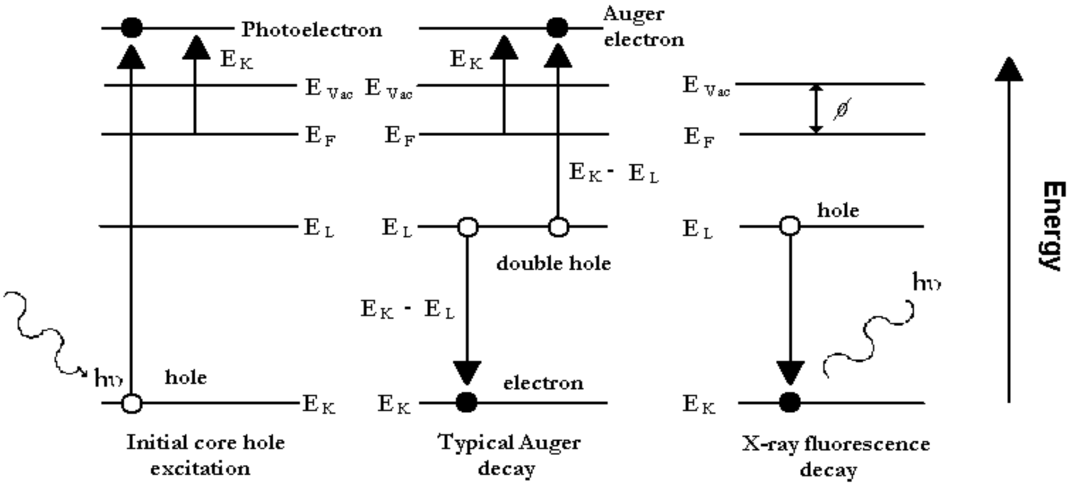
Photoelectron
E K
E Vac
E F
E L
E K
hν
hole
Initial core hole excitation
Auger electron
E K
E Vac
E F
E K - E L
E L
double hole
E K - E L
electron
E K
Typical Auger decay
E Vac
ϕ
E F
hole
E L
hν
E K
X-ray fluorescence decay
Energy

Figure 2.12: Schematic depiction of different core-hole relaxation processes after initial excitation with a photoelectron (left), including Auger electron emission (centre) and X-ray fluorescence (right).

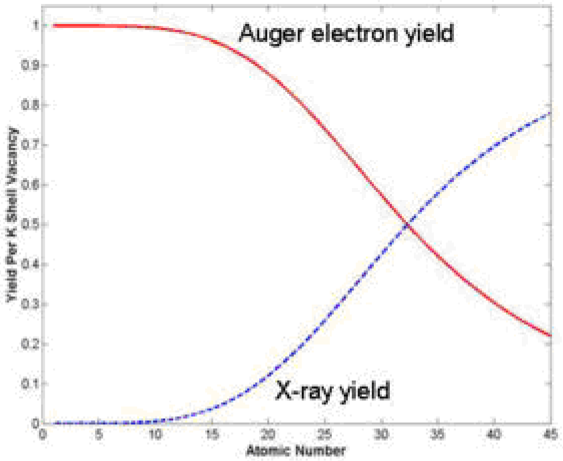

Figure 2.13: How the yield of de-excitation decay processes varies as a function of Z.

As a direct result of excitations in the surface layers by X-rays, photoelectrons are generated from a depth of 10 nm. The excited electrons move through the solid undergoing both inelastic and elastic scattering in which some will escape into the vacuum to be detected by the spectrometer. Only those photoelectrons that have been subject to either elastic or conversely no scattering whatsoever result in the discrete peaks on a spectrum whose energies reflect the quantised shell structure of the sample under investigation. Consequently electrons more loosely bound to the atom in higher shell configurations which escape from the solid without energy loss appear at a very high kinetic energy (or low binding energy) in XPS spectra. This is often labelled the no-loss or primary spectrum. In addition, there will also be intrinsic excitations occurring at the same time as the transfer of energy to the core level electron that appear as characteristic losses. Hence the primary spectrum consists of a peak or peaks together with a tail to higher binding energies that may or may not have significant structure [27]. Moreover, there are electrons that have lost energy through extrinsic inelastic processes as they traverse the solid and these appear as a background which extends from the peak energy to zero kinetic energy. This is called the inelastically-scattered background. A further, secondary, electron cascade background from electron collisions within the material which can result in secondary electron emission from atomic neighbours extends throughout the spectral range but is most intense at kinetic energies < 250 eV. This cascade effect is modest however and since few photoelectric peaks exist at such low kinetic energies it is generally ignored in XPS.

2.4.1: The VSW ESCA Instrument

All XPS experiments were conducted on the VSW ESCA instrument based in the T8 Laboratory of the Chadwick building at the University of Liverpool. A schematic of the main chamber with the monochromated X-ray source, hemispherical analyser, lens system and main pumping system comprising of ion and turbo pumps is presented in Figure 2.14.

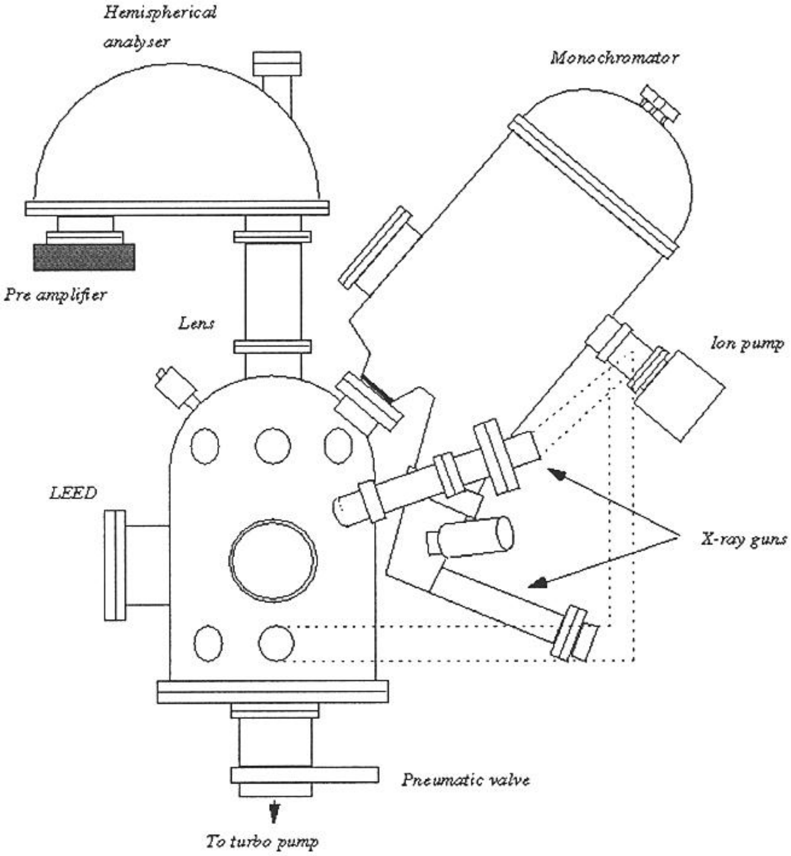
Hemispherical analyser
Monochromator
Pre amplifier
Lens
Ion pump
LEED
X-ray guns
Pneumatic valve
To turbo pump

Figure 2.14: Schematic of the VSW ESCA Spectrometer taken from [27].

Both the preparation and main chambers of the apparatus are each pumped by a turbo pump backed by an alcatel pump which encompasses a molecular drag pump backed by a diaphragm pump. A pneumatic valve on the preparation chamber offers protection against vacuum accidents such as unexpected venting. Additional pumping to reach and sustain the required UHV level is provided by titanium sublimation pumps in each chamber.

2.4.2: Monochromated X-ray Source

The instrument described above is equipped with a monochromated Al K_α X-ray source of the Henke design [29]. Thermionic electrons from a tungsten filament are accelerated onto an Aluminium anode held at a high potential of approximately 12.5 kV. The anode is cooled by a water pump of minimum flow rate 5 l/m and also pumped by an ion pump. Both anode and filament shape are carefully designed to produce a sharp focus of e^- onto a small spot on the anode thereby generating a sharply focused spot ~ 2 x 3 mm^2 in size. Core-level electrons are removed from the K-shell of atoms in the anode when electrons from the tungsten filament impact upon it. Core-hole states created through this process decay through characteristic emission of K-shell X-rays of 1486.6 eV.

A crystal monochromator is housed in a UHV maintained vessel terminating in a 1500 mm flange. An X-ray transparent Mylar window isolates the monochromator vacuum from the main experimental chamber. This window also protects samples from the relatively high pressure in the monochromator chamber caused by outgassing of the X-ray gun while preventing contamination of monochromator crystals through desorption of the specimen surfaces.

Monochromation of the X-rays is suitably attained by first order diffraction of the Al K_α radiation. The diffractor is a 200 mm^2 surface consisting of 35 quartz crystals cut parallel to the (1010) plane while the source, sample and monochromator lie on a 686 mm Rowland circle. The Bragg angle is set to 78.5° to satisfy the Bragg condition for first order diffraction of the subject radiation. The crystals themselves are mounted in accordance with Johann geometry providing a radiation spot size in relation to the size of the X-ray source. Mechanical adjustment of the orientation and position of the crystals relative to source and sample is made possible through three precision micrometers on the vacuum housing.

2.4.3: Analysis of Photoelectron Energies

To accurately resolve and analyse the spectrum of photoelectron energies requires a

150 mm hemispherical analyser be employed. A six element electrostatic lens which retards photoelectrons helps to focus them onto then entrance slits of the analyser. These electrons are then fed into channel plates to provide a platform for 16 channel detection. As is shown in Table 2.1, there are five choices for entrance slit width: 5 and 1 mm diameter holes and 2 X, 4 X and 6 X 12 mm slits. These can be changed externally along with 4 different pass energies enabling the user to balance resolution with count rate. The analyser has an acceptance angle (α) of 4° and the energy resolution is calculated from Equation (2.37):

$$\Delta E = E_0 (\frac{d}{2R_0} + \frac{\alpha^2}{4}) \tag{2.37}$$

where E_0 is the energy being analysed (pass energy), d is the chosen slit width and R_0 is the mean radius of the hemisphere (150 mm).

The energy scale of the spectrometer can be accurately calibrated enabling detailed binding and Auger energies to be determined. The analyser power supplies are driven by a 0 – 10 V output from a computer controlled DAC. R. Unwin from Scientific Instruments Consultants in 2003 (Version 8.5-D-A) has written software to control analyser voltages and calibration.

Photoelectrons dispersed in energy across the exit focal plane emerge from the analyser and enter microchannel plates. Two channel plates are situated directly beneath the analyser exit slit. Whilst a scan is engaged the channel plates are run sequentially through each energy point on the spectrum meaning that each channel contributes equally to each data point. The effect of this multi-detector array is to greatly improve sensitivity and in conjunction with the monochromated Al K_α source results in highly precise and resolved measurements.

2.5: References

[1] T. E. Jenkins, *J. Phys. D: Appl. Phys.* **32**, R45 (1999)

[2] K. Vedam, *Thin Solid Films* **313**, 1 (1998)

[3] P. Weightman, *Surface Science Lecture Series* (2005)

[4] *Ellipsometery and Polarised Light*, R. M. Azzam and N. M. Bashara (Amsterdam: Elsevier, 1977)

[5] J. F. McGilp, *Prog. Surf. Sci.* **49**, 1 (1995)

[6] D. E. Aspnes, E. Colas, A. A. Studna, R. Bhat, M. A. Koza and V. G. Keramidas, *Phys. Rev. Lett.* **61**, 2782 (1988)

[7] P. Weightman, D. S. Martin, R. J. Cole and T. Farrell, *Rep. Prog. Phys.* **68**, 1251 (2005)

[8] B. Sheridan, D. S. Martin, J. R. Power, S. D. Barret, C. I. Smith, C. A. Lucas, R. J. Nichols and P. Weightman, *Phys. Rev. Lett.* **85**, (21) 4619 (2000)

[9] C. I. Smith, A. J. Maunder, C. A. Lucas, R. J. Nichols and P. Weightman, *J. Electrochem. Soc.* **150**, E233 (2003)

[10] C. I. Smith, G. J. Dolan, T. Farrell, A. J. Maunder, D. G. Fernig, C. Edwards and P. Weightman, *J. Phys.: Condens. Matter* **16**, S4385 (2004)

[11] R. LeParc, C. I. Smith, M. C. Cuquerella, R. L. Williams, D. G. Fernig, C. Edwards, D. S. Martin and P. Weightman, *Langmuir* **22**, 3413 (2006).

[12] C. I. Smith, A. Bowfield, G. J. Dolan, M. C. Cuquerella, C. P. Mansley, D. G. Fernig, C. Edwards and P. Weightman, *J. Chem. Phys.* **130**, 044702 (2009)

[13] A. Bowfield, C. I. Smith, G. J. Dolan, M. C. Cuquerella, C. P. Mansley, and P. Weightman, *e-J. Surf. Sci. Nanotech.* **7**, (2009)

[14] G. Dolan, *PhD Thesis*, University of Liverpool (2006)

[15] N. Blanchard, *PhD Thesis*, University of Liverpool (2004)

[16] A. Maunder, *PhD Thesis*, University of Liverpool (2001)

[17] *A First Course in Electrode Processes,* D. Pletcher (The electrochemistry consultancy, 1991)

[18] *Interfacial Electrochemistry: Theory, Experiment and Applications*, edited by A. Wieckowski (Marcel Dekker Inc., 1999)

[19] D. C. Graham, *Chem. Rev.* **41**, 441 (1946)

[20] D.M. Kolb, *Surf. Sci.* **500**, 722 (2002)

[21] N. Almond, *PhD Thesis*, University of Liverpool (2008)

[22] H. Hertz, *Sitzungsbericht der Berliner Akademie der Wissenschaften* **9**, June (1887) & *Ann. Physik* **31**, 983 (1887)

[23] A. Einstein, *Ann. der Physik* **17**, 132 (1905)

[24] P. Weightman, *Rep. Prog. Phys.* **45**, 753 (1982)

[25] K. H. Williams, *M. Phil. Thesis*, University of Liverpool (2006)

[26] P. Auger, *J. Phys. Radium* **6**, 205 (1925)

[27] *Surface Analysis by Auger and X-ray Photoelectron Spectroscopy*, edited by D. Briggs and J. T. Grant (IM Publications, 2003)

[28] A. Domke, *PhD Thesis*, University of Liverpool (1999)

[29] B. L. Henke, *Adv. X-ray Anal.* **4**, 244 (1961)

Chapter 3: The Au(110) Surface

This chapter reviews the previous work on Au(110) in both electrochemical and UHV environments with a discussion on how its physical and electronic structure relate to features observed in its RA profile. Also introduced are the three-phase and Lorentzian transition models which allow simulations of RA spectra to be performed and interpreted in terms of a number of defined optical transitions. Au(110) is known to form different surface reconstructions dependent upon applied electrode potential and electrolyte. An electrochemical study is also presented and the spectral signatures of the different reconstructions of Au(110) are assigned.

3.1: Introduction

The inherent anisotropy of the Au(110) surface, which is characterised by a (1x2) "missing row" reconstruction after preparation [Figure 3.1], makes the surface a highly advantageous substrate on which to study molecular adsorption since sample anisotropy is a fundamental requirement of the RAS technique to ensure surface specificity. The (110) surface of this crystal is made more attractive as a platform for RAS studies since the two other ideally terminated low-index faces of gold, (100) and (111), are both intrinsically isotropic and consequently produce a zero RAS signal. The preparation procedure, described later in this chapter, means RAS investigations are not confined to UHV environments and the material then allows for reproducible surface structures which is crucial for laboratory studies.

3.2: Surface Phase Transitions

Phase transitions occur in many physical systems and classifications of such systems are described by two broad categories; first-order transitions which involve a latent heat and occur mainly through a mixed phase regime where some parts of the system have completed the transition and others have not and include the solid/liquid/gas transitions, and second-order (continuous) phase transitions which do not involve a latent heat and include the emergence of superconductivity in certain materials below a threshold temperature and superfluidic transitions in He. These transitions occur due to the penchant of systems in thermodynamic equilibrium at constant volume and temperature to minimise their free energy, F.

$$F = U - TS$$

Transitions between different states occur at varying temperatures because they separate their free energy between the internal energy U(T) and entropy S(T) in dissimilar ways. Order parameters, which reflect the degree of order prevalent in the system, allow characterisation of phase transitions and exhibit differing behaviours as the transition temperature, T_C, is reached depending on the nature of the phase transition involved. First-order transitions involve a discontinuous change as conversion from one equilibrium phase to another occurs while such discontinuities are absent from second-order transitions.

As will be discussed within this section, Au(110) undergoes a phase transition between (1x2) and (1x1) surface conformations. This transition can be induced either thermally in UHV conditions or potentiostatically during electrochemical investigations. The exact nature of the phase transition has generated significant research activity and an overview of the previous work on this subject will be conducted.

3.3: Physical Structure of the Au(110) Surface

A fundamental understanding of the transitional nature of the (110) surface in different environments is necessary to underpin interpretations of and modifications to the spectral profile of the system as a function of temperature and applied electrode potential. This section gives an overview of the findings of previous literature on the structure and conformation of the surface in both UHV and electrolyte environments so as to enable a better understanding of the dynamics of structural reconstruction and their causes. However, it is sensible to note that direct comparisons between these disparate external surroundings are difficult and as such an exclusively qualitative and empirical approach is taken. An exhaustive literature review was recently conducted by N. J. Almond [1] on this issue and I shall outline the main findings from this work in the following section.

3.3.1: Au(110) in UHV

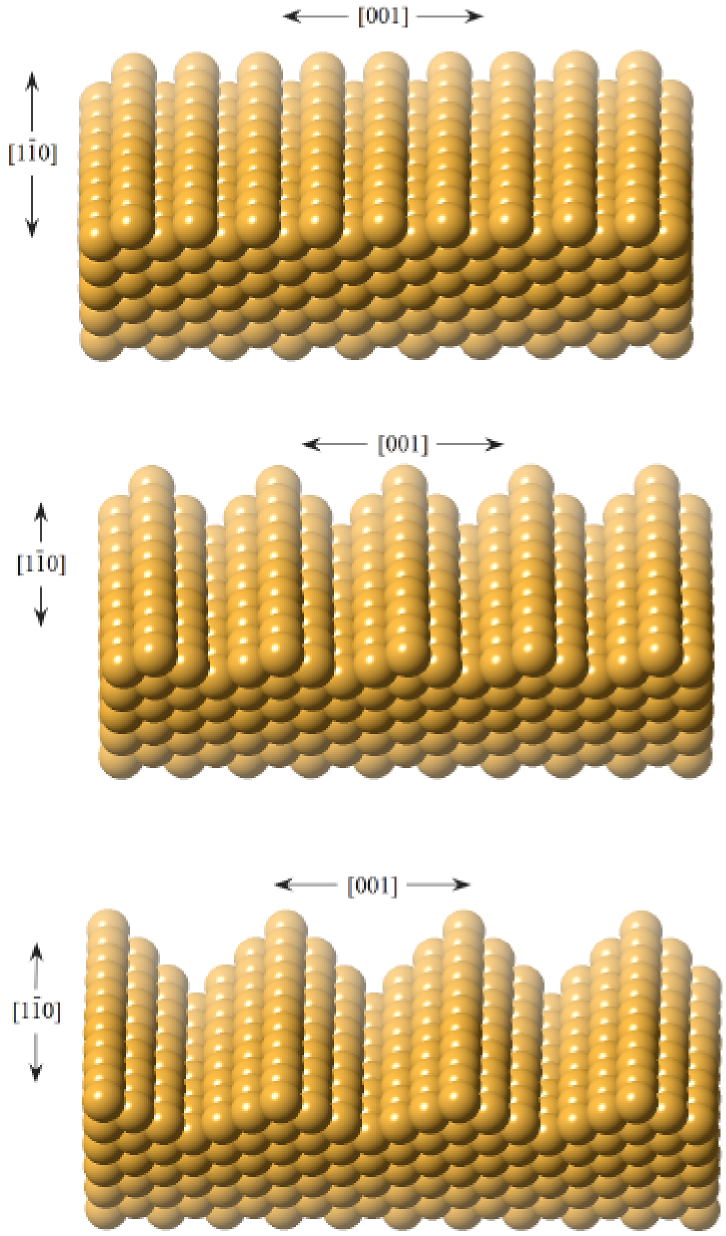
[001]
[1$\bar{1}$0]
[001]
[1$\bar{1}$0]
[001]
[1$\bar{1}$0]

Figure 3.1: Schematic of the (1x1) (top), (1x2) (middle) and (1x3) (bottom) reconstructions.

The (110) surface is the most open of the low Miller index surfaces of FCC crystals and as such has both the lowest atomic density and highest surface energy. These intrinsic characteristics lead to a propensity towards reconstruction, the most typical of which is the (1x2) surface reconstruction as shown in Figure 3.1.

The (1x2) structure was first revealed using LEED [2,3] through a reversible temperature induced (1x2) to (1x1) phase transition. This transition involves extensive reorganisation of the topmost surface atoms coupled to minor atomic displacement in the underlying layers [4]. R-factor analysis and XRD [5,6] showed that a missing row model was the most likely explanation though some groups rejected the findings [7,8] due to the mass transport problem. The mass transport problem is a discrepancy between the transition and self-diffusion times necessary for movement of Au atoms over hundreds of Angstroms. Campuzano *et al* [9] proposed that the thermally induced (1x1) phase transition belongs to the 2D Ising universality class [10] of transitions and does not entail substantial mass transport. In this model, the (1x1) reconstruction can be considered a disordered lattice gas phase where the topmost atoms are randomly placed on the surface rather than aligned in rows.

STM is useful for investigating phase transitions as it can image the changes in structural details such as step formations, anti-phase domain walls and microfaceting. The STM work of Binnig *et al* [11] confirmed the missing row structure as that taken by the surface after reconstruction. The (1x2) reconstruction is characterised by a surface phase transition facilitated by the removal of every second row of surface atoms along the $[1\bar{1}0]$ direction which opens up (111) microfacets between the rows of atoms in this crystal axis [11]. Ref. [11] also suggested that formation of (111) microfacets are the principal driving force of the reconstruction mechanism as they result in a more energetically stable surface due to their more compact nature.

STM has also been used to provide insight into the dynamics of surface structure during the transitional process [12-18]. These studies found that step structure was critically important to the phase transitions, with observation of a mesoscopic “fish scale pattern” on the surface; a structure that is associated with large numbers of anti-phase domain boundaries consisting of (111) step edges [16]. The monatomic step arrangement on Au(110), primarily confined along $[1\bar{1}0]$ as steps along [100] are hindered at room temperature, was found to promote the growth of large terraces terminated with steps parallel to the close packed rows, thus bringing about the intrinsic anisotropy of the surface. The disordered lattice gas model [9] explained only part of the process and was found to apply if the surface consisted solely of domain wall defects. However, if steps were the only defect present on the surface, a roughening transition would occur. Since both step and domain wall defects are present on Au(110), it was concluded that the surface first undergoes a 2D Ising transition at which the surface deconstructs (T_D) and at higher temperatures a roughening transition (T_R). Both these transitions occur within a 100 K range of each other.

STM [14] also showed that a well formed (1x2) reconstruction cannot be terminated on both sides of a step along $[1\bar{1}0]$ by (111) microfacets alone and established that adjacent (1x2) regions must be in anti-phase to one another, separated by a (1x3) domain boundary which facilitates their proliferation across the surface.

Evidence was provided that the (1x2) surface reconstruction was stable at high temperatures close to T_R at interior terrace regions [4,17]. The function of the deconstruction transition was found to primarily disorder step edges in disagreement with the lattice gas model. A large variation in the temperature of deconstruction is reported for Au(110) (850 K - 1080 K) due to the influence of surface step density, which varies with preparation and quality of the crystal, on T_D. Considering step density varies between surfaces, it is surprising that STM shows that the average step density for any particular surface remains approximately constant up to T_D. The consistency of surface step density also points towards a solution for the mass transport problem in that a transition to (1x1) from the ordered (1x2) requires a movement of 50% of the surface atoms. Hence, movement of steps and growth of terraces on a surface-wide scale would be reflected in varying step density and it is therefore more likely that the (1x1) consists of a disordered half monolayer of atoms which would require only a local displacement of the order of a lattice spacing.

A clean Au(110) surface exhibits the (1x2) reconstruction along with the other

5*d* FCC metals Ir and Pt when under UHV conditions [19,20]. Stabilisation of the missing row reconstruction with highly coordinated atoms in the (111) microfacets, was found to be primarily due to the need to lower the kinetic energy of the *s-p* electrons at the surface by delocalisation thereby avoiding the need to increase the number of broken bonds and lowering the surface electronic density whilst retaining much of the bulk cohesion [21]. However, this is not the case for the isoelectronic 3*d* and 4*d* FCC transition and noble metals (Ni, Cu, Rh, Pd and Ag) which retain a (1x1) structure in such conditions. A similar argument to that above was used to explain the presence of the (1x2) reconstruction on Ag(110) following adsorption by submonolayer quantities of potassium [22]. In this instance it is thought charge transfer from the alkali to the surface increases the surface electronic charge density of the *s-p* electrons making the (1x2) more energetically favourable through the need to reduce surface kinetic energy. The RA profile associated with the (1x2) reconstruction is shown in Figure 3.2.

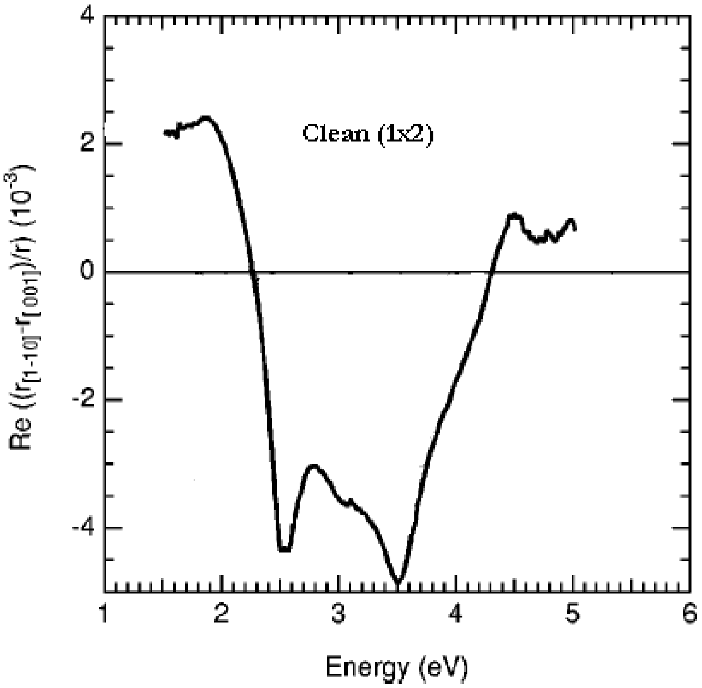

Figure 3.2: Au(110) in UHV displaying the RA profile of the (1x2) reconstruction from [19].

3.3.2: Electrochemistry of Au(110)

It is clear from the above discussion that an understanding of the mechanisms involved in reconstruction of Au(110) has been gained in the UHV environment. Unfortunately electrochemical conditions make information from the surface much more difficult to interpret due to the bulk electrolyte. Electrochemical STM has so far provided most information on the surface. Analysis of the Au(110) electrode in aqueous perchloric acid ($HClO_4$) [23] showed the surface behaves similarly to the UHV environment at applied potentials slightly negative of the PZC [Chapter 2.3]. At -0.02 V vs SCE the surface was observed to consist principally of (1x2) domains with some small areas of (1x3). The stability of this structure was preserved even at applied electrode potentials of -0.3 V. The surface electronic charge density will be negative at these potentials, as in UHV, thereby encouraging reconstruction due to minimisation of surface kinetic energy. A reversible transition to the unreconstructed (1x1) structure was also recorded at zero Volts, the speed of which (within ~ 2 s) can be attributed to low atomic density of the surface and the need for only short range motion of atoms.

A more thorough report on Au(110) in perchloric and sulphuric acid (H_2SO_4) [24] confirmed that the reconstruction elements of the surface in electrolyte, with 700 Å terraces separated by monatomic steps, closely matched those witnessed in UHV. However, homogeneously distributed anisotropic Au islands deposited atop half of the terraces on the surface were only observed in electrochemical environments as a consequence of annealing performed before experimentation. In UHV on the other hand the density of the islands, which are (1x2) in character and arise due to varying levels of kinetic freedom obtained during sample preparation, were only reduced in the immediate vicinity of the steps thereby leaving only small areas with an ideal (1x2) reconstruction. The (1x2) reconstruction was only preserved below potentials of +0.05 V while at +0.25 V, the surface consisted of the unreconstructed (1x1) phase. In between these potentials the surface existed in a dynamic equilibrium between reconstructed and unreconstructed conformations. This study found the potential below which the surface adopts the missing-row reconstruction was 0.3 V higher than that established by Gao *et al* [23]. Nonetheless it is consistent with the theory that at potentials surrounding the PZC this should be the most prevalent reconstruction matching the surface in UHV which is known to be similarly reconstructed. Minimal numbers of steps exist at potentials above +0.2 V and the surface is littered with isotropically shaped islands and holes of a monolayer size. The locations of these islands correlate well with the location of anisotropic islands on terraces that were previously (1x2) reconstructed, displaying their ability to be converted from one structure to another. A large-scale roughening of the surface occurred as the potential was increased above +0.8 V associated with oxidation of the substrate.

Step structure stabilisation in the electrochemical environment is also mediated by the formation of (111) microfacets even though the (1x2) regions are smaller than in UHV. Magnussen *et al* [24] concurred with previous work [14] and observed numerous occurrences of anti-phase domain boundaries separating (1x2) terraces inferring that (1x3) domains have a crucial role in the mechanism of the phase transition itself. It is in the effort to form stable configurations of (111) microfacets on both sides of the terrace ledge to achieve low kink density that (1x3) structures are prevalent.

A surface X-ray scattering study [25] agreed with STM results for the reconstructed surface in perchloric acid. The formation of a (1×2) reconstruction was recorded at 0.0 V vs SCE, which consisted of predominantly (1×2) domains with small (1×3) elements. The effects of a number of salt solutions on the reconstruction were also investigated. The onset of hydrogen evolution is delayed until more negative potentials in alkaline than in acid and therefore allows a greater potential window to be studied. The salt solutions were found to encourage the (1×3) reconstruction at sufficiently negative potentials. As the applied potential traversed the positive regime, the surface adopted the unreconstructed (1×1) structure without the formation of the intermediate (1×2) missing row phase. The observation of a direct (1x1) → (1x3) phase transition is consistent with findings in UHV following the adsorption of small concentrations of alkali metals, suggesting that a sufficiently negative surface charge induces a (1×3) reconstruction. Further studies also agree with these conclusions [26-28].

In summary, the electrochemical studies discussed above indicate that the surface adopts the (1×2) reconstruction at potentials approaching or slightly negative of the PZC and that the unreconstructed (1×1) phase becomes dominant at positive surface charges. When placed in alkaline solutions the (1x3) surface structure becomes prevalent due to the larger negative excess charge obtainable in these electrolytes. The presence of a direct phase transition from the (1×3) reconstruction to the unreconstructed (1×1), even at low negative surface excess where the (1×2) usually exists is not fully understood. One possible explanation may lie in the effect of different anions and their role in promoting or preserving reconstructions and a thorough investigation into these effects is carried out later in this section.

It is clear from the discussion above that the mechanisms and principles underpinning surface phase transitions on Au(110) are nontrivial. This thesis exclusively studies Au(110) in liquid, but it is important that reference to UHV work be central to any proposed arguments as there are similarities between the work in either environment and, of course, UHV does not have interference from bulk media. The role of (111) microfacets including their proliferation and stability are central to monitoring the surface reconstructions and using RAS to interpret their corresponding optical response. In order to do this we must first discuss the electronic structure of the surface, since this is the immediate origin of the RA spectral profile.

3.4: Electronic Structure of Au(110)

It is single particle excitations between states in the band structure of gold which give rise to the typical RA profile of the material. We know this as experimental techniques such as electroreflectance spectroscopy (ERS) make it possible to map the band structure of metals and semiconductors alike. ERS [29] established that Au(110) was infact anisotropic when reconstructed and that the states occupied by surface electrons are sensitive to the arrangement of atoms. ERS was also employed to observe optical transitions between surface states of the low Miller index gold surfaces [30]. A comparison was then made with pseudo-potential calculations of the bulk and electronic structure. This system assumed an almost free electron model with crystal induced states and related surface states compared to symmetry points on the Surface Brillouin Zone (SBZ). Alas, the model is based on an ideally terminated (1x1) surface and therefore does make allowances for the presence of a surface reconstruction. The effect of such surface reconstruction was accounted for in two studies [21,31] by the halving of the SBZ and these calculations were validated by photoemission measurements [32]. Figure 3.3 shows the calculated electronic structure of Au(110) by Xu *et al* [31].

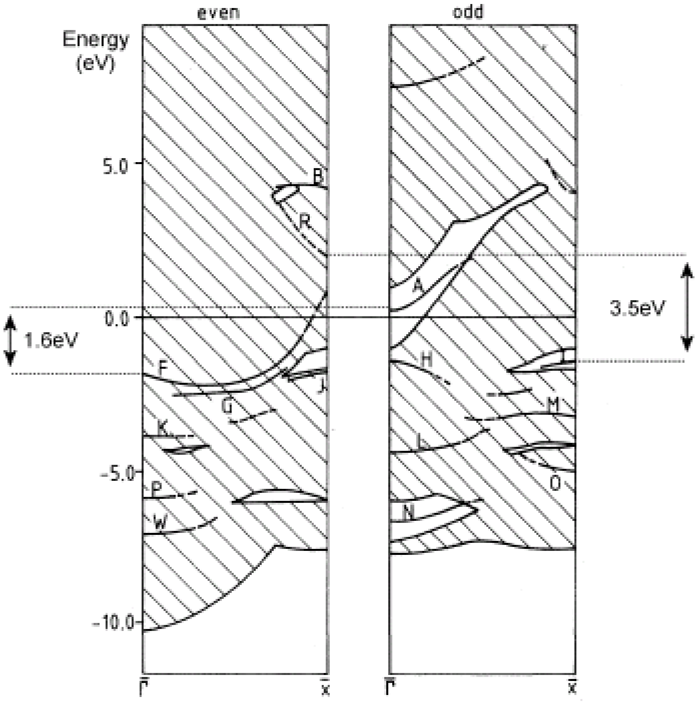

Figure 3.3: The electronic structure of Au(110) generated by the calculations of Xu *et al* [31].

3.5: RAS of Au(110): Origin of Spectral Features

If a consistent explanation and understanding of the origin of spectral features in RAS is to be achieved, it is attractive to underpin data obtained experimentally with a theoretical simulation in order to extend and predict such formalisms to other complex systems. Such a rigorous foundation for the nature of RA measurements is still in its infancy and while such calculations exists for the (110) faces of Cu, W and Ag, the simulation of experimental spectra of Au(110) from first principles is not yet possible, probably due to the transitional character of the surface.

Initial experiments utilising RAS recorded the optical response of both Ag(110) and Au(110) surfaces in 1994 [33] with the first RA spectral profile of Au(110) in ambient conditions published alongside a theoretical reproduction employing the surface local-field effect (SLFE) model as a basis. The RAS of Au(110) in this reference differs somewhat from profiles produced by modern spectrometers and there was a sizeable divergence between experimental and theoretical results. Still, the study established the surface sensitivity of RAS to cubic crystals such as Au(110). This same calculation was also used to explain the Au(110) in UHV but again failed to adequately simulate experimental RA spectra [34]. In spite of this discrepancy, the authors produced calculated spectra for the (1x1) → (1x2) phase transition characterised by an increase in the feature at ~ 2.5 eV. This behaviour was ascribed to the screened local field on d-band transitions and has been replicated in more recent studies [1,35,36] including this thesis. This trend however, is at odds with a combined STM and RAS study from 1999 [37]. These authors were the first to record the RAS of Au(110) in an electrochemical environment and indeed reported a decrease in the 2.5 eV peak intensity at -0.2 V where they observed a “poorly reconstructed” (1x2) surface structure. Interestingly, the same authors latterly labelled an extremely similar RA profile to that of an “optical fingerprint” of a perfect (1x2) reconstruction on Au(110) [38]; an assignment the current work disagrees with. Weightman *et al* [39] suggested that the source of this inconsistency lies in the differing surface morphology of the gold crystals used in each study. While such an explanation is certainly valid, this thesis also investigates an alternative possible contributing factor to the discrepancy between the optical profiles which will be discussed in-depth later in this chapter.

The RA profile of Au(110)-(1x2) was interpreted by Sheridan *et al* [35] in terms of optical transitions between $\overline{\Gamma}$ and $\overline{X}$ points in surface bands determined from first principle calculations [31]. Using these calculations, along with results from inverse photoemission experiments [40], the authors [35] were able to identify spectral features of Au(110) with transitions between states in its surface electronic structure. The peak at ~ 2.5 eV in the optical spectrum of Au(110) is the result of a transition at the Γ point between an occupied surface resonance of odd symmetry arising from *d* states of *yz* character and an empty surface state ~ 0.3 eV above the Fermi energy with even symmetry and predominantly *p* character. It is expected that the region of the spectrum up to this energy will be sensitive to variations in the physical or electronic structure of the surface due to the involvement of the surface state [35]. The ~ 3.5 eV feature is attributed to a transition between an empty state of even symmetry and predominantly *sp* character and a *d* derived filled state of odd symmetry. The ~ 3.5 eV feature is less surface sensitive since the transition arises from surface resonance derived from a bulk state to a final state dominated by contributions from the second layer of atoms.

Figure 3.2 shows that the RA spectral profile of Au(110) in UHV is characterised by a positive feature in the 1.6 - 2.4 eV range, negative features at approximately 2.5 and 3.5 eV and a further positive feature centred at 4.5 eV. Previous work discussed above has determined to some extent that the origin of the first three of these features can be found in the electronic structure of the surface and immediate underlying layers whereas the remaining region of the spectrum between 4.0 and 5.0 eV involves more qualitative analysis. It was shown by studies [20] involving RAS in conjunction with STM in UHV that the large positive feature centred at 4.5 eV was a reflection of surface morphology in terms of its step structure and roughness. This peak was found to be indicative of the presence of monatomic high steps on the surface aligned along the $[1\overline{1}0]$ axis. Displayed in Figures 3.4 (a) and (b) are the STM and associated RAS of a freshly prepared Au(110) crystal displaying the RA profile of the (1x2) reconstruction and the associated monatomic steps taken from [20].

After this data was recorded, the surface was subjected to Ar ion bombardment for fixed time intervals and probed with STM, LEED and RAS. The sensitivity of the feature at 3.5 eV to surface order was shown through its almost immediate removal from the RA profile after 3 minutes exposure. STM showed that the long step structures present in the image of the clean Au(110) surface is lost over a similar time scale to that of the 3.5 eV feature, thereby implying a sensitivity to surface morphology. Accompanying this was the loss of the 4.5 eV feature, which is sensitive to steps, which

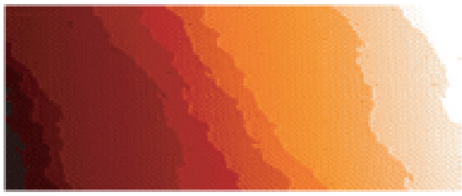

Figure 3.4 (a): Contrast STM of Au(110) in UHV after annealing showing the monatomic steps and large terraces associated with the (1x2) reconstruction.

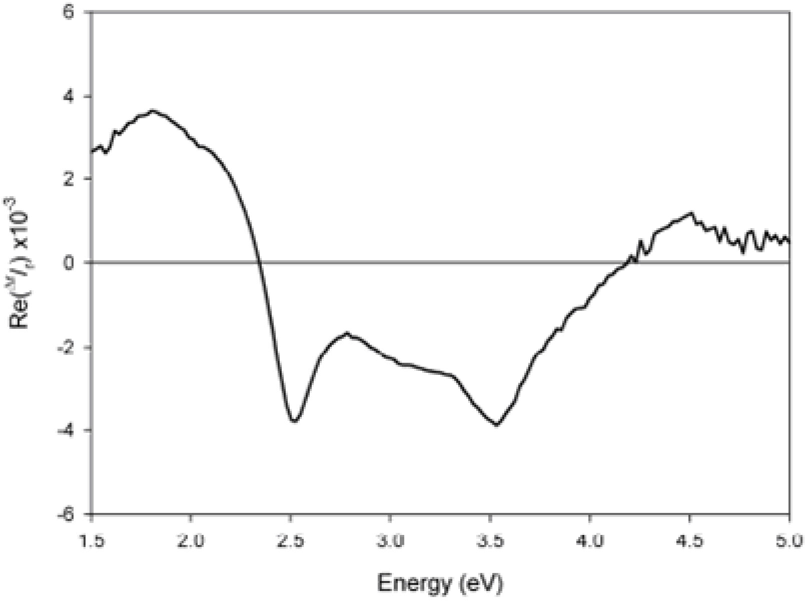

Figure 3.4 (b): Associated RA profile of the Au(110) crystal shown in (a).

becomes a flat line after only 3 minutes. Similar modification to the RA profile was observed for Cu(110) [41] which was attributed to introduction of anisotropy to the surface by bombardment which does not coincide with the principle crystallographic directions. The 1.5 - 2.4 eV region of the Au spectra also reduces, signalling a reduction in the truncation and anisotropy of the surface layer thereby reducing contributions from the surface state. Although the 2.5 eV peak lost intensity, its definition was retained after 36 minutes bombardment corresponding to the slow removal of the (1x2) reconstruction to (1x1). The study shows that this feature is sensitive to reconstruction but also relatively insensitive to surface roughness. Moreover, the surface is unlike the truncated surfaces of the (1x2) and (1x3) reconstructions in that any contribution from the second and third atomic layers layer is likely to be of a disordered fashion and therefore not provide any surface anisotropy. This may explain the persistence of the surface states and destruction of the bulk states which are modified by the surface which contribute to the region. This agrees with previous studies [19,34] which state that this feature is derived from inter-band transitions involving bulk d-bands.

The effect of temperature on the RA profile of Au(110) in UHV has also been investigated to understand spectral origins further [19,42]. The two studies give consistent results with features losing definition as the temperature is raised to 800 K [19] and 1000 K [42] which is above both T_c and T_R for this surface. Features at 1.8, 2.5, 3.5 and 4.5 eV are identified and tracked. The characteristics of the positive feature at 1.8 eV are unaffected by temperature variation but there is an intensity reduction between this feature and the negative peak at 2.5 eV which is again reflective of increasing atomic disorder due to the phase transition which is expected to occur in this temperature range. The energy of the 2.5 eV feature remains constant up to 580 K, after which, a small shift to higher energy is noted. This feature then broadens in the high temperature range and subsequently loses its definition at approximately T_R (~700 to 815 K). The modifications to the negative peak at 3.5 eV are much more noticeable with a shift to 3.1 eV and broadening which occurs progressively with increasing temperature. Similar behaviour is observed with the feature between 4.0 and 5.0 eV, which is again indicative that these features are closely related.

These results were analysed using a derivative model [43] and the variation of energy with temperature in this study [42] was found to agree well with a thermovariation spectroscopy study [44] which showed that the main features of the bulk dielectric function, ε_b, for Au are derived from interband transitions in the vicinity of the L point of the bulk BZ. Such consistencies lead to the peaks at 3.5 and 4.5 eV being assigned the $E_F \rightarrow L_1^u$ and $L_2^{'} \rightarrow L_1^u$ transitions respectively. This was the first study to establish this link and as such showed that the 2.5 - 4.5 eV region of the spectrum is derived from contributions of what are essentially surface modified bulk states. The assignment of $E_F \rightarrow L_3$ to the 2.5 eV feature is responsible for the sharp rise in $A(\omega)$ (section 3.6.2) however, its variation with temperature cannot be explained by this analysis.

It is interesting to note that the thermally induced transition to an unreconstructed surface and the resultant variation in energy of the peaks at ~ 2.5 and ~ 3.5 eV correlates well with the change in peak energy found from the three-phase model (section 3.6) for the same transition in the electrochemical environment [1]. As there are no abrupt changes in the profiles however, it is still not clear specifically where the (1x2) – (1x1) transition occurs in either case. This is an inherent problem with the technique since RAS details a large scale of the surface in a single measurement and may be recording the shift in equilibrium of a mixture of domains comprising of all three reconstructions.

Studies on monitoring the underpotential deposition (UPD) of copper onto gold surfaces have offered further insight [45-51]. These investigations also used a range of surface specific probes including RAS [51]. The RA profile of Au(110) in $H_2SO_4/CuSO_4$ in the positive potential regime detailed changes in the optical response of the system with one monolayer of adsorbed Cu at +0.1 V vs SCE, where the (1x2) reconstruction should occur, compared to no copper adsorption at +0.4 V where the surface should be predominantly (1x1). These changes manifested themselves in a marked increase in the 3.5 eV feature coupled with a smaller reduction in the negative peak at 2.5 eV and changes to the spectrum below this energy. Analysis using the three-phase model [1] showed that these changes were consistent with the changing of the reconstruction from a (1x1) to a (1x2) structure in electrolyte; the implication being that UPD of copper does not hinder this phase transition. Subtraction spectra of Au(110) in H_2SO_4 at +0.1 V and +0.4 V with and without $CuSO_4$ also showed that the modifications to the optical response of the system were as a result of the action of the UPD layer and not a transition towards a more reconstructed state. It was shown that a layer of copper terminates the surface and makes the surface more bulk like. This induces an increase in the 3.5 eV region since there is now increased anisotropy in the atomic layers immediately below the surface. The deposition of 2ML of palladium on Au(110) showed the deposited metal layer was below the surface [52]. A reduction in the 3.5 eV feature is explained by the composition of the second and third atomic layers consisting of a mixed Pd/Au layer which would consequently lack anisotropy. The reduction in this spectral region may then be due to comparable lack of modification of bulk states or due to the damping of these bulk transitions due to the palladium subsurface layer.

It is apparent that RAS is sufficiently sensitive to monitor structural reconstructions and reflects this in notable modifications to spectral features as external parameters are varied. Its versatility and applicability to both UHV and electrochemical environments makes the probe an appealing technique to investigate the themes discussed in this chapter.

3.6: The Three-Phase Model

While the Jones matrix formalism describes what happens when polarised light is reflected by a surface, to interpret the RA spectrum we must also understand why. In the absence of *ab initio* theoretical treatments, McIntyre and Aspnes [53] applied a

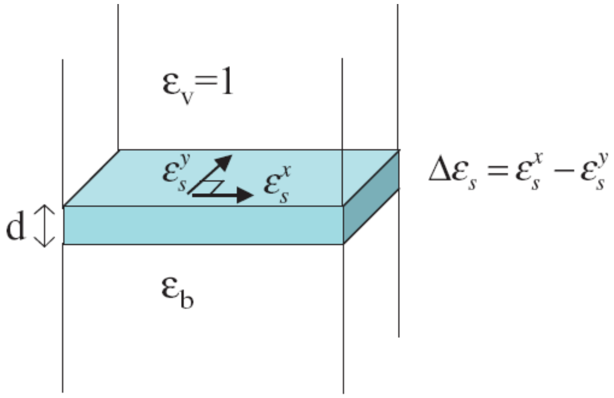

Figure 3.5: Illustration of the three-phase model.

linear approximation to the reflectivity expressions which arise in multiphase stratified systems such as the interfacial surface region of Au(110) in electrolyte or vacuum in an attempt to extract more information. This resulted in the creation of a phenomenological three-phase model, developed from Fresnel theory [54], which is depicted in Figure 3.5. The three-phase model assumes homogeneous media are separated by abrupt interfaces i.e. semi-infinite isotropic bulk and ambient layers either side of an anisotropic thin film surface layer.

3.6.1: The Dielectric Function

The interaction of light with a homogenous medium is described by the dielectric function of the material [55]. The three-phase model assumes there are three different media involved in this interaction; the bulk, surface and ambient/vacuum layer [Figure 3.5], each possessing a distinct dielectric function. The dielectric functions for the semi-infinite bulk (ε_b) and ambient/vacuum layers (ε_v) are isotropic. However, the dielectric response of the surface layer in the two principle directions (ε_s^x, ε_s^y) may be non-equivalent due to the inherent anisotropy of the sample. The difference between the dielectric response in the x and y directions, $\Delta\varepsilon_s$, is known as the surface dielectric anisotropy (SDA) and gives rise to a RAS signal when $\varepsilon_s^x \neq \varepsilon_s^y$. Assuming that $d << \lambda$ (as $d \sim 10^{-9}$ m this thin film approximation allows for the probing of the optical properties of the surface at optical wavelengths), and that $\varepsilon_v = 1$, it can be shown that, given $r_x - r_y = \Delta r$, the RAS equation can be defined in terms of the surface and bulk dielectric functions:

$$\frac{\Delta r}{r} = -\frac{2i\omega d}{c}\left[\frac{\varepsilon_s^x - \varepsilon_s^y}{1-\varepsilon_b}\right] \tag{3.1}$$

where ω is the angular frequency and c is the speed of the wave. Equation (3.1) converts an experimentally measured quantity ($\Delta r/r$) to a material property $\Delta\varepsilon_s$.

All the RA spectra presented in this thesis measure the real part of the RAS signal to represent the optical response of the system and one can extract the real parts of Equation (3.1):

$$\mathrm{Re}\left(\frac{\Delta r}{r}\right) = \frac{2\omega d}{c}\,\mathrm{Im}\left[\frac{\Delta\varepsilon_s}{1-\varepsilon_b}\right] \tag{3.2}$$

3.6.2: The Lorentzian Transition Model

Before considering how to interpret transitions and consequently simulate RA profiles using the three-phase model, a parameterised representation of surface electronic transitions must be obtained, which can be well approximated through Lorentz contributions. To this end, it is convenient to firstly introduce the bulk dielectric function in terms of the functions *A(ω)* and *B(ω)*, defined by:

$$A(\omega) - iB(\omega) = \frac{1}{1 - \varepsilon_b(\omega)} \tag{3.3}$$

The values of $A(\omega)$ and $B(\omega)$ are calculated from the bulk dielectric function, which in turn can be calculated from the refraction coefficient, n, and the extinction coefficient, k, using the simple relation $\varepsilon = N^2$, where N, the refractive index, is defined as $N = n - ik$. The values of n and k for Au can be determined by spectroscopic ellipsometry [56]. The well defined data set of Blanchard *et al* [57,58] is used for the range up to 5.0 eV while the coarser data of Palik [59] is employed beyond this energy. The shape of the $A(\omega)$ and $B(\omega)$ functions is shown in Figure 3.6. The small discontinuity at 5.0 eV is due to the jump between the differing data sets. Using Equation (3.3), the real part of Equation (3.1) can be written in terms of $A(\omega)$ and $B(\omega)$:

$$\mathrm{Re}\left(\frac{\Delta r}{r}\right) = -\frac{2\omega d}{c}\left[A(\omega)\,\mathrm{Im}(\Delta\varepsilon_s) + B(\omega)\,\mathrm{Re}(\Delta\varepsilon_s)\right] \tag{3.4}$$

This expression allows us to generate simulated RA spectra in terms of the bulk optical response of Au and a parameterised representation of surface electronic transitions. The SDA is calculated by selecting transitions within the surface layer, in the x or y direction, of energy ω_t, intensity S, and line width Γ (Full Width at Half Maximum) [60]. Each transition has a Lorentzian form given by:

$$\varepsilon_s^{\,x,y} = 1 + \frac{S/\pi}{\omega_t - \omega + i\Gamma/2}, \quad \varepsilon_s^{\,y,x} = 1 \tag{3.5}$$

Thus with appropriate selection and variation of a number of empirical parameters (energy, relative intensity and linewidth) a model SDA, and hence from Equation (3.5)

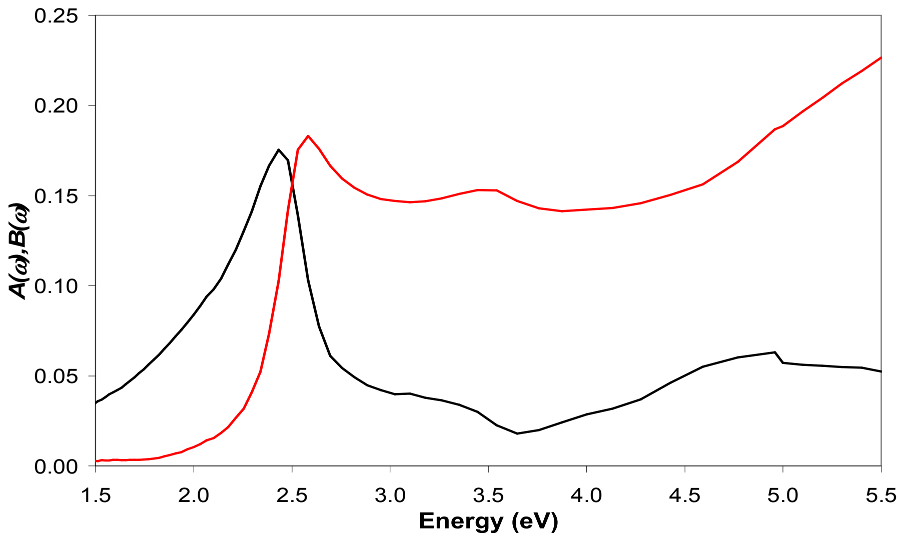

Figure 3.6: The *A(ω)* (black line) and *B(ω)* (red line) functions for gold from [57-59].

a model RA spectrum, can be generated.

3.7: Crystal Preparation

The Au(110) crystals used throughout this thesis are single crystals of 99.999% purity in the form of a disc of diameter 10 mm, thickness 2 mm, with an exposed area of 0.5 cm^2 (when in the electrochemical cell) and is oriented to an accuracy of 0.1° by X-ray diffraction. Prior to experimental usage, the crystals were mechanically polished to 0.25 μm using cycles of diamond paste of 6 μm, 1 μm, and 0.25 μm and cleaned in an ultrasonic bath. A butane micro-torch was then used to flame anneal the crystals. This involved heating the samples in the flame until it glowed orange, and then allowing it to cool before repeating the process 15 times [61,62]. Following the flame anneal the crystals were cooled in air before quenching in ultra-pure water (Millipore Q System, 18 MΩ cm) and then transferred to the electrochemical cell. This procedure is known to preserve the (1x2) missing row reconstruction [23,63].

3.8: Simulations Using the Three-Phase Model

Very successful simulations of RA spectral profiles can be achieved by the utilisation of the three-phase model. Outlined here is an introduction to the fitting procedure and parameter boundaries so as to keep simulations as physically reasonable as possible.

Au(110) requires 5 transitions in order to adequately reproduce its spectral profile and each of these has three related variables; energy, width and intensity. Previous simulations of Au(110) [1,35,64] have enabled these variables to be well constrained within defined margins: the energy of the 1st transition is generally located between 1.6 and 2.0 eV, the 2nd between 3.3 and 3.5 eV, the 3rd transition between 3.8 and 4.0 eV, the 4th between 4.3 and 4.8 eV and the energy of the 5th transition lies in the 5.4 to 5.8 eV region. The width of each transition, the FWHM of the Lorentzian shaped transition, is constrained between 0.3 - 2.5 eV to prevent break down of the model. While the absolute intensity of each transition is unrestrained, their relative intensities after normalisation are considered to be within pre-defined ranges.

Variations to each of these parameters have differing effects upon the simulation. An increase or reduction in energy tends to result in the same effect on the transition intensity in that region of the spectrum. Reducing Γ also increases intensity, while the opposite behaviour is observed if one increases the line-width thus reducing the intensity. This would be expected from the transition as Γ is effectively a measure of how well defined or 'sharp' the contribution is.

In recent work [64], the values for the gold transitions are deduced in the manner described with the addition of two new transitions in order to be able to quantitatively describe the effect of biomolecular adsorption. Modifications to the optical response of the gold were evident and these were reflected in changes to the transitions to successfully simulate the RA spectral profile. In these studies, the energies of the respective transitions were fixed and only variations to the width and intensity were deemed necessary to simulate the spectra. Such a method allows the clear separation of gold surface effects from those of the adsorbed molecule.

3.9: Spectral Signatures of the Different Reconstructions of Au(110): An Electrochemical Investigation

As has been explained previously, the identification of defined RA profiles with the different surface reconstructions of Au(110) is difficult, in part due to the variation in morphology due to crystal preparation [1,35-39]. Further differences are noted between the anions present in the electrolyte; with strongly adsorbing anions such as SO_4^{2-} having a greater effect on surface processes than weakly adsorbing species such as ClO_4^- [24,49,65-70]. It is expected that at potentials positive of the PZC, anions from the electrolyte will specifically adsorb onto the crystal surface. In order to try and reduce systematic error and effects of different anions in an effort to identify specific changes to the optical response of the surface, experiments were conducted concurrently on a single crystal in H_2SO_4/Na_2SO_4 (pH 1.36), $NaClO_4$/$HClO_4$ (pH 1.18) and $NaClO_4$ (pH 6.14) electrolytes. This allows for a direct comparison between anion and pH effects on surface reconstruction to be made. Although every effort was made to reduce sources of systematic error to a minimum, it is well known that surface morphology varies with crystal preparation [1,35-39]. One would expect this to result in persistent minor variations in the spectral profile between the different experiments above 2.5 eV which is sensitive to such morphology.

It is known that at sufficiently negative applied electrode potentials below the PZC the surface exhibits a (1x3) double missing row reconstruction as its preferred lowest energy state [25-28]. It has also been suggested that the (1x2) to (1x1) phase transition is completely reversible [2,3,23,24,37,38] and that oxidation of the surface does not damage surface reconstruction [1,71]. Considering these points, it was decided to conduct cyclic potential variations in the order 0.0 V → 0.6 V → 0.0 V → 1.2 V → -0.6 V → 0.0 V in 0.1 V increments to ensure a spectrum of a freshly prepared sample was taken through the reversible phase transition at potentials below oxidation first, then through oxidation and finally through to the negative potential induced (1x3) reconstruction returning to neutral potential on each occasion to try and restore original surface morphology and the (1x2) reconstruction through applied potential [63]. It is important to note that oxidation will be discussed only briefly in this thesis (section 3.9.5) and for a more thorough analysis on the RAS of oxidation of Au(110), interested readers should read [1,71] where the spectral signatures for adsorption of hydroxide (OH^-) and oxidation are assigned.

Some uncertainty remains as to the effect of specific anion adsorption on surface structures and the difference between this action and that of varying applied electrode potential. Indeed, the ClO_4^- anion present in perchloric acid is very weakly adsorbing and doubt still persists whether this species does in fact adsorb at potentials positive of the PZC. A combined CV capacitance and ERS study of Au(110) in perchlorate [72] concluded that the lifting of the (1x2) reconstruction at positive potentials was a direct result of specific adsorption by the anion. This deduction was based on the reconstruction lifting at higher potentials when the surface was immersed in ClO_4^- compared to when the surface was in the presence of the stronger adsorbing SO_4^{2-} or Cl^- anions. While this study indicates the existence of an anionic effect on surface reconstruction, it also discounts the effect of surface charge on this sensitive behaviour. Another investigation [73] detailed how both the lowering of the PZC and increase in the potential of oxidation was independent of electrolyte concentration; typical behaviour for anions which do not specifically adsorb. The authors stated that the reason for this lay in the low bond strength of the perchlorate anion which allows the hydroxide anion to replace it as early as possible.

The inconsistencies discussed above make this investigation an interesting study as both these anions are used.

3.9.1: Au(110) in 0.1 M H_2SO_4/Na_2SO_4 at pH 1.36

Figure 3.7 (a) shows the first positive potential cycle of Au(110) from 0.0 V to +0.6 V and back again in 0.1 M H_2SO_4/Na_2SO_4. For clarity of presentation, the potentials are

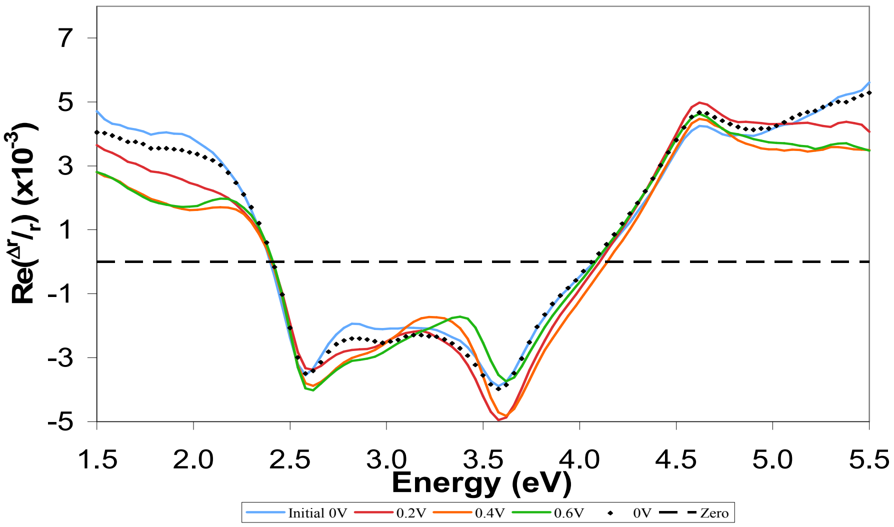

Figure 3.7 (a): Anodic region potential variation of Au(110) in 0.1 M H_2SO_4/Na_2SO_4.

shown in 0.2 V increments without spectral profiles at +0.4 and +0.2 V as the potential was reduced back to neutral potential. It is known from previous work [24,35,37,38] that the surface should be predominantly (1x2) in character at 0.0 V and that as the electrode potential is increased, the transition to the unreconstructed (1x1) will occur. A qualitative analysis of these line shapes over the 0.0 V to +0.6 V potential regime show a reduction in the broad positive feature in the low energy region of the spectrum (< 2.5 eV) accompanied by a systematic increase of the intensity of the 2.5 eV peak. The broad plateau between the principle peaks of the spectral profile also changes progressively into an increasingly positive going slope. A sharp increase in the 3.5 eV peak to +0.4 V is observed before decreasing again at +0.6 V. Although the peak at 4.5 eV remains relatively unmoved by the process, further modifications are seen to higher energy of this feature, where a slightly positive slope at 0.0 V becomes rather featureless at the highest positive potential. It must be noted that minor optical improvements to the RA spectrometer have increased its sensitivity above 5.0 eV and as such, minor differences occur in this region between 0.0 V and +0.6 V which have not been observed in previous works [1,36,64].

It is known that the (1x2) reconstruction is only preserved in this electrolyte below +0.05 V and that the (1x1) is the major reconstruction above +0.25 V [24]. The characteristics of the profile at 0.0 V are a broad positive feature below 2.5 eV, negative peaks at ~2.5 and 3.5 eV which share approximately the same intensity separated by a broad plateau, a defined peak at 4.5 eV indicative of surface morphology and a gentle positive slope above 5.0 eV. If one studies the RA profiles in depth and compares the spectral profile at 0.0 V with that at +0.2 V, it is clear that the major variations in spectral profile outlined previously have already occurred at this potential; a potential which is expected to result in a predominantly (1x1) unreconstructed surface. It is therefore clear in the data presented in the current work that RAS is extremely sensitive to this phase transition through major variation to the optical profile of the system. This study concurs with Magnussen *et al* [24] and is suggestive that the RA profiles at 0.0 V and +0.3 V are indicative of the (1x2) and (1x1) surface reconstructions in electrolyte respectively.

If one now studies the 0.0 V spectrum after cyclic potential variation, it is clear to see that this profile matches that of the original spectrum, some minor variations to lower energies apart. This is confirmation using RAS that the (1x2) to (1x1) phase transition of Au(110) is reversible in this electrolyte.

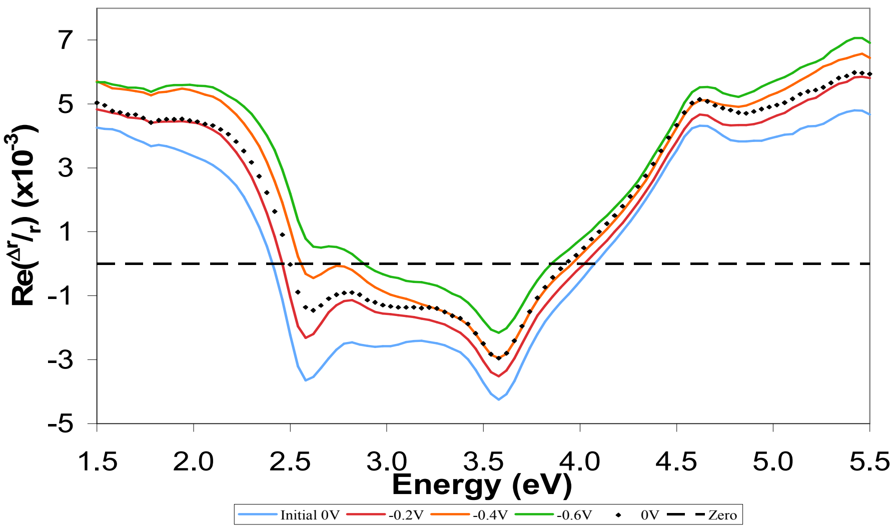

Figure 3.7 (b): Negative cyclic potential variation of Au(110) in 0.1 M H_2SO_4/Na_2SO_4.

Displayed in Figure 3.7 (b) is the negative cyclic potential variation. As the potential is decreased to -0.6 V, a very clear and rapid destruction of the feature at 2.5 eV is immediately noticeable. This is coupled to an increase in the broad positive feature below 2.5 eV. Although the negative peak at 3.5 eV loses intensity, it retains its defined nature even at -0.6 V. This behaviour is also observed for the features towards higher energies which retain their character despite variations in absolute intensity. At potentials sufficiently below the PZC, the surface is expected to predominantly form a (1x3) reconstruction [25-28]. This would obviously entail destruction of the surface state involved in the (1x2) reconstruction and Figure 3.7 (b) certainly seems to confirm that that is indeed the case in this instance. Unlike at positive potentials, major variations to the spectral profile are observed until -0.6 V which suggests the formation of the (1x3) reconstruction requires more driving than that needed to lift or form the (1x2) reconstruction. This is reasonable since the (1x3) structure involves a double missing row reconstruction. The profile at -0.6 V is extremely similar to previous work on Au(110) in Na_2SO_4 which designate this the [1x3] reconstruction [37,38]. It is also very similar to the spectrum of Au(110) in KOH at -0.8 V which is known to be in a predominantly (1x3) structural formation [1]. (Note that no damage is caused to the surface at -0.6 V in sulphuric acid before the onset of hydrogen gas evolution). Due to the above considerations, it is possible to assign the spectrum of Au(110) at -0.6 V in H_2SO_4/Na_2SO_4 as a spectral signature of the (1x3) reconstruction.

Also of interest in Figure 3.7 (b) is the spectrum at 0.0 V after potential variation. The RA profile does not recover to intensities seen before potential variation and the feature at 2.5 eV has little definition. This result could be another reason as to the different assignment of the (1x2) structure in previous investigations [37,38,39]. The authors of Refs. [37] and [38] conducted their experiments on Au(110) in Na_2SO_4 starting from -0.6 V. The data presented here points towards the (1x2) reconstruction having never fully formed after preparation in their studies. It is also suggestive that the (1x3) to (1x2) reconstruction is not fully reversible. Another point of difference between this study and those discussed above is the selection of a reference electrode.

All investigations used in this thesis employ a SCE whereas in [37,38] a Ag/AgCl reference electrode is employed. In order to compare directly, our 0.0 V is actually -0.045 V in their studies. So as to investigate this further, the Au(110) was left at a negative potential of -0.245 V for 60 minutes after recording a spectrum at 0.0 V. The crystal was then left at 0.0 V for 360 minutes and spectra recorded at intervening periods to see if the feature at 2.5 eV recovered its original character. This data is shown in Figure 3.8. As can be clearly viewed from inspection of this figure, the feature at 2.5 eV does not recover its defined character even after 360 minutes at a potential which is supposed to drive the surface into a (1x2) reconstruction. Interestingly, the other major discrepancies are observed below 2.5 eV, an area also associated with surface states whereas the 3.5 eV feature fully regains its defined nature after 60 min at 0.0 V. Figure 3.8 highlights again the sensitivity of the surface to excess surface charge in the region of the spectrum expected to be responsive to the effect of physical and electronic structure variations coupled to the ability of RAS to be able to detect this subtle hysteresis.

The conclusions from Figures 3.7 (b) and 3.8 suggest that experimental procedure may also be a reason for differences between studies along with the well

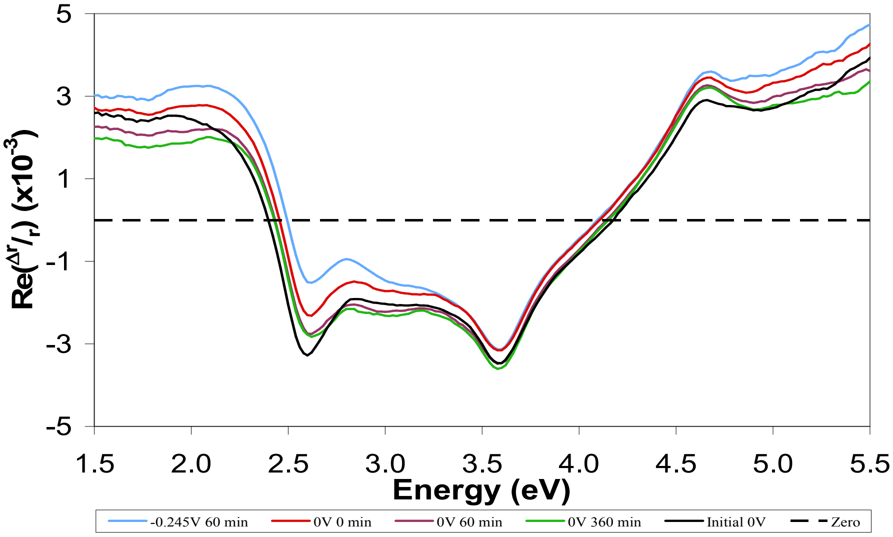

Figure 3.8: RA profiles of Au(110) probing the sensitivity of the 2.5 eV feature.

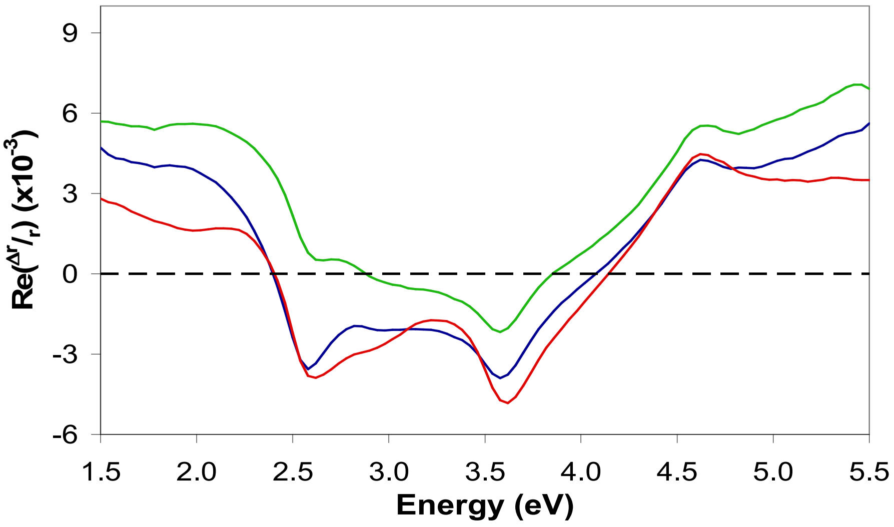

Figure 3.9: Au(110) in 0.1 M H_2SO_4/Na_2SO_4 displaying the spectral signatures of the (1x3) -0.6 V (green line), (1x2) 0.0 V (blue line) and (1x1) +0.3 V (red line) reconstructions.

known surface morphological considerations. This study suggests, in this electrolyte at least, that traversing into sufficiently negative potentials and formation of the (1x3) reconstruction damages the surface structure thus preventing full re-establishment of the preferred (1x2) reconstruction at neutral potentials.

Since it has been established that the region of the spectrum below 2.5 eV is sensitive to surface states [19,20,29,34,35,42], that the 3.5 eV feature is responsive to modifications to bulk layers affected by surface behaviour [20,35,42,51] and that the feature to higher energies is reflective of the presence of steps [20], one can characterise the variations in RA profiles as a function of the different surface reconstructions present. Figure 3.9 shows the spectral signatures of the (1x1), (1x2) and (1x3) surface reconstructions as a function of applied potentials +0.3 V, 0.0 V and -0.6 V respectively and clear differences across the energy range are immediately noticeable in all of the main features of the spectrum of Au(110).

The sulphate anion is known to be one of the most strongly adsorbing and sensitive information on its effects can be observed using CV. Figure 3.10 details the cyclic voltammogram associated with Au(110) in 0.1 M H_2SO_4/Na_2SO_4 and displays a full oxidation/reduction cycle. The (1x2) to (1x1) phase transition, as noted in RA profiles in Figure 3.9, has been shown to occur in the region detailed by this CV but there is no indication of this structural transformation in Figure 3.10. This is due to there being only a small PZC shift between the two surface reconstructions [74]. What is interesting about this CV is the presence of a peak at +0.46 V in the anodic oxidation cycle. Since the surface is already in the unreconstructed (1x1) phase at this potential [24,37,38] and oxidation is shown to only occur at approximately +1.2 V, this leads to the conclusion that this peak is a sign of specific anion adsorption on Au(110) by the sulphate anion. This concurs well with the RA profiles detailed above in Figure 3.7 (a) since the spectral signature of the (1x1) was observed at +0.3 V; a potential just below that which induces specific anion adsorption. Further, the small positive feature at +0.9 V is the first electron transfer mechanism of pre-oxidation formation of the OH^- hydroxide monolayer which facilitates oxidation of the surface towards higher potentials [74,75]. The adsorption of the hydroxide anion is a complex process whereby adsorbed species from the monolayer form polar bonds with the surface. This

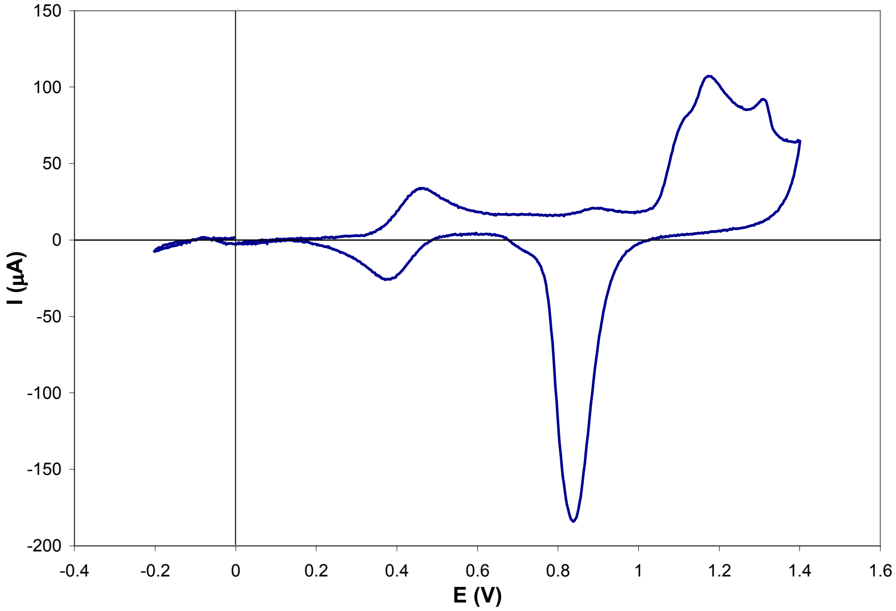

Figure 3.10: CV of Au(110) in H_2SO_4/Na_2SO_4 using a scan rate of 20 mVs^{-1}.

causes a place-exchange process which involves adsorbed anions being replaced with gold atoms from the first atomic layers which results in further hydroxide adsorption. The next step involves deposition of hydroxide anions into the overturned sub-lattice of Au which initiates the transfer of the second electron. This occurs at approximately +1.2 V and can be considered to be the potential at which the OH^- species is oxidised to form the surface oxide. These steps are observed in sequence above +1.0 V in the CV and the electron transfer mechanism can be adequately described by Equations (3.6) and (3.7):

$$Au + H_2O \leftrightarrow AuOH + H^+ + e^- \tag{3.6}$$

$$AuOH \leftrightarrow Au\text{-}O + H^+ + e^- \tag{3.7}$$

If one studies the cathodic or reduction potential cycle, it is clear the major negative peak at +0.83 V signals the reverse of this process and the removal of the oxidised layer from the crystal. It is expected that anion adsorption will again occur in this region and this is observed by the appearance of another negative peak at +0.36 V with a return to the current density observed before oxidation.

In order to compare the CV with the oxidation of Au(110) observed by RAS, Figure 3.11 depicts the positive potential cyclic variation up to +1.2 V and back again. A significant change in the profile is observed at +0.8 V accompanied by almost complete removal of the 2.5 eV feature. A comparison of these RA profiles with the CV shows that hydroxide formation begins at approximately the same region as this and as such the spectral profile at +0.8 V can be assigned as that which is indicative of the beginning of hydroxide layer formation. The spectrum recorded at +1.0 V is strikingly similar to the profile recorded at -0.6 V in the same electrolyte and also to the hydroxide spectrum of Au(110) in $HClO_4$ electrolyte also at +1.0 V which was assigned the characteristic hydroxide monolayer spectrum for this surface [71]. As has been discussed, the (1x3) reconstruction is expected to inhabit the majority of the surface at

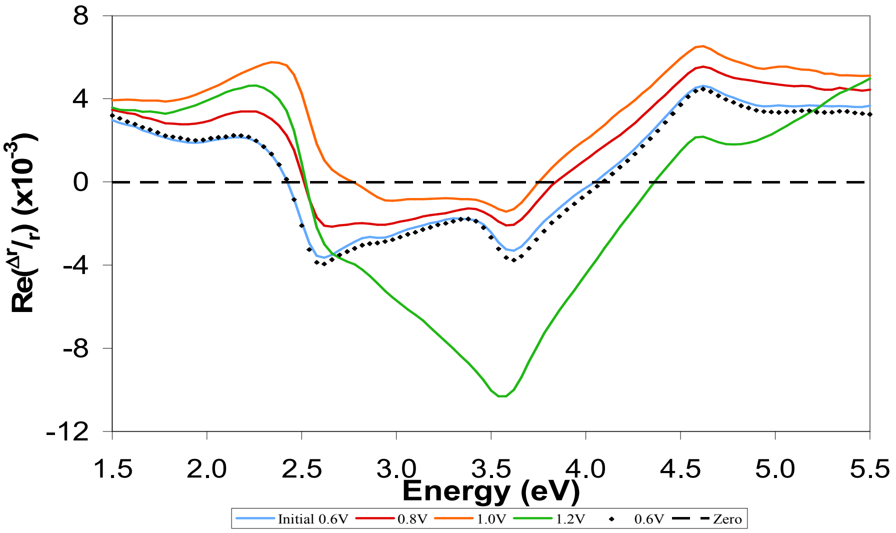

Figure 3.11: Oxidation of Au(110) in sulphate as a function of applied potential.

a negative potential of -0.6 V and as such agrees with the SXS study of Tidswell *et al* [27] which found that the adsorbed hydroxide anion induces the (1×3) reconstruction. The RAS profile of the oxidisation of the surface concurs with CV and it is therefore possible to attribute the large peak in the spectrum at +1.2 V to this process [71].

The differences caused in the spectra as a function of applied potential have been discussed above. If one now inspects the tables of the fitting parameters required to produce simulations of these spectra [Figure 3.12], clear trends can be seen which have the effect of turning the spectral profile from that which simulates a (1x1) reconstruction to that which reflects a (1x3) reconstruction (% increase or decrease in brackets). There is a systematic increase in the energy of the 1st transition from 1.26 to 1.55 eV (+23%) and finally to 1.59 eV (1x3) (+3%,+26% overall). This is accompanied by a similar decrease in the width of the transition from 0.90 to 0.60 eV as the (1x2) is formed (-33%) but this then increases to 0.73 eV at -0.6 V (+22%,-19% overall). The energy of the 2nd transition decreases systematically from 3.41 to 3.29 (-4%) and finally to 3.15 eV (-4%,-8% overall). The energies of the final three transitions remain fairly consistent with only minor changes. The widths of the second and fourth transitions consistently increase as the (1x3) reconstruction is obtained from 0.75 to 0.81 (+8%) to

1.10 eV (+36%,+47% overall) for the 2nd and from 2.00 to 2.10 to 2.20 eV for the 4th transition. Interestingly, the width of the 3rd transition at ~4.0 eV increases markedly between +0.3 V and 0.0 V from 1.70 to 2.10 eV (+24%) and then decreases again to 1.90 eV (-10%,+12% overall) when the (1x3) reconstruction is simulated. Furthermore, there are consistent trends observed in the relative strength of each transition with the 2nd increasing from 0.16 to 0.18 (+13%) and then to 0.27 (+50%,+69% overall), the 4th from 0.75 to 0.99 (+32%) to 0.97 (-2%,+29% overall) and the 5th also having a markedly greater influence with decreasing potential from 0.19 to 0.24 (+26%) to 0.36 (+50%,+89% overall). There is also a notable change in the relative contribution of the 3rd transition from 0.56 to 0.65 (+16%) at neutral potential and finally to 0.31 at -0.6 V (-52%,-45% overall).

It is the effect of these trends when combined which reflect the changes in the RA profile of the surface as potential drives the surface from the (1x1) to the (1x2) and eventually (1x3) reconstructions. It is the variations in energy, width and relative

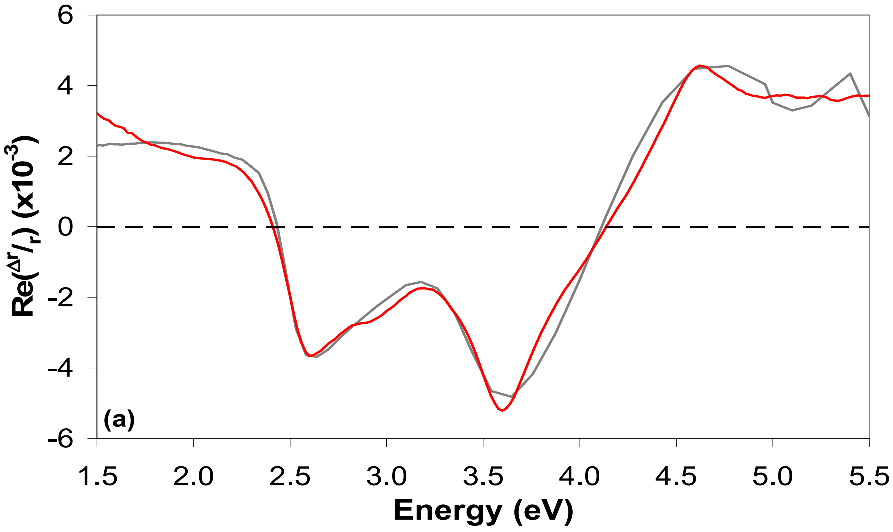

0.3 V	Transition	1	2	3	4	5
	Direction	[001]	[001]	$[1\bar{1}0]$	[001]	[001]
Au	ω_t/eV	1.26	3.41	4.03	4.65	5.65
	Γ/eV	0.90	0.75	1.70	2.00	0.54
	S^a	1.00	0.16	0.56	0.75	0.19

[a]Relative intensities. Absolute intensity of transition 1 is 8000.

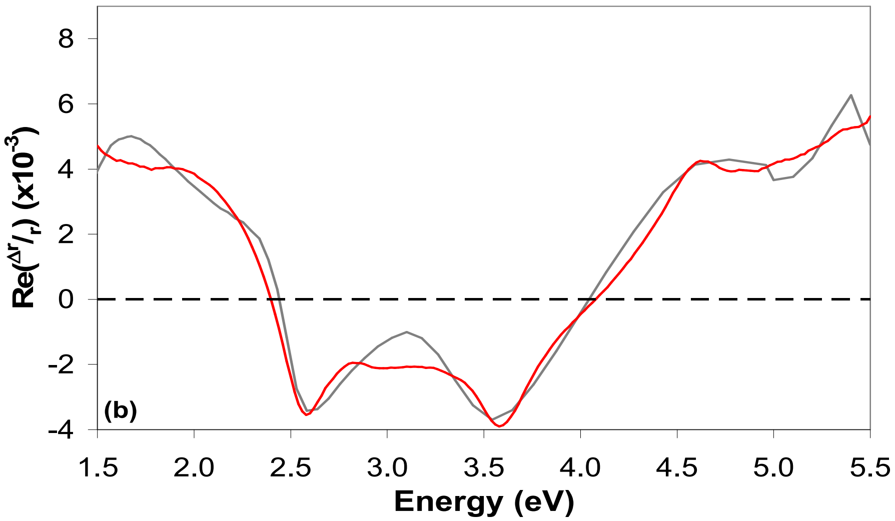

0.0 V	Transition	1	2	3	4	5
Au	Direction	[001]	[001]	$[1\bar{1}0]$	[001]	[001]
	ω_t/eV	1.55	3.29	4.10	4.65	5.63
	Γ/eV	0.60	0.81	2.10	2.10	0.50
	S^a	1.00	0.18	0.65	0.99	0.24

[a]Relative intensities. Absolute intensity of transition 1 is 6980.

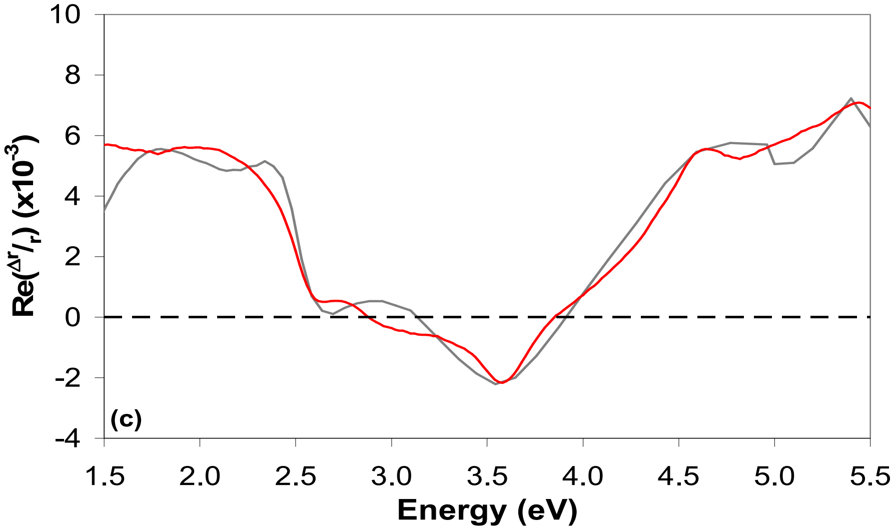

-0.6 V	Transition	1	2	3	4	5
Au	Direction	[001]	[001]	$[1\bar{1}0]$	[001]	[001]
	ω_t/eV	1.59	3.15	4.10	4.70	5.70
	Γ/eV	0.73	1.10	1.90	2.20	0.62
	S^a	1.00	0.27	0.31	0.97	0.36

[a]Relative intensities. Absolute intensity of transition 1 is 7500.

Figure 3.12: RA profiles of Au(110) in 0.1 M H_2SO_4/Na_2SO_4 (red lines) at (a) +0.3 V, (b) 0.0 V and (c) -0.6 V showing characteristic spectral features of the different reconstructions and their simulations using the three-phase model (grey lines). Also shown are the tabulated fitting parameters required to produce each simulation.

strength which increases the broad positive feature to low energy, decreases the intensity and character of the 2.5 eV peak, turns the positive going slope between 2.5 and 3.5 eV into firstly a broad plateau and then a negative slope, reduces the intensity of the peak at 3.5 eV whilst retaining its prominence and lifts the region of the spectrum above 4.0 eV to more positive RA units as the potential is reduced and thereby reflecting the resulting change in surface structure from a (1x1) unreconstructed surface to that of the double missing row character of the (1x3) reconstruction. RAS is proven to be sensitive to these reconstructions from this study.

Also shown in Figures 3.13 (a) to (c) are the individual contributions to the RAS model that resulted from the tabulated parameters defined in Figure 3.12. Immediately noticeable from these charts is the reduction in the 2nd contribution; increase in width (47%) and reduction in energy (8%) decreases intensity even

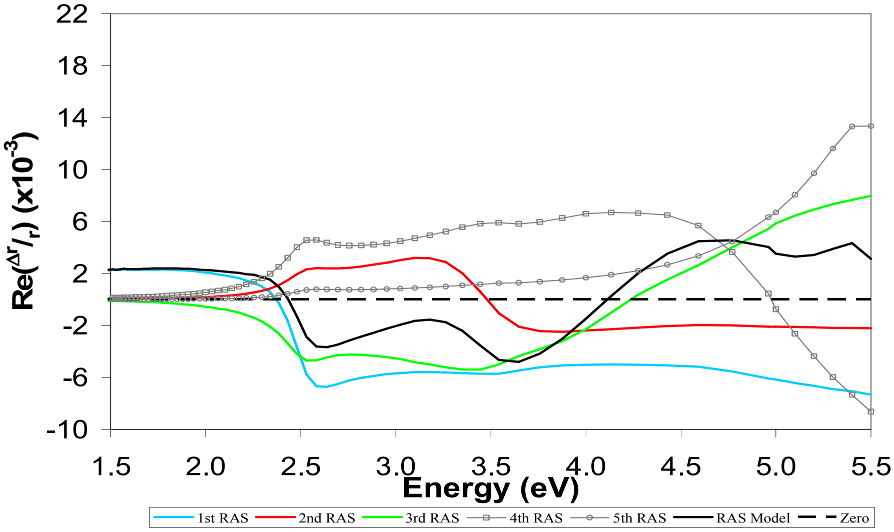

Figure 3.13 (a): Individual contributions of the different transitions to the RAS model from the simulation at 0.3 V [Figure 3.12 (a)].

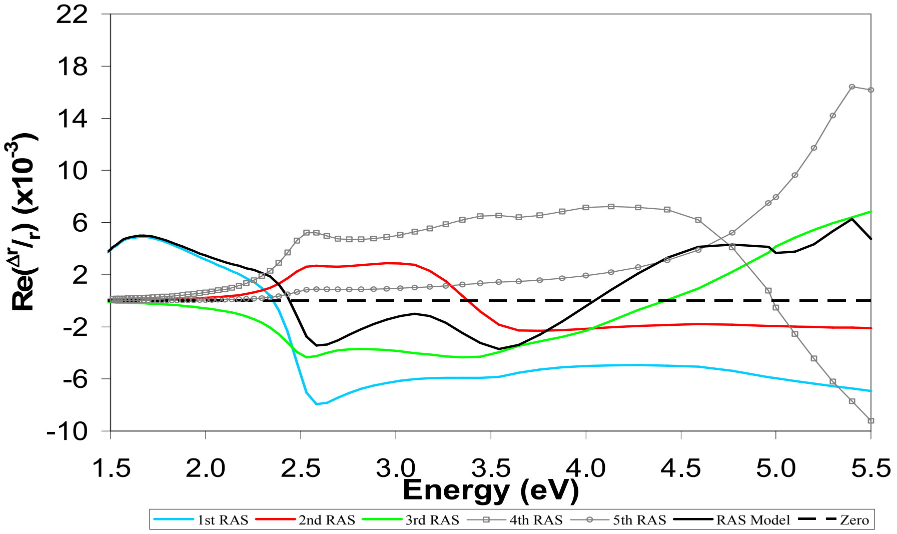

Figure 3.13 (b): Individual contributions of the different transitions to the RAS model from the simulation at 0.0 V [Figure 3.12 (b)].

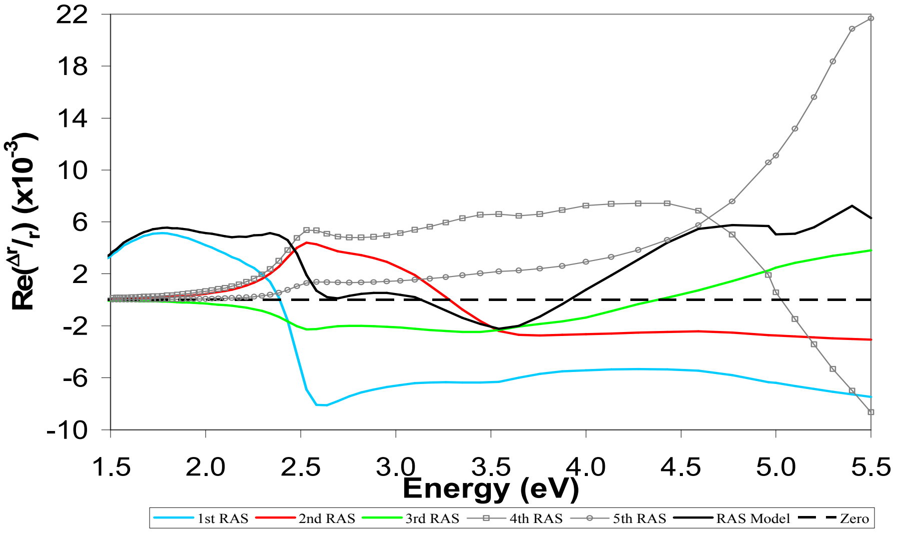

Figure 3.13 (c): Individual contributions of the different transitions to the RAS model from the simulation at -0.6 V [Figure 3.12 (c)].

though relative contribution increases by 69% as to be expected from the trends in the parameters discussed above. The 3rd transition also becomes flatter due to reductions in both width and strength while an increase in the 5th contribution (+89%) as the potential is decreased reflects the raising of the area of the spectrum above 4.0 eV as the (1x3) reconstruction is formed. The above discussion highlights the pivotal importance of the 2.5 - 3.5 eV region of the spectrum in changing reconstruction.

3.9.2: Au(110) in 0.1 M $NaClO_4/HClO_4$ at pH 1.18

In order to determine if the results of the above investigation are reflective of the surface rather than the identity of the anion, a comparison with a different acidic anion could shed more light on this difficult area. Figures 3.14 (a) and (b) show the positive and negative cyclic potential variations in 0.1 M $NaClO_4/HClO_4$ acidic electrolyte.

These spectra behave in an almost identical manner to that observed in the above investigation though there do appear to be greater variations within this data set as a function of potential than in the sulphate electrolyte mainly manifest in variations

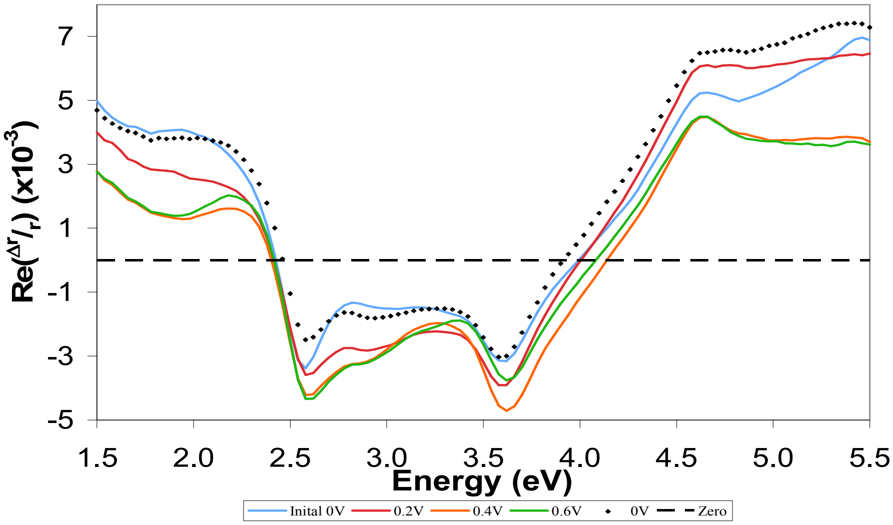

Figure 3.14 (a): Positive cyclic potential variation of Au(110) in $NaClO_4/HClO_4$.

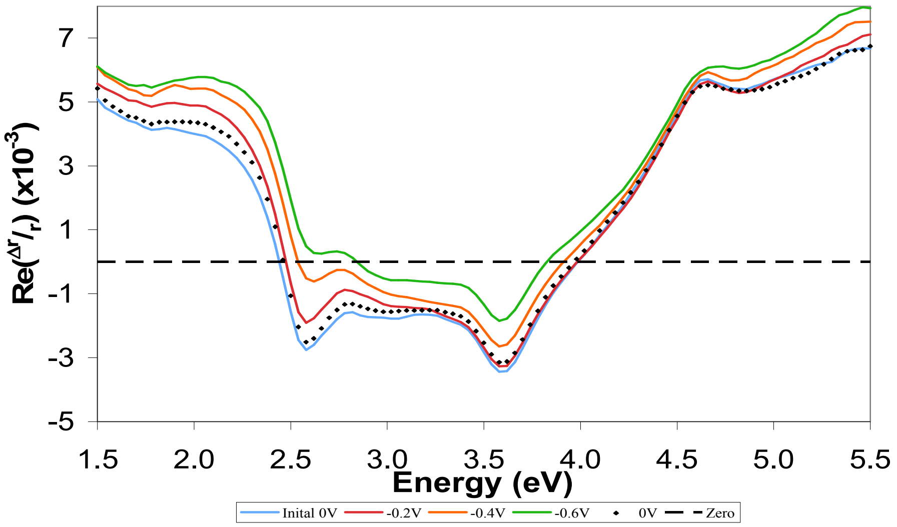

Figure 3.14 (b): Negative cyclic potential variation of Au(110) in $NaClO_4/HClO_4$.

to surface morphology in the positive potential regime. Both the (1x2) → (1x1) and (1x2) → (1x3) transitions occur through the same variations in spectral profiles as in the sulphate study with the main features at low energy and at 2.5, 3.5 and 4.5 eV undergoing almost identical modification as surface reconstruction changes This is to be expected from STM studies of the surface in various acidic electrolytes [24] and has also been observed previously [1,36]. The small differences between the sets of spectra are probably due to the influence on the surface of the stronger adsorbing SO_4^{2-} anions [68]. Further evidence to support this point can be seen in the 0.0 V spectrum after the negative cyclic potential variation [Figure 3.14 (b)]. Here, the spectrum is virtually identical to the 0.0 V spectrum observed prior to entering the negative potential regime. This behaviour is the opposite of that observed in sulphate and quite clearly points to an anionic effect in returning the surface to the (1x2) reconstruction after forming (1x3) double missing rows due to the lack of a strongly adsorbing anion.

Figure 3.15 details the spectral signatures of the various reconstructions on Au(110) in this electrolyte and again, if one compares this to the sulphate profiles [Figure 3.9] there are very few spectral variations. The changes to the optical profile of the system as the applied electrode potential is reduced are consistent between the two

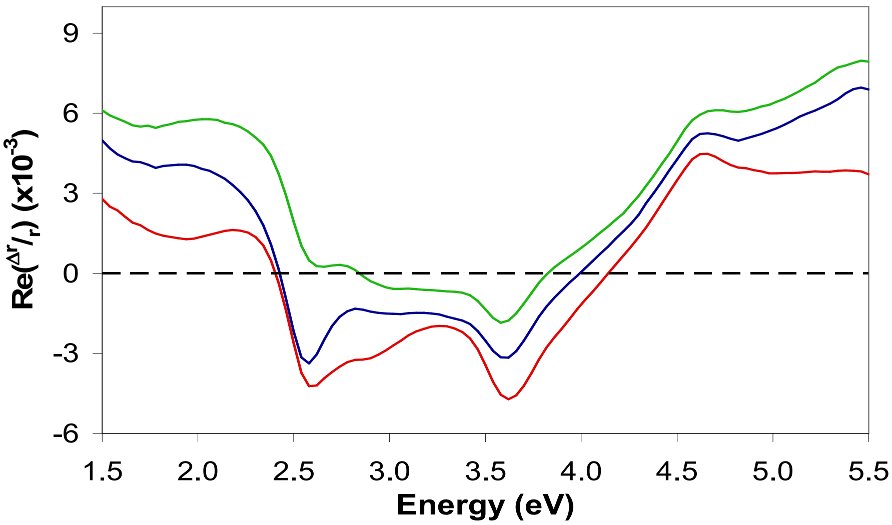

Figure 3.15: Au(110) in 0.1 M $NaClO_4/HClO_4$ displaying the spectral signatures of the (1x3) -0.6 V (green line), (1x2) 0.0 V (blue line) and (1x1) +0.3 V (red line) reconstructions.

studies. Even accounting for the minor spectral variations due to surface morphology, it is clear that a consistent trend has emerged that can be modelled by the application of the three phase model.

In order to correlate what is observed in the RA profiles as a function of potential, it is again pertinent to include the CV of Au(110) in this electrolyte to observe anion adsorption and oxidation. As can be seen from Figure 3.16, it is still not possible to view the (1x2) to (1x1) phase transition using cyclic voltammetry and there are no major variations in the CV until just before oxidation in the same region as sodium sulphate where hydroxide layer formation was observed. This confirms that the anion in this electrolyte is less adsorbing than the SO_4^{2-} anions as no major specific anion adsorption peak is seen. A subtle feature just above +0.4 V is suggestive that some adsorption is occurring but not in a major fashion. In the region of the CV where oxidation occurs, the sharp peaks recorded in sulphate are absent to be replaced by a far more 'smooth' oxidation. Magnussen *et al* [24] observed a roughening of the surface above +0.8 V and the CV presented here also shows this feature. The important thing of note about this CV is that the start of specific anion adsorption, hydroxide layer

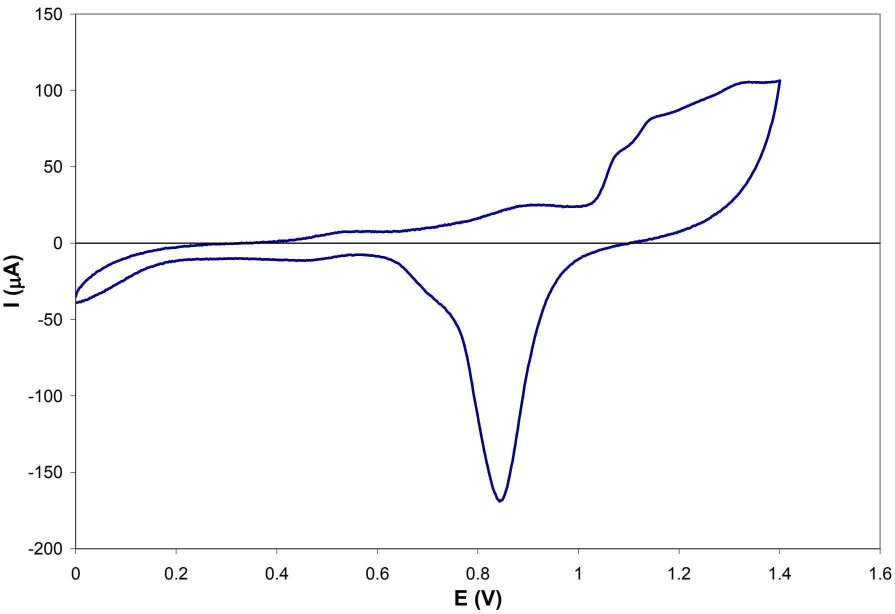

Figure 3.16: Cyclic voltammogram of Au(110) in 0.1 M $NaClO_4/HClO_4$ using a scan rate of 20 mVs^{-1}.

formation, oxidation and reduction all occur in the same potential vicinity as the CV of sulphate.

The RA profile of the system as it is taken through oxidation and back is shown in Figure 3.17. The removal of the 2.5 eV peak into a shoulder heralding hydroxide layer and hence (1x3) formation is clearly visible at +1.0 V as is the oxidation of the surface at +1.2 V. Here, however, the surface does not return to a similar RA profile following reduction as is seen in the sulphate electrolyte. Indeed, there appears to be some additional positive intensity at approximately 2.4 eV contributing to the spectrum. Such behaviour has been observed previously [1] and it was suggested in this work that the existence of a two stage chemical and morphological hysteresis between oxidation and reduction, which implied some restructuring of the surface and the presence of the double layer [Chapter 2.3] during the stepped return to the (1x2) reconstruction, was the reason for this discrepancy.

Figures 3.18 (a) to (c) detail the RA spectra of Au(110) in 0.1 M $NaClO_4/HClO_4$, their simulations and also the fitting parameters that gave rise to such

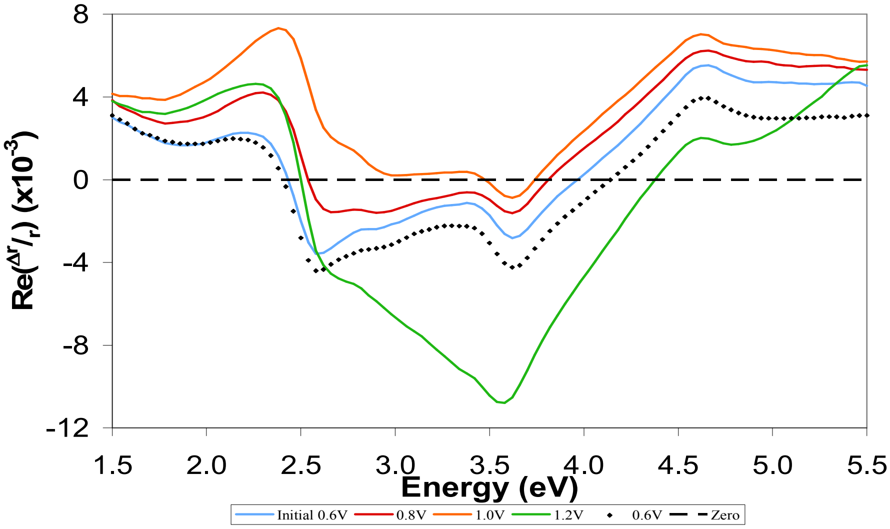

Figure 3.17: Oxidation of Au(110) in $NaClO_4/HClO_4$.

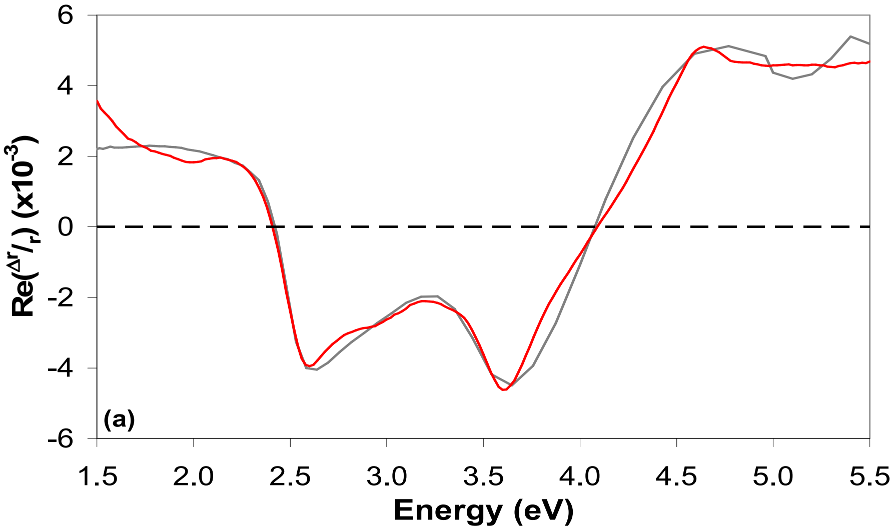

+0.3 V	Transition	1	2	3	4	5
Au	Direction	[001]	[001]	$[1\bar{1}0]$	[001]	[001]
	ω_t/eV	1.26	3.47	3.93	4.65	5.70
	Γ/eV	0.90	0.78	1.62	2.20	0.55
	S^a	1.00	0.18	0.61	0.78	0.19

[a]Relative intensities. Absolute intensity of transition 1 is 7700.

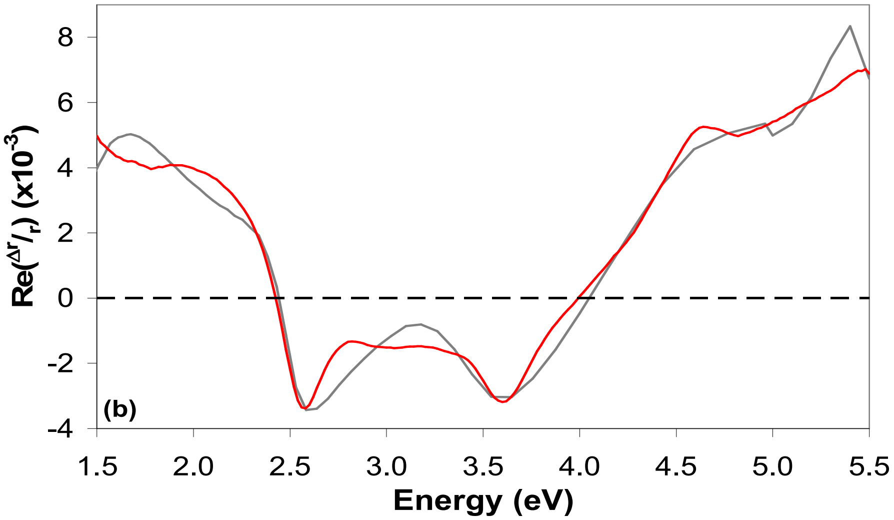

0.0 V	Transition	1	2	3	4	5
	Direction	[001]	[001]	$[1\bar{1}0]$	[001]	[001]
Au	ω_t/eV	1.55	3.36	4.15	4.65	5.64
	Γ/eV	0.60	0.86	2.05	2.10	0.54
	S[a]	1.00	0.18	0.64	0.99	0.29

[a]Relative intensities. Absolute intensity of transition 1 is 7000.

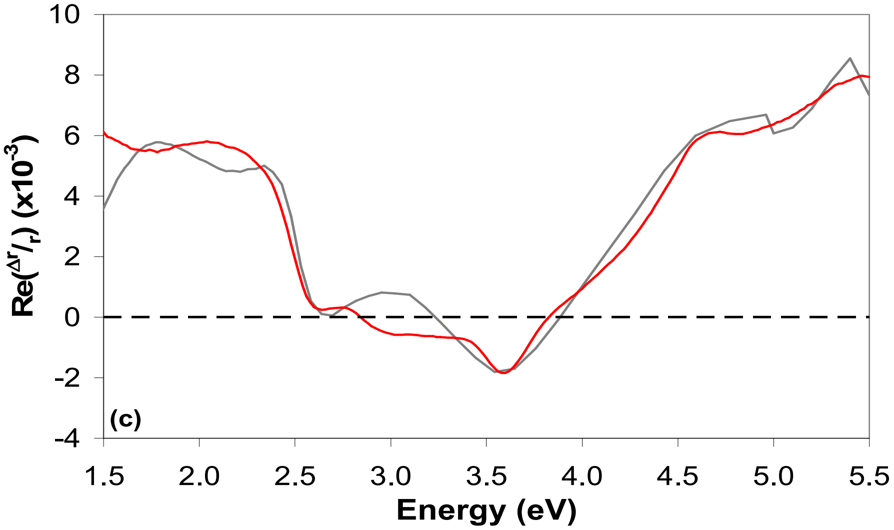

-0.6 V	Transition	1	2	3	4	5
	Direction	[001]	[001]	$[1\bar{1}0]$	[001]	[001]
Au	ω_t/eV	1.60	3.20	4.10	4.70	5.70
	Γ/eV	0.70	1.10	1.90	2.20	0.65
	S[a]	1.00	0.27	0.31	0.97	0.40

[a]Relative intensities. Absolute intensity of transition 1 is 7500.

Figure 3.18: RA profiles of Au(110) in 0.1 M $NaClO_4/HClO_4$ (red lines) at +0.3 V (a), 0.0 V (b) and -0.6 V (c) showing characteristic spectral features of the different reconstructions and their simulations using the three-phase model (grey lines). Also shown are the tabulated fitting parameters required to produce each simulation.

simulations. The tabulated parameters presented in Figure 3.18 are remarkably similar to those presented for the sulphate electrolyte. Indeed the trends outlined in the earlier study are also very similar to those used in this investigation. Patterns such as the 27% increase in energy and reduction in width of the 1st transition from 0.90 to 0.60 between +0.3 V and 0.0V, the 47% and 69% increases in width and relative strength of the 2nd transition respectively (41% and 50% in this study respectively) and 89% increase in relative strength of the 5th transition (110% here) occur in this set of data to within a sensitivity of approximately 10%. These are incredibly consistent results between two differing data sets. Not only do they show the remarkable similarity between the spectral profiles at potentials which are expected to result in altering surface reconstructions, they show that the modifications to the spectral profiles are indicative of such reconstructions and that the application of the three-phase model can quantify such behaviours.

3.9.3: Au(110) in 0.1 M $NaClO_4$ at pH 6.14

This investigation was carried out to determine if pH variation had an effect on surface reconstruction and the related changes to the optical response of the system using the same anion as in section 3.9.2 so as to try and confine explanations for any differences.

Figures 3.19 (a) and (b) display the positive and negative cyclic potential variations in sodium perchlorate at an almost neutral pH. The difference between these spectra and those shown earlier are mainly found in the definition of each of the main features of the spectral profile and the lack of substantial modification to the spectra below 2.5 eV. The same transitional behaviour as that found in the acidic electrolytes is still observed while neither of the 0.0 V spectra on returning to neutral potentials from

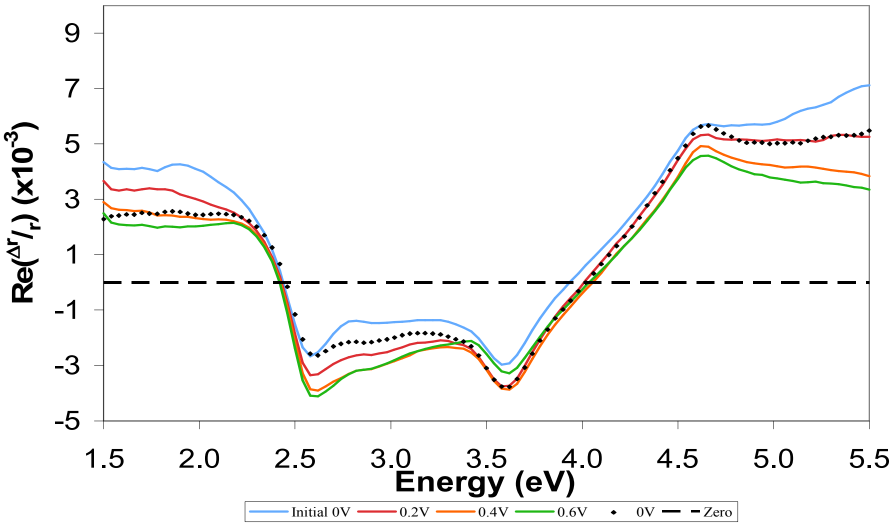

Figure 3.19 (a): Positive cyclic potential variation of Au(110) in NaClO$_4$.

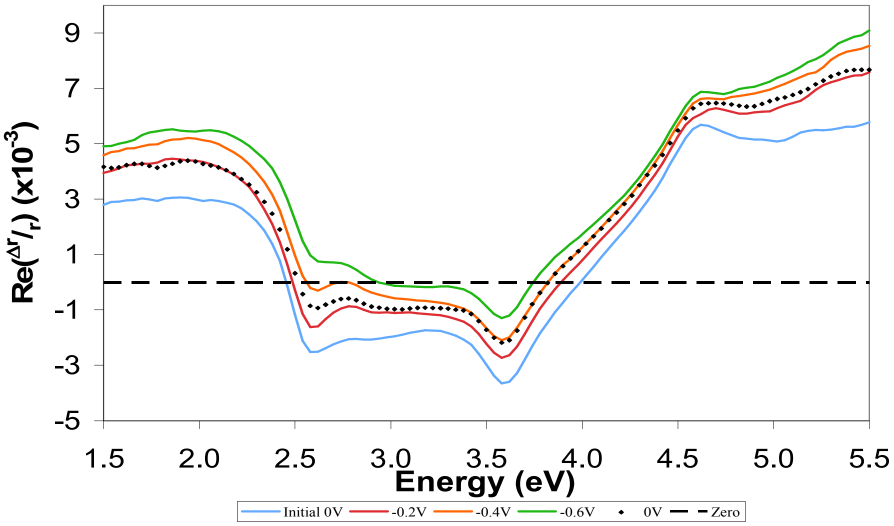

Figure 3.19 (b): Negative cyclic potential variation of Au(110) in NaClO$_4$.

both the (1x1) and (1x3) reconstructions have their spectral profiles restored to as they were before cyclic potential variation. After positive cyclic variation [Figure 3.19 (a)], the 0.0 V spectrum lacks the strong positive features originally present at both energy extremes and indeed has some additional intensity in the 3.5 eV region similar to that recorded at positive potentials; a region where the spectrum is expected to be sensitive to the effect of surface modification of bulk states. It does however match the intensity but not the character of the 2.5 eV peak and is extremely similar to the +0.2 V spectrum above this region. The only difference between this experiment and that in the acidic electrolyte using the same anion and cation is the concentration of H^+ ions to make the pH more neutral. This could therefore be pointing to a pH dependent hysteresis before the surface enters the oxidation phase.

The lack of re-endowment of the features of the RA profile at 0.0 V after negative cyclic variation is also observed. Here also, the spectrum lies somewhere in the middle of the -0.2 V and –0.4 V spectra indicating in this electrolyte at this pH that the formation of the (1x3) reconstruction prevents the surface then re-forming the 'ideal' (1x2) reconstruction observed initially at 0.0 V. This could be from the faceting of the surface which facilitates the existence and proliferation of the (1x3) reconstruction across the vast majority of the surface [25-28]. What's more, the initial profile at 0.0 V before negative potentials are applied is remarkably similar to that associated with the (1x1) of the previous two studies.

Despite these differences, similar spectral profiles are attained for the spectral signatures of the (1x1), (1x2) and (1x3) reconstructions. These are displayed in Figure 3.20 and the major differences as noted before lie in the definition of the major spectral features. However, the characteristic negative slope separating the 2.5 and 3.5 eV features and flat region above 4.5 eV at +0.3 V, the two main peaks at 2.5 and 3.5 eV having approximately the same intensity separated by a broad plateau at 0.0 V and the near total removal of the 2.5 eV feature at -0.6 V designating the specific characteristics of the different reconstructions are all present in this chart. A comparison of the three different electrolytes at the three potentials at which it is

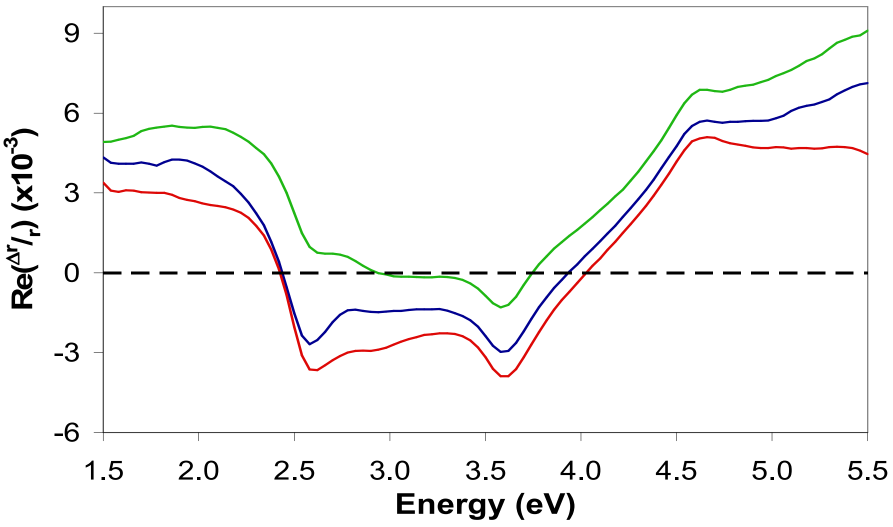

Figure 3.20: Au(110) in 0.1 M $NaClO_4$ displaying the spectral signatures of the (1x3) -0.6 V (green line), (1x2) 0.0 V (blue line) and (1x1) +0.3 V (red line) reconstructions.

expected that the surface will herald the different surface reconstructions and therefore optical responses is discussed later in this chapter.

The CV of this system is displayed in Figure 3.21 and appears to be very complex. Oxidation of the surface is found to occur at approximately +1.0 V in this electrolyte and this is accompanied by a very broad feature just above +0.4 V. It is important to note that oxidation occurs in this study at +1.0 V; 0.2 V earlier than in the acidic electrolytes. Since one of those electrolytes employed is the same anion as in this experiment, this is observation of a direct pH effect on oxidation of Au(110). It is interesting to note that there is no shoulder on the oxidation peak in the CV of Au(110) in this electrolyte, indicating an apparent lack of hydroxide adsorption. An increase in the concentration of hydroxide anions at the working electrode would change the local pH, which the solution would then rapidly restore to the original value, removing the excess hydroxide anions and preventing adsorption. Moreover, the current density here is much higher than in the previous two studies. More interesting features of this CV are found in the reduction cycle. Here, instead of a large single peak characterising reduction, there are three separate smaller peaks which detail the slow

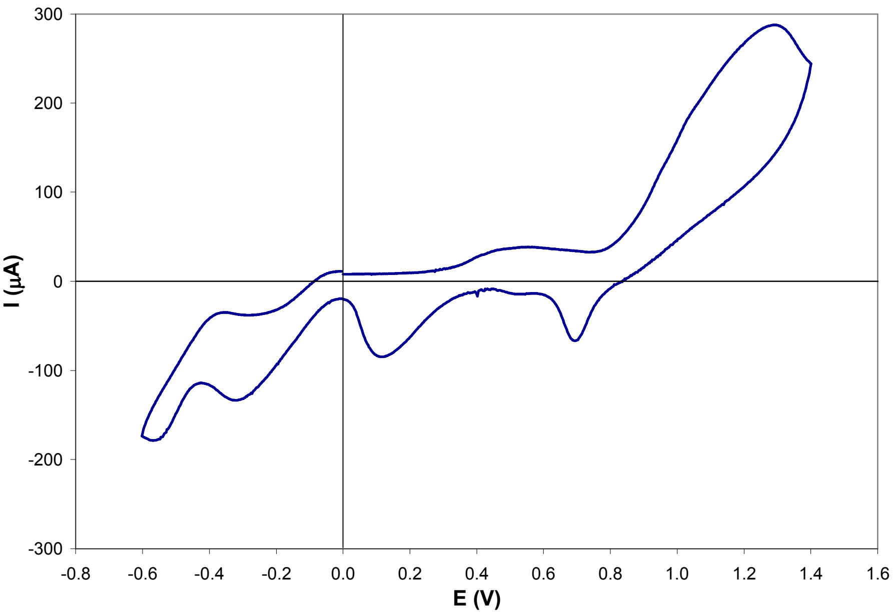

Figure 3.21: Cyclic voltammogram of Au(110) in $NaClO_4$ at a scan rate of 20 mVs^{-1}.

removal of oxygen from the surface, the last of which occurs at a potential of approximately -0.3 V. The CV displayed in Figure 3.21 is highly suggestive that the presence of a very weakly adsorbing anion such as ClO_4^- and an electrolyte at an almost neutral pH, gives rise to quite large hysteresis between the anodic and cathodic potential cycles. The lack of distinct sharp features at approximately +1.0 V and above in this CV, an area quite clearly where oxidation of the surface is occurring, points towards oxidation not being as defined in this system as in the earlier experiments. Considering that the CV only enters negative values at approximately +0.8 V in the reduction cycle and continues in a series of negative undulations rather than a single sharp reduction peak is indicative that the removal of oxide is more gradual in these circumstances with stepped potential.

Figure 3.22 shows the corresponding RA profiles of oxidation of the surface with the cyclic voltammogram. RAS confirms that oxidation of Au(110) in this electrolyte and pH is seen to occur at +1.0 V, that the intensity of the oxidation peak increased as the potential applied to the electrode was driven to +1.2 V and that there could also be additional structure contributing to an increase in intensity above 4.5 eV.

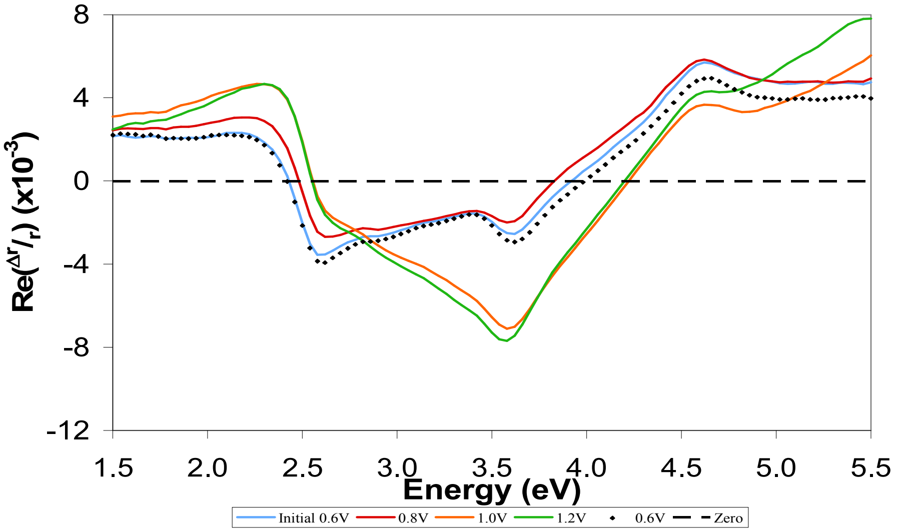

Figure 3.22: Oxidation of Au(110) in sodium perchlorate.

At higher pH values, oxidation will occur at lower voltages, owing to the increased concentration of hydroxide ions in solution, hence the oxidation peak in the RA spectrum at +1.0 V at pH 6.14. It appears in this instance, that the intensity of the spectrum above 2.5 eV has been 'raised' to more positive RAS units when compared to the RAS of oxidation in the previous two studies. Also, the spectrum at +0.6 V returns to very similar values to those it had before oxidation had occurred and only minor variations are noted in absolute intensity compared to spectral contour. This appears to disagree with the CV of this system which quite clearly observes some remnant hysteresis between the oxidation and reduction cycles. However, as is already known CVs are not able to detail the specific reconstruction on the surface and this discrepancy probably points towards the (1x1) unreconstructed lattice gas being present across the surface with the addition of adsorbed oxygen which the CV is sensitive to.

Figures 3.23 (a) – (c) are the associated RA profiles associated with this system at applied potentials of +0.3 V (a), 0.0 V (b) and -0.6 V corresponding to the (1x1), (1x2) and (1x3) surface reconstructions respectively. Also shown are the tabulated parameters which define the simulation of these spectra utilising the three-phase model which comprises Lorentzian contributions.

Even though there is some variation in the spectral profiles due to the pH of this solution, the patterns that emerge from analysis of these parameters, while subtle, certainly detail a pH effect in certain areas of the spectrum. The energy of the 1st transition varies by a marked 0.25 eV, but this is approximately 0.10 eV less than in both sulphate (0.34 eV) and perchlorate acidic (0.33 eV) electrolytes. The energy of the 3rd transition undergoes major modification between +0.3 V where it is centred at 3.92 eV and 0.0 V where it is centred at 4.25 eV; this difference of 0.33 eV is the most observed for this transition compared to the previous studies where it changed by approximately 0.10 eV. These variations in position are also found in the 4th transition which changes by as much as 0.12 eV in this investigation compared to as little as 0.05 eV previously. The relative strength of this transition is also higher in all three simulations than in the other two electrolytes. These trends are in addition to the previously identified patterns and as such are considered to be reflective of the pH effect on the substrate.

Also displayed in Figures 3.23 (a) – (c) are the individual contributions to each of the simulations from the three-phase model. One must note the change in scale of these graphs compared to those presented in section 3.9.1. This is due to the variation in absolute intensity of each of the transitions between each RA spectrum. As stated before however, it is the change in relative contribution that specifically details the variation in each contribution. Inspection of these charts reveals the trends explained above in that the 1st transition increases its influence in the low energy region of the spectrum as the (1x3) reconstruction is formed as expected from the increase in intensity is this area with decreasing potential. The 2nd transition becomes more defined in RAS units in the positive direction and also contributes further to the feature at 3.5 eV while the 3rd transition 'smoothes' and is less defined as a function of the changing reconstruction. Also noticeable are the increasing strength of the 4th and 5th transitions as a function of potential showing their increased influence as the intensity above 4.5 eV increases as the (1x3) reconstruction becomes the predominant

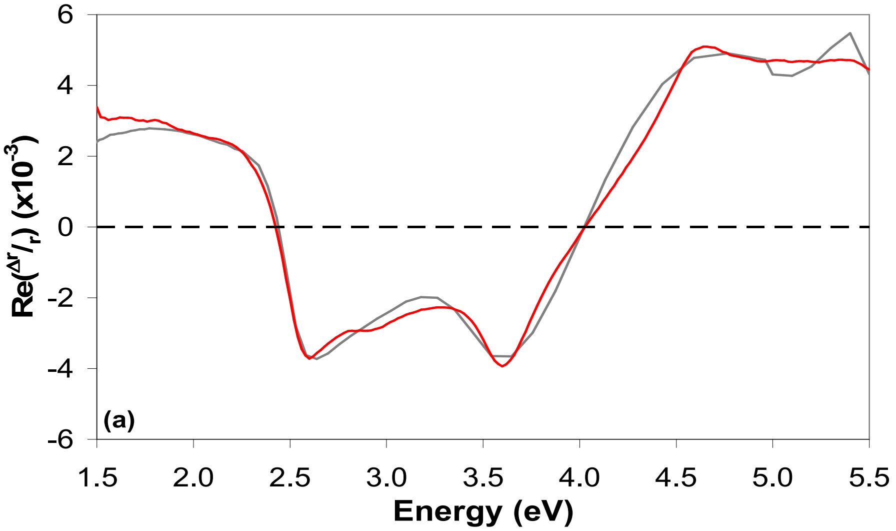

+0.3 V	Transition	1	2	3	4	5
	Direction	[001]	[001]	[1$\bar{1}$0]	[001]	[001]
Au	ω_t/eV	1.35	3.45	3.92	4.58	5.65
	Γ/eV	0.90	0.80	1.65	2.25	0.55
	S^a	1.00	0.16	0.67	0.89	0.20

[a] Relative intensities. Absolute intensity of transition 1 is 6900.

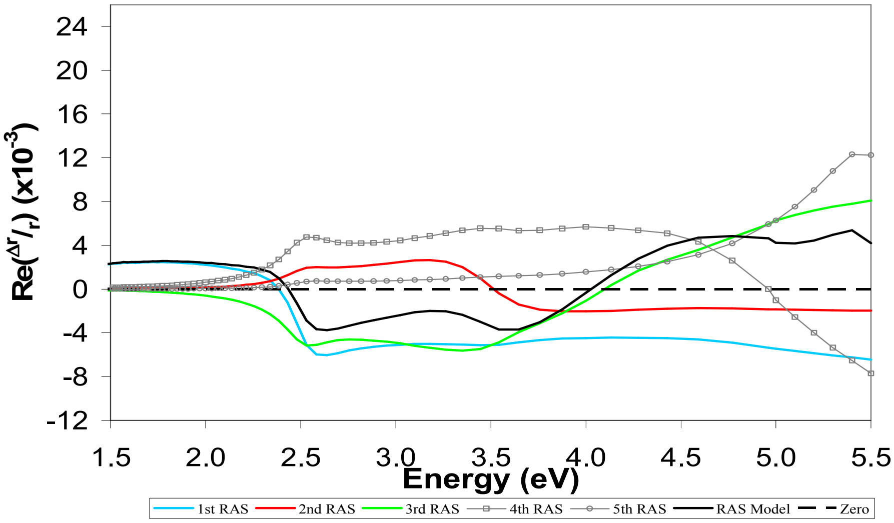

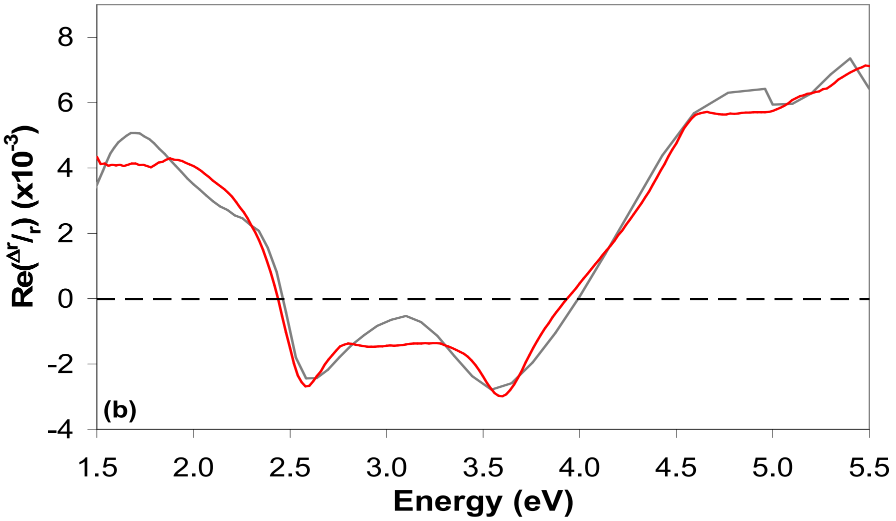

0.0 V	Transition	1	2	3	4	5
	Direction	[001]	[001]	[1$\bar{1}$0]	[001]	[001]
Au	ω_t/eV	1.59	3.28	4.25	4.70	5.70
	Γ/eV	0.57	0.90	2.00	2.00	0.65
	S^a	1.00	0.20	0.73	1.12	0.37

[a] Relative intensities. Absolute intensity of transition 1 is 6150.

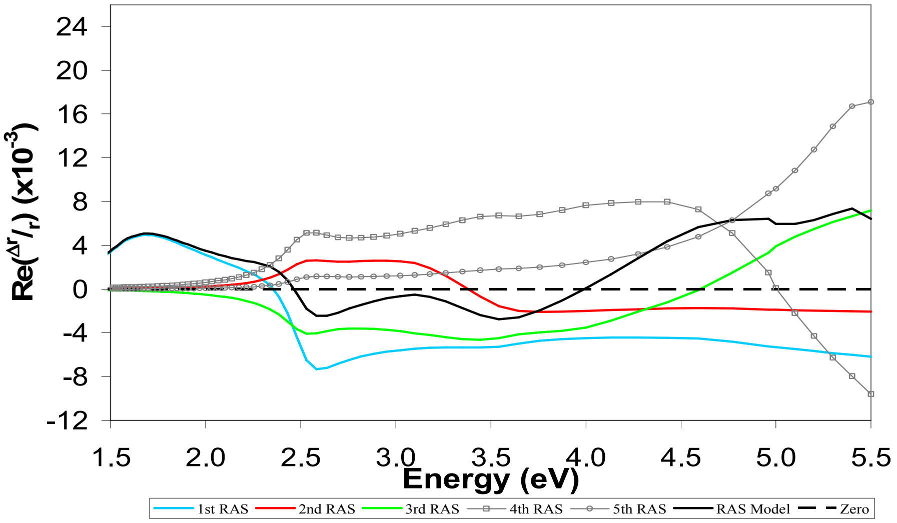

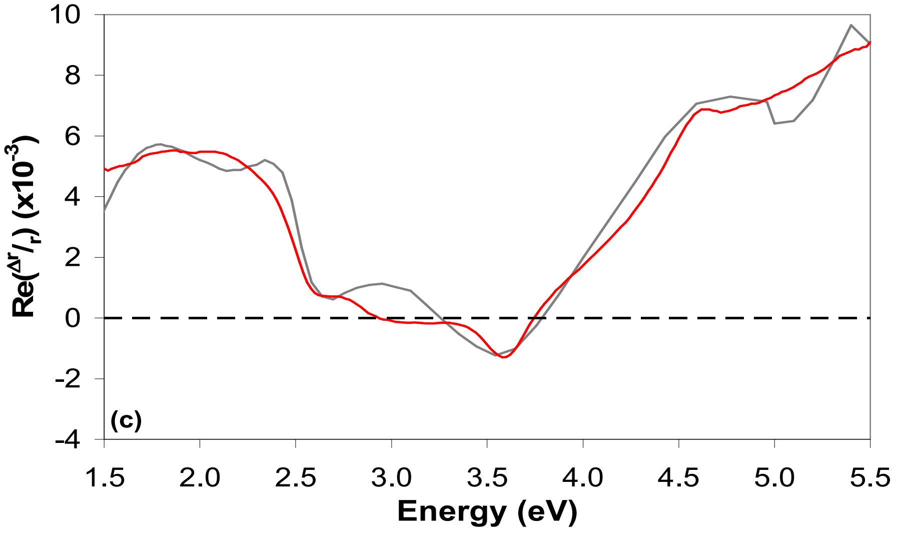

-0.6 V	Transition	1	2	3	4	5
	Direction	[001]	[001]	$[1\bar{1}0]$	[001]	[001]
Au	ω_t/eV	1.60	3.15	4.15	4.70	5.70
	Γ/eV	0.70	1.10	1.90	2.05	0.60
	S^a	1.00	0.27	0.31	1.03	0.42

[a] Relative intensities. Absolute intensity of transition 1 is 7400.

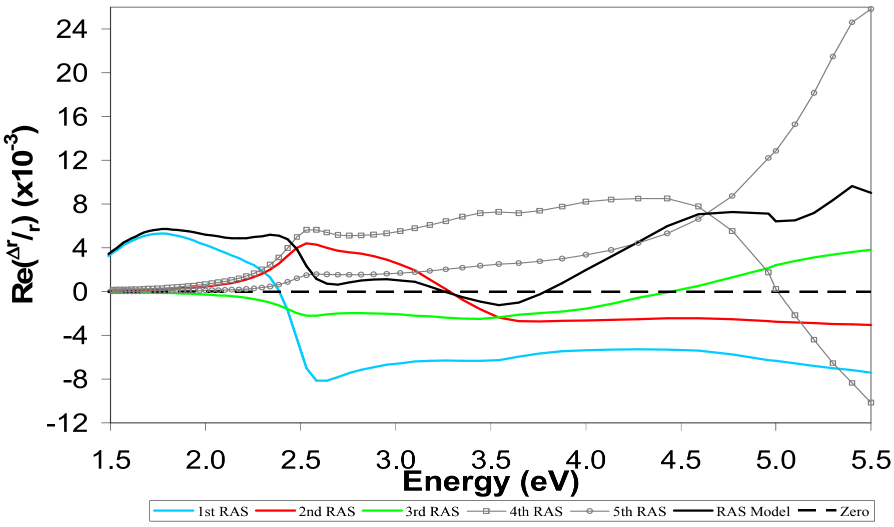

Figure 3.23: RA profiles of Au(110) in 0.1 M $NaClO_4$ (red lines) at +0.3 V (a), 0.0 V (b) and -0.6 V (c) showing characteristic spectral features of the different reconstructions and their simulations using the three-phase model (grey lines). Also shown are the tabulated fitting parameters required to produce each simulation.

reconstruction present on the Au(110) crystal surface.

3.10: Comparison of the (1x1), (1x2) and (1x3) Reconstructions in Different Electrolytes and Varying pH.

A direct comparison between the different reconstructions in the different electrolytes is needed to determine if there is any specific anion or pH dependent effects on these structures which alters their optical response. These can be viewed in Figures 3.24 (a) to (c) and it is clear from these charts that spectral variations between the different electrolytes are relatively subtle. Still, they are significant.

Figure 3.24 (a) shows the (1x3) reconstruction in the various electrolytes at -0.6 V vs SCE. The spectra are almost identical in the low energy region and differences between the solutions only become apparent at approximately 3.0 eV. This is in the region of the spectrum where surface modified bulk layers are expected to contribute to the optical response of the system. These variations are limited to the absolute intensity of the spectral profiles rather than to specific variations in the RAS line-shape. As such, these can be explained by the differences in surface morphology due to the effect of flame annealing procedures and also to possible slight variation in the step structure due to more strongly adsorbing anions in the case of the acidic solutions. Even so, it is clear from this graph that all three surfaces exhibit the typical RA profile associated with the (1x3) reconstruction at this potential [1,35,37,38,71].

The typical RA profile of the (1x2) reconstruction is displayed in Figure 3.24 (b). From the discussion earlier in the chapter, it is known that the Au(110) surface exhibits the (1x2) reconstruction at an applied potential of 0.0 V in electrolyte

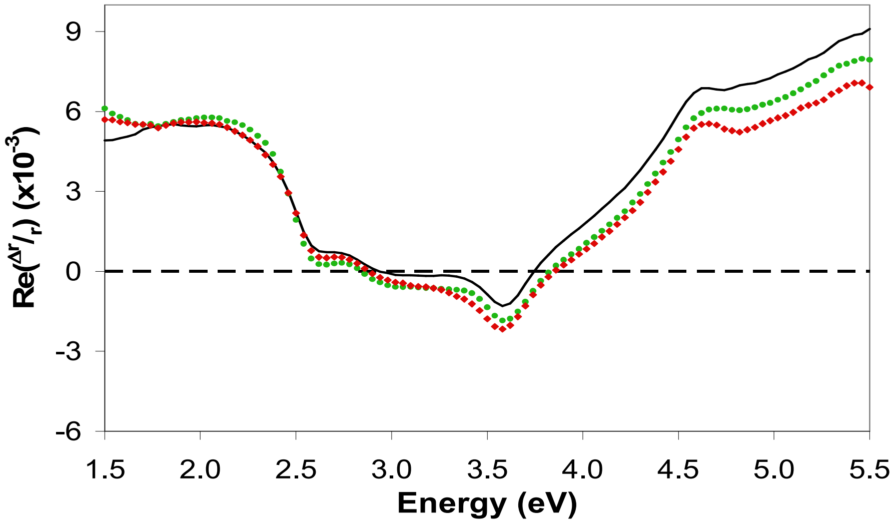

Figure 3.24 (a): Au(110) displaying the (1x3) reconstruction at -0.6 V vs SCE in 0.1 M H_2SO_4/Na_2SO_4 (◆), $NaClO_4/HClO_4$ (●) and $NaClO_4$ (black line).

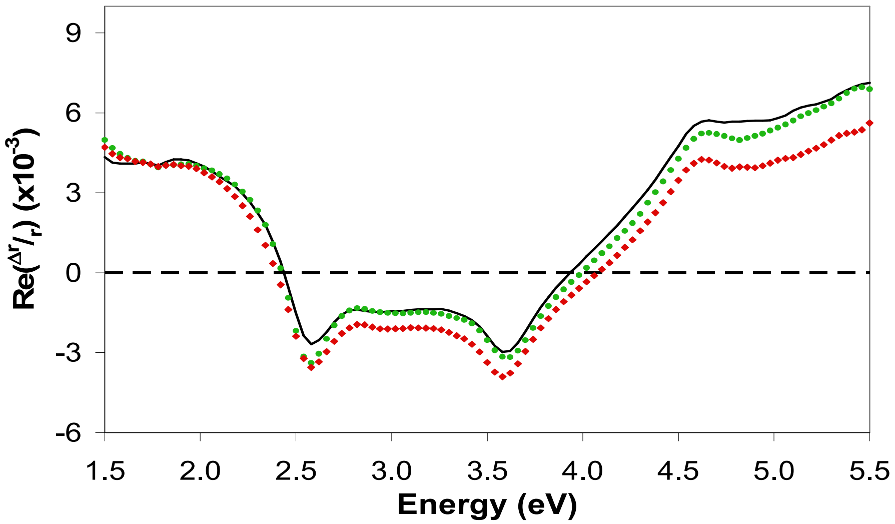

Figure 3.24 (b): Au(110) displaying the (1x2) reconstruction at 0.0 V vs SCE in 0.1 M H_2SO_4/Na_2SO_4 (◆), $NaClO_4/HClO_4$ (●) and $NaClO_4$ (black line).

[23,24,63]. The limited variation in the RA profiles between the acidic electrolytes at -0.6 V is only preserved until ~2.7 eV when at an applied potential of 0.0 V. At this potential, the neutral and sulphate solutions have the least and most well-defined features at 2.5 and 3.5 eV respectively while the acidic perchlorate solution is very similar to the sulphate solution up until approximately 2.7 eV and then apes the neutral perchlorate solution throughout the remainder of the spectrum. The typical features of a (1x2) reconstruction are common to each profile but they do differ slightly. If one considers Figure 3.24 (b), the sensitivity of the surface to anion identity and pH value is clear with the acidic but more weakly adsorbing perchlorate anion having a less-well defined peak at 3.5 eV which is commensurate with the SO_4^{2-} anion having interacted with the surface more to promote the (1x2) reconstruction due to its more strongly adsorbing nature. The neutral solution is the least adsorbing, possibly not adsorbing at all from the CV, and as such does not produce as defined features in the RA profiles.

The Au(110) crystal in the three different solutions at an applied potential of +0.3 V which is expected to result in a predominantly (1x1) surface reconstruction [24] is shown in Figure 3.24 (c). Again in this graph, the difference between the acidic

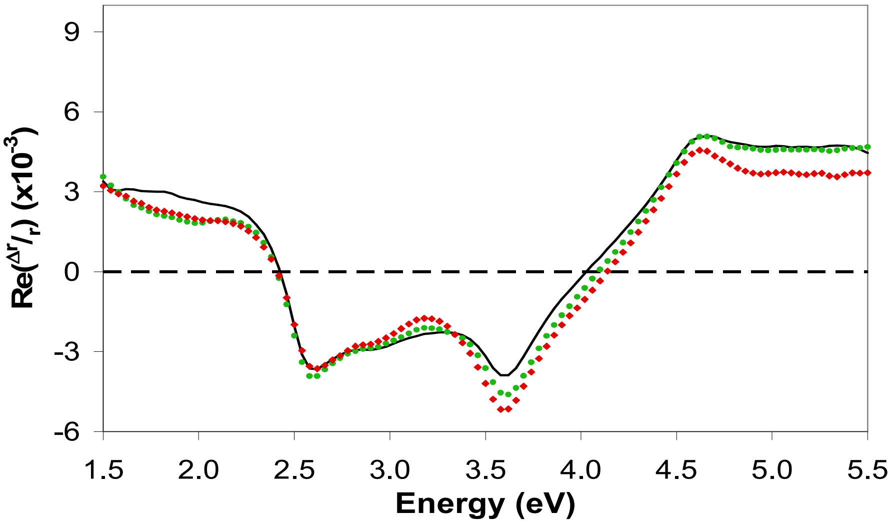

Figure 3.24 (c): Au(110) displaying the (1x1) reconstruction at +0.3 V vs SCE in 0.1 M H_2SO_4/Na_2SO_4 (◆), $NaClO_4/HClO_4$ (●) and $NaClO_4$ (black line).

electrolytes is confined to the region above 2.6 eV in the area where the surface modified bulk layers and steps dominate the RA response. At this potential, there is slight variation below 2.5 eV between the acidic and neutral solutions not observed at the other potentials. This may be due to the fact that in a neutral solution, it is not expected that the (1x2) reconstruction 'fully' lifts off the surface and is preserved somewhat due to the lack of specific anion adsorption. This would then mean that the surface state associated with this reconstruction would be preserved until more positive potentials in this solution and consequently explaining the more positive feature in this spectral region for the neutral solution. This data suggests that both acidic electrolytes are fully (1x1) due to the lack of a broad plateau separating the two main features at 2.5 and 3.5 eV and the imbalance between their relative intensities. This is not observed to the same extent in the neutral solution with a far less developed feature at 3.5 eV and a more positive going slope separating these two features. This is suggestive that at +0.3 V in neutral perchlorate solution, the surface is a slight mixture of (1x2) with predominantly (1x1) reconstructions. This behaviour has been previously observed in phosphate buffer at lower potentials (PZC at +0.1 V [35]) but this has a more strongly adsorbing anion in PO_4^{3-} and this is a reasonable conclusion considering no specific anion adsorption appears to be present in the CV.

One must also add a note about the differences observed between the (1x1) in electrochemical environments and that observed in UHV conditions. It is known that in vacuum, the (1x2) reconstruction is the most energetically favourable and therefore most stable at room temperature [19,20,77]. However, once the temperature is increased the (1x1) phase detected by LEED is not an unreconstructed surface, but a very disordered surface with local (1x2) regions. Due to thermal instability and the moving of missing rows, spatial coherence is lost and the highly anisotropic (1x2) is no longer observed. However, in electrolyte the (1x1) reconstruction is a local and ideal unreconstructed surface without missing rows. It is therefore an ordered phase and not a disordered phase like that observed in UHV. This does not mean the surface is completely free of defects such as corrugation because of the number of steps present on the surface [24]. Goa *et al* [23] show atomic resolution electrochemical STM of the unreconstructed (1x1) phase without the presence of the missing row structure.

3.11: Simulation of (1x2)

As has been discussed, the assignment of the (1x2) reconstruction has met with some controversy due to the varying spectral profiles different groups have assigned to this surface structure [35,37-39]. Section 3.9.1 showed that one of the possible reasons for this discrepancy was experimental procedure where it was shown in sulphate electrolyte that the (1x3) reconstruction damages the characteristic 2.5 eV feature common to (1x2) spectra; the feature was not restored to its previous character and intensity even after being held at 0.0 V for 360 minutes which is expected to drive the surface into the (1x2) reconstruction possibly leaving the surface with large remnants of the (1x3) reconstruction. Further evidence for this conclusion can be sought in Figures 3.25 (a) and (b). Here, shown below a reproduction of the data recorded by the authors in Ref. [38], is a linear addition of the characteristic (1x3) and (1x2) spectra from the sulphate electrolyte from the current work used to discover if the spectral profile from previous literature [38] at 0.0 V in 0.1 M Na_2SO_4 could be simulated using Equation (3.8):

$$\{\text{RAS (1x2)}\} = A\{-0.6\text{ V } (H_2SO_4/Na_2SO_4)\} + B\{0.0\text{ V } (H_2SO_4/Na_2SO_4)\} \qquad (3.8)$$

Where {RAS (1x2)} = RA spectral profile assigned as an ‘optical fingerprint’ of the (1x2) reconstruction in [38], {-0.6 V (H_2SO_4/Na_2SO_4)} = RA profile of Au(110) in 0.1 M H_2SO_4/Na_2SO_4 at -0.6 V from this study and {0.0 V (H_2SO_4/Na_2SO_4)} = RA profile of Au(110) in 0.1 M H_2SO_4/Na_2SO_4 at 0.0 V from this study. A and B are independent multiplicity factors.

Figure 3.25 (b) is the result of the attempt to simulate the RA profile from [38]

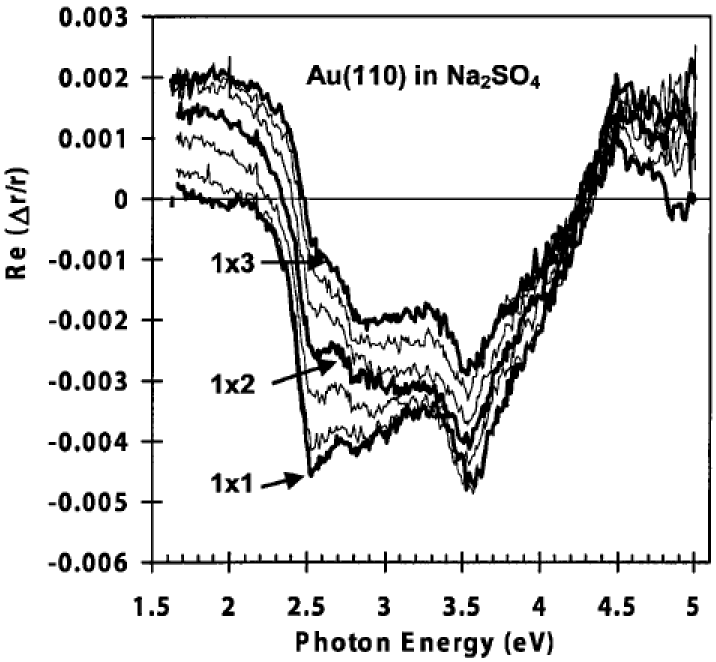

Figure 3.25 (a): RA spectral profiles of Au(110) in 0.1 M Na_2SO_4 from [38] noting the (1x1), (1x2) and (1x3) reconstructions at applied potentials of +0.6 V, 0.0 V and -0.6 V vs Ag/AgCl respectively.

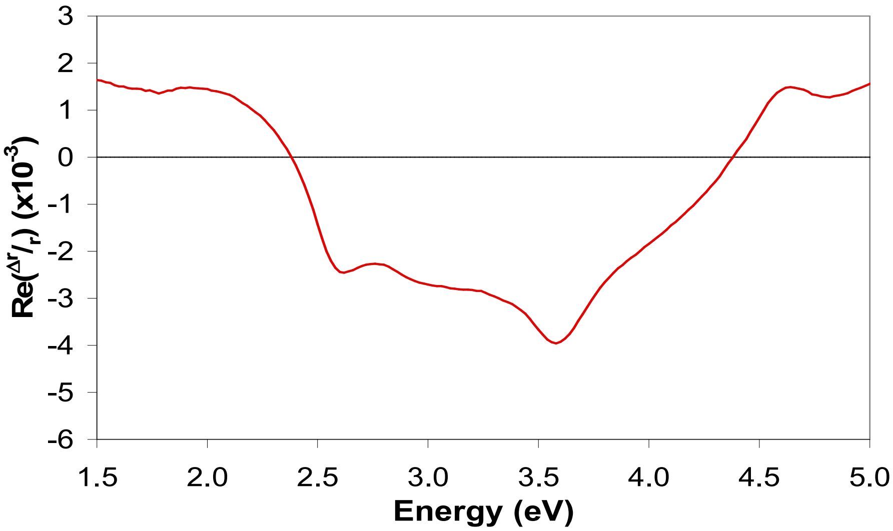

Figure 3.25 (b): RA profile (red line) of the (1x2) reconstruction from [38] simulated using Equation 3.8

using Equation (3.8). Comparison of the two spectra reveals a very good simulation is achieved using values of A = 0.3 and B = 0.1. Figure 3.25 (b) effectively means that the spectra labelled as the optical fingerprint of a (1x2) reconstruction in [38] is, infact, constituted of approximately 75% (1x3) and only 25% (1x2). Of course, the above spectrum has been translated and multiplied to offset the differences in absolute intensities between differing samples since RA signals are normalised [76], however it is the replication of the spectral shape from 75% (1x3) and only 25% (1x2) which enforces the sensitivity of RAS to experimental procedure. The assignment of both the (1x3) reconstruction and (1x1) unreconstructed phases with the RA profiles displayed in Ref. [38] are on the other hand, confirmed and re-enforced by the studies detailed in the current work.

3.12: Summary

The physical and electronic structure of the Au(110) surface and the considerations of the effects of excess surface charge in modifying the preferred lowest energy surface reconstructions have been discussed in depth in this chapter. A review of literature in both UHV and electrochemical environments has introduced the antiphase domain boundaries, (111) microfacets, gold islands and the step and terrace structure which characterise the highly anisotropic (1x2) reconstruction and the role of these surface features in promoting and lifting of this configuration. Understanding the contributions of each of these factors in the context of the optical response of Au(110) as a function of applied electrode potential will allow their undoubted importance to molecular adsorption be more fully appreciated and explored in the future.

Application of the three-phase model comprising optical Lorentzian transitions confined within localised surface states and those sensitive to surface morphology has been shown to simulate the spectral profile of Au(110) to a good degree across the energy range of the spectrum. Quantitative data provided by this framework allows for a comparison between the three different reconstructions and the effect they have on these Lorentzian transitions to be made. As such, the potential decrease from +0.3 V to 0.0 V and finally to -0.6 V where the reconstructions inhabiting the surface are expected to change from (1x1) → (1x2) → (1x3), were found to result in certain trends in the simulation parameters mainly focused on the 2nd transition. This contribution was found to consistently decrease in energy, increase in width and also make a stronger relative contribution to the simulation as the (1x3) reconstruction was formed; this was obviously reflective of the destruction of the 2.5 eV feature at sufficiently negative potentials and the increase in the broad positive feature in the 1.6 eV region as the (1x2) reconstruction is lifted from the surface. There were also major increases in intensity of the 5th transition to account for the increasing intensity to high energy as the potential was made more negative along with a sizeable rise in the contribution from the 4th transition between (1x1) and (1x2) to reflect the formation of steps and (111) microfacets which facilitate the formation of the (1x2). These patterns were found to agree well with previous simulations of Au(110) in varying electrolytes of different pH [1].

The spectral variations between acidic electrolytes were found to be minor and probably due to a mixture of strength of anion adsorption and surface morphology caused by crystal preparation. The addition of a more neutral solution using the same anion as that present in one of the acidic electrolytes was found to decrease the defined nature of each of the features common to the spectral profile of Au(110) and also cause oxidation to occur 0.2 V earlier than in the acidic solutions. Specific anion adsorption was also absent from the CV of Au(110) in the neutral solution and this appeared to be confirmed by RAS.

3.13: References

[1] N. Almond, *PhD Thesis*, University of Liverpool (2008)

[2] D. G. Fedaks and N. A. Gjoste, *Acta Metallurgica* **15**, 23 (1967)

[3] D. G. Fedaks and N. A. Gjoste, *Surf. Sci.* **8**, 77 (1967)

[4] C. Hofner and J. W. Rabalais, *Surf. Sci.* **400**, 189 (1998)

[5] C-M. Chan, M. A. Van Hove, W. H. Weinberg and E. D. Williams, *Surf Sci* **91**, 440 (1980)

[6] I. K. Robinson, *Phys. Rev. Lett.* **50**, 1145 (1983)

[7] J. R. Noonan and H. L. Davis, *J. Vacuum Sci. Technol* **16**, 587 (1979)

[8] B. Reihl and B. T. Dunlap, *Appl. Phys. Letters* **37**, 941 (1980)

[9] J. C. Campuzano, M. S. Foster, G. Jennings and R. F. Willis, *Phys. Rev. Lett.* **54**, 2684 (1985)

[10] L. Onsager, *Phys. Rev.* **65**, 117 (1944)

[11] G. Binning, H. Rohrer, Ch. Gerber and E. Weibel, *Surf. Sci.* **131**, L379 (1983)

[12] Y. Kuk, P. J. Silverman and H. Q. Nguyen, *J. Vac. Sci. Technol. A* **6**, 524 (1988)

[13] K. Gimzewski, R. Berndt and R. R. Schlittler, *Surf. Sci.* **247**, 327 (1991)

[14] T. Gritsch, D. Coulman, R. J. Behm and G. Ertl, *Surf. Sci.* **257**, 297 (1991)

[15] R. Koch, M. Borbonus, O. Haase and K. H. Rieder, *Appl. Phys. A* **55**, 417 (1992)

[16] S. Speller, S. Molitor, C. Röthig, J. Bömermann, W. Heiland, *Surf. Sci.* **312**, L748 (1994)

[17] M. Sturmat, R. Koch and K. H. Rieder, *Phys. Rev. Lett.* **77**, 5071 (1996)

[18] R. Koch, M. Sturmat and J. J. Schulz, *Surf. Sci.* **454**, 543 (2000)

[19] K. Stahrenberg, Th. Herrmann, N. Esser, W. Richter, S. V. Hoffmann, Ph. Hofmann, *Phys. Rev. B* **65**, 035407 (2001)

[20] D. S. Martin, N. P. Blanchard and P. Weightman, *Surf. Sci.* **532**, 1 (2003)

[21] K. M. Ho and K. P. Bohnen, *Phys. Rev. Lett.* **59**, 1833 (1987)

[22] J. W. M. Frenken, R. L. Krans and J. F. van der Veen, *Phys. Rev. Lett.* **59**, 2307 (1987)

[23] X. Gao, A. Hamelin and M. J. Weaver, *Phys. Rev. B* **44**, 10983 (1991)

[24] O. M. Magnussen, J. Wiechers and R. J. Behm, *Surf. Sci.* **289**, 139 (1993)

[25] B. M. Ocko, G. Helgesen, B. Schardt, J. Wang and A. Hamelin, *Phys. Rev. Lett.* **69**, 3350 (1992)

[26] X. Gao and M. J. Weaver, *Surf. Sci.* **313**, L775 (1994)

[27] I. M. Tidswell, N. M. Marković and P. N. Ross, *Surf. Sci.* **317**, 241 (1994)

[28] X. Gao, G. J. Edens, A. Hamelin and M. J. Weaver, *Surf. Sci.* **318**, 1 (1994)

[29] R. Koffman, P. Cheyssac and J. Richard, *Surf. Sci.* **77**, 537 (1978)

[30] S. H. Liu, C. Hinnen, C. Nguyen, N. R. De Tacconi and K. M. Ho, *J. Electroanal. Chem.* **176**, 325 (1984)

[31] C. H. Xu, K. M. Ho and K. P. Bohnen, *Phys. Rev. B* **39**, 5599 (1989)

[32] M. Sastry, K. C. Prince, D. Cvetko, A. Morgante and F. Tommansi, *Surf. Sci.* **271**, 179 (1992)

[33] W. L. Mochán, R. G. Barrera, Y. Borenztein and A. Tadjeddine, *Physica A* **207**, 334 (1994)

[34] J-K. Hansen, J. Bremer, L. Seime and O. Hunderi, *Physica A* **298**, 46 (2001)

[35] B. Sheridan, D. S. Martin, J. R. Power, S. D. Barret, C. I. Smith., C. A. Lucas, R. J. Nichols and P. Weightman, *Phys. Rev. Lett.* **85**, 4618 (2000)

[36] G. J. Dolan, *PhD Thesis*, University of Liverpool (2006)

[37] V. Mazine, Y. Borensztein, L. Cagnon and P. Allongue, *phys. stat. sol, (a)* **175**, 311 (1999)

[38] V. Mazine and Y. Borensztein, *Phys. Rev. Lett.* **88**, 147403 (2002)

[39] P. Weightman, C. I. Smith, D. S. Martin, C. A. Lucas, R. J. Nichols and S. D. Barret, *Phys. Rev. Lett.* **92**, 199707 (2004)

[40] R. A. Bartynski and T. Gustafsson, *Phys. Rev. B* **33**, 6588 (1986)

[41] J. Bremer, J-K. Hansen and O Hunderi, *Surf. Sci.* **436**, L735 (1999)

[42] D. S. Martin, R. J. Cole, N. P. Blanchard, G. E. Isted, D. S. Roseburgh and P. Weightman, *J. Phys. Condens. Matter* **16**, S4375 (2004)

[43] U. Rossow, L. Mantese and D. E. Aspnes, *J. Vac. Sci. Technol. B* **14**, 3070 (1996)

[44] P. Winsemius, F. F. van Kampen, H. P. Lengkeek and C. G. van Went, *J. Phys. F: Met. Phys.* **6**, 1583 (1976)

[45] M. J. Bennahmias, S. Lakkaraju, B. M. Stone and K. Ashley, *J. Electroanal. Chem.* **280**,429 (1990)

[46] O. M. Magnussen, J. Hotlos, R. J. Nichols, D. M. Kolb and R. J. Behm, *Phys. Rev. Lett.* **64**, 2929 (1990)

[47] X. H. Xia, L. Nagle, R. Schuster, O. M. Magnussen and R. J. Behm*, Phys. Chem. Chem. Phys.* **2**, 4387 (2000)

[48] M. Cappadonia, U. Linke, K. M. Robinson and U. Stimming, *J. Electroanal. Chem.* **405**, 227 (1996)

[49] O. M. Magnussen, J. Hotlos, G. Breitel, D. M. Kolb and R. J. Behm, *J. Vac. Sci. Technol. B* **9**, 969 (1991)

[50] M. S. Zei, G. Qiao, G. Lehmpfuhl and D. M. Kolb, *Phys. Chem.* **91**, 349 (1987)

[51] C. I. Smith, T. Farrell, C. A. Lucas, R. J. Nichols, and P. Weightman, *phys. stat. sol. (b)* **242**, 2595 (2005)

[52] N. J. Almond, N. P. Blanchard, D. S. Martin and P. Weightman, *phys. stat. sol. (c)* **2**, 4003 (2005)

[53] J. D. E. McIntyre and D. E. Aspnes, *Surf. Sci.* **24**, 417 (1971)

[54] E. Hecht, *Optics*, third edition, pp111-121 (Addison-Wesley Publishing, 1998)

[55] C. Kittel, *Introduction to Solid State Physics*, seventh edition (John Wiley & Sons, 1996)

[56] K. Vedam, *Thin Solid Films* **313**, 1 (1998)

[57] N. P. Blanchard, C. I. Smith, D. S. Martin, D. J. Hayton, T. E. Jenkins and P. Weightman, *phys. stat. sol. (c)* **0**, 2931 (2003)

[58] N. P. Blanchard, *PhD Thesis*, University of Liverpool (2004)

[59] *Handbook of Optical Constants of Solids*, edited by E. D. Palik, Vol 1 (Academic, New York, 1985 and 1991)

[60] R. J. Cole, B. G. Frederick and P. Weightman, *J. Vac. Sci. Technol. A* **16**, 3088 (1998)

[61] A. Maunder, *PhD Thesis*, University of Liverpool (2001)

[62] B. Sheridan, *PhD Thesis*, University of Liverpool (2000)

[63] D. M. Kolb, *Prog. Surf. Sci.* **51**, 109 (1996)

[64] P. Weightman, G. J. Dolan, C. I. Smith, M. C. Cuquerella, N. J. Almond, T. Farrell, D. G. Fernig, C. Edwards and D. S. Martin, *Phys. Rev. Lett.* **96**, 086102 (2006)

[65] D. M. Jaffery and R. J Madix, *Surf. Sci.* **258**, 359 (1991)

[66] J. X. Wang, G. M. Watson and B. M. Ocko, *J. Phys. Chem.* **100**, 6672 (1996)

[67] O. M. Magnussen, *Chem. Rev.* **102**, 679 (2002)

[68] A. Hamelin, *J. Electroanal. Chem.* **407**, 1 (1996)

[69] A. Hamelin, M. J. Sottomayor, F. Silva, S-C. Chang and M. J. Weaver, *J. Electroanal. Chem.* **295**, 291 (1990)

[70] Z. Borkowska and U. Stimming, *J. Electroanal. Chem.* **312**, 237 (1991)

[71] C. I. Smith, N. J. Almond and P. Weightman, *J. Electrochem. Soc.* **154**, F90 (2007)

[72] D. M. Kolb and J. Schneider, *Electrochim. Acta* **31**, 929 (1986)

[73] Z. Borkowska and U. Stimming, *J. Electroanal. Chem.* **312**, 237 (1991)

[74] P. Hale, S. Thurgate and P. Wilkie, *Surf. Interface Anal.* **32**, 240 (2001)

[75] A. Chen and J. Lipkowski, *J. Phys. Chem. B* **103**, 682 (1999)

[76] C. P. Mansley, T. Farrell, C. I. Smith, P. Harrison, A. Bowfield and P. Weightman, *J. Phys. D: Appl. Phys.* **42**, 115303 (2009)

[77] Y. Borensztein, *private communication*

Chapter 4: Determination of the Structure of Adenine Monolayers Adsorbed at Au(110)/electrolyte Interfaces

RAS has been used to study the three-dimensional orientation of adenine and its associated monophosphate in electrochemical buffer. A sub-saturation coverage is determined and comparisons made between adsorption behaviours of the base and monophosphate molecules. Electrode potential and pH were also varied so as to probe adsorption kinetics in differing environments.

4.1: Introduction

It is important to obtain an understanding of the interactions between biological molecules and metal/liquid interfaces in order to optimise the development of biosensors and biocompatible materials. The structure and stability of organic monolayers of model species such as amino acids and nucleic acid bases grown on well characterised metal substrates are relevant in this context and can also provide insight into the behaviour of more complex systems [1,2]. The adsorption of nucleic acids onto surfaces has been extensively studied by techniques such as electrochemistry [3] and SERS [4]. More recently, the development and application of AFM and STM have renewed interest in the adsorption process [5,6].

This chapter uses RAS to detail the three-dimensional orientation of the nucleic acid base adenine adsorbed onto a Au(110) single crystal in an electrochemically controlled environment and in doing so aims to build on previous efforts to understand the adsorption behaviour and kinetics of biological molecules at interfaces. RAS has already been utilised in investigations of the DNA base cytosine and its monophosphate on a Au(110) substrate [7], the study of amino acids [8] and long sequences of single and double strand DNA adsorbed at Au(110)/electrolyte interfaces [9]. These experiments along with others have shown that this form of spectroscopy is an extremely sensitive, surface specific optical probe which can both record the optical response of surfaces, revealing details of their conformation, and biological molecules in an effort to provide information on adsorption kinetics and interfacial effects [7-19].

Initial investigations into adenine adsorbing onto Hg electrodes showed the molecule undergoes a phase transition from a planar to a vertical orientation as the electrode potential is varied [20,21] while an electrochemical study of the adsorption of adenine onto Au(111) presented evidence of similar transitional behaviour [22]. Moreover, oxidation of the bare Au is suppressed by molecular adsorption and the capacitance data is suggestive of the formation of an organic film. A further study on Au(100) showed evidence that adenine lifted the different reconstructions of the gold surfaces [23].

Only one previous experimental investigation of adenine adsorbed on a variety of Au single crystal faces, including Au(110), exists and its aim was to establish the effect of surface roughness on the organisation of DNA bases on this substrate [24]. It was found that as the density of steps increased the phase transition between the molecule orientated planar to the surface, the physisorbed phase, and the molecule orientated vertically on the surface, the chemisorbed phase, became less pronounced and ultimately disappeared. A chemisorbed film was observed to form spontaneously on Au(110) almost immediately following immersion of the crystal in solution. This film was found to be stable over the potential regime -0.5 to +0.9 V.

Recent theoretical studies into the adsorption of isolated adenine molecules have focused on their physical and electronic structure on the Cu(110) [25] and Au(110) surfaces [26]. The same group [27] have provided a first principles analysis of the driving forces behind the observed [28] self-assembly of adenine-dimer chains on Cu(110) surfaces in ultra high vacuum (UHV).

There has also been a comprehensive experimental and theoretical study of the dielectric functions of films formed from DNA bases grown on H-terminated Si(111) surfaces [29] and a study in which RAS was used to monitor the formation of biomolecular films of DNA bases on vicinal Si surfaces [30].

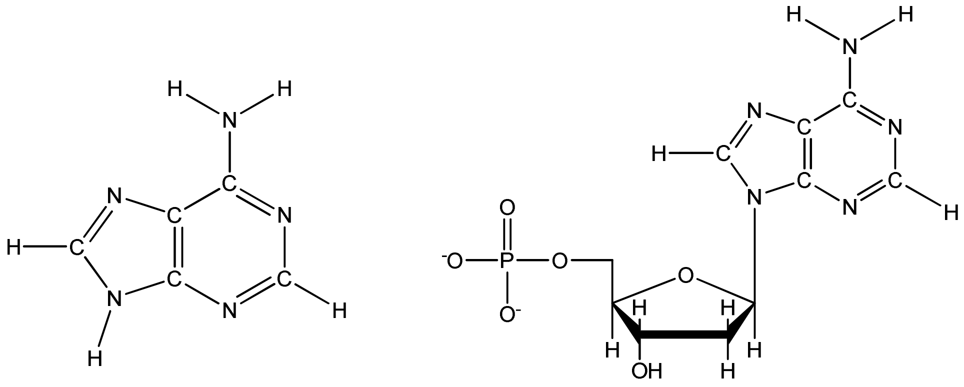

Figure 4.1: Structure of adenine (left) and adenosine 5´-monophosphate (right).

4.2: Concentration Effect of Adenine Adsorption

The Au(110) crystal and electrochemical cell were prepared as has been previously described in Figure 2.8 and Chapter 3.7 respectively. The solutions were prepared from H_2SO_4 (BDH, Aristar grade), NaH_2PO_4, K_2HPO_4, KOH (BDH, Analar grade), adenine and AMP (Aldrich) [Figure 4.1] without further purification in Millipore ultra-pure water (18 MΩcm) and made oxygen-free by purging with argon prior to use.

The RAS of the Au(110) surface has a pronounced negative peak at 2.6 eV and the intensity of this peak increased as adenine is adsorbed onto the surface. In order to investigate the influence of the concentration of the adenine solution on the magnitude of the RAS, the signal obtained at 2.6 eV was recorded as a function of time following the addition to the cell of solutions of concentrations 0.1 μM, 0.5 μM, 20 μM and 100 μM. RA spectra which measure the change in intensity at a solitary wavelength are called RAZ spectra and this data is shown in Figure 4.2. To achieve a final concentration* of 0.1 μM required 5 μl of 1 mM adenine be injected into the cell,

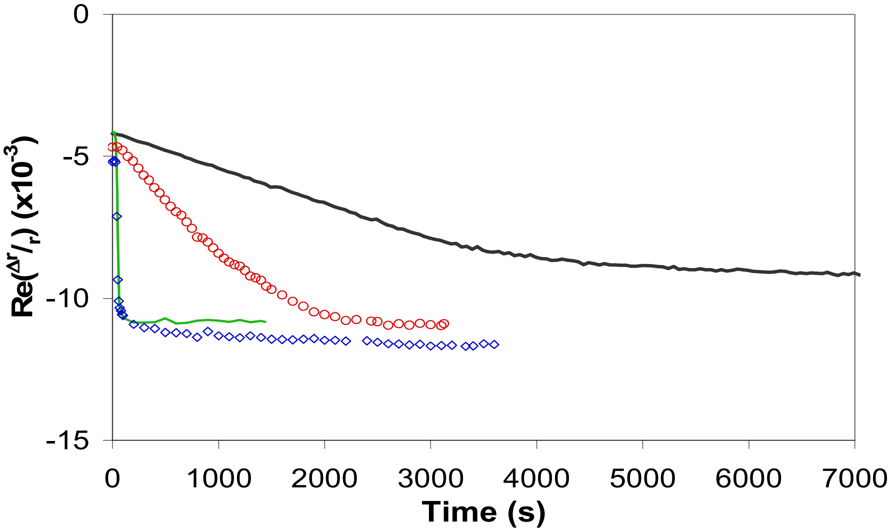

Figure 4.2: RAZ spectrum recorded at 2.6 eV with the addition of adenine at 0.0 V vs. SCE in 0.1 M NaH_2PO_4/K_2HPO_4 (pH 7.1) to give a final concentration of 0.1 μM (black line), 0.5 μM (○), 20 μM (green line) and 100 μM (◇).

See end of section 4.10: References

0.5 μM required 25 μl, 20 μM required 1 ml and the injection of 5 ml of 1 mM adenine resulted in a final concentration of 100 μM. The consideration of light adsorption by solution is not a factor in this instance since the concentration range in which the experiments were conducted is far below the boundary of 0.35 mM where this effect becomes significant [31].

The rate of increase in intensity of the RA signal along with the final magnitude reached in each of the four experiments is determined by the concentration of the solution. The variation in the strength of the RAS signal at 2.6 eV with the concentration of the solution can be explained by assuming that the adenine adsorbs on the Au(110) surface until a saturation coverage is reached and that this occurs with the three highest concentrations. However, for the lowest concentration the results are suggestive that the solution is essentially exhausted by adsorption before saturation is achieved. The volume of the cell was 50 ml which with an adenine concentration of 0.1 μM gives a total of 3×10^{15} adenine molecules. The exposed area of the Au(110) crystal was 0.5 cm^2 and if all the molecules in the weakest solution adsorbed on this surface this would give a very high density of 3 molecules per 5 $Å^2$. Nonetheless it is likely that the adenine molecules would also reach and adsorb on the rear surface of the Au crystal reducing the estimate of the surface density by half. More importantly, given the large area of the cell, any adsorption on the cell walls would dramatically reduce this estimate of the surface concentration indicating a less than fully saturated surface and certainly bringing the estimated coverage to values comparable with ~ 42 $Å^2$ for the area occupied by one adenine molecule on the gold surface found previously through differential capacitance measurements [23,32,33].

The RAS of Au(110) surfaces obtained after four different flame annealing treatments are shown in Figure 4.3 (a). These spectra were obtained with the potential applied to the Au(110) surface held at 0.0 V and in a solution at pH 7.1. RAS has already been shown to be sensitive to the Au(110) surface morphology [16,34-36] and there is some variation in the spectra obtained from the clean surfaces that probably arises from variations in the flame annealing procedure though they are similar to those

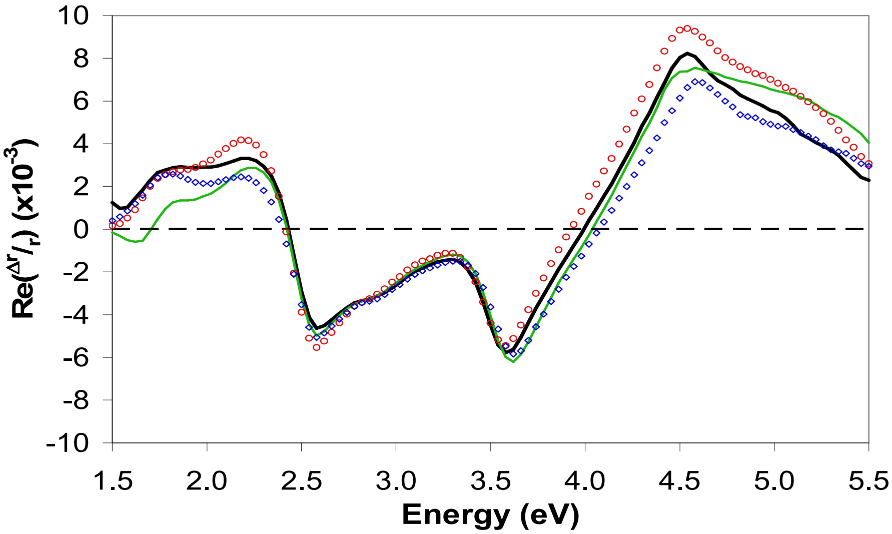

Figure 4.3 (a): RA Spectra of Au(110) used in the 0.1 μM (black line), 0.5 μM (○), 20 μM (green line) and 100 μM (◇) experiments.

obtained in previous studies [10]. The spectra are remarkably similar between 2.5 and 3.5 eV but vary slightly in the spectral regions outside this range. The low energy region of the profile (< 2.5 eV) is associated with transitions involving surface states whereas the high-energy region is expected to be sensitive to surface step contributions. This is an interesting correlation with the Cu(110) surface in that studies have shown that changes in the surface step and terrace structure can have a significant impact on the characteristics of surface states when, as in the Au(110) case, one of the surface states is close to the Fermi energy [37-40] this can have a major influence on the RA profile.

As the solutions of different concentration were added to the electrochemical cell [Figure 4.3 (b)] the RAS in the low energy range remain unchanged and the differences between the RAS in the initial experiments on the four different clean Au(110) surfaces are preserved in detail. Conversely from 2.5 eV onwards the negative amplitude of the RAS for all concentrations increased notably and beyond 3.5 eV the signal continues in a sequence of broad negative undulations rather than exhibiting the characteristic positive peak of the Au(110) surface centred at 4.5 eV. In addition to enhancing the amplitudes of the negative features present in the RAS of the clean

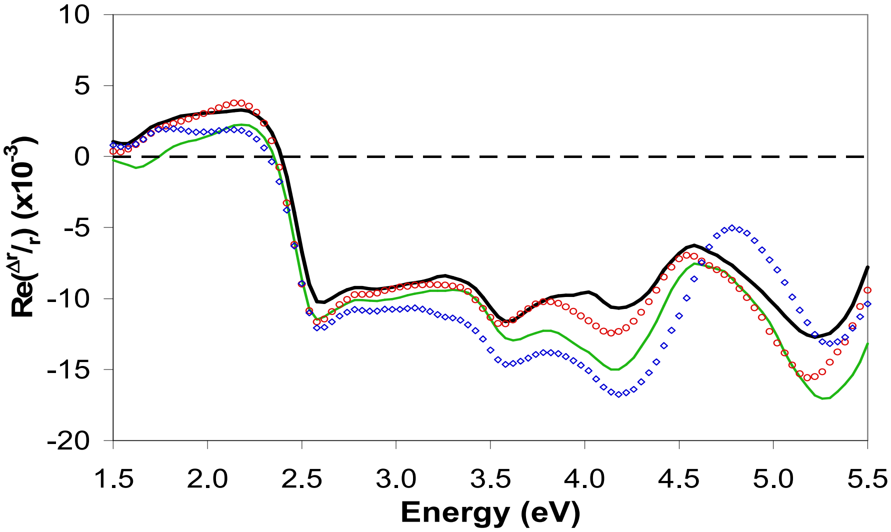

Figure 4.3 (b): RA Spectra of Au(110) + 0.1 μM (black line), + 0.5 μM (○), + 20 μM (green line) and + 100 μM (◇) of 1 mM adenine at 0.0 V vs SCE and pH 7.1.

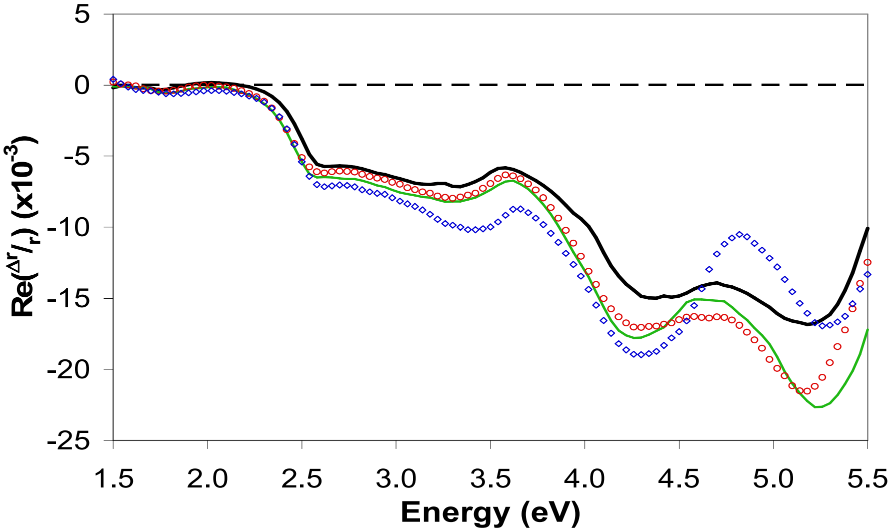

Figure 4.3 (c): Adenine spectra, at the various concentrations previously specified, obtained by subtraction of the corresponding Au(110) spectra.

surfaces at 2.5 eV and 3.5 eV, the adsorption of adenine also gave rise to two new broad negative peaks at 4.2 eV and 5.3 eV.

The changes that the addition of adenine induced in the RAS of the Au(110) surfaces are more clearly brought out when the spectra of the clean surfaces are subtracted from the spectra of Au(110) + adenine [Figure 4.3 (c)]. The RAS obtained for the adenine on Au(110) surfaces depends on the concentration of the solution and this dependence is larger than the variation between the RAS obtained for the initial clean surfaces, hence the subtractions shown in Figure 4.3 (c) can be considered to capture the effects of the concentration of the adenine solution on the RAS of the adsorbed adenine. In the spectral region up to 4.5 eV the shape of the negative RA signal is essentially independent of the concentration of the adenine solution, nevertheless this is not so for the associated increases in amplitude as beyond this energy the data show a more complex reliance on adenine concentration. The spectra obtained with the intermediate concentrations are almost identical, the small differences between them having a significant contribution from the small differences in the spectra of the initial clean surfaces. In addition both have a larger intensity than that obtained with the least concentrated solution. The addition of the most concentrated adenine solution however gave rise to a significant difference from the previous spectra recorded using the lower concentrations. This spectrum preserved the two negative features at 4.2 eV and 5.3 eV but the positive dip between these two peaks, centred at 4.5 eV and which was present in all spectra, is now much more pronounced. The observation of a strong RA profile directly attributable to adsorbed adenine proves that the molecules must adopt an anisotropic alignment at the Au(110)/electrolyte interface. If they did not, there would be no overall optical response due to the anisotropic nature of the RAS measurement. If molecular anisotropy were not apparent, then one would expect Figure 4.3 (c) to be featureless.

The data shown in Figures 4.2 and 4.3 lead to interesting conclusions on the concentration effect of adsorbed adenine: primarily that the three highest concentrations of 0.5 μM, 20 μM and 100 μM reached a saturating coverage on the

Au(110) substrate while the least concentrated solution failed to achieve full coverage due to exhaustion of the solution [Figure 4.2]; secondly, that the variation in the strength of the RAS signal at 2.6 eV is dependent upon the concentration of solutes and thirdly, not only do differences exist between the RA profiles of the partially and fully saturated surfaces in both intensity and contour but striking differences also exist between the highest and two intermediate concentrations themselves all of which are at saturation. This latter point being highly suggestive of a variation in macro-molecular orientation as solution concentration increases. It is important to note that as the concentration of the solutions used in the current work was relatively low, "crowding effects" [41] need not be considered while the self-assembly of an adenine monolayer at the gold surface is also distinct from such effects.

4.3: Azimuth-Dependent RAS

As shown in previous work [7,10,42,43], crucial information on the alignment of the optical axes of an adsorbed species can be obtained from the variation in the RAS as a function of the angle θ between the polarisation direction of the incident light and the optical axes of the surface. To conduct such rotation experiments, the crystal is orientated such that the principle axes of Au are 45° to the plane of polarisation of the incident light to obtain a maximal RA signal. If the sample is then rotated in the plane of the surface, the angle between the substrate axes and the plane of polarisation of the incident light vector (the *azimuth* angle) will vary.

The characteristic RA profile of a clean Au(110) crystal varies as $\cos 2\theta$ with rotation where θ is defined as the angle of rotation from the initial starting position. Consequently, as sample rotation occurs the RA spectrum will tend to zero as θ tends to 90°, there being no anisotropy in the reflected light since the polarisation direction of the incident light will be coincident with one of the optical axes of the surface and orthogonal to the other. As $\theta \rightarrow 135^\circ$, the RA spectrum will tend to a maximum intensity of opposite sign but the same magnitude as that found at $\theta = 45^\circ$. This is due to the anisotropic response arising from $r_{[001]} - r_{[1\bar{1}0]}$ rather than $r_{[1\bar{1}0]} - r_{[001]}$. Of course it is inherent in this approach that the spectrum will only return to its original maximum at $\theta = 225^\circ$. Figure 4.4 (a) shows the rotation of the clean Au(110) crystal through 90° while Figure 4.4 (b) details the variation in the intensity of the three major spectral features apparent in Figure 4.4 (a) at energies of 2.6, 3.6 and 4.5 eV rotated through 180°. Both of these figures clearly show the cos2θ dependence of the intensity of the gold spectrum as a function of azimuth angle and as such it is clear that this symmetric behaviour is borne out.

When there is the addition of an ordered adlayer on a surface there is no guarantee that it will share the same optical axes as the substrate. If this occurs there will understandably be a more complex relationship with azimuthal rotation arising from the relative contributions from the two anisotropies as θ is varied. Obviously in Figure 4.4 the intensity tends to zero as the polarisation direction of the incident light becomes commensurate with one of the substrate's optical axes however, if an

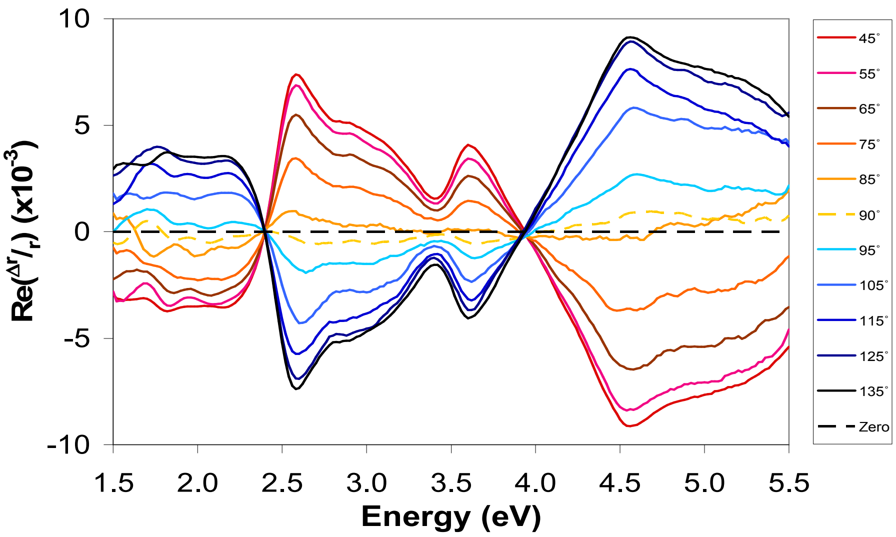

Figure 4.4 (a): RA Spectra of Au(110) as a function of rotation, θ, through 90° with increments of 10° in 0.1 M NaH_2PO_4/K_2HPO_4 at pH 7.1.

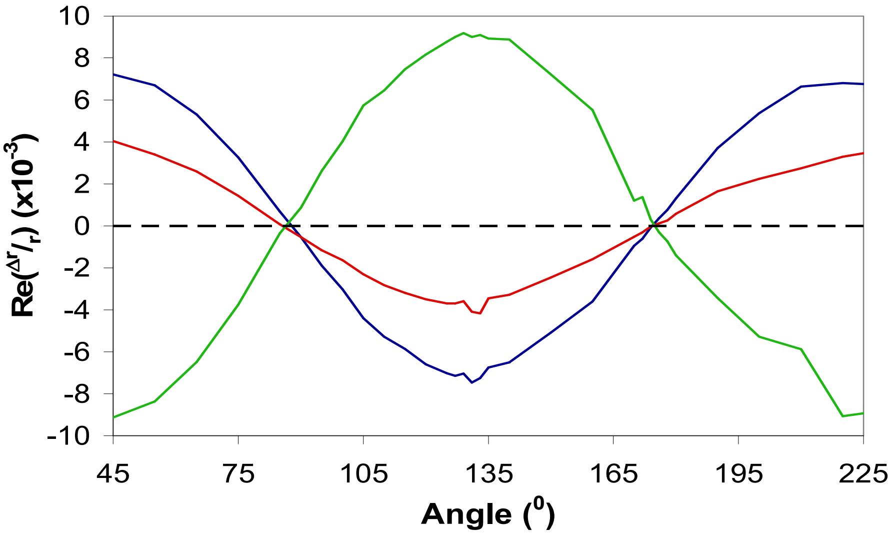

Figure 4.4 (b): Intensity variations of the 2.6 (blue line), 3.6 (red line) and 4.5 eV (green line) peaks as shown in Figure 4.4 (a) as a function of rotation clearly showing their cos2θ dependence as a function of azimuth angle.

adsorbed species were present and its optical axes were not aligned with those of the surface there would be a remaining contribution from the adlayer itself even if the spectrum attributable to the substrate collapses to zero. Macdonald *et al* [43] used azimuth-dependent RAS (ADRAS) to determine the angle between two competing optical axes. This technique studies RA spectra at a solitary wavelength as a function of azimuth angle.

Angular rotations of the RAS obtained using the lowest (0.1 μM) and highest (100 μM) adenine concentrations were conducted and the results are displayed in Figures 4.5 (a) and 4.5 (b). These figures show that although the RAS obtained following the addition of different adenine concentrations to the cell varies not only in intensity across the whole spectrum but also in the strength of the dip in the profiles at about 4.5 eV, the RAS in each case reduced to zero across the spectral range at θ = 90°. This result establishes that at both saturated and unsaturated coverage's, the optical axes of the adenine molecule were coincident with those of the Au(110) surface which are along the [001] and [1$\bar{1}$0] directions. This finding coupled with the known

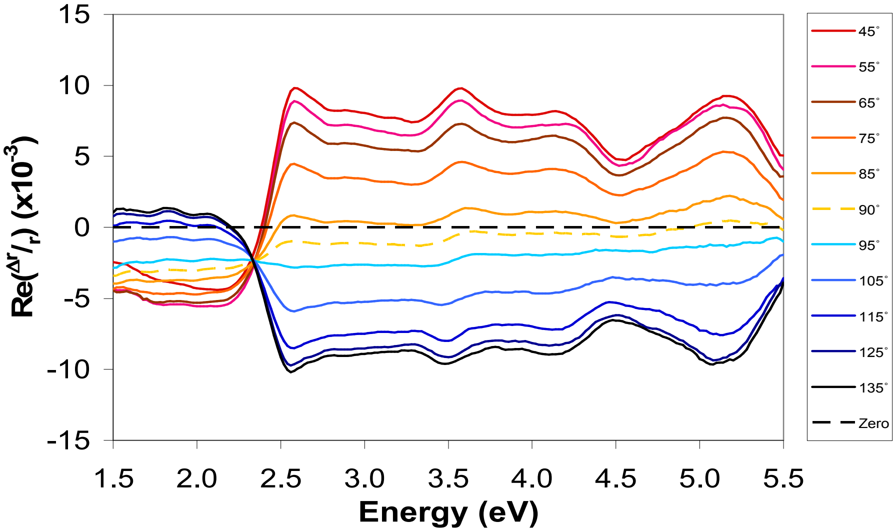

Figure 4.5 (a): RA Spectra of Au(110) + 0.1 μM adenine as a function of rotation, θ, through 90° with increments of 10° at 0.0 V vs SCE and pH 7.1.

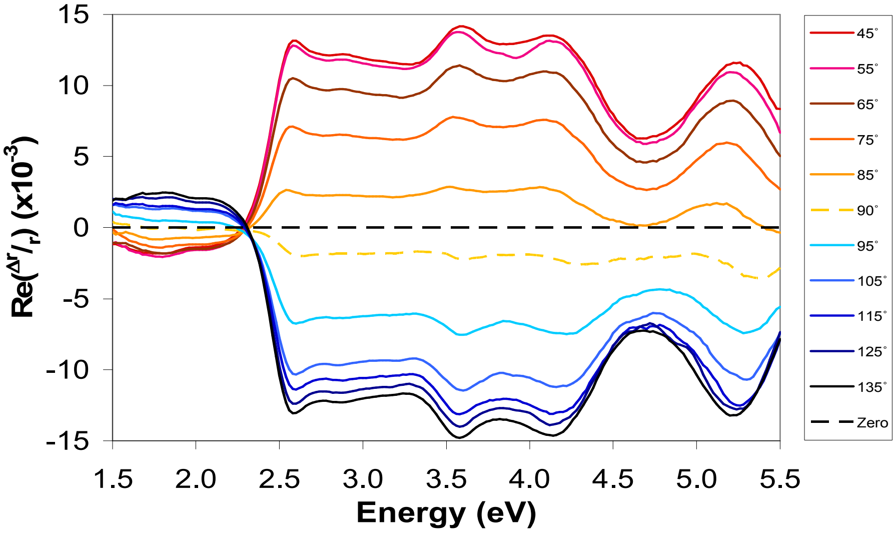

Figure 4.5 (b): RA Spectra of Au(110) + 100 μM adenine as a function of rotation, θ, through 90° with increments of 10° at 0.0 V vs SCE and pH 7.1. It is important to note that the increased intensity of the detected signal in a region of the spectrum with no molecular contribution (<2.5 eV) is real since the DC was recorded and did not vary.

tendency of nucleic acid bases to adopt stacking arrangements in which the bases are aligned parallel to each other [44-46] implies that the adenine molecules are aligned in rows orientated along one of the principal directions of the Au(110) surface.

Figure 4.6 (a) shows the RAS obtained from a freshly prepared Au(110) crystal and the change in the spectrum produced by the addition of 100 μM AMP. The addition of AMP gave rise to a change in the RAS that was remarkably similar to that induced by the addition of adenine [Figure 4.3]. More specifically, the negative features at 4.2 eV and 5.3 eV are somewhat weaker than found for adenine. Figure 4.6 (b) displays the change in the RAS of AMP/Au(110) as the angle, θ, between the polarisation direction of the incident light and the crystal axes was varied. An important observation from the RAS of AMP as a function of rotation is that, as found for the RAS of adenine, the spectrum reduces to zero across the whole spectral range at $\theta = 0^\circ$ or 90°. This result establishes that the optical axes of the adsorbed AMP are coincident with those of the Au(110) surface in agreement with the results found for adenine.

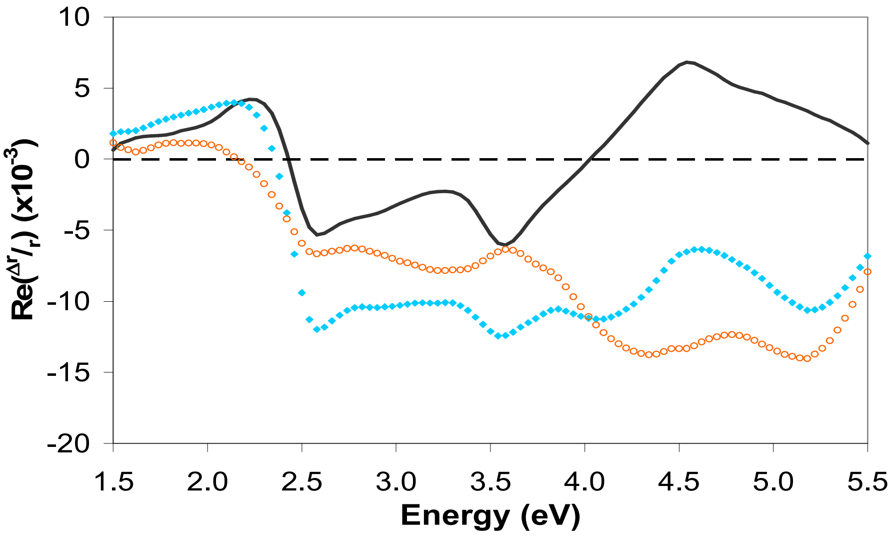

Figure 4.6 (a): RA Spectra of Au(110) (black line), Au(110) + 100 μM AMP (◆) and AMP spectrum obtained by subtraction of the corresponding Au(110) (○) all recorded at 0.0 V vs SCE and pH 7.1.

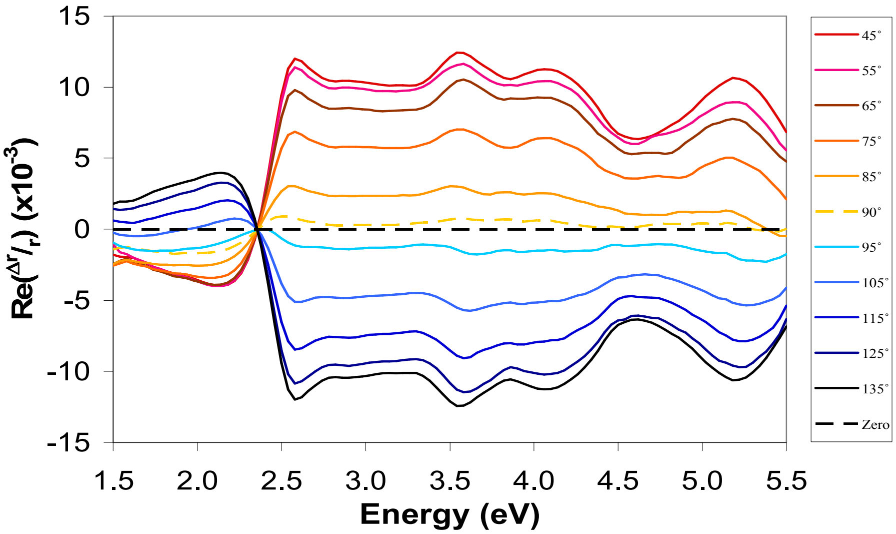

Figure 4.6 (b): RA Spectra of Au(110) + 100 μM AMP as a function of rotation, θ, through 90° with increments of 10° at 0.0 V vs SCE and pH 7.1.

A comparison of the RAS of adenine and AMP provides valuable information on the orientation of both molecules. Since the sugar and phosphate groups of AMP do not contribute to the optical response in the spectral range of the instrument, the RAS of both AMP and adenine arise from the dipole transitions of the base and to first order these should be identical for the two molecules. In spite of this the expectation that AMP and adenine should have an identical optical response does not imply that they should yield identical RA spectra since the relative contribution of different dipoles to the overall profile will depend on the orientation of the molecule as a whole. Still, the RA spectra of AMP and adenine adsorbed at the Au(110)/electrolyte do have very similar profiles. Both show a similar enhancement of the spectral region between 2.2 and 3.5 eV associated with the RAS on the Au(110) surface and both show features peaking at 4.2 and 5.3 eV. The close similarity of the RAS profiles of adenine and AMP suggests that the orientation of the bases on the surface is very similar for the two molecules.

The increase in the optical response in the range 2.2 eV to 3.5 eV caused by the addition of both adenine and AMP to the cell can be attributed to a coupling between the dipole transitions in the base and the dielectric response of Au [10]. The fact that this increase is similar for adenine and AMP signifies that AMP must adsorb on the surface through sites located on the base. Such a conclusion originates from a comparison of the RAS of single (ss) and double (ds) stranded DNA which showed a similar effect when single stranded DNA adsorbed through the bases but a much reduced intensity is recorded when the optical transitions of the bases are screened from the Au by adsorption by the phosphate groups [9].

The conclusion that both adenine and AMP adsorb on the Au(110) surface through sites on the bases combined with the similarity of their respective spectra indicates that the same sites are involved in both instances. The only way to satisfy this condition is if the adsorption of both molecules is through sites on the side of the molecule on which the N(7) atom and the NH_2 group are located [Figure 4.7]. This assignment is consistent with the conclusions of Xiao *et al* [47], from SERS studies of adenine on polycrystalline Au, that there is direct contact between the N(7) atom and the NH_2 group with the Au surface at positive potentials. This assignment is also in agreement with the results of a recent theoretical study [26] which showed that adenine binds to the Au(110) surface through these N atoms.

4.4: Electronic Spectrum of Adenine

The observation of a strong RAS profile from molecules adsorbed at a surface proves that the molecules adopt an anisotropic alignment at the surface. If the optical response of the molecule arises from a number of well-defined dipole transitions and if the orientations of these transitions with respect to the molecular axes are known then RAS can yield information on the orientation of the molecule with respect to the surface as shown in the recent study of cytosine and CMP [7] adsorbed at the Au(110)/electrolyte interface. In order to deduce further information about the orientation of the molecules at the Au(110)/electrolyte interface, it is necessary to consider the dipole transitions that are expected to contribute to the optical response of the molecule.

It is important to first summarise the conclusions of experimental and theoretical work on the optical transitions of adenine. The absorption spectra of adenine has given rise to considerable discussion over several decades, due mainly to the discrepancies between the various experimental and theoretical techniques employed in the different investigations [48-65]. The spectra are thought to consist of a number of $\pi \rightarrow \pi^*$ transitions, polarised in directions confined to the plane of the nucleic acid base, and a few $n \rightarrow \pi^*$ transitions polarised normal to the plane of the base. These latter transitions are approximately two orders of magnitude weaker than the former and as such are ignored in the final analysis of the RAS results.

Table 4.1 is a considered summary of the results of experimental studies [48,49,51,55,60-65] of the $\pi \rightarrow \pi^*$ optical transitions of the adenine molecule. The different studies show good agreement in relation to the energies of the transition although significant discrepancies are apparent in the results reported for the oscillator strengths and transition moment directions, ϕ [Figure 4.7], with respect to the optical axes of the molecule. This latter variation is captured by the multiple entries in the final column of Table 4.1.

A consensus has emerged in the past decade that adenine gives rise to a transition at 4.90 eV in the gas phase which is red-shifted and split, when observed using LD of adenine partially orientated in poly vinyl alcohol film and methyl-substituted single crystal adenine, into two separate $\pi \rightarrow \pi^*$ transitions centred approximately at (I) 4.6 eV and (II) 4.8 eV [48,49,51,55,60,63,65] with the second transition being twice as intense as the first [49,51,65]. Currently there is no agreement on the origin of this splitting. It has been suggested that it arises from the tauterism of the adenine molecule, which exists as ~ 22% N(7)H whilst in an aqueous solution [48,54,55]. However, observations from LD experiments exclude this possibility since changes are seen on the long wavelength side of the first absorption band that could not arise from tauterism [48]. An alternative explanation of the splitting is that it arises

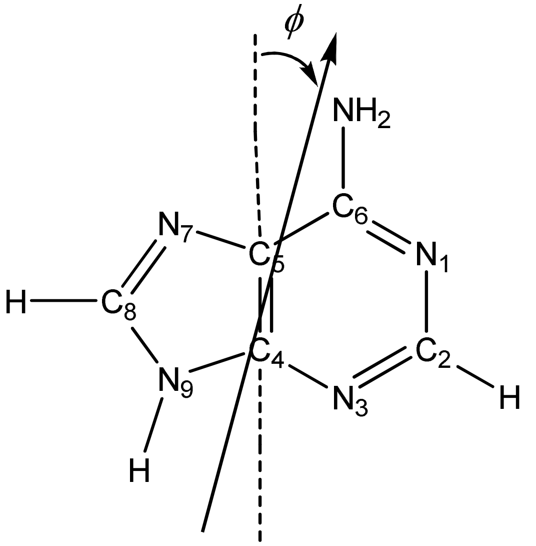

Figure 4.7: The Devoe-Tinoco convention for molecular transition directions [66]. The azimuth angle ϕ is measured from the C(4)-C(5) axis towards the NH_2 group.

TABLE 4.1: Summary of the results of experimental studies of the electronic transitions of Adenine, its chromophore and methyl substituted derivatives. Only $\pi \rightarrow \pi^*$ transitions are included. The three strongest transitions are in bold. f is the transition strength and ϕ, the molecular transition direction, is defined in Figure 4.7.

Transition	λ (nm)	Energy (eV)	f	ϕ°
I	273	4.56 +/- 0.15	0.09 +/- 0.04	66[a] / 67[b] / 83[c]
II	259	4.80 +/- 0.15	0.18 +/- 0.04	19[a] / 25[c] / 35[b]
III	**213**	**5.85 +/- 0.05**	**0.25 +/- 0.10**	**-21[a] / -45[b,c]**
IV	197	6.30 +/- 0.05	…	…
V	**183**	**6.81 +/- 0.05[c,d]**	**0.30[c]**	**72[c]**
VI	**161**	**7.75 +/- 0.05[c,d]**	**0.23[c]**	**6[c]**

[a]Reference 55, [b]Reference 65, [c]Reference 50, [d]Reference 63.

from intermolecular interactions in single crystal adenine that do not occur in the gas phase. The splitting is not observed in CD [61,62] but is recorded in Magnetic CD [63], Polarised Adsorption [51] and LD [48]. Moreover, both Holmen *et al* [55] and Mennucci *et al* [58] conclude that the sum of the oscillator strengths for these two transitions is invariably the same but their relative intensity varies significantly between PVA film and methyl-substituted single crystal adenine. Further, Holmen *et al* discuss how the LD spectrum of adenine is very different from that of both 9 methyl-substituted adenine and adenosine and hence any investigation using LD or isotropic absorption must account for the tauterism of the adenine chromophore.

Matsuoka and Nordén [48] reported an angle of $\phi = 9^\circ$ for the orientation of transition (II) with respect to the molecular axes in agreement with the views of Holmen [55] and Clark [49,51] that transition (II) is essentially short-axis polarised whereas the original LD work by Stewart and Jensen [60] disagreed and assigned short and long axis polarisation's for (I) and (II) respectively. There is now general agreement that transition (I) at 4.6 eV is close to being polarised along the long axis of the molecule with Clark [49,51] recording a value of $\phi = 83^\circ$ and Holman [55] $\phi = 66^\circ$. There is similar agreement that the strongest low energy transition at 4.8 eV is polarised close to the short axis with Clark giving a value of $\phi = 25^\circ$ and Holman $\phi = 19^\circ$. The argument advanced by Sreerama *et al* [53] that the disparity between transition moment directions and oscillator strengths measured in the different environments are the result of the crystal field breaking the symmetry inherent in the gas phase and thereby allowing mixing of $n \rightarrow \pi^*$ and $\pi \rightarrow \pi^*$ transitions and making it difficult to distinguish between the two is not supported by Clark [49,51,65]. Although Clark's model ignored crystal field affects for closely spaced transitions, recent work supports Clark's data on the transition moment directions for the adenine molecule [55]. Petke *et al* [50] concluded that the polarisation of the transition labelled (II) in the present work lies between 40° to 70° and was dependent upon molecular environment.

There is evidence for the existence of a transition at approximately 5.3 eV [48,55] although it is not recorded in other investigations [49,51,60,65] which could possibly be explained by its very weak transition strength [55]. A transition at 5.4 eV has been observed in CD studies of the adenosine complex that has been attributed to a n → π* transition [61,62]. This 5.4 eV transition is also observed in LD investigations [48,55] while another transition observed using the same method is also directly attributed to the N(7)H tautomer at 5.55 eV [55]. Clark has detailed two further n → π* transitions at 5.1 and 6.1 eV [65]. A number of studies utilising different experimental techniques identified a transition at approximately 5.8 eV [49,51,55,61,63,65]. CD and MCD investigations also revealed a transition at ~ 6.3 eV [61-63] which is not observed in other experimental studies [48,49,51,60,63,64]. Two suggestions have been put forward as to the origin of the transition at 6.3 eV; (a) since the $5^1A'$ state of adenine at 6.72 eV has a dipole moment double that of the ground state, a transition involving this state may be strongly red-shifted in polar solvents into the 6.3 eV region; (b) it could arise from a transition in the N(7)H tautomer that is calculated to have an energy of 6.5 eV [54]. It should be noted that CD spectra often record n → π* transitions as they frequently have considerable magnetic dipole moments [53] possibly explaining some of the disparities between these studies. To higher energies and beyond the range of the RAS instrument, transitions are observed at ~ 6.8 eV orientated towards the long axis and a high intensity transition at 7.75 eV which is short axis polarised [51,64].

The main body of theoretical work on the adsorption spectrum of adenine employs a number of approaches including; TDDFT [58,59], INDO/S [53,56], CNDO [52], CASPT2 [54,57] and CIPSI [58]. All these techniques provide information on the energies, directions and oscillator strengths of the transitions associated with the molecule. There is some correlation between the results of early theoretical work [50] and INDO/S calculations [56] while CIPSI and TDDFT are in good agreement in gas-phase calculations but diverge in solvated systems because of the different characteristics of the two approaches. Menucci *et al* [58] argue that, in solution at least, CIPSI is the more reliable basis set. The latest theoretical work on adenine's absorption spectrum [26] is calculated in the gas phase and highlights recent developments in the understanding of the mixing of the $\pi \rightarrow \pi^*$ transitions with the weak $n \rightarrow \pi^*$ transitions [59]. The results of the theoretical studies are in general in good agreement with experiment for the energies of the principal transitions. Nevertheless, theoretical work predicts many more transitions of recordable strength than are observed by any experimental technique. In addition the theoretical studies give rise to wide variations in the predictions of the intensities and transition moment directions with respect to the molecular axes.

The considered analysis of the optical transitions of the adenine molecule suggests that in the range of the RAS instrument two strong transitions at 4.56 eV and 4.8 eV should be observed. Although the energy separation between the two transitions is small and there is as yet no agreement on the precise orientations of each of the transitions with respect to the molecular axes, an important point is that there is concurrence that the difference in their relative orientation is quite large: Ref. [55] giving 47° and Ref. [51] 58°. Further, while there is a similar divergence as to the orientation of the transition at 5.85 eV there is agreement that the direction of the transition moment is significantly different from those at lower energies. The disparity in the relative orientation of these three transitions is crucial since if the molecule adsorbed with the plane of the molecular ring parallel to the surface, then the intensity of each of the transitions would vary as $\cos 2\theta_1$, $\cos 2\theta_2$ and $\cos 2\theta_3$ as the sample is rotated where θ_1, θ_2 and θ_3 are the angular projections of the transition moment directions in the plane of the molecule onto the surface plane. As such large differences exist in the orientation of the transitions it is highly unlikely that their total contribution to the RA spectrum would reduce to zero since they are almost completely out of phase and hence the RA spectrum would not tend to zero through rotation as some residual contribution would always remain.

The fact that the RAS of both adenine and AMP go to zero across the whole spectral range as θ between the polarisation direction of the incident light and the crystal axes was varied means that both molecules must be orientated essentially vertically on the surface and with the plane of the base oriented along one of the principal axes of Au(110). Additionally, for the reasons advanced above, it is possible to conclude from Figures 4.5 (a) and 4.5 (b) that even though the detailed RA profiles are different for the spectra obtained from the lowest and the highest concentrations, the molecules are orientated vertically on the surface, probably in a base stacking configuration in both cases.

4.5: Simulation of Au & Au + Adenine RA spectra

It was possible to simulate RA spectra obtained in the four separate experiments on the Au(110) surfaces shown in Figure 4.3 (a) using the empirical Lorentzian Transition Model described in Chapter 3 and employed in previous work [7,16,67,68]. The four RA spectra were very similar and precise simulations could be achieved with five transitions, four, with energies of 1.60 ± 0.20 eV, 3.45 ± 0.06 eV, 4.60 ± 0.06 eV and 5.63 ± 0.15 eV, polarised along [001] and one with an energy of 3.90 ± 0.07 eV polarised along $[1\bar{1}0]$. With some exceptions below ~ 2.2 eV, accurate simulations of the RAS of the Au(110) were achieved through relatively small variations in the line-widths (Γ) and relative intensities (S) associated with these transitions as shown in Figure 4.8 (a). The contributions of the individual components to the RAS line shape for the solution containing 20 μM adenine are displayed in Figure 4.8 (b). The parameters used to generate these simulations are shown in Table 4.2 and are in extremely good agreement with those used in simulating Au(110) spectra obtained in an earlier study [7]. It is important to note that two high energy transitions polarised along [001] were required to reproduce the positive feature that develops in the spectral profile from ~ 4 eV onwards and which correlates with the presence of $[1\bar{1}0]$ orientated monatomic steps on the surface.

While simulations of the RAS of Au(110) surfaces produced using the model as previously described are almost certainly not unique, their purpose is to provide a basis on which to interpret the changes induced in the substrate in the spectral region

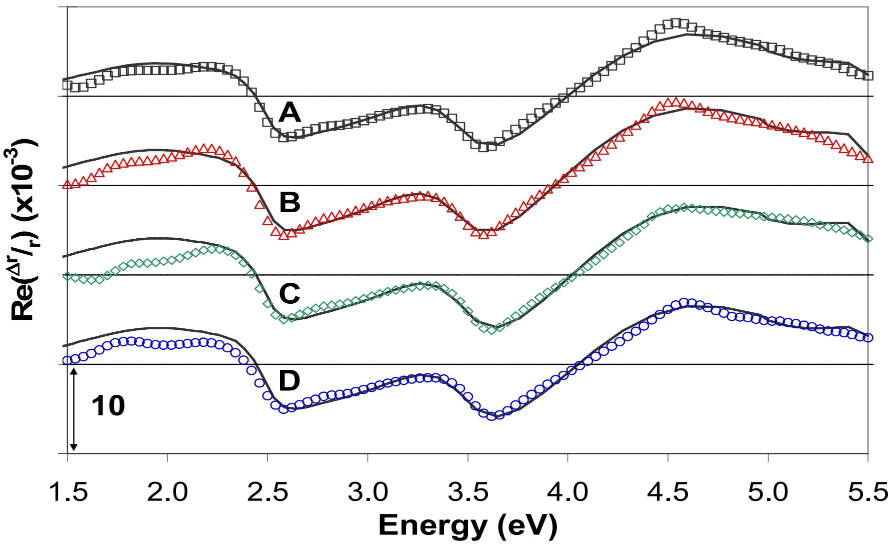

Figure 4.8 (a): RA Spectra of the four Au(110) surfaces prior to the addition of different concentrations of adenine at A 0.1 μM (□), B 0.5 μM (△), C 20 μM (◇) and D 100 μM (○) and their corresponding simulated spectral profiles (black lines). The graphs have been offset on the y-axis for clarity and the horizontal lines define zero RAS intensity for each experiment.

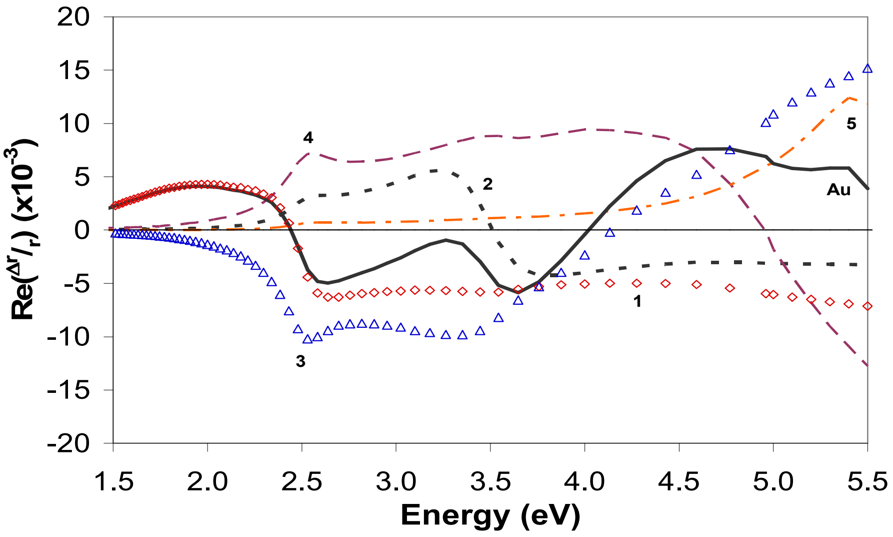

Figure 4.8 (b): Individual contributions to the simulated RAS profile (black line) of the gold surface in the 20 μM concentration experiment using the parameters defined in Table 4.2.

beyond ~ 2.5 eV by molecular adsorption. The analysis of the optical transitions of adenine leads us to expect two closely spaced transitions at 4.6 eV and 4.8 eV within the spectral range of the RAS instrument and a third just outside it at 5.9 eV. It would be surprising if the characteristics of these transitions were not altered by adsorption onto the Au(110)/electrolyte interface and indeed previous studies of molecules adsorbed on Si(001) have suggested that the electronic structure of gas phase molecules as well as the semiconductor bulk wavefunctions are strongly modified by the adsorption process and give rise to new optical finger-prints [69,70]. The changes in the RAS of Au(110) induced by this process show that the molecular transitions make a very broad contribution to the spectrum mediated by the interaction between the dipole transitions in the molecule and the dielectric response of the Au substrate. This interaction can be represented very successfully by the empirical model employed.

A minimum of two additional transitions were required to describe the RAS of the adsorbed adenine compared to that of the clean gold surfaces and in each case

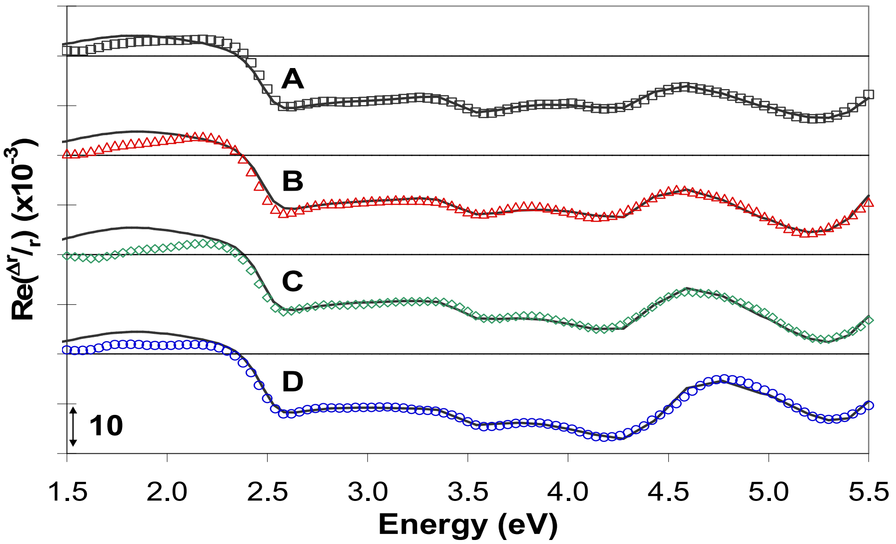

Figure 4.9 (a): RA Spectra of the four different Au surfaces after the addition of A 0.1 µM (□), B 0.5 µM (△), C 20 µM (◇) and D 100 µM (○) adenine with the corresponding simulated RAS profiles (black lines). The graphs have been offset on the y-axis for clarity and the horizontal lines define zero RAS intensity for each experiment.

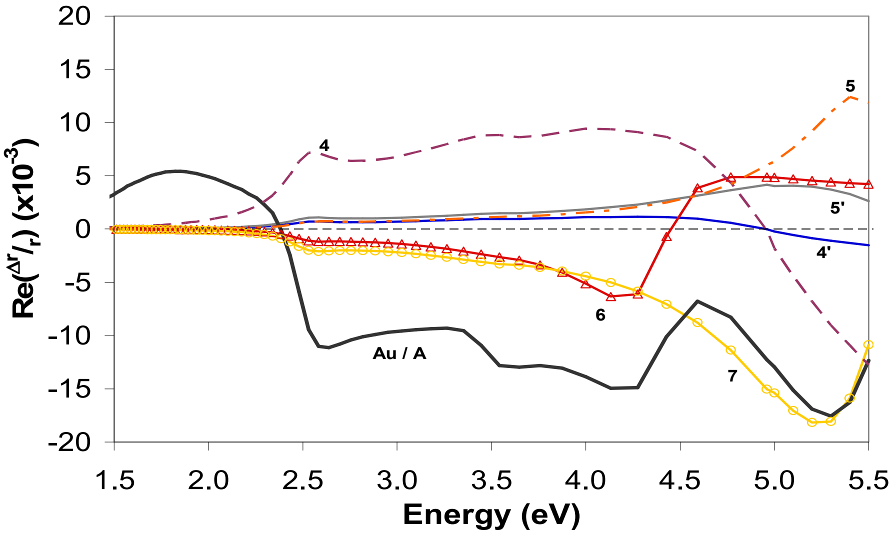

Figure 4.9 (b): Individual contributions to the simulated RAS profile (black line) of the 20 μM concentration experiment highlighting the reduction in intensity of the high energy contributions labelled 4 and 5 from the gold simulations into 4´ and 5´ respectively, coupled with the appearance of the two new contributions from adenine adsorption labelled 6 and 7.

good simulations of the spectra, shown in Figure 4.9 (a), were obtained provided both are polarised along the $[1\bar{1}0]$ direction and that they have energies of 4.38 ± 0.05 eV and 5.54 ± 0.06 eV. The parameters used in these simulations are also shown in Table 4.2. The simulations are similar to those obtained previously by Weightman *et al* [7] and have been achieved by making minor alterations to the line-width (Γ) and intensity (S) (Equation 3.5) of the first transition used in simulating the Au(110) spectra. By contrast, the second transition required its width be halved and its intensity reduced by a factor of approximately 6 while the intensity of the third transition required decreasing by a factor of 5. The fourth and fifth transitions were fitted by radically reducing their intensities and line widths and the two negative features attributable to adenine adsorption required the addition of two extra transitions labelled 6 and 7.

In detail, the reduction in the intensities of the fourth and fifth transitions, which are polarised along the [001] direction, and the addition of the two new transitions polarised along the $[1\bar{1}0]$ direction have the same effect on the RAS;

turning a strong positive signal in the high energy region of the gold spectrum into a strong negative signal for the adsorbed molecules. This can be seen in Figure 4.9 (b) where the contributions made by these two transitions to the simulation of the RAS of adenine/Au(110) obtained using the 20 μM concentration are compared with the contributions made by the two transitions of similar energy, but polarised along [001], to the RAS of Au(110). It is likely that some coupling occurs between the parameters of the fourth and fifth transitions of the simulations of the Au(110) spectra and the two new transitions added to simulate the adenine spectra. Even so it is clear that the adenine solution can be captured by varying the absolute and relative intensities of the additional transitions in the simulations.

The simulations described in Table 4.2 and shown in Figures 4.8, 4.9 and 4.10 establish that the basal planes of the adenine molecules were orientated along the $[1\bar{1}0]$ direction on the Au(110) surface. The energies of the two transitions required to simulate the RAS of the adsorbed adenine are very close to those of the transitions expected for the adenine molecule at 4.56 eV, 4.80 eV and 5.85 eV. One would of course not anticipate being able to distinguish between the contributions of the two low energy transitions in the simulation. However, there is an important difference between the two low energy transitions expected for the adenine molecule in the orientation of their transition dipole moments with respect to the molecular axes. If the molecule was orientated vertically on the Au(110) surface then the difference in the directions of the dipole moments would, in the geometry of the RAS experiment, only affect the relative intensity of the contributions from the two transitions and this difference could not be captured in the simulation. More importantly, the difference in the relative orientations of the two low energy transitions and the 5.85 eV transition, together with the fact that it was necessary to include a significant contribution from both the 4.40 eV and the 5.54 eV transitions in order to simulate the RA spectra of adsorbed adenine, establishes that the basal plane of the molecule was orientated essentially vertically on the Au(110) surface. In light of the above it is possible to conclude that adenine adsorbed on the Au(110) surface in base stacked layers with

TABLE 4.2: Parameters for the Simulated RA Spectra of Au & Au + Adenine.

0.1 µM	Transition	1	2	3	4	5	6	7
	Direction	[001]	[001]	$[1\bar{1}0]$	[001]	[001]	$[1\bar{1}0]$	$[1\bar{1}0]$
Au	ω_t/eV	1.60 ± 0.20	3.44 ± 0.06	3.90 ± 0.07	4.60 ± 0.07	5.65 ± 0.15	…	…
	Γ/eV	1.10 ± 0.20	0.61 ± 0.13	1.90 ± 0.15	2.10 ± 0.15	0.55 ± 0.07	…	…
	S^a	1.00 ± 0.10	0.24 ± 0.03	1.30 ± 0.08	1.27 ± 0.13	0.17 ± 0.01	…	…
Au / A	ω_t/eV	1.60 ± 0.10	3.44 ± 0.07	3.70 ± 0.15	4.65 ± 1.00	5.60 ± 1.00	4.36 ± 0.05	5.55 ± 0.06
	Γ/eV	0.90 ± 0.25	0.30 ± 0.05	1.80 ± 0.20	1.90 ± 0.30	1.90 ± 0.40	0.38 ± 0.10	0.95 ± 0.06
	S^b	1.00 ± 0.10	0.05 ± 0.01	0.36 ± 0.07	0.04 ± 0.02	0.01 ± 0.01	0.08 ± 0.01	0.33 ± 0.04
	Contribution to fitted spectrum	…	…	…	…	…	43.55	124.01

[a,b] Relative intensities. Absolute intensities of transition 1 are 6600 (Au), 6900 (Au/A).

0.5 µM	Transition	1	2	3	4	5	6	7
	Direction	[001]	[001]	$[1\bar{1}0]$	[001]	[001]	$[1\bar{1}0]$	$[1\bar{1}0]$
Au	ω_t/eV	1.60 ± 0.20	3.43 ± 0.06	3.85 ± 0.08	4.60 ± 0.07	5.62 ± 0.14	…	…
	Γ/eV	1.10 ± 0.20	0.62 ± 0.08	1.92 ± 0.15	2.10 ± 0.15	0.55 ± 0.08	…	…
	S^a	1.00 ± 0.11	0.25 ± 0.03	1.33 ± 0.09	1.29 ± 0.14	0.19 ± 0.02	…	…
Au / A	ω_t/eV	1.60 ± 0.10	3.43 ± 0.07	3.70 ± 0.12	4.65 ± 0.70	5.60 ± 1.00	4.36 ± 0.04	5.49 ± 0.06
	Γ/eV	0.90 ± 0.20	0.35 ± 0.08	1.80 ± 0.30	1.90 ± 0.30	1.90 ± 0.40	0.38 ± 0.07	0.90 ± 0.06
	S^b	1.00 ± 0.10	0.04 ± 0.01	0.25 ± 0.08	0.06 ± 0.03	0.10 ± 0.05	0.09 ± 0.01	0.37 ± 0.04
	Contribution to fitted spectrum	…	…	…	…	…	56.45	158.35

[a,b] Relative intensities. Absolute intensities of transition 1 are 7200 (Au), 7900 (Au/A).

20 μM	Transition	1	2	3	4	5	6	7
	Direction	[001]	[001]	$[1\bar{1}0]$	[001]	[001]	$[1\bar{1}0]$	$[1\bar{1}0]$
Au	ω_t/eV	1.60 ± 0.10	3.46 ± 0.05	3.93 ± 0.06	4.60 ± 0.06	5.63 ± 0.15	…	…
	Γ/eV	1.10 ± 0.20	0.61 ± 0.09	1.92 ± 0.15	2.10 ± 0.15	0.54 ± 0.07	…	…
	S[a]	1.00 ± 0.12	0.24 ± 0.03	1.30 ± 0.07	1.27 ± 0.13	0.19 ± 0.02	…	…
Au / A	ω_t/eV	1.60 ± 0.10	3.45 ± 0.10	3.90 ± 0.20	4.65 ± 1.00	5.60 ± 1.00	4.37 ± 0.04	5.55 ± 0.05
	Γ/eV	0.85 ± 0.20	0.33 ± 0.12	2.00 ± 0.40	1.80 ± 0.40	2.00 ± 0.40	0.48 ± 0.10	0.95 ± 0.10
	S[b]	1.00 ± 0.10	0.04 ± 0.01	0.17 ± 0.06	0.11 ± 0.02	0.23 ± 0.07	0.15 ± 0.02	0.45 ± 0.09
	Contribution to fitted spectrum	…	…	…	…	…	96.46	207.59

[a,b] Relative intensities. Absolute intensities of transition 1 are 7300 (Au), 8600 (Au/A).

100 μM	Transition	1	2	3	4	5	6	7
	Direction	[001]	[001]	$[1\bar{1}0]$	[001]	[001]	$[1\bar{1}0]$	$[1\bar{1}0]$
Au	ω_t/eV	1.60 ± 0.09	3.47 ± 0.06	3.93 ± 0.07	4.60 ± 0.05	5.65 ± 0.15	…	…
	Γ/eV	1.10 ± 0.20	0.62 ± 0.09	1.92 ± 0.15	2.15 ± 0.15	0.50 ± 0.09	…	…
	S[a]	1.00 ± 0.08	0.24 ± 0.02	1.26 ± 0.09	1.25 ± 0.11	0.16 ± 0.02	…	…
Au / A	ω_t/eV	1.60 ± 0.15	3.44 ± 0.10	3.90 ± 0.20	4.75 ± 1.00	5.60 ± 1.00	4.43 ± 0.04	5.58 ± 0.10
	Γ/eV	0.90 ± 0.30	0.24 ± 0.15	1.80 ± 0.40	1.80 ± 0.40	1.90 ± 0.40	0.53 ± 0.07	0.80 ± 0.10
	S[b]	1.00 ± 0.11	0.02 ± 0.01	0.29 ± 0.09	0.01 ± 0.01	0.07 ± 0.05	0.24 ± 0.04	0.37 ± 0.04
	Contribution to fitted spectrum	…	…	…	…	…	130.40	166.67

[a,b] Relative intensities. Absolute intensities of transition 1 are 7200 (Au), 7500 (Au/A).

individual molecules orientated vertically on the surface and with the long axis of the molecule orientated along the [1 $\bar{1}$ 0] direction. The data also suggests that the bonding to the Au(110) involves the NH_2 group and possibly also the N(7) site [26,47].

It was then possible to use the relative intensities of the transitions expected to contribute to the RA profile of adenine to explore how the relative contributions of those transitions vary as the molecule rotates within the vertical plane [Figure 4.10]. If adenine is orientated with the NH_2 - C(6) bond vertical to the Au(110) surface, it is then possible to calculate the relative intensity of the three transitions, I, II and III of Table 4.1 as a function of the angle α between the NH_2 - C(6) bond and the normal to the surface. There is agreement, within rather large error margins, on the relative orientations with respect to the molecular axes. Consequently, two calculations were performed; model 1 assuming the values of ϕ for transitions I, II and II are 66°, 19° and -21° [55] and respectively and model 2 assuming these values are 83°, 25° and -45° respectively [51]. Figures 4.11 (a) and 4.11 (b) show how the intensities of the three transitions vary with α in model 1 and model 2 respectively. Since the first two transitions were too close in energy to be distinguished, Figures 4.12 (a) and 4.12 (b)

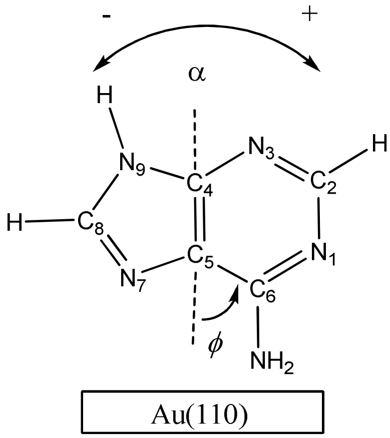

Figure 4.10: Schematic of the adenine molecule defining the angle α. The diagram assumes the molecule is adsorbed vertically on the Au(110) surface with its long axis parallel to the [1 $\bar{1}$ 0] direction.

show how the ratio of the intensity of the third transition to the sum of the intensities of the two low energy transitions vary with α in model 1 and 2 respectively. The large uncertainty in the intensities of the three transitions resulted in a large spread in the predictions of how the relative intensities of the high and low energy transitions vary with the orientation of the molecule on the surface. For completeness it is important to note that it was not physical to consider angles of $\alpha < \sim -35^\circ$ since at this angle the N(7) atom is in contact with the Au(110) surface.

The horizontal lines in Figures 4.12 (a) and 4.12 (b) are the relative intensities of the total contributions that the two adenine transitions make to the observed RA profiles as deduced from fits to the spectra [Table 4.2] of the 0.1 μM & 0.5 μM (grey dashed line), 20 μM (yellow dashed line) and 100 μM concentrations (orange line). The results from simulating the spectra obtained from the two lowest concentrations are indistinguishable. In principle the intersections of these lines with the curves from the model will indicate the orientation, α, of the molecule on the surface. However the wide margin of error in the expected intensities of the transitions gave rise to such

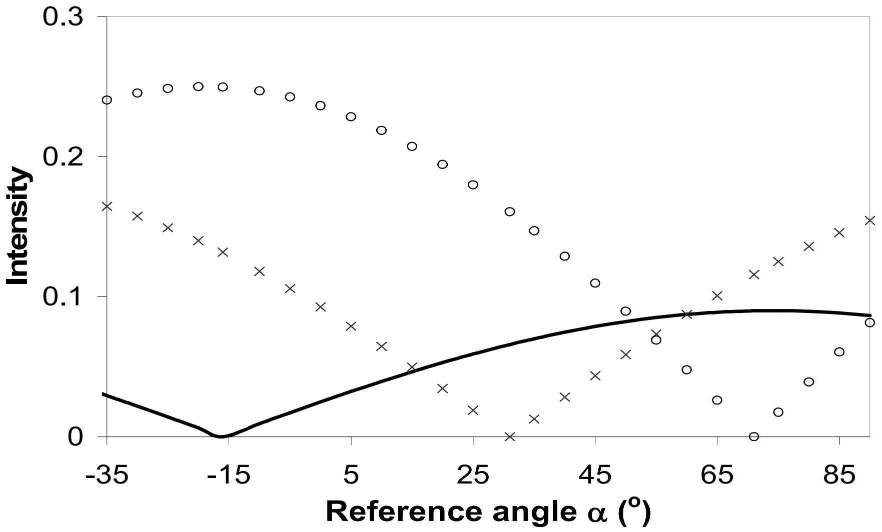

Figure 4.11 (a): Plots of the intensity of Transition I (black line), Transition II (x) and Transition III (O) as a function of the angle α between the NH_2 - C(6) bond and the normal to the surface using the polarisations of reference [55].

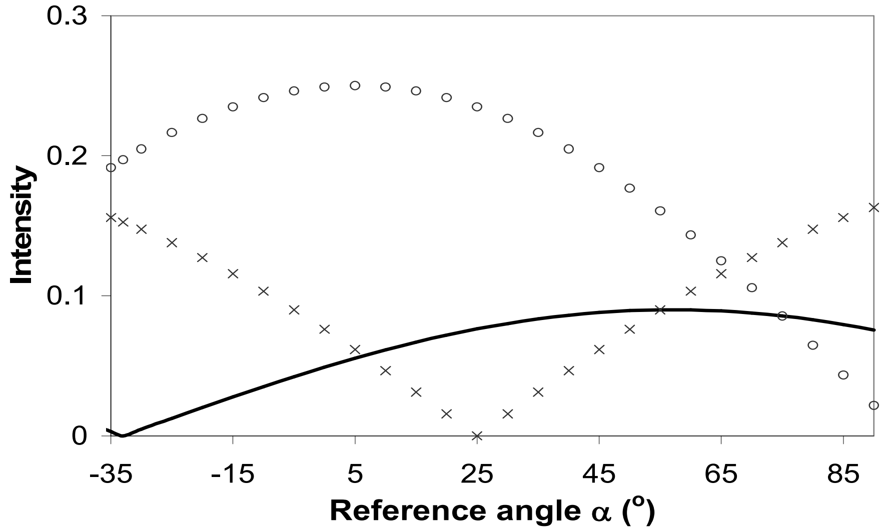

Figure 4.11 (b): Plots of the intensity of Transition I (black line), Transition II (x) and Transition III (O) as a function of the angle α between the NH_2 - C(6) bond and the normal to the surface using the polarisations of reference [51].

large uncertainties in the results obtained from the models that it was not possible to deduce molecular orientation from this analysis. Despite this the above analysis showed that the relative contribution of the high and low energy adenine transitions to the RA spectra was very sensitive to the orientation of the molecule and that the variation in the spectral profiles obtained from the adsorption from the different concentrations could be explained by variations in the angle α. For example if the central values of the intensity ratios deduced from model 2 are considered then the intersection with the ratio of the intensity of the two high energy transitions given by the simulation of the RAS obtained for the most concentrated solution is consistent with α = -35° i.e. the N(7) atom touching the Au(110) surface as found in previous literature [26,47]. A change in orientation to α = 20° would then yield the RAS profile obtained from the least concentrated solution.

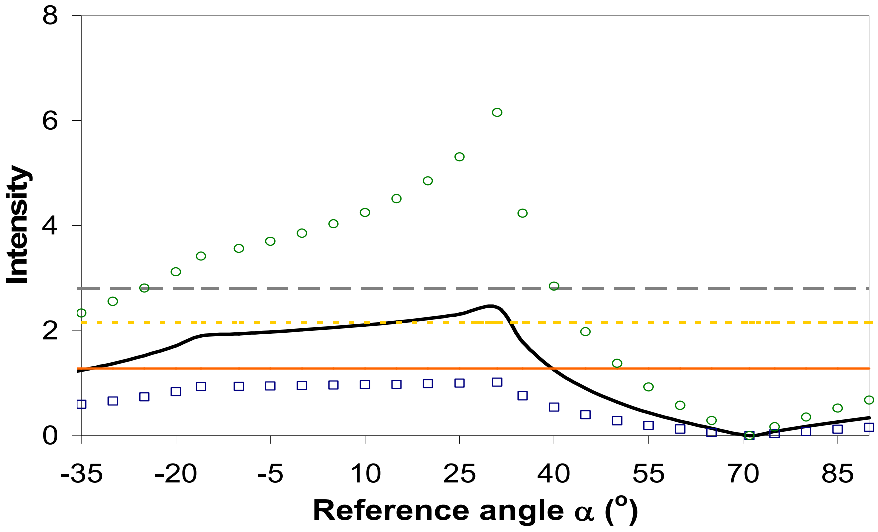

Figure 4.12 (a): Simulation showing the ratio of Transition III / (Transition I + Transition II) (solid curve) varying as a function of α between the NH_2 - C(6) bond and the normal to the surface using experimental transition strengths from [53]. The upper (○) and lower (□) error boundaries arise from the uncertainty in the transition strengths, f, given in Table 4.1.

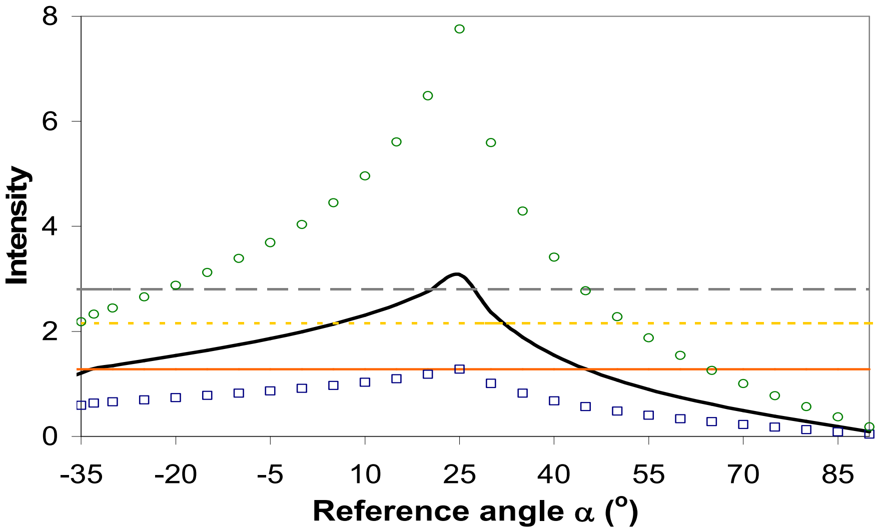

Figure 4.12 (b): Simulation showing the ratio of Transition III / (Transition I + Transition II) (solid curve) varying as a function α between the NH_2 - C(6) bond and the normal to the surface using experimental transition strengths from [49]. The upper (○) and lower (□) error boundaries arise from the uncertainty in the transition strengths, f, given in Table 4.1.

4.6: Simulation of Sub-Saturation Adenine Spectrum

It is clear from Figure 4.3 that the RA profiles obtained from the two intermediate concentrations are very similar and differ from the RAS obtained from the lowest concentration. Since the former corresponded to saturation coverage of adenine while the latter resulted from sub-saturation coverage, the likely explanation for these spectral differences originates from the fact that at sub-saturation coverage there was a significant contribution to the RAS from areas of the surface with no adenine adsorption. If this was so, and if the orientation of the adenine was the same at both saturation and sub-saturation coverage, which would be expected if the molecules adsorbed by forming rows of close stacked bases, then it should be possible to represent the observed RA profile at sub-saturation coverage as a linear sum of the profiles of the clean Au(110) surface and the RAS obtained at saturation coverage. This calculation is demonstrated in Figure 4.13.

The simulation was successfully achieved using the equation:

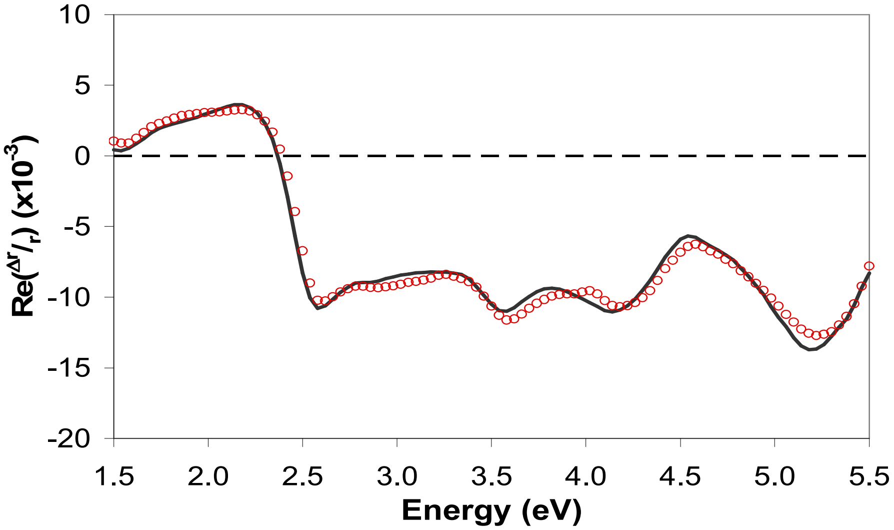

Figure 4.13: RA Spectrum of Au(110) + 0.1 μM adenine (○) and its simulation (black line).

$$\text{RAS }\{\text{Au}(110) + 0.1\ \mu\text{M}\} = \text{A}\{\text{Au}(110)\} + \text{B}\{\text{Au}(110) + 0.5\ \mu\text{M}\}$$

where A and B are independent multiplicity factors and A = 0.07 and B = 0.9. This result indicates that the adsorption of adenine from the least concentrated solution yielded a surface of 93% adsorbed adenine and 7% bare Au(110) with the adenine adopting the same structure as that obtained for the experiment which used a concentration of 0.5 μM. The success of the linear summation of RA profiles shown in Figure 4.13 is to be expected since the parameters required to capture the contribution of the two adenine transitions to the RAS obtained from the two lowest concentrations were essentially identical as displayed in Figure 4.12 (b).

4.7: The Effect of Electrode Potential on Adenine Adsorption

The detailed RA profile of the Au(110)/electrolyte interface depends upon the electrode potential in the range in which the Au(110) surface is known to adopt different surface reconstructions. This is discussed in depth in Chapter 3 and while other studies have also investigated this phenomenon [10,16,34-36] an unambiguous conclusion as to the specific effects molecular adsorption have upon these reconstructions and hence the associated RA profile has not yet been made. Therefore analysis is limited to a consideration of the differences between the RAS of the molecules adsorbed on the Au(110) surface and that of the clean gold substrate. It is implicit in this approach that any changes in the RAS of the Au(110) caused by adsorption are small compared to the contribution to the RAS made by the molecules. There is no way of checking this assumption empirically yet it has proved very useful [8,9], although two previous studies have detailed how the electronic structure of gas phase molecules were strongly affected by adsorption processes [69,70].

The most concentrated adenine solution was used in all potential variation experiments and the subtractions are shown in Figure 4.14 when adenine was added to

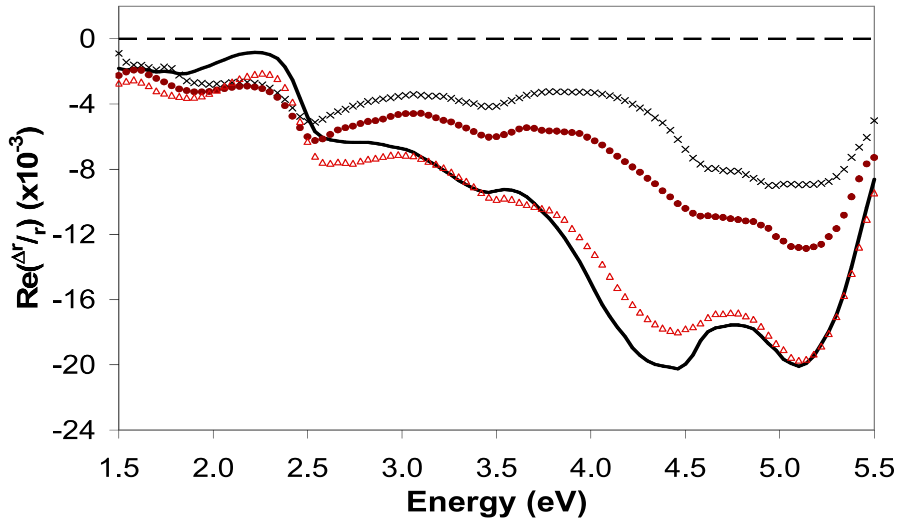

Figure 4.14 (a): RA Spectra of 100 μM of adenine added at -0.6 V obtained after subtraction of corresponding Au(110) at -0.6 V (X), -0.4 V (●),-0.2 V (△) and 0.0 V (black line) vs. SCE. A through analysis of the modification to the spectral profile of Au(110) as a function of applied potential is showed in Chapter 3.9. It is unclear still as to the specific effects of molecular adsorption on surface reconstructions.

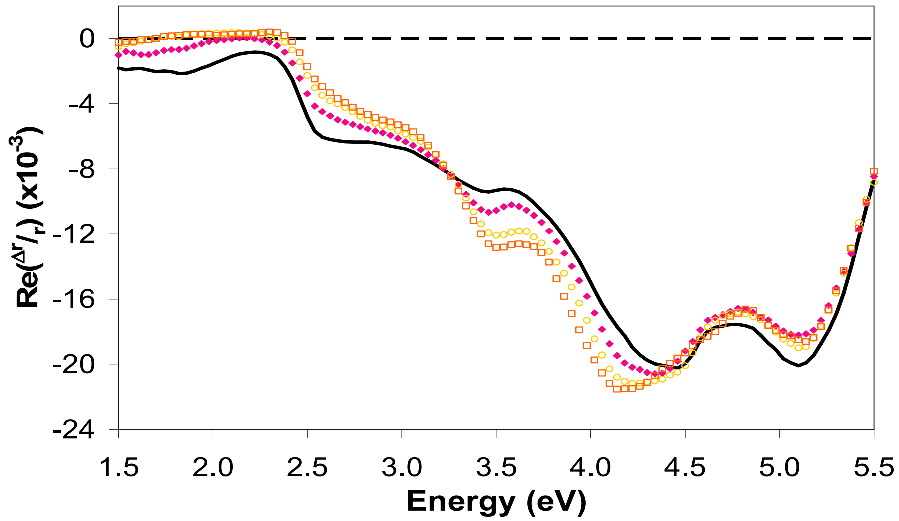

Figure 4.14 (b): RA Spectra of 100 μM of adenine added at -0.6 V obtained after subtraction of corresponding Au(110) at 0.0 V (black line), +0.2 V (◆), +0.4 V (○) and +0.6 V (□) vs SCE.

the cell with the potential held at -0.6 V and then varied in the sequence -0.6 V to +0.6 V in 0.2 V steps. Figure 4.15 shows the spectra obtained when adenine was added to the cell with the potential at 0.0 V and varied from 0.0 to +0.6 V [Figure 4.15 (a)] and then 0.0 to -0.6 V [Figure 4.15 (b)]. The spectra shown in Figure 4.16 were acquired with the solution of adenine added to the cell with the potential held at +0.6 V and then varied in the sequence +0.6 V to -0.6 V in 0.2 V steps.

Figure 4.14 (a) shows there was a modest increase in the RAS after adenine was added to the cell at -0.6 V indicating that limited molecular adsorption occurred at the interface at a negative potential and that the adsorption rate increased as the potential was made more positive. Of the two negative features identified earlier at ~ 4.2 and 5.3 eV the second was more intense in the negative potential range. The two features had equal intensity at 0.0 V and as the potential turned positive the 4.2 eV feature became the most intense [Figure 4.14 (b)].

The addition of adenine to the cell at 0.0 V [Figure 4.15 (a)] gave rise to a strong RA signal comparable to the results already described for saturation coverage.

At first, the RA spectrum was almost identical to that observed when the

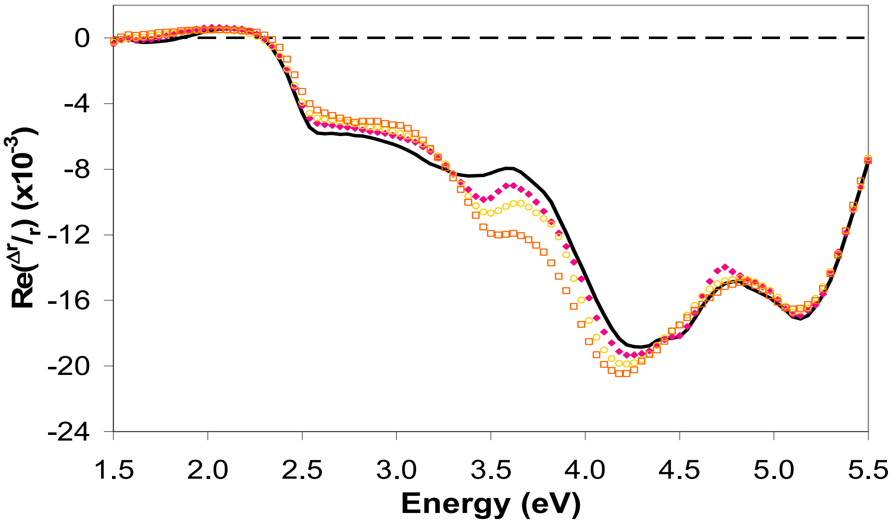

Figure 4.15 (a): RA Spectra of 100 μM of adenine added at 0.0 V obtained after subtraction of corresponding Au(110) at 0.0 V (black line), (◆), +0.4 V (○) and +0.6 V (□) vs SCE.

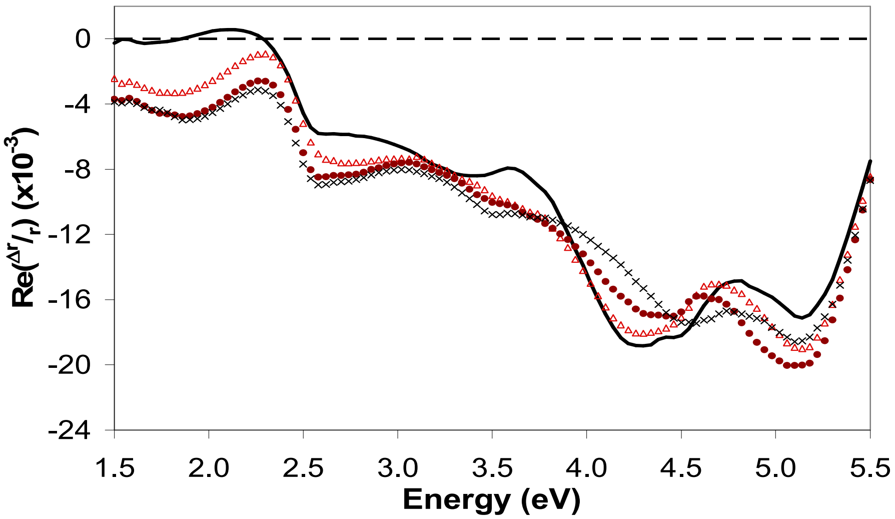

Figure 4.15 (b): RA Spectra of 100 μM of adenine added at 0.0 V obtained after subtraction of corresponding Au(110) at 0.0 V (black line), -0.2 V (△), -0.4 V (●) and -0.6 V(X) vs. SCE.

molecule was added at -0.6 V and the potential increased to 0.0 V. Moreover, as the potential was increased to +0.6 V the small changes that occurred in line shape were extremely similar in development to those found for this voltage range in the previous experiment. In spite of this, when the applied voltage was reduced in sequence from 0.0 V to -0.6 V [Figure 4.15 (b)] the RA profile did not return to analogous values found for this potential regime when the solution was added at -0.6 V. Instead, the total RAS intensity across the energy spectrum remained approximately the same as that found at 0.0 V though this was accompanied by changes in line shape. The line shape modifications do however mirror those found in this potential range when the solution was added at -0.6 V in that at more negative voltages the peak at 5.3 eV was more intense than that at 4.2 eV.

Figure 4.16 shows the effect of adding the solution at an applied potential of +0.6 V and then reducing the potential in 0.2 V increments from +0.6 to -0.6 V. Initially the RAS signal almost matched that acquired in the earlier experiments for the positive potential range and the minor changes in line shape that occurred as the potential was reduced towards zero mirrors those found earlier. When the applied

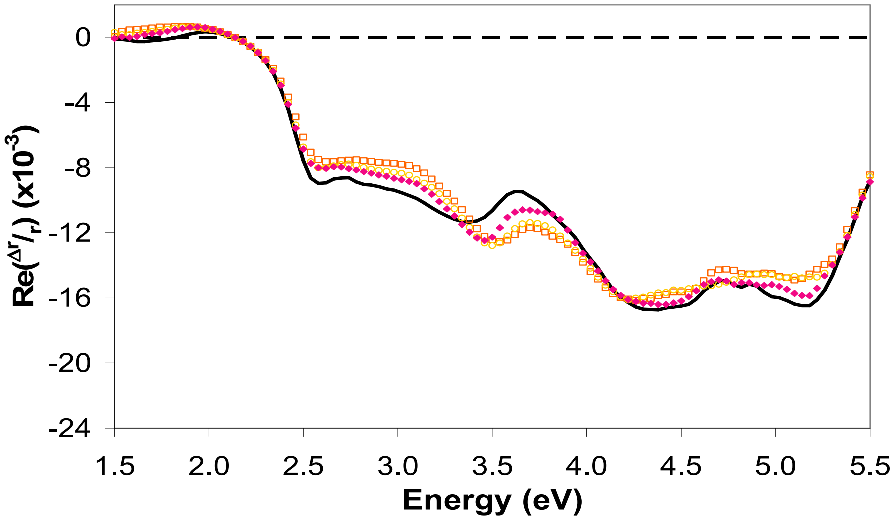

Figure 4.16 (a): RA Spectra of 100 μM of adenine added at 0.6 V obtained after subtraction of corresponding Au(110) at (a) +0.6 V (□), +0.4 V (○), +0.2 V (◆), 0.0 V (black line).

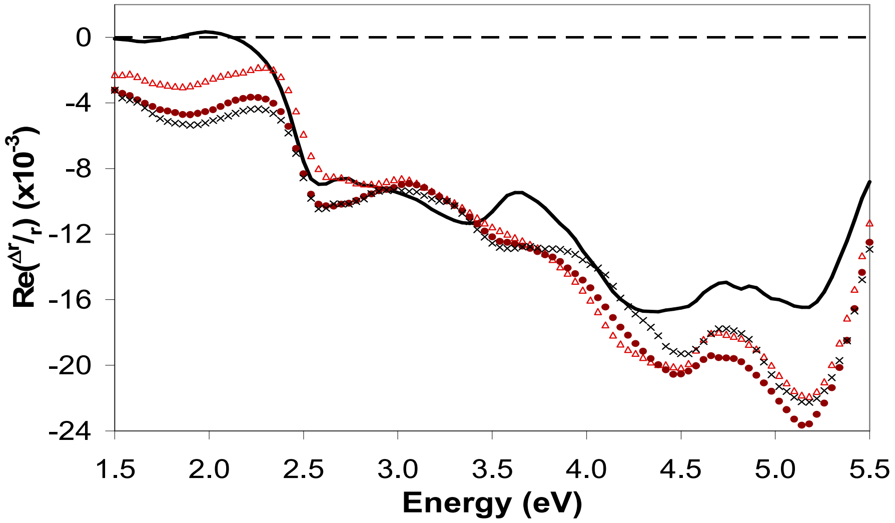

Figure 4.16 (b): RA Spectra of 100 μM of adenine added at 0.6 V obtained after 0.0 V (black line), -0.2 V (△), -0.4 V (●), -0.6 V (X) vs. SCE.

potential was taken through the negative potential regime, the results were similar though the changes slightly more pronounced to those obtained for this range of potentials when the solution was added at 0.0 V. More specifically the 5.3 eV became more intense than the 4.2 eV feature at negative potentials.

A clear result from the studies of the dependence of the RAS signal on the potential applied to the Au(110) electrode is that at 0.0 V and all positive potentials the total intensity across the spectrum is the same to within the systematic errors arising from the variation in the preparation of the Au(110) surfaces and that at positive potentials the 4.2 eV feature is the most intense while at negative potentials the 5.3 eV feature is the more intense.

A comparison of the nucleic acid base adenine with both ss and ds DNA, resulted in differing adsorption behaviours due to potential variation. Both ss and ds DNA did not adsorb on the Au(110)/electrolyte interface at -0.6 V and both molecules desorbed at this potential following adsorption at more positive potentials [9]. It is found in this work that the isolated base adenine adsorbed at -0.6 V though at significantly less than saturation coverage. Furthermore, once saturation coverage was reached by adsorption at more positive potentials the adenine did not then desorb when the potential was lowered to -0.6 V although differences were apparent in the relative intensity of the 4.2 eV and 5.3 eV features between negative and positive potentials. The difference in the behaviour of adenine and DNA is probably due to the absence of the negatively charged phosphate groups in the former since these are expected to be repelled from the surface at negative potentials. For applied potentials of 0.0 V and at positive potentials adenine established a saturation coverage of the surface irrespective of the applied potential at which the solution was added to the cell.

It has been determined that at least two strong transitions of the adenine molecule contributed to the RAS of adsorbed adenine on Au(110). What's more the plane of the molecule adopted an essentially vertical orientation on the surface with its long axis parallel to the $[1\bar{1}0]$ direction. Since there is a significant difference in the directions of the dipole moment transitions with respect to the molecular axes, they are expected to make different contributions to the intensity of the RAS signal as the orientation of the molecules is modified. It is likely that the small changes in the relative intensity of the 4.2 eV and 5.3 eV features as the applied potential was made either positive or negative arose from the changes in the orientation of the molecules on the surface. The more significant differences in the relative intensity of these two features in the RA spectra obtained following adsorption from the most concentrated and least concentrated solutions could therefore also arise from variations in the molecular orientation in the vertical plane. The results of Figure 4.5 together with the analysis in terms of the phenomenological model described formerly demonstrate that in each case the plane of the adenine molecule was orientated in an essentially vertical direction parallel to the $[1\bar{1}0]$ axes of the Au(110) surface. However, a rotation of this plane about an axis parallel to the [001] direction in the Au surface could account for the differences observed between the RAS of Figures 4.5 (a) and 4.5 (b). RAS has been shown to be sensitive to similar changes in the orientation of stacked planes of 9-anthracene carboxylic acid (9ATC) on the Cu(110) surface [14].

4.8: Effect of pH Variation in the Supporting Electrolyte

In order to investigate the influence of the pH of solution on the adsorption of adenine on Au(110), experiments were performed in which adenine concentrations of 100 μM were added to the electrochemical cell, with the gold electrode held at 0.0 V, containing 0.1 M H_2SO_4 and 0.1 M KOH to produce pH's of 1.2 and 12.8 respectively. These results together with the data obtained at pH 7.1 [Figure 4.3] are shown in Figure 4.17. A larger variation in the RAS of the initial surfaces was obtained in these experiments [Figure 4.17 (a)] than in those in which the concentration of the solution was varied. Some of this variation was probably due to a sensitivity of the Au(110) surface to the pH of the electrolyte. The results obtained from the addition of an adenine solution of 100 μM to the cell with electrolytes of varying pH are shown in Figure 4.17 (b) and the results for the RAS of adsorbed adenine found by subtracting

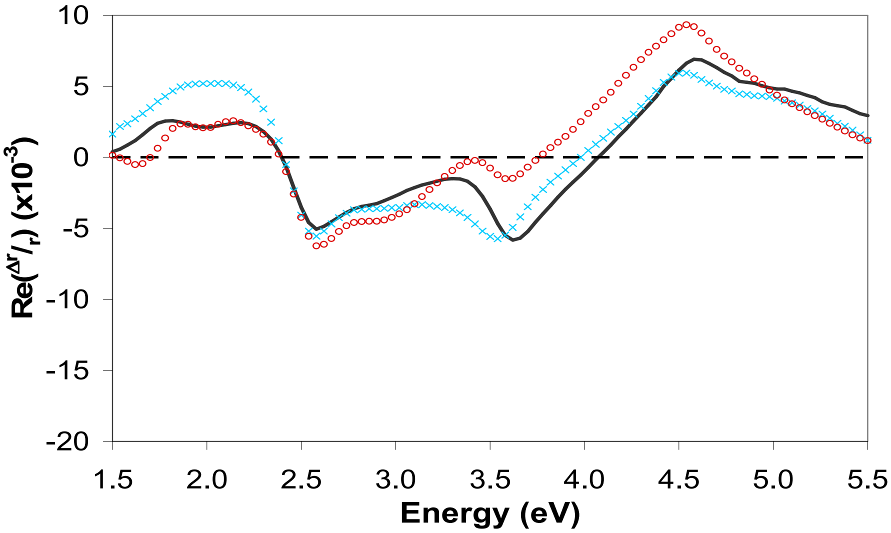

Figure 4.17 (a): RA Spectra of Au(110) at pH 1.2 (X), pH 7.1 (black line) and pH 12.8 (○).

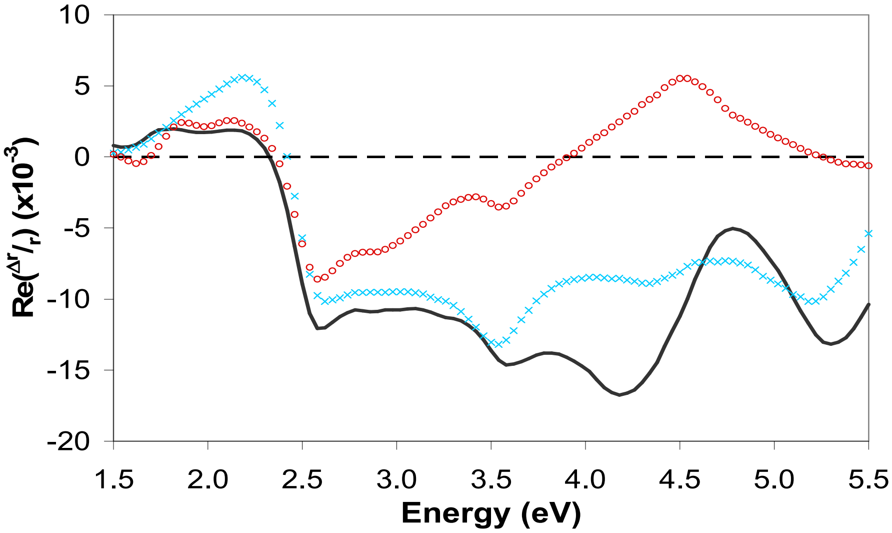

Figure 4.17 (b): RA Spectra of Au(110) + 100 μM adenine at pH 1.2 (X), pH 7.1 (black line) and pH 12.8 (○).

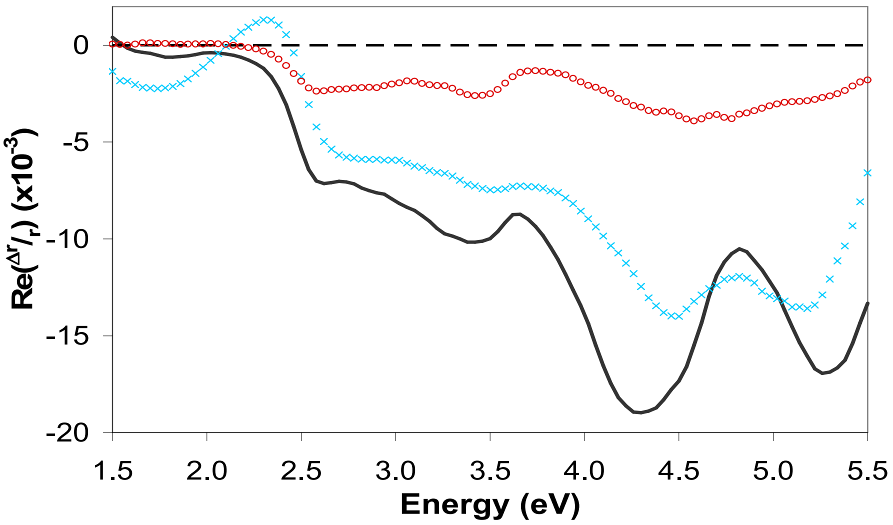

Figure 4.17 (c): Adenine spectra at the three pH's obtained by subtraction of the corresponding Au(110) spectra.

the RAS of the initial surfaces are shown in Figure 4.17 (c).

There was negligible change in the RAS of Au(110) when the adenine solution was added at pH 12.8 indicating that adenine did not adsorb on the Au(110) surface held at 0.0 V as observed in Figure 4.17 (c). This could be due to the negative charge on the N(9) atom at this pH since it is clear from the results shown in Figure 4.14 (a) that neutral molecules only adsorb weakly on Au(110) held at negative potentials and that the adsorption increased as the applied potential was made more positive. Figure 4.18 depicts how the protonation of the adenine molecule varies as the pH of the surrounding environment changes. Also noted are the pH values at which 50% of the molecules are protonated (pK_a) i.e at pH 4.2, 50% of the molecules present are in their neutral form and 50% are positively charged on the N(1) site. When adenine was added to the solution at pH 1.2, the overall intensity of the RAS of adsorbed adenine was reduced across the spectral range relative to that obtained at pH 7.1. The likely explanation for this difference is that at this pH there is a positive charge on the N(1) site and this disrupts the π stacking interactions between molecules.

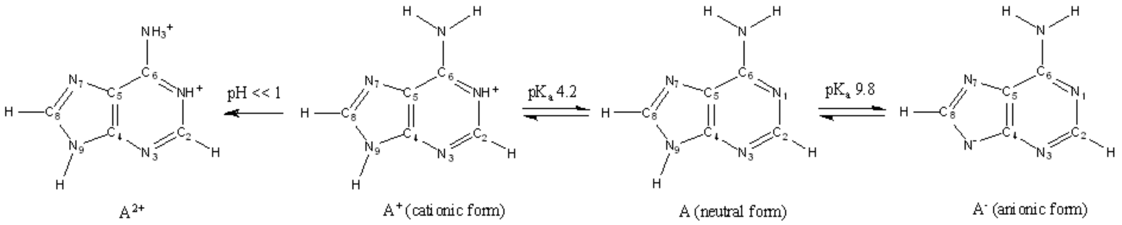

Figure 4.18: Variation of protonation of the adenine molecule as a function of pH.

4.9: Summary

It has been shown that the three most concentrated solutions gave rise to a saturation adenine coverage of the Au(110) surface. This is consistent with the results of Martins *et al* [24]. The least concentrated solution did not produce this saturation however, the success of the simulation shown in Figure 4.13 established that at this coverage, the surface consisted of regions of bare Au(110) along with regions of adsorbed adenine in which the orientation of the molecules is the same as that resulting from adsorption from the lowest concentration that resulted in a saturation coverage.

The variation of the RAS intensity with the polarisation direction of the incident light of the adenine structures resulting from sub-saturation and saturation coverage established that in both cases the optical axes of the molecules were coincident with those of the Au(110) substrate. That this is also true for adsorbed AMP together with the similarity of the RAS of adsorbed AMP and adenine indicated that for both molecule the adsorption occurred through the NH_2 and possibly also the N(7) sites.

In spite of disagreements in detailed results, the analysis of experimental and theoretical studies on the optical spectra of adenine established that at least two transitions contributed to the RAS in this spectral region and that their respective transition moment directions were significantly different. The analysis of the RAS of the Au(110) substrate and of the adenine adsorbed on Au(110) in terms of a potential model showed that in all cases the adenine contribution to the RAS could be captured in simulations that required the inclusion of two high energy transitions, polarised along $[1\bar{1}0]$ directions. The energies of these transitions are in good agreement with those expected from previous work. The expectation that there will be a significant difference in the orientation of these transitions with respect to the axes of the molecule coupled with the observation the molecular axes are aligned along the optical axes of the substrate resolved that the adenine molecules are orientated with the plane of the base normal to the surface with their long axes along $[1\bar{1}0]$ directions. This, together with the known tendency for adenine to adopt a base stacking configuration suggests that adenine forms base stacked layers the orientation of which is determined by the substrate.

An analysis of the dependence of the relative intensity of the two adenine transitions on the angle α, between the normal to the Au(110) surface and the short axis of the molecule, shows that the dependence of the RA profile on the adsorption from solutions of different concentration could arise from variations in the orientation of the base stacked layers on the Au(110) surface. The dependence of the RAS on the potential applied to the electrode could have a similar origin. Unfortunately, the uncertainties in the experimental results for the relative intensities of the various adenine transitions are too great for this analysis to yield precise results for these variations in molecular orientation and should be noted as the crucial focus of future work.

Finally it is suggested that at a high alkaline pH of 12.8, adenine does not adsorb on the subject interface held at 0.0 V and that the changes that occurred in the RAS of adenine adsorbed at such interfaces at pH 1.2 are caused by the positive charge on the N(3) site disrupting the π stacking interactions between molecules.

4.10: References

[1] J. Lipkowski and L. Stolberg, *Adsorption of Molecules at Metal Electrodes*, edited by

J. Lipkowski and P. N. Ross (VCH, New York, 1992)

[2] C. Buess-Herman, *Prog. Surf. Sci.* **46**, 335 (1994)

[3] H. Kinoshita, S. D. Christian and G. Dryhurst, *J. Electroanal. Chem.* **83**, 151 (1977)

[4] A. Rodger and B. Nordén, *Circular Dichroism and Linear Dichroism*, (Oxford University Press, Oxford, 1997)

[5] *Imaging of Surfaces and Interfaces*, edited by J. Lipkowski and P. N. Ross (Wiley-VCH, New York, 1999)

[6] J. P. Rabe, *Ultramicroscopy* **42-44**, 41 (1992)

[7] P. Weightman, G. J. Dolan, C. I. Smith, M. C. Cuquerella, N. J. Almond, T. Farrell, D. G. Fernig, C. Edwards and D. S. Martin, *Phys. Rev. Lett.* **96**, 086102 (2006)

[8] R. LeParc, C. I. Smith, M. C. Cuquerella, R. L. Williams, D. G. Fernig, C. Edwards, D. S. Martin and P. Weightman, *Langmuir* **22**, 3413 (2006)

[9] M. C. Cuquerella, C. I. Smith, D. G. Fernig, C. Edwards and P. Weightman, *Langmuir* **23**, 2078 (2007)

[10] P. Weightman, D. S. Martin, R. J. Cole and T. Farrell, *Rep. Prog. Phys.* **68**, 1251 (2005)

[11] P. Weightman, *phys. stat. sol. (a)* **188**, 1443 (2001)

[12] D. S. Martin and P. Weightman, *Thin Solid Films 455/6*, 752 (2004)

[13] J.R. Power, P. Weightman, S. Bose, A. I. Shkrebtii and R. Del Sole, *Phys. Rev. Lett.* **80**, 3133 (1998)

[14] B. G. Frederick, J. R. Power, R. J. Cole, C. C. Perry, Q. Chen, S. Haq, Th. Bertrams, N. V. Richardson and P. Weightman, *Phys. Rev. Lett.* **80**, 4490 (1998)

[15] B. G. Frederick, R. J. Cole, J. R. Power, C. C. Perry, Q. Chen, N. V. Richardson, P. Weightman, C. Verdozzi, D. R . Jennison, P. A. Schultz and M. P. Sears, *Phys. Rev. B* **58**, 10883 (1998)

[16] B. Sheriden, D. S. Martin, J. R. Power, S. D. Barrett, C. I. Smith, C. A. Lucas, R. J. Nichols and P. Weightman, *Phys. Rev. Lett.* **85**, 4618 (2000)

[17] C. I. Smith, A. J. Maunder, C. A. Lucas, R. J. Nichols and P. Weightman, *J. Electrochem. Soc.* **150**, E233 (2003)

[18] C. I. Smith, G. J. Dolan, T. Farrell, A. J. Maunder, D. G. Fernig, C. Edwards and P. Weightman, *J. Phys.: Condens. Matter* **16**, S4385 (2004)

[19] C. I. Smith, N. J. Almond and P. Weightman, *J. Electrochem. Soc.* **154**, F90 (2007)

[20] V. Brabec, M. H. Kim, S. D. Christian and G. Dryhurst, *J. Electroanal. Chem.* **100**, 111 (1979)

[21] C. Prado, I. Navarro, M. Rueda, H. François and C. Buess-Hermann, *J. Electroanal. Chem.* **500**, 356 (2001)

[22] A. P. M. Camargo, H. Baumgärtel and C. Donner, *Phys. Chem. Comm.* **5**, 151 (2002)

[23] C. Prado, F. Prieto, M. Rueda, J. Feliu and A. Aldaz, *Electrochim. Acta* **52**, 3168 (2007)

[24] A. Martins, A. Queirós and F. Silva, *Chem. Phys. Chem.* **6**, 1056 (2005)

[25] M. Preuss, W. G. Schmidt and F. Bechstedt, *Phys. Rev. Lett.* **94**, 236102 (2005)

[26] E. Rauls, S. Blankenburg and W. G. Schmidt, *Surf. Sci.* **602**, 2170 (2008)

[27] M. Preuss and F. Bechstedt, *Surf. Sci.* **602**, 1643 (2008)

[28] Q. Chen, D. J. Frankel and N. V. Richardson, *Langmuir* **18**, 3219 (2002)

[29] S. D. Silaghi, M. Friedrich, C. Cobet, N. Esser, W. Braun and D. R. T. Zahn, *phys. stat. sol. (b)* **242**, 3047 (2005)

[30] S. D. Silaghi and D. R. T. Zahn, *Appl. Surf. Sci.* **252**, 5462 (2006)

[31] C. I. Smith, *Private communication*

[32] K. Takamura, A. Mori and F. Watanabe, *Bioelectrochem.* **8**, 125 (1981)

[33] K. Takamura, A. Mori and F. Watanabe, *J. Electroanal. Chem.* **102**, 109 (1979)

[34] V. Mazine, Y. Borensztein, L. Cagnon and P. Allongue, *phys. stat. sol. (a)* **175**, 311 (1999)

[35] V. Mazine and Y. Borensztein, *Phys. Rev. Lett.* **88**, 147403 (2002)

[36] P. Weightman, C. I. Smith, D. S. Martin, C. A. Lucas, R. J. Nichols and S. D. Barrett, *Phys. Rev. Lett.* **92**, 199707 (2004)

[37] D. S. Martin and P. Weightman, *J. Phys.: Condens. Matter* **14**, 675 (2002)

[38] P. Weightman, D. S. Martin and A. Maunder, *J. Electron Spectroscopy and Related Phenomena* **114-6**, 1069 (2001)

[39] D. S. Martin, A. Maunder and P. Weightman, *Phys. Rev. B* **63**, 155403 (2001)

[40] D. S. Martin, A. M. Davarpanah, S. D. Barrett and P. Weightman, *Phys. Rev. B* **62**, 15417 (2000)

[41] H-X. Zhou, G. Rivas and A. P. Minton, *Annu. Rev. Biophys.* **37**, 375 (2008)

[42] R. J. Cole and B.F. Macdonald, *Appl. Phys. Lett.* **80**, 3527 (2002)

[43] B. F. Macdonald, J. S. Law and R. J. Cole, *J. Appl. Phys.* **93**, 3320 (2002)

[44] N. J. Tao, J. A. DeRose and S. M. Lindsay, *J. Phys. Chem.* **97**, 910 (1993)

[45] T. Boland and B. D. Ratner, *Langmuir* **10**, 3845 (1994)

[46] J. Isaksson, S. Acharya, J. Barman, P. Cheruku and J. Chattopadhyaya, *Biochemistry* **43** 15996 (2004)

[47] Y-J. Xiao, Y-F. Chen and X-X. Gao, *Spectrochim Acta* A **55**, 1209 (1999)

[48] Y. Matsuoka and B. Nordén, *J. Phys. Chem.* **86**, 1378 (1982)

[49] L. B. Clark, *J. Phys. Chem.* **93**, 5345 (1989)

[50] J. D. Petke, G. M. Maggiora and R. E. Christoffersen, *J. Am. Chem. Soc.* **112**, 5452 (1990)

[51] L. B. Clark, *J. Phys. Chem.* **94**, 2873 (1990)

[52] A. Volosov and R. W. Woody, *J. Phys. Chem.* **96**, 4845 (1992)

[53] N. Sreerama, R. W. Woody and P. R. Callis, *J. Phys. Chem.* **98**, 10397 (1994)

[54] M. P. Fülscher, L. Serrano-Andrés and B. O. Roos, *J. Am. Chem. Soc.* **119**, 6168 (1997)

[55] A. Holmén, A. Broo, B. Albinsson and B. Nordén, *J. Am. Chem. Soc.* **119**, 12440 (1997)

[56] A. Broo and A. Holmén, *J. Phys. Chem. A* **101**, 3589 (1997)

[57] A. C. Borin, L. Serrano-Andrés, M. P. Fülscher and B. O. Roos, *J. Phys. Chem. A* **103**, 1838 (1999)

[58] B. Mennucci, A. Toniolo and J. Tomasi, *J. Phys. Chem. A* **105**, 4751 (2001)

[59] A Tsolakidis and E. Kaxiras, *J. Phys. Chem. A* **109**, 2373 (2005)

[60] R. F. Stewart and L. H. Jensen, *J. Chem. Phys.* **40**, 2071 (1964)

[61] C. A. Sprecher and W. C. Johnson Jr., *Biopolymers* **16**, 2243 (1977)

[62] W. C. Brunner and M. F. Maestre, *Biopolymers* **14**, 555 (1975)

[63] J. C. Sutherland and K. Griffin, *Biopolymers* **23**, 2715 (1984)

[64] T. Yamada and H Fukutome, *Biopolymers* **6**, 43 (1968)

[65] L. B. Clark, *J. Phys. Chem.* **99**, 4466 (1995)

[66] H. Devoe and I. Tinoco Jr., *J. Mol. Biol.* **4**, 500 (1962)

[67] N. P. Blanchard, C. I. Smith, D. S. Martin, D. J. Hayton, T. E. Jenkins and P. Weightman, *phys. stat. sol. (c)* **0**, 2931 (2003)

[68] R. J. Cole, B. G. Frederick and P. Weightman, *J. Vac. Sci. Technol. A* **16**, 3088 (1998)

[69] A. Hermann, W. G. Schmidt and F. Bechstedt, *J. Phys. Chem. B* **109**, 7928 (2005)

[70] A. Hermann, W. G. Schmidt and F. Bechstedt, *Phys. Rev. B* **71**, 153311 (2005)

[*] Concentrations are calculated using the Beer Lambert Law which states that Absorption = εcl where Abs is the molecular absorption, ε the extinction coefficient (13400 cm^{-1}), c the concentration and l the path length of the cell in which the solution is placed to determine concentration (usually 1 cm).

Chapter 5: RAS of Alkanethiol Adsorption at Au(110)/liquid Interfaces

The following chapter presents the first investigation using RAS to investigate the adsorption kinetics of decanethiol onto a Au(110) single crystal in a ethanol environment. The changes in contributions to the RA signal as coverage increases have been used to monitor the adsorption of decanethiol and these changes are understood in terms of the behaviour of the molecule. A conclusion is made as to whether molecular orientation varies as surface saturation is reached and the orientation of the molecule with respect to the substrate axes.

5.1: Introduction

The formation of a stable self assembled monolayer by alkanethiols is invaluable in the understanding of the adsorption behaviour of biological molecules on well characterised metal substrates since the sulphur headgroup, hydrophobic alkyl chain and methyl group termination, which result in weak chain–chain/headgroup–chain reactions, provide a robust predominantly 2-dimensional structure on which other biologically important molecules such as DNA and amino acids can be assembled [1]. Although the precise preferential binding of such headgroups to allow film growth to proceed is yet to be established, it is generally thought the S–H bond is broken to allow the formation of a Au–S covalent bond in the case of adsorption on gold [2]. While other groups have favoured an alternative explanation in that the formation of a disulphide bond has been detected [3,4]. The structure and adsorption kinetics of these systems are important to numerous interfacial processes including the preparation of thin films, molecular electronics and electrochemistry. The alkanethiol SAMs are usually prepared through either spontaneous adsorption from an ethanol solution [2-10] or vapour phase deposition [11-15]. UHV/STM [2,4,7-9,11-13], LEAD [14,15], XPS [5,14], X-ray diffraction [3,10,14] and AFM [6] have been the techniques most widely used to study SAM formations while at an intermediate surface coverage during film growth. Three groups have also reviewed the field [16-18].

Decanethiol ($CH_3(CH_2)_9SH$) [Figure 5.1] has been one of the most widely studied alkanethiols adsorbed onto Au(111) [2-4,7-15] and although there is agreement that the molecules adopt a c(4x2) superlattice of the close packed hexagonal $(\sqrt{3}x\sqrt{3})R30^o$ structural motif with the alkyl chain tilted 60° from the surface plane at saturation coverage [2,3,7-15], domains and phase transitions at below substrate saturation, where the so-called ‘pin-stripe’ structures dominate, are still under investigation.

Using vapour phase deposition, Poirier *et al* [11-13] established six different fundamental phases which characterise the growth of a DCNT film as a function of

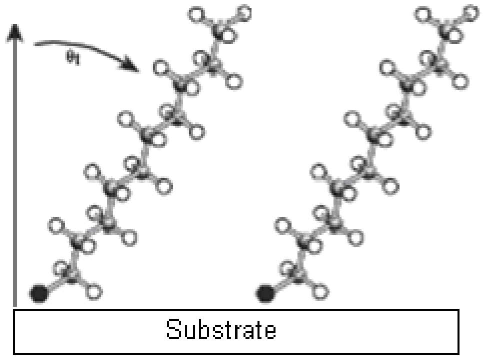

Figure 5.1: A schematic of the decanethiol molecule consisting of the sulphur head group (dark circle), hydrogen atoms (open circle) and carbon backbone (shaded circles) of the hydrophobic alkyl chain and exhibiting the typical standing up orientation with tilt angle θ_t at 30° to the surface normal [16].

coverage on Au(111). Initially, a disorganised lattice gas with high molecular mobility was adopted at the lowest surface coverage. This phase then co-existed with a pin-stripe pair organisation lying in a parallel/anti-parallel orientation from the closely aligned sulphur headgroups where the alkyl chains form corrugated rows along the <121> direction in the Au(111) substrate. They orientated with a 5 Å corrugation periodicity and a stripe separation between different rows of sulphur headgroups of 32 Å with a 2.5 Å shift between adjacent pairs [2]. Fenter *et al* [10] and Camillone *et al* [15] found that this inter row spacing is dependent upon alkyl chain length. These two phases occurred until approximately 27% of 1ML (Monolayer) [16] was achieved. As coverage increased towards 40% of surface saturation, a mixture of the pin-stripe phase combined with areas of disorganised and organised stacking was observed with the headgroups still closely aligned. Sparse nucleation of the c(4x2) superlattice of the cph(√3x√3)R30° structure began after approximately 50% saturation [16] but only saturated the surface after melting of the previous three striped phases. Schreiber *et al* [14] agree with this sequence of phases explaining that the adsorption process, while driven by molecular coverage, is not as a result of variations in molecular orientation nor do the phases exist in isolation with discrete phase boundaries.

Annealing of decanethiol monolayers on Au(111) also exhibited these intermediate pin-stripe structures [2,4].

The spontaneous adsorption of alkanethiols from solution is most directly related to the environment in which our experiments were conducted. Tamada *et al* [6] found some domain formation on Au(111) after a number of seconds from both single and mixed chain alkanethiols. Yamada and Uosaki [7] used electrochemical STM to observe decanethiol adsorption from a 0.3 μM heptane solution and noted at least three stages during self assembly. Initially there was no molecular ordering followed by pin-stripe structures and finally the $(\sqrt{3}x\sqrt{3})R30^o$ structure. These stages again agreed with those reported using vapour phase deposition studies [11-14]. They also reported however that these steps vary dependant upon the concentration of the solution used. S-S Li *et al* [8] immersed Au(111) in ethanol containing 1 μM decanethiol for different immersion times. They proposed a five step process for formation of the SAM which illustrates the time-dependent organisation in solution: 1) random molecular orientation, 2) small pin-stripe areas, 3) pin-stripes and some stacking, 4) organised stacking and 5) the high density saturation structure.

This is the first study of DCNT adsorbed on Au(110) and this work aims to ascertain whether the orientation of DCNT adsorbed at the Au(110)/liquid interface changes with coverage and whether RAS is sensitive to these variations if, indeed, they do occur.

5.2: Experimental Procedure

The Au(110) crystal was prepared as described earlier through polishing with diamond paste and flame annealing to preserve the (1x2) missing row reconstruction [19]. DCNT obtained from Sigma-Aldrich, without further purification, was dissolved in ethanol (Fluka) to give a 10 mM solution.

The RAS of the Au(110) surface in 20 ml of ethanol has a pronounced negative

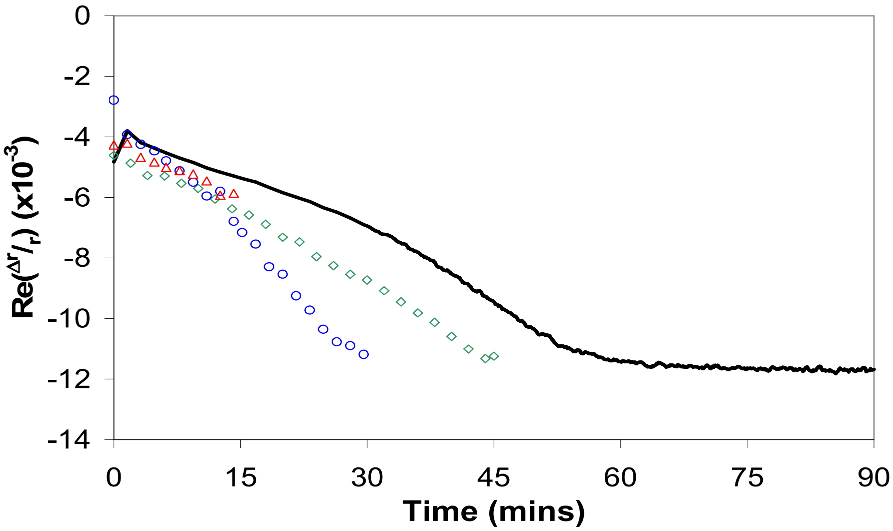

Figure 5.2: RAS intensity of Au(110)/ethanol recorded at 2.5 eV with the addition of DCNT to give a final concentration of 0.5 μM recorded for 15 min (△), 30 min (O), 45 min (◇) and 60 min (solid line).

peak at 2.5 eV and the intensity of this peak increased as DCNT was adsorbed onto the surface. In order to investigate the influence of the formation of the SAM on the magnitude of the RAS, the signal obtained at 2.5 eV was recorded as a function of time following the addition to the cell of solutions of 1 μl of 10 mM decanethiol to produce a final concentration of 0.5 μM. The experiment was halted after 15, 30, 45 and 60 minutes by extraction of the solution and rinsing thoroughly with fresh ethanol to remove any physisorbed material. RA spectra which measure the change in intensity at a solitary wavelength are called RAZ spectra and this data is shown in Figure 5.2. This graph clearly establishes that it took 60 minutes for DCNT to completely saturate the surface.

In separate experiments, RA spectra of the Au(110) in 20 ml ethanol were recorded prior to and after the addition of 0.5 μM concentrations of DCNT using the same time intervals as in Figure 5.2 to track the changes in the RA profile as a function of surface coverage. The results of these experiments are displayed in Figure 5.3.

Low resolution XPS broadscans were conducted both before and after adsorption in order to compare directly the changes DCNT has upon the gold crystal. XPS investigations were recorded in a photoelectron spectrometer [20] of pressure no greater than 10^{-10} Torr employing a monochromated Al K_{α} source of 1486.6 eV.

5.3: The Orientation of DCNT as a Function of Coverage

The RAS technique is very sensitive to the morphology of the Au(110) surface [21-24] and there is some variation in the spectral profiles obtained from the Au(110) surfaces in ethanol that probably arise from variations in the flame annealing procedure [Figure 5.3]. The small variations in the spectral profiles obtained in the different experiments are however very similar to those produced in previous work on Au(110) [25,26]. A detailed explanation of the origin of the main features of the RA profile of a clean Au(110) single crystal can be found in Chapter 3.

XPS was employed to determine the presence of all elements on the surface

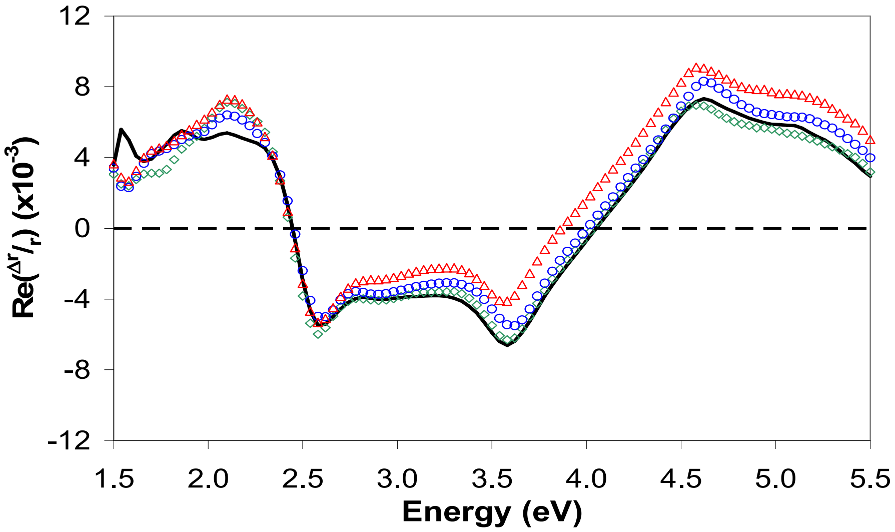

Figure 5.3: RA spectra of Au(110) + 20 ml ethanol obtained in the 15 min (△), 30 min (O), 45 min (◇) and 60 min (black line) timed experiments.

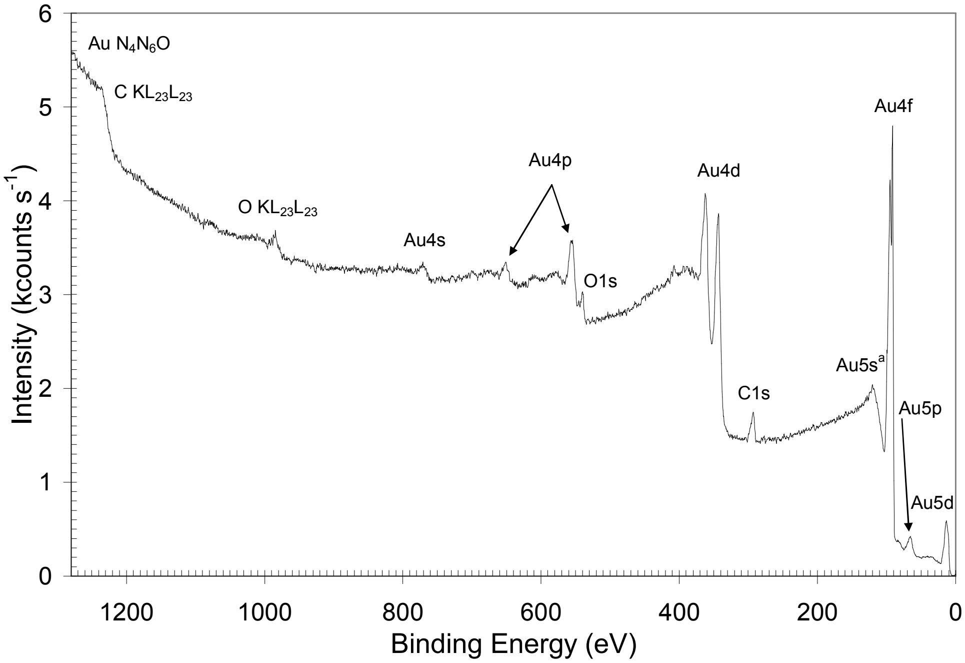

Figure 5.4: A XPS broadscan of the freshly prepared Au(110) single crystal before saturation with decanethiol.

[a] The Au(5s) peak is of low intensity and is often in the shake-up structure of the (4f) photoelectric peaks [27].

after crystal preparation. Apart from trace amounts of oxygen and carbon, which are to be expected due to sample oxidation whilst being transferred from the chemical laboratory to the XPS machine and the possibility of some contamination from the diamond paste used to polish the crystal, the major photoemission peaks one would anticipate from pure Au are easily identifiable. It is clear from Figure 5.4 that there are no other contaminants which could result in misleading data after DCNT has been adsorbed onto the substrate.

The spectra recorded after the surface had been exposed to DCNT in the four different experiments are shown in Figure 5.5 (a). The main feature of these spectra is the enhancement of the negative peak at 2.5 eV which has previously been identified as characteristic of the Au-S bond [1]. As the DCNT molecule adsorbs on the Au(110) surface over longer time spans, there are systematic increases in the intensity of both

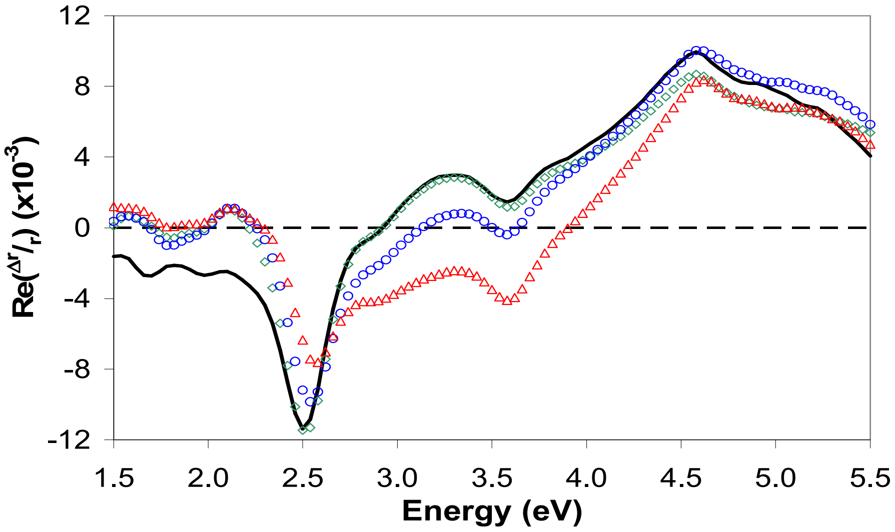

Figure 5.5 (a): RA spectra of Au(110)/ethanol + DCNT after adsorption for 15 min (△), 30 min (O), 45 min (◇) and 60 min (black line).

the 2.5 eV and 4.5 eV features accompanied by a reduction in the intensity of the dip at 3.5 eV. Although the spectral profiles of both the 45 min and 60 min experiments are very similar, the maximum intensities of the main features of the RA profile of DCNT are only obtained after 60 minutes thereby indicating that a saturating coverage has been exclusively achieved in the lengthiest experiment. Further evidence to support this conclusion can be seen in Figure 5.5 (b). Here, the corresponding RA spectra of Au(110)/ethanol have been subtracted from the spectra obtained in the four different experiments to directly observe the change in contribution to the RA signal from the DCNT molecule. Again, systematic changes are visible in the main features at 2.5, 3.5 and 4.5 eV until saturation is complete after 60 minutes (black line). Figure 5.5 (b) shows that even after subtraction of the corresponding gold spectra a significant RA profile remains and thus a significant change in the optical response due to the presence of molecules. This fact means that the decanethiol molecule must contribute to the optical response of the system. If this were not so, one would expect these profiles to be flat.

Figure 5.6 displays the XPS broadscan of Au(110) after adsorption by DCNT.

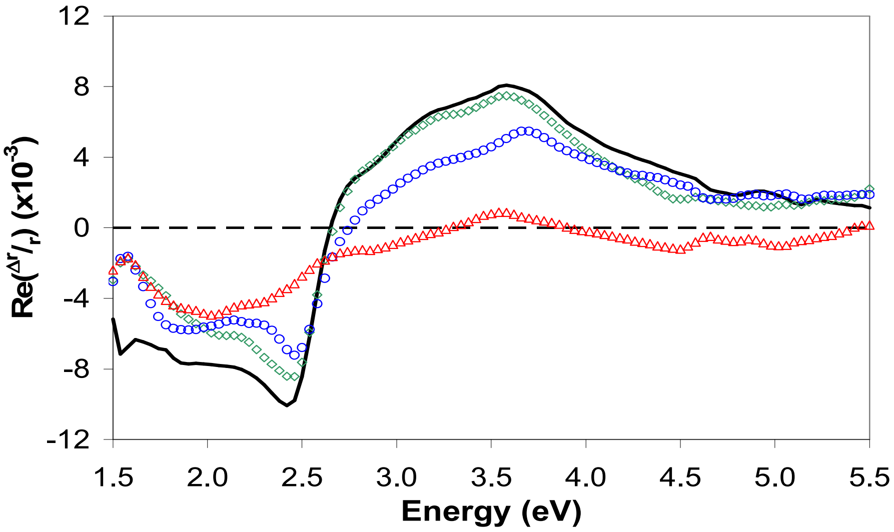

Figure 5.5 (b): The spectral profile attributed to DCNT obtained by subtraction of the corresponding Au(110)/ethanol spectra.

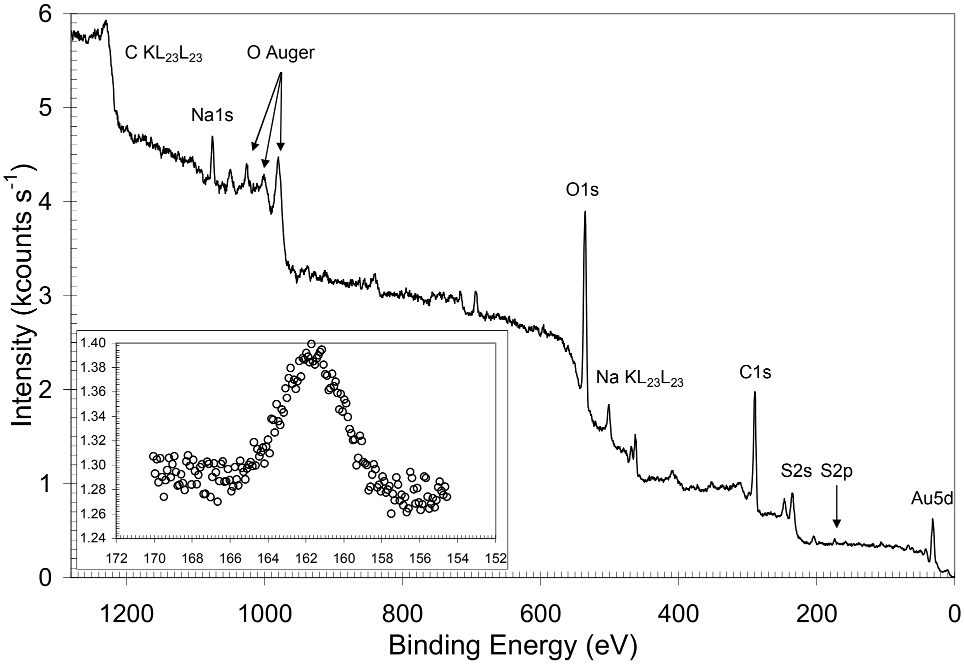

Figure 5.6: XPS broadscan of Au(110) + DCNT at saturation coverage. Inset: expanded higher resolution spectrum of the sulphur 2p peaks.

The differences between this spectrum and that shown in Figure 5.4 are marked and manifest themselves mainly in suppression of the low binding energy Au4f and Au4d peaks suggesting that monolayer coverage has been achieved. Further, appearance of characteristic sulphur 2s and 2p photoemission peaks confirm that DCNT must be attached across the vast majority of the surface. Also shown in Figure 5.6 is the higher resolution spectrum of the S2p peak clearly confirming the presence of sulphur on the surface.

The RAS of adsorbed molecules is expected to be sensitive to the orientation of the molecules and this sensitivity was used in a recent study to determine the three-dimensional orientation of cytosine adsorbed at the Au(110)/electrolyte interface [25]. If the orientation of the DCNT molecules does not change with coverage then the RAS at intermediate coverage's should be a linear sum of the RAS of the Au(110)/ethanol + DCNT at an early stage in molecular adsorption and the RAS of DCNT adsorbed at this interface at saturation coverage. In particular the RAS obtained after exposure to DCNT for 30 minutes should be given by a linear sum of the RA profile recorded after exposure to DCNT for 15 minutes and the RAS recorded after exposure to DCNT for 60 minutes. If this is true the spectral profile will obey Equation (5.1):

$$\{\mathrm{Au(110)} + \mathrm{DCNT}\}_{30} = A\{\mathrm{Au(110)} + \mathrm{DCNT}\}_{15} + B\{\mathrm{Au(110)} + \mathrm{DCNT}\}_{60} \qquad (5.1)$$

where $\{\mathrm{Au(110)} + \mathrm{DCNT}\}_{30}$ = RA spectrum of Au(110)/ethanol plus DCNT after 30 minutes adsorption, $\{\mathrm{Au(110)} + \mathrm{DCNT}\}_{15}$ = RA spectrum of Au(110)/ethanol plus DCNT after 15 minutes adsorption and $\{\mathrm{Au(110)} + \mathrm{DCNT}\}_{60}$ = RA spectrum of Au(110)/ethanol plus DCNT after saturation adsorption (60 minutes). A and B are independent multiplicity factors.

Figure 5.7 is the result of the attempt to simulate the spectra using Equation (5.1). In this simulation, A = 0.48 and B = 0.59 which are the best values to simulate adequately the RA profile across the energy range as well as the absolute intensity of

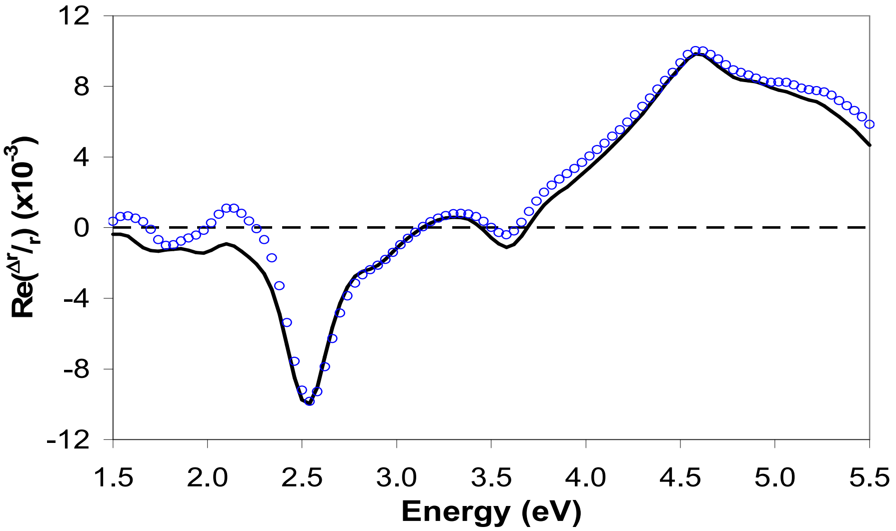

Figure 5.7: Simulated spectra (black line) of Au(110)/ethanol + DCNT after 30 min (O).

the three main features. These values mean that ~ 45% of the simulation is derived from Au(110)/ethanol + DCNT after 15 minutes adsorption while ~ 55% originates from Au(110)/ethanol + DCNT at saturation coverage. Figure 5.7 shows that the simulation of the RA profile during an intermediary stage of adsorption was successful as the contours and absolute intensities are reproduced accurately across the whole spectrum. The fact that the simulation contains contributions from both the DCNT molecule and the Au(110) surface, albeit small, allows a complete picture of the molecular interaction at the interface to be formed. The success of the simulation coupled with the sensitivity of the RAS to the orientation of adsorbed molecules [28-30] implies that DCNT does not change its orientation on the Au(110) surface as coverage increases and this behaviour is in contrast to that observed on the Au(111) surface. The sulphur head group and alkyl chain must have the same orientation in relation to the substrate at the vast majority of binding sites without having to modify domain structure to allow more molecules to adsorb as coverage increases. The work of Schreiber *et al* [14] supports the conclusion that film growth is not facilitated by a change in molecular orientation itself.

It is also interesting that the spectrum of the DCNT/Au(110) taken at 30 minutes represents half of the time taken to completely saturate the surface. Therefore if the process were linear, as is suggested by this work, the factor multiplying each spectrum should represent approximately 50% of the total contribution to the simulation. The experimental results are very close at ~ 55% and ~ 45% respectively.

5.4: Azimuth Dependent RAS as a Function of Surrounding Environment

As has been discussed in depth in Chapter 4.3, the azimuthal rotation of a sample about the direction of incident light after molecular adsorption on the crystal can give detailed information on molecular orientation. To this end, rotations were conducted with the Au(110) placed in a surrounding environment of ethanol before and after the addition of DCNT as displayed in Figures 5.8 (a) and (b). As is to be expected, Figure 5.8 (a) clearly displays the cos2θ behaviour associated with rotations involving Au(110) as a function of θ.

An important point about the spectra of Au(110)/ethanol + DCNT [Figure 5.8

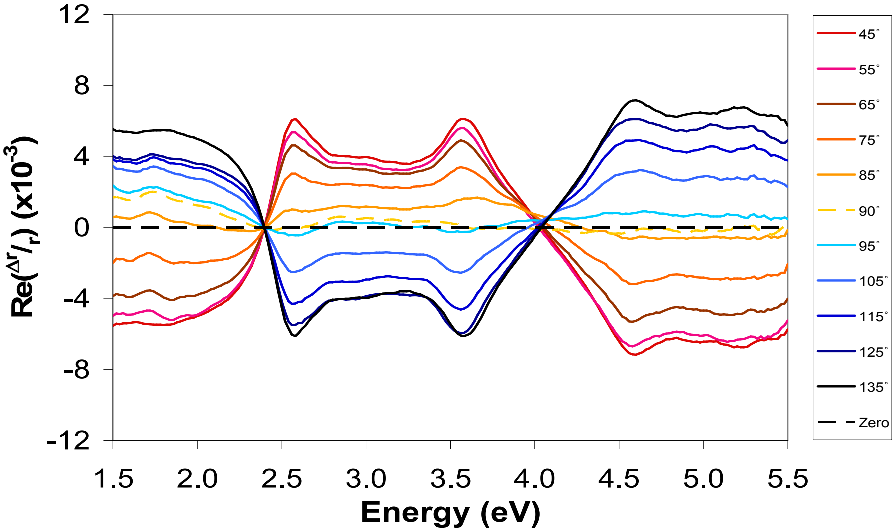

Figure 5.8 (a): RA spectra of Au(110) in ethanol rotated through 90°.

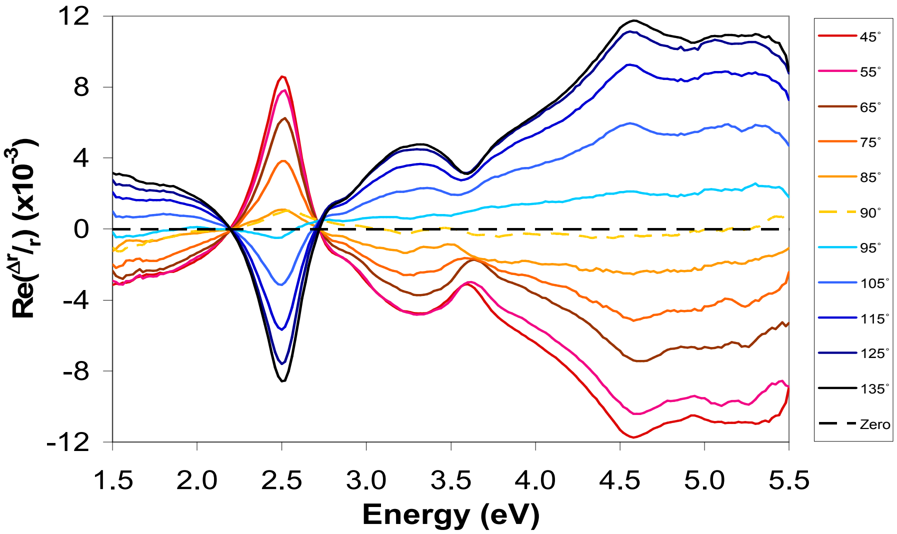

Figure 5.8 (b): RA profiles of Au(110)/ethanol after adsorption of DCNT rotated through the same angles as in Figure 5.8 (a).

(b)] is that as $\theta \rightarrow 90^\circ$, the detected RA signal → 0 across the whole spectrum. This is the same result as found for the rotation of Au(110) after adenine had adsorbed on the surface and hence a similar argument to that used for adenine can be used to establish that the DCNT must align along one the principal axes of the gold substrate. One must clarify this argument in that it is not suggested the hydrophobic backbone lies along either of the substrate axes, just that the optical dipoles that give rise to the RA spectrum are orientated along one of the primary axes of the substrate.

Figure 5.8 (c) shows the resultant RA profile of DCNT after subtraction of the corresponding Au(110) spectra at the same angle. Since a substantial RA signal remains after this subtraction, the adsorbed molecule must make a significant contribution to the optical response of the system and since these spectra are symmetrical after rotation through 90°, the molecule must be adsorbed anisotropically. The variation beyond 5 eV in the RA spectra recorded in this section compared to those displayed in Figures 5.3 and 5.5 are due to minor improvements in the RAS instrument which result in a small increase in intensity above 5 eV.

Since the backbone of DCNT is hydrophobic, its orientation with respect to

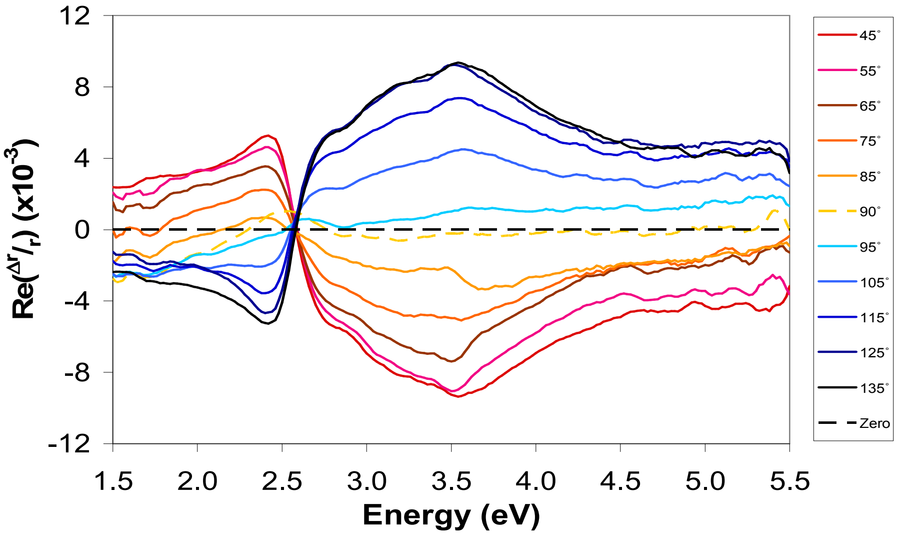

Figure 5.8 (c): Resultant RA profiles originating from the optical response of DCNT after the subtraction of corresponding Au(110) spectra.

the surface normal would be expected to be sensitive to changes in the external environment dependent upon the polarity of the solvent. To ascertain whether RAS is able to detect these small variations, further rotations of the Au(110) crystal following adsorption by DCNT were conducted in both air and then phosphate buffer (NaH_2PO_4/K_2HPO_4 at pH 7.1) after the supporting ethanol solution was removed from the sample holder. Air is hydrophobic since it mainly constitutes oxygen and nitrogen which are non-polar while phosphate buffer is a polar liquid and therefore one might expect a modification of the orientation of the backbone as its surrounding environment is changed from ethanol to air and finally to buffer. Figures 5.9 and 5.10 show the results of rotating the specimen in air and phosphate buffer respectively. Profiles were only obtained at large angular increments in air [Figure 5.9] to highlight spectral differences as DCNT oxidises off the surface quickly when in air [31].

A comparison of Figures 5.8 (b), 5.9 and 5.10 show that there are differences in the angular dependence of the RAS of DCNT adsorbed on Au(110) in the three environments. These differences are clearer in Figure 5.11 which displays the RA profiles of Au(110) + DCNT in ethanol, air and phosphate buffer at the same angle

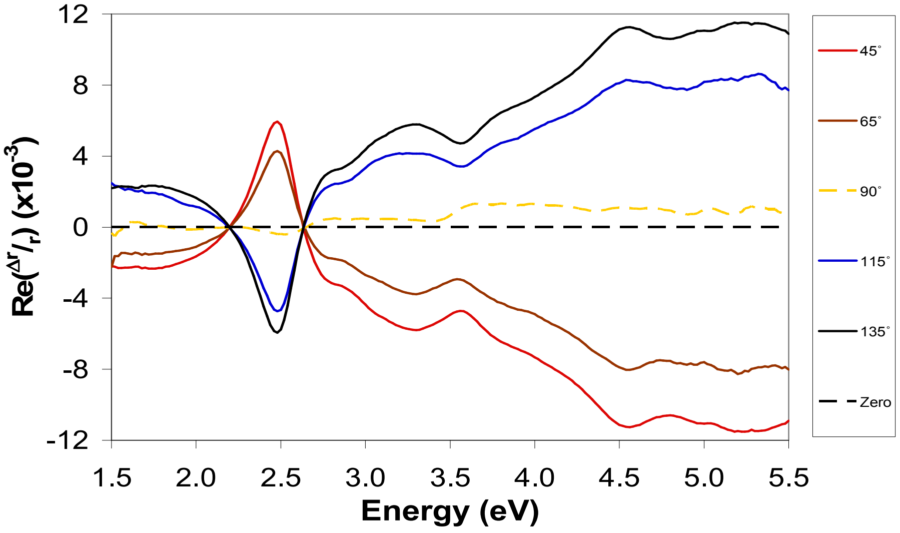

Figure 5.9: RA spectra of Au(110) + DCNT in air. Only the results obtained at large angular increments are shown in order to briefly outline spectral variations between air, ethanol and phosphate buffer as DCNT oxidises off the surface the longer it is not in a liquid environment [31].

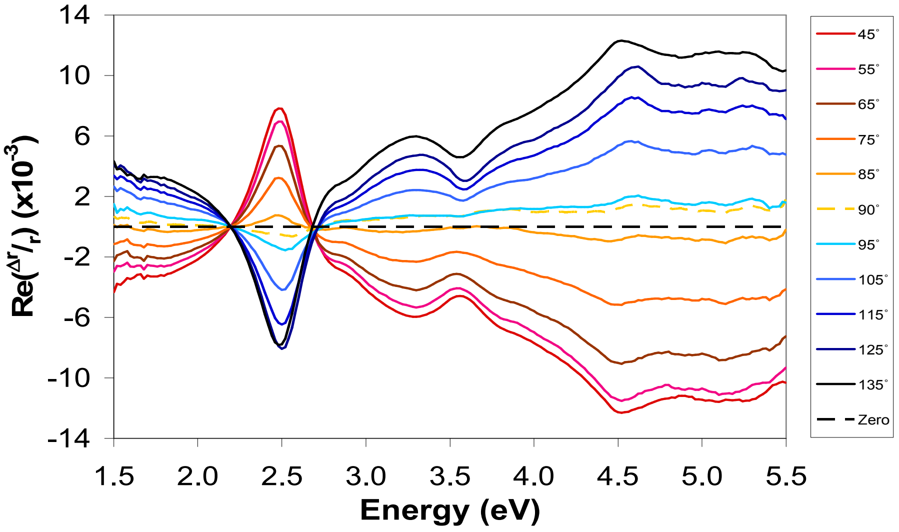

Figure 5.10: RA spectra of Au(110) + DCNT in NaH_2PO_4/K_2HPO_4 at pH 7.1 rotated through 90°.

respectively. It is clear from Figure 5.11 that there are small but significant differences in the optical response of the system in the different environments. There is a small difference in intensity of the characteristic gold/sulphur peak at 2.5 eV when the crystal is in ethanol compared to buffer. This characteristic peak is weaker when the specimen was recorded in air. Moreover, the broad feature between 2.7 – 3.7 eV appears almost identical when the crystal is in either air or buffer compared to when it is in ethanol; the latter environment giving rise to an intense peak at 3.5 eV. At energies > 3.7 eV the contours of the profiles recorded in ethanol and buffer are very similar save a small difference in absolute intensity while that recorded in air has a much shallower feature at ~4.5 eV accompanied by a more developed broad feature between 5.0 – 5.5 eV.

The presence of such disparities in the RA profiles caused by the differing environments is suggestive of slight modifications of the orientations of the carbon backbone of the molecules in the different environments. It is important to note that although differences in the RAS profiles in the three environments are small, the spectra were obtained from the same specimen in a series of experiments conducted in

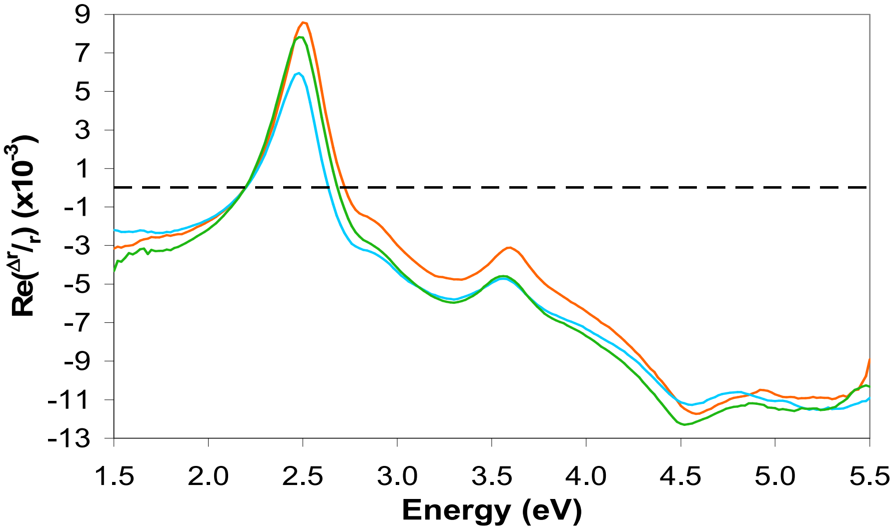

Figure 5.11: Comparison of the spectral profiles of Au + DCNT in ethanol (orange line), air (blue line) and phosphate buffer (green line) at 45˚.

a lone sequence. Furthermore, it has previously been established that the Au-S bond is highly stable [1] and it is more likely that the backbone of the decanethiol will be influenced by the change in environment than this covalent bond. This view is supported by the absence of any change in the position and shape of the peak at 2.5 eV in any of the different environments. There is however a small change in the intensity of this feature as displayed in Figure 5.11 which could be caused by the movement of the alkyl structure.

The three studies of DCNT adsorbed on Au(110) in ethanol, air and phosphate buffer have identified marked spectral differences in the optical response of the system in these three different environments. Considering that the alkyl backbone of DCNT is hydrophobic, the molecule would orientate in such a fashion so as to exclude the effect of hydrogen bonding in the supporting liquid and this orientation would be expected to be sensitive to changes in the nature of that environment. As ethanol is less polar than phosphate buffer, air is hydrophobic and phosphate buffer is strongly polar, one would therefore expect modifications to the orientation of the alkyl chain in these environments and the data presented herein suggest that this is the primary cause of the changes observed in the RAS of these systems. In addition, although the chain is expected to be sensitive to the surrounding environment, the orientational changes may well be small since there is a monolayer coverage on the surface.

5.5: Summary

This results of this work suggest that the orientation of DCNT on Au(110) does not vary as a function of coverage. A calculation was employed which showed that the RAS profile at half monolayer coverage was able to be simulated using an empirical linear summation of the RAS profiles at 0.25 and 1ML coverage to support the above conclusion which would not have been possible if orientation was modified as a function of surface saturation.

Rotations of DCNT adsorbed onto Au(110) in ethanol showed that the molecule must adsorb along one of main axes of the gold substrate, probably through a covalent gold/sulphur bond, as a cos2θ relationship was observed as a function of angle between the substrate axes and that of the incident light. This relationship was also found for rotations conducted in air and in phosphate buffer.

Rotations of Au(110) + DCNT in ethanol, air and buffer suggest that the orientation of the alkyl backbone of the molecule changed as the surrounding environment was modified as shown through small but significant variations in the spectral profiles of the systems studies.

5.6: References

[1] R. LeParc, C. I. Smith, M. C. Cuquerella, R. L. Williams, D. G. Fernig, C. Edwards, D. S. Martin and P. Weightman, *Langmuir* **22**, 3413 (2006)

[2] R. Staub, M. Toerker, T. Fritz, T. Schmitz-Hübsch, F. Sellam and K. Leo, *Langmuir* **14**, 6693 (1998)

[3] P. Fenter, A. Eberhardt and P. Eisenberger, *Science* **266**, 1216 (1994)

[4] O. Cavalleri, A. Hirstein, J-P. Bucher and K. Kern, *Thin Solid Films* **284-285**, 392 (1996)

[5] D. G. Castner, K. Hinds and D. W. Grainger, *Langmuir* **12**, 5083 (1996)

[6] K. Tamada, M. Hara, H. Sasabe and W. Knoll, *Langmuir* **13**, 1558 (1997)

[7] R. Yamada and K. Uosaki, *Langmuir* **13**, 5218 (1997)

[8] S.-S. Li, L-P. Xu, L-J. Wan, S-T. Wang and L. Jiang, *J. Phys. Chem. B* **110**, 1794 (2006)

[9] G. E. Poirier, M. J. Tarlov and H. E. Rushmeier, *Langmuir* **10**, 3383 (1994)

[10] P. Fenter, P. Eisenberger and K. S. Liang, *Phys. Rev. Lett* **70**, 2447 (1993)

[11] G. E. Poirier, *Langmuir* **15**, 1167 (1999)

[12] G. E. Poirier, W. P. Fitts and J. M. White, *Langmuir* **17**, 1176 (2001)

[13] W. P. Fitts, J. M. White and G. E. Poirier, *Langmuir* **18**, 2096 (2002)

[14] F. Schreiber, A. Eberhardt, T. Y. B. Leung, P. Schwartz, S. M. Wetterer, D. J. Lavrich, L. Berman, P. Fenter, P. Eisenberger and G. Scholes, *Phys. Rev. B* **57**, 12476 (1998)

[15] N. Camillone III, T. Y. B. Leung, P. Schwartz, P. Eisenberger and G. Scoles, *Langmuir* **12**, 2737 (1995)

[16] F. Schreiber, *J. Phys.: Condens. Matter* **16**, R881 (2004)

[17] R. K. Smith, P. A. Lewis and P. S. Weiss, *Prog. Surf. Sci.* **75**, 1 (2004)

[18] L. H. Dubois and R. G. Nuzzo, *Annu. Rev. Phys. Chem.* **43**, 437 (1992)

[19] D. M. Kolb, *Prog. Surf. Sci.* **51**, 109 (1996)

[20] P. Weightman, *Physica. Scripta.* **T41**, 277 (1992)

[21] V. Mazine, Y. Borensztein, L. Cagnon and P. Allongue, *phys. stat. sol. (a)* **175**, 311 (1999)

[22] B. Sheriden, D. S. Martin, J. R. Power, S. D. Barrett, C. I. Smith, C. A. Lucas, R. J. Nichols and P. Weightman, *Phys. Rev. Lett.* **85**, 4618 (2000)

[23] V. Mazine and Y. Borensztein, *Phys. Rev. Lett.* **88**, 147403 (2002)

[24] P. Weightman, C. I. Smith, D. S. Martin, C. A. Lucas, R. J. Nichols and S. D. Barrett, *Phys. Rev. Lett.* **92**, 199707 (2004)

[25] P. Weightman, G. J. Dolan, C. I. Smith, M. C. Cuquerella, N. J. Almond, T. Farrell, D. G. Fernig, C. Edwards and D. S. Martin, *Phys. Rev. Lett.* **96**, 86102 (2006)

[26] P. Weightman, D. S. Martin, R. J. Cole and T. Farrell, *Rep. Prog. Phys.* **68**, 1251 (2005)

[27] *Surface Analysis by Auger and X-ray Photoelectron Spectroscopy*, edited by D. Briggs and J. T. Grant (IM Publications, 2003)

[28] J. R. Power, P. Weightman, S. Bose, A. I. Shkrebtii and R. Del Sole, *Phys. Rev. Lett.* **80**, 3133 (1998)

[29] B. G. Frederick, J. R. Power, R. J. Cole, C. C. Perry, Q. Chen, S. Haq, Th. Bertrams, N. V. Richardson and P. Weightman, *Phys. Rev. Lett.* **80**, 4490 (1998)

[30] B. G. Frederick, R. J. Cole, J. R. Power, C. C. Perry, Q. Chen, N. V. Richardson, P. Weightman, C. Verdozzi, D. R. Jennison, P. A. Schultz and M. P. Sears, *Phys. Rev. B* **58**, 10883 (1998)

[31] C. I. Smith, *private communication*

Chapter 6: Detection of DNA Hybridisation on a Functionalised Diamond Surface

This investigation takes advantage of recent developments of functionalising polycrystalline diamond surfaces in order to tether ss-DNA molecules to a well ordered platform. Integrity of the functionalised layer is demonstrated through hybridisation with a homologous oligonucleotide probe. This approach avoids the complication of a RAS signal arising from the substrate since polycrystalline diamond produces no RA spectral profile.

6.1: Introduction

The interaction of nucleic acids with the surfaces of materials is important because it enables the identification of specific gene sequences via hybridisation and the detection and magnitude of gene expression [1-4]. A number of technologies have been developed that have the capacity for high-throughput analysis e.g. DNA arrays allow expression of thousands of genes to be monitored, pyrosequencing allows between 1 and 9 Giga bases of DNA to be sequenced at a time. However, relatively little is known about the physical and chemical forces that allow nucleic acids to bind to surfaces and more importantly how the molecules are aligned. Methods that aim to rapidly identify nucleic acid interactions are important for understanding how binding to a surface influences structure, interactions and functionality and this may lead to more efficient analytical methods [5]. The capacity to produce ordered and defined layers of attached single stranded DNA molecules on a surface that would bind to the homologous strands would be an important step to realising these aims particularly if it was combined with a method of monitoring such ordered layers and detecting hybridisation between complimentary DNA sequences. Such a capability is detailed herein using DNA molecules attached to a diamond surface and employing RAS as the monitoring technique. This approach also has potential in the developing field of pharmocogenomics for monitoring DNA damaging chemicals. Diamond is a particularly attractive substrate for the grafting of alkenes due to the presence of C-C bonds formed at the interface which confer the monolayers with very high chemical stability under a wide range of conditions [6]. Furthermore, its robust nature and high biocompatibility can be applied in electrical sensing due to its wide band gap and large electrochemical potential window [7,8]. Its versatility is enhanced as it can be easily doped and deposited as thin films on a variety of other substrates at relatively low temperatures.

The RA spectrometer used for the purposes of this investigation is of the same design as that which features in the rest of this thesis with some additional minor optical modifications which enabled the range of the instrument to be extended from 5.0 eV to 6.0 eV. RAS has previously been used to probe the adsorption of ss and ds DNA at Au(110)/liquid interfaces [9,10] and these studies showed that both conformations of DNA bind to the gold surface and that RAS could detect this interaction. The RA spectral profiles resulting from each system confirmed that both types of DNA formed ordered layers on the metal surface and that adsorption was both improved and prevented by modifying the potential applied to the gold electrode. Furthermore, it was noted that ss-DNA gave larger RAS signals than ds-DNA. The observation that ss-DNA bound to a gold substrate gave a more intense optical response than that recorded for ds-DNA can be explained if the ss-DNA attached to the surface through its bases which resulted in greater interactions than ds-DNA, which presumably interacted with the surface via the negatively charged phosphate backbone [9-11]. The conclusion to be drawn from the investigations discussed above was that RAS is unable to detect DNA-DNA hybridisation at the Au(110)/liquid interface since the strong interactions of the bases of ss-DNA with the Au(110) surface made them inaccessible for hybridisation with any incoming homologous strands. The fact that the Au(110)

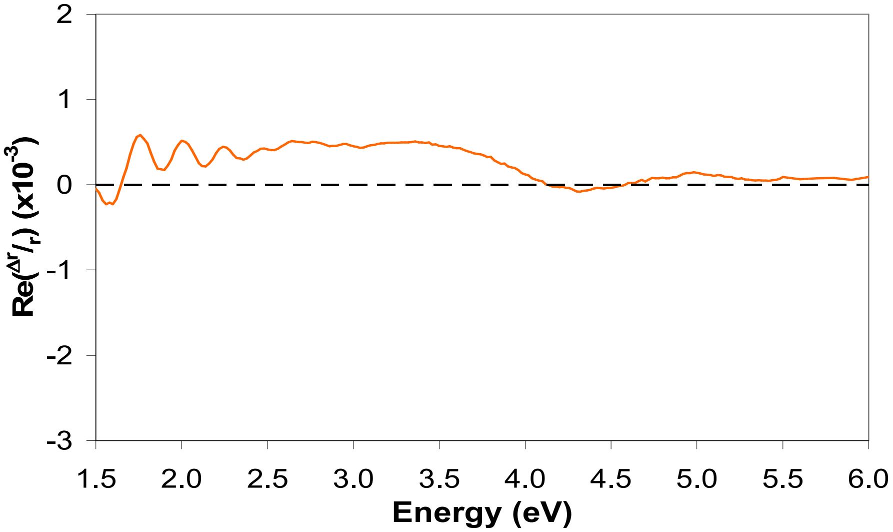

Figure 6.1: RA profile of clean CVD diamond. The periodic oscillations seen below 2.5 eV are due to interference in the passage of light rather than to a specific sample effect.

surface has a strong RAS signal [12] in the absence of bound molecules also mitigated against the use of RAS to detect DNA hybridisation on this surface since, as in previous work [9,13], it would be necessary to subtract the Au(110) signal from that of the Au(110) plus the attached molecule. A surface that has no intrinsic RAS signal would therefore maximise the detection of the spectra of bound molecules.

An earlier work reported the RAS of the single crystal diamond (100) surface [14] and it was anticipated that the symmetry requirements inherent to the system would mean that the development of a methodology for observing the RAS of DNA attached to diamond surfaces would require the use of a single crystal surface. In practice however, the scarcity of high quality substrates would limit the scope for exploiting a genetic screening methodology based on single crystal diamond. Such a methodology would find much easier application if it could be carried out using polycrystalline CVD diamond and for this reason it was decided to explore the use of the latter substance as a possible platform for covalent attachment of ss-DNA.

The RA spectrum of a CVD diamond sample is shown in Figure 6.1 and this profile clearly exhibits no intrinsic RAS profile therefore confirming that polycrystalline diamond met the requirement that the substrate used for the attachment of ss-DNA be isotropic.

6.2: Experimental Procedure

Boron doped polycrystalline diamond grown by CVD was obtained from Element Six (Ascot). The functionalisation procedure as detailed in the following paragraphs has been previously established [6-8,15-26] and all samples were prepared by collaborators in the United States [27]. The diamond samples were initially hydrogen terminated [Figure 6.3 (i)] in a 13.56 Mhz inductively coupled RF H_2 plasma (20 Torr) at 650°C for 10 minutes, cooled under plasma for 15 min and then further cooled in pure H_2 for > 30 min. This procedure was implemented as it preferentially removes any graphite or sp^2

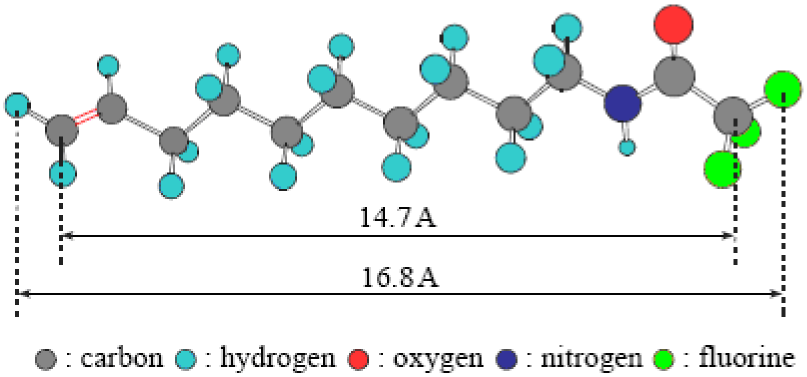
14.7 A
16.8 A
● : carbon ● : hydrogen ● : oxygen ● : nitrogen ● : fluorine

Figure 6.2: Amino-dec-1-ene molecule protected with a trifluoroacetic acid group as determined by Nebel *et al* [22].

hybridised carbon and leaves the surface fully H-terminated [7,15,18,21-23,26].

Chemical functionalisation was realised by photochemically reacting the key linker molecule, a long chain ω-unsaturated amine labelled trifluoroacetamide-protected 10-aminodec-1-ene (TFAAD) [Figure 6.2], with the surface (ii). Neat TFAAD liquid (5 – 10 μL) was positioned on the substrates and sealed with a quartz slide to both provide a thin organic film and also prevent evaporation of the liquid. Samples were then placed inside a nitrogen-purged reaction chamber and the cell was illuminated with UV light from a low-pressure mercury vapour quartz grid lamp ($\lambda = 254$ nm (4.9 eV), 15 mW/cm^2) for ~ 10 hours. 4.9 eV is significantly below the bulk band gap of pure diamond (5.5 eV) however, synthetic diamond samples normally display a strong absorption at wavelengths below ~ 400 nm due to residual π-bonded carbon and the effect of nitrogen impurities [18]. After the reaction with UV light to enable TFAAD binding, samples were sonicated individually in chloroform (5 min) and electronic grade methanol (5 min) to remove any physisorbed material and dried under N_2. The steps of this process have been shown to be sufficient to induce a reaction which results in a self-terminated monolayer coverage of TFAAD [7,8,15,18,20-22].

Infrared reflectance absorption spectroscopy (IRRAS) studies [6,23-25] have proposed that the disappearance of the vinyl C=C and C-H stretching bands in IRRAS spectra upon grafting of TFAAD strongly suggests that the molecule bonds to the diamond substrate through the olefin moiety. Further evidence to support this conclusion can be found from angle-resolved XPS measurements which confirm the TFA protecting group is located at the organic layer/vacuum interface [20-22] while chemical measurements have also shown that the TFAAD groups are chemically accessible after grafting [8,15]. It is thought that the photochemical attachment of organic alkenes to carbon substrates occurs by a mechanism through which photoemission of electrons from the valence band of the diamond localised at the surface, excited by the incident UV light, creates reactive species in the fluid in the immediate vicinity to the surface. It is these reactive species in the liquid phase which facilitate the reaction by withdrawing hydrogen as H^+ from the C-H surface species which allows the surface to undergo radical reactions with alkenes through the C=C bond [6,8,18,21,23-26]. Hence, the requirement for the surface to be initially terminated with hydrogen enables such efficient photochemical functionalisation on diamond as it promotes photoemission from the localised valence states due to the negative electron affinity of H-terminated surfaces [6,21]. XPS characterisation spectra of a TFAAD protected sample are displayed in Figures 6.4 and 6.5.

In order to provide chemically reactive primary amine groups [7,15,18-20] the trifluoroacetamide group was deprotected by refluxing the TFAAD modified samples in 2:5 $MeOH/H_2O$ with 7% (w/w) K_2CO_3 for approximately 3.5 hrs (iii). The amine terminated diamond surfaces were then reacted with a 14 nM solution of sulfosuccinimidyl 4-(N-maleimidomethyl)cyclohexane-1-carboxylate (SSMCC) in 0.1 M pH 7.0 triethanolamine (TEA) buffer solution for 20 min in a humid chamber. The maleimide moiety was then reacted with 200 μl of 250 M HS-ssDNA in TEA buffer which was added to the surface (iv) and left overnight in the chamber at room temperature [7,15]. SSMCC is a heterobifunctional cross-linker that has one site which is highly reactive toward primary amines and a second that is reactive toward thiols consequently, the action of the SSMCC is to create a thiol-reactive, maleimide-terminated surface that can covalently interact with thiol modified DNA oligonucleotides [19,20]. The NHS-ester group belonging to the SSMCC reacts

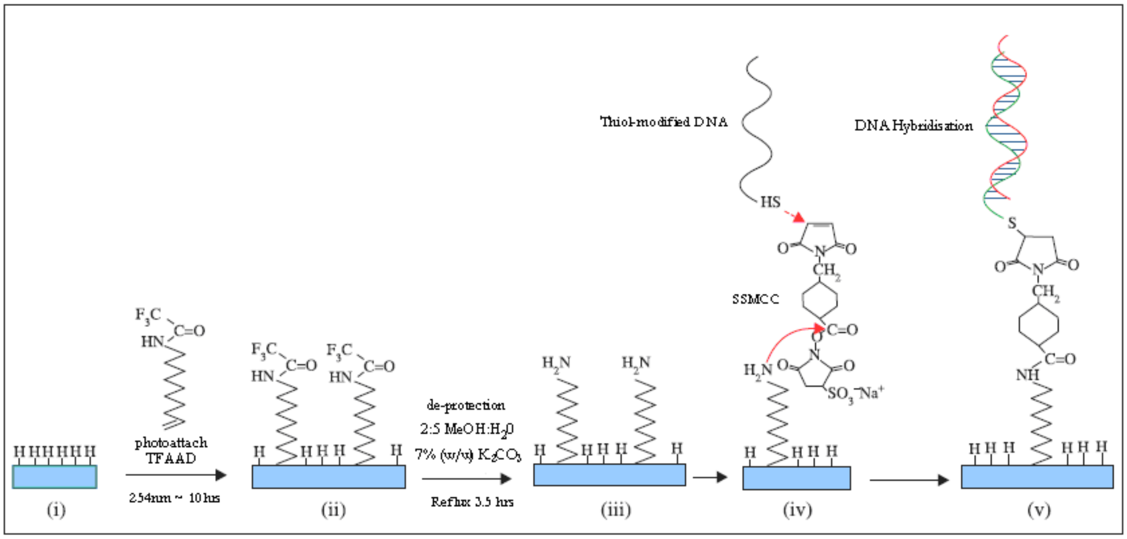

Figure 6.3: Reaction scheme in order to attach ss-DNA to an amine functionalised diamond substrate in preparation for DNA hybridisation. Adapted from [22].

specifically with the amine groups terminating the surface to form stable amide bonds [22]. The thiolated oligonucleotide (TTTTTTTTTTTTTTTGCTTATCGAGCTTTC) was purchased from Sigma Genosys as a protected disulphide. The disulphide bond was cleaved using 0.04 M dithiothreitol (DTT) in 0.17 M phosphate buffer (pH 8) for 16 hrs at room temperature. The thiol by-products and DTT were removed by passage through a NAP-10 column (Amersham Biosciences) and the HS-ssDNA was eluted in TEA buffer. This procedure is known to yield a surface density of ~ 3 x 10^{12} DNA molecules per cm^2 [8,15,22]. The step by step process of generating free-amine terminated surfaces to allow subsequent attachment of DNA oligonucleotides is displayed in Figure 6.3.

For the experiment investigating the detection of DNA hybridisation (v), the diamond substrate (after ss-DNA attachment) was placed in 5 μL of the homologous probe (5 μM in an aqueous buffer of 0.3 M NaCl, 0.02 M $NaPO_4$, 0.002 M ethylenediaminetetraacetic acid (EDTA), and 0.2% sodium dodecyl sulphate) and incubated for 20 min at room temperature [15]. The sample was then soaked twice (5 min) with the buffer to remove any excess un-hybridised homologous strands, dried in argon and the RA spectra recorded.

6.3: XPS of Amine Functionalised TFAAD Protected Diamond

A detailed quantitative analysis of a TFAAD modified sample was undertaken so as to characterise the effect of chemical functionalisation with the protecting TFA group. High resolution XPS spectra of the C(1s), F(1s), N(1s) and O(1s) peaks were recorded at zero degrees relative to the surface normal in the XPS instrument described in Chapter 2.4 utilising the monochromatic Al K_{α} source of 1486.6 eV. Characterisation spectra were analysed by fitting raw data using XPSPEAK 4.1 after a baseline correction. Atomic area ratios were determined after normalisation to the C(1s) peak intensity and adjusted for photoionisation cross-sections (C = 1.00, F = 4.43, N = 1.80, O = 2.93) [6-8,15,18,20-22,24-26,28]. Figure 6.4 shows the broadscan XPS spectra of a

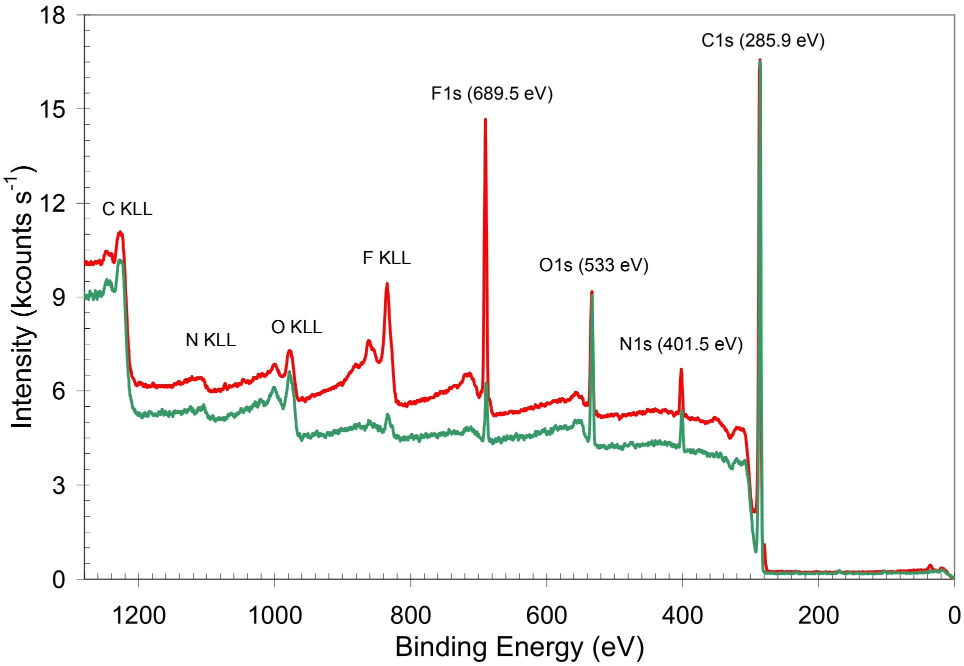

Figure 6.4: XPS broadscan of a CVD diamond sample protected with TFAAD (red line) and the same sample after deprotection leaving a primary amine terminated surface (green line).

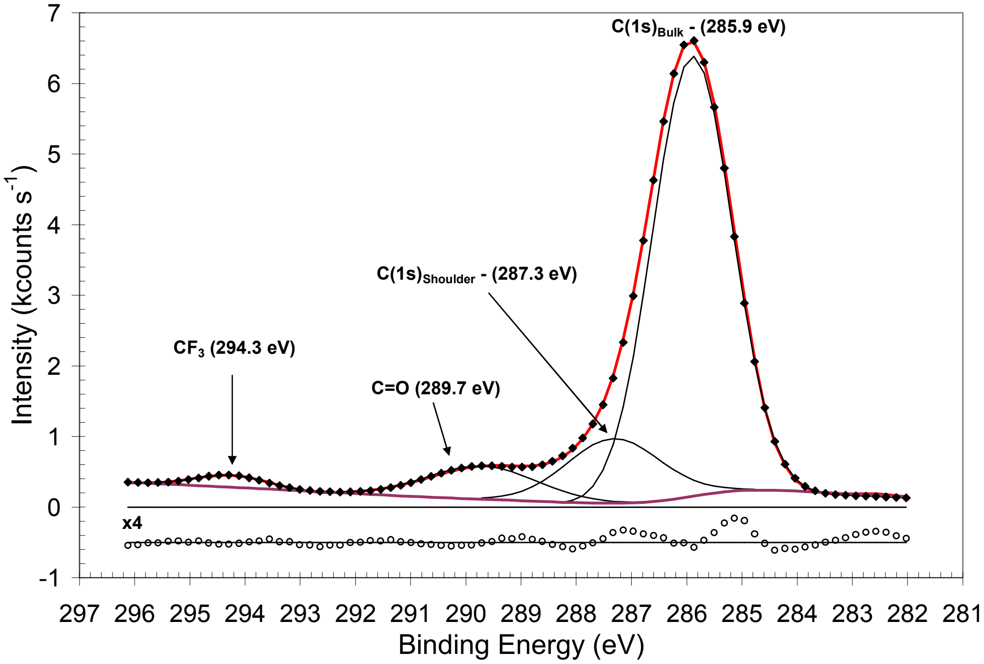

Figure 6.5 (a): Peak sum (◆), Shirley baseline correction (purple line) and constituent components (black curves) of the C(1s) peak (red line) along with residuals (○) of the fit.

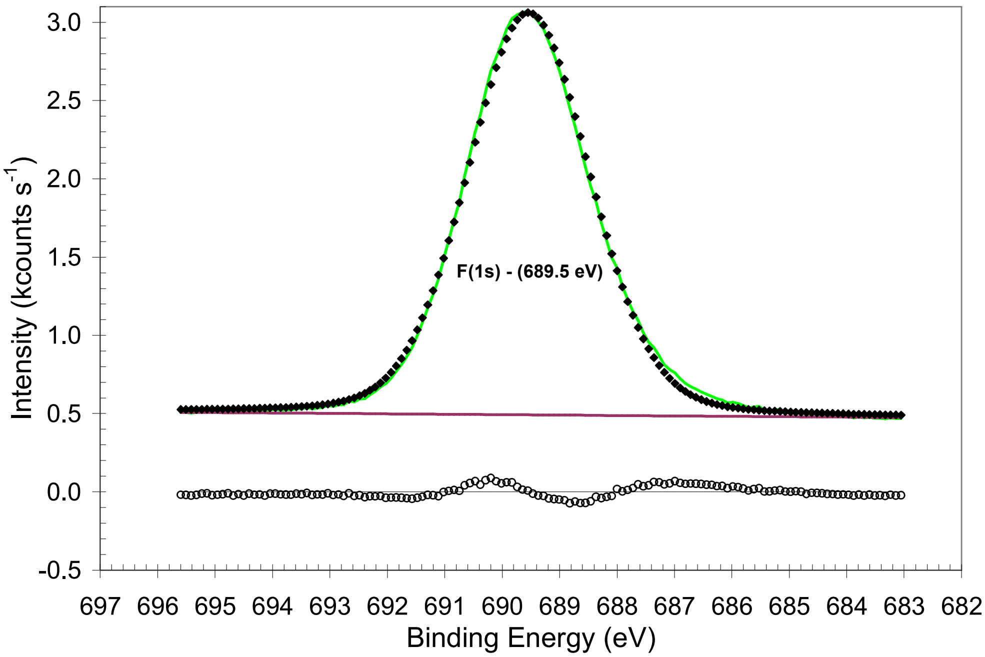

Figure 6.5 (b): Peak sum (◆), Shirley background (purple line) and residuals (○) of the high resolution spectrum of fluorine (green line).

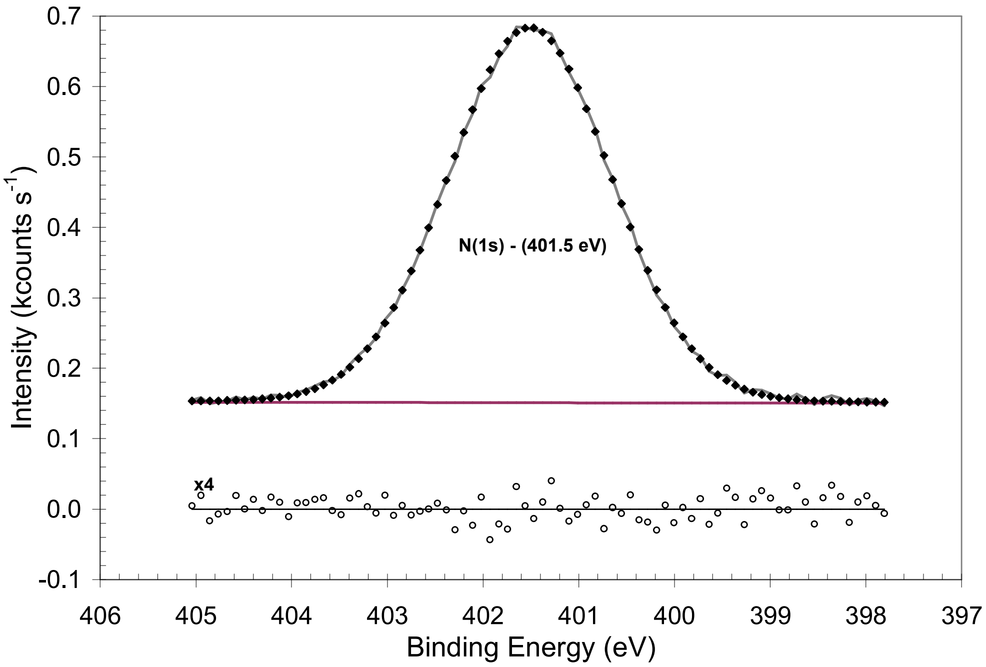

Figure 6.5 (c): Peak sum (◆), background (purple line) and residuals (○) of the N(1s) spectrum (grey line).

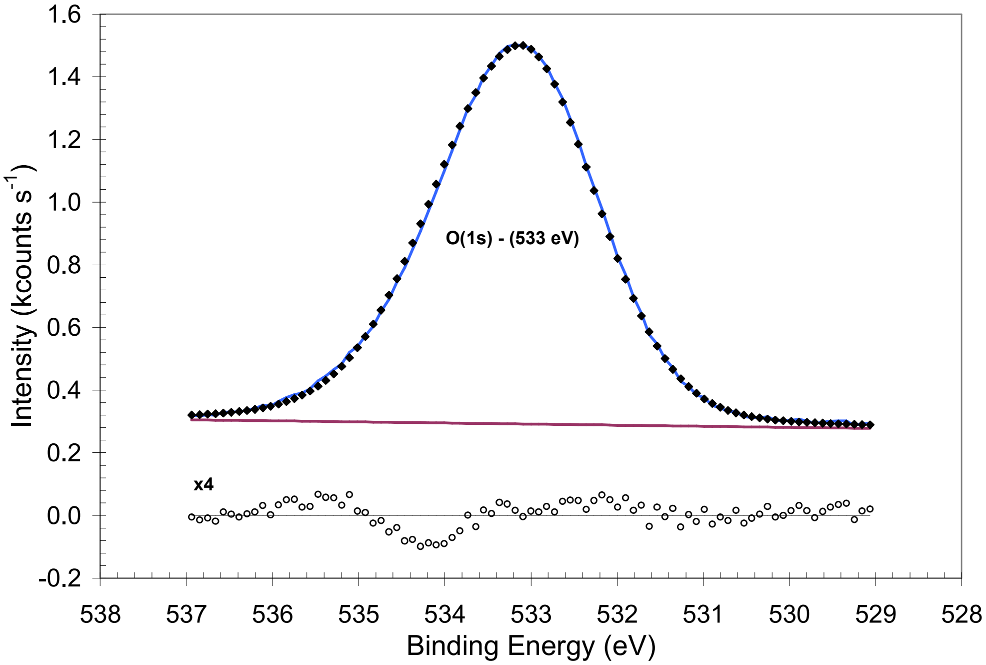

Figure 6.5 (d): High resolution XPS spectrum of oxygen (blue line), background correction (purple line), its fit (◆) and residuals (○).

TFAAD protected and deprotected sample clearly highlighting the large relative reduction in the fluorine Auger and (1s) peak as to be expected from the deprotection process. The spectra are scaled so that the C(1s) peaks are of equal height [23]. The fitted XPS spectra of the contributing elements to the TFAAD overlayer are displayed in Figures 6.5 (a) – (d) along with residuals from each of the respective calculations which have been multiplied to offer the reader clearer guidance on the success of the fit in each particular case. The data are shifted on the y axis for clarity of presentation.

XPSPEAK 4.1 employs either the Gaussian-Lorentzian product function or Gaussian-Lorentzian sum function to fit energy distribution curves *(E)* in photoelectron spectroscopy data. The sum function has been shown in the past to be a superior way to fit spectra compared to the Gaussian-Lorentzian product function [29] and is used in the analysis that follows. The sum function is displayed in Equation (6.1):

$$f(E) = hM_v \left\{ 1 + \left[\frac{E - E_0}{\beta + \alpha(E - E_0)} \right]^2 \right\}^{-1} + h(1 - M_v)\exp\left\{ -\ln 2 \left[\frac{E - E_0}{\beta + \alpha(E - E_0)} \right]^2 \right\} \tag{6.1}$$

where h is the peak height, β is half the FWHM, E_0 is the peak position, α is the asymmetry index (used for asymmetrical peaks instead of just the peak width function β) and M_v is the Gaussian Lorentzian mixing ratio. Since no information exists on the exact parameters used to fit individual high resolution spectra from TFAAD protected diamond samples and this being the only investigation which employed electron takeoff angles at zero degrees with respect to the surface normal, all parameters were allowed to vary freely with no constraints to achieve the best possible fit.

The first thing of note about the spectra shown in Figures 6.4 and 6.5 is their striking resemblance to those recorded in previous investigations [7,8,15,18,20-23,25]. This confirmed that the samples as received from the United States were similar in chemical make-up to those previously studied and as such direct comparison could be made between the data presented here and in the past literature as well as with de-protected samples.

The XPS spectrum of C(1s) from the TFAAD functionalised sample is shown in Figure 6.5 (a) and a sharp peak at 285.9 eV is clearly visible along with a significant shoulder at 287.3 eV. These two peaks comprise contributions from both bulk diamond and the alkyl chain of the molecule and are unable to be separated in this analysis since the signal from the bulk diamond is much larger than that attributable to the molecular backbone. One possible explanation for the two different peaks comprising the main carbon signal may be that the peak at 287.3 eV originates from carbon at the surface, bonded as C-H from hydrogen termination, which has not reacted with any TFAAD molecules due to density considerations and has been oxidised. Unfortunately, detailed X-ray analysis of this region for the purposes of determining individual contributions was beyond the scope of this investigation. Since fluorine is strongly electron withdrawing, the two further satellite peaks observed at 289.7 and 294.3 eV have previously been identified as originating from the carbonyl (C=O) and CF_3 groups of the protecting TFA layer respectively [7,8,15,18,20-22]. It is important to note that the energy separation between the four constituent peaks which comprise the total C(1s) signal (i.e. 8.4 eV separation between the peaks located at 285.9 and 294.3 eV etc.) were chosen to correlate with previous investigations to ensure consistency [7,15,18,20-22,25].

The F(1s) spectrum showed a single narrow peak centred at 689.5 eV originating from the trifluoroacetic cap while the N(1s) and O(1s) spectra are also characterised by solitary peaks at 401.5 and 533 eV respectively which is again in agreement with previous literature [7,8,15,18,20,21,25]. Figures 6.5 (b) – (d) show that single photoemission peaks arising from fluorine, nitrogen and oxygen are adequate to capture the high resolution XPS spectra of the TFAAD monolayer. One would expect this to be so since in TFAAD all three fluorine atoms are bound to a solitary carbon atom along with one site each for nitrogen and oxygen and, providing the molecule attached to the diamond through the vinyl C=C bond in an upstanding fashion as

Table 6.1: Fitted components of the characteristic XPS spectra originating from the TFAAD functionalised diamond sample.

Peak	Baseline	E_B (eV)	I (cs^{-1})	Area	% Area	FWHM[a] (eV)	%G	$\Sigma\chi^2$
$C(1s)_B$	S + L	285.9	6226.6	11013	76.3	1.70	100	0.81
$C(1s)_S$		287.3	913.0	1979	13.7	2.02	100	
C=O		289.7	470.5	1165	8.1	2.32	100	
CF_3		294.3	176.5	271	1.9	1.44	100	
F(1s)	S	689.5	2568.9	7443	100	2.51	83	0.61
N(1s)	S	401.5	531.8	1160	100	2.01	96	0.02
O(1s)	S	533.1	1207.9	3320	100	1.94	100	0.08

[a] The total instrumental FWHM due to broadening effects, Γ_I, comprises contributions from both the Analyser (Γ_A = 0.884 eV) and Monochromator (Γ_M = 0.420 eV) Gaussian resolution functions [Chapter 2.4]. This leads to an expected broadening of the peaks due to the XPS instrument of Γ_I = 0.979 eV.

expected, therefore only a single binding environment exists for each species. Consequently, the data is highly suggestive that the diamond substrate must be functionalised by the protecting overlayer in a non-random manner across the surface.

Table 6.1 displays the quantitative information from the fits to the TFAAD protected diamond sample where Baseline defines the background correction using either a linear (L) or Shirley (S) [30] function, E_B is the binding energy of each component, I is the background corrected intensity, FWHM is the full width at half maximum intensity of the fitted peak and %G details how much of each respective contributory peak belongs to a Gaussian distribution (G) where the Lorentzian contribution = 100-G and is included to allow the effect of broadening of the peaks to be separated between the instrument and the lifetime of the core-hole created by the incoming X-rays [Chapter 2.4]. The final column gives a measure of the accuracy of the fit.

The sharp C(1s) peak at 285.9 eV and shoulder at 287.3 eV account for 90% of the total peak area of carbon in agreement with a previous study [7] while the chi-squared for the high resolution carbon scan is also reasonable at a value of 0.81. The

$\Sigma\chi^2$ values for the three peaks specific to the TFA protecting layer of 0.61, 0.02 and 0.08 show that the fitting procedure was highly accurate in capturing the information from the three photoemission peaks.

6.4: Determination of Elemental Ratios:

Since the protecting TFA group has three fluorine atoms and one each of oxygen and nitrogen, a simple calculation relating the signal strength $I_i(E)$ due to electrons which originate from atoms of type i and energy E to the characteristics of the XPS instrument to determine specific relative concentrations of species of known chemical composition within adlayers can be conducted. This is shown in Equation (6.2) [31,32]:

$$I_x(E) = I_o n_x(E)\sigma_x Q(E) \tag{6.2}$$

where I_0 is the primary X-ray beam flux, $n_x(E)$ is the spectrum emitted from element x, σ_x is the photoionisation cross-section, and $Q(E)$ is the sensitivity of the particular instrument for given settings as a function of kinetic energy (transmission function). If the instrumental settings such as pass energy, retardation ratio, slit widths, sample and X-ray source position etc. are kept constant then $Q(E)$ will also remain constant and all spectra from that instrument are modified in the same way [32]. Thus, all high resolution XPS spectra displayed in this chapter have the same experimental conditions applied so as to try and reduce variability between spectra to as negligible a level as possible. Equation (6.2) can therefore be utilised to derive relative elemental densities on a substrate as described in Equation (6.3):

$$\frac{N_x}{N_y} = \frac{I_x \sigma_y Q(E_y)}{I_y \sigma_x Q(E_x)} \tag{6.3}$$

M. P. Seah [32] has precisely calculated the transmission functions of 58 different XPS instruments and determined for the experimental set-up for the data presented herein that:

$$Q(E) \propto (E)^{-n} \text{ where } n = 0.80 \pm 0.03$$

It was therefore possible to quantitatively describe and compare elemental ratios using Equation (6.3). Employing the photoionisation cross sections determined by Scofield [28] quantitative calculations found that the N(F):N(O):N(N) ratio present at the surface was 3.03:1.75:1.00; these values correspond closely to those expected from the molecular formula of TFAAD, $C_{12}H_{20}F_3NO$, of 3:1:1. The higher amount of oxygen is probably due to a small amount of contaminant oxygen initially on the H-terminated sample [21] and also possibly explains the presence of the 287.3 eV peak on the high resolution C(1s) spectrum.

Previously, studies have monitored the $A_{F(1s)}/A_{C(1s)}$ area ratio as a function of illumination time to characterise the kinetics of TFAAD grafting and find that for complete functionalisation of the diamond substrate to be achieved, the $A_{F(1s)}/A_{C(1s)}$ area ratio reaches a saturating limit of ~ 0.2 after ~ 10 hours illumination on H-terminated diamond substrates [6,18,21,24-26]. The value of 0.24 calculated from the data presented here indeed confirms that a single monolayer of TFAAD terminates the surface. Further calculations of relative areas showed that both nitrogen and oxygen have areas approximately 5.86% and 12.93% those of the total carbon signal respectively. However, use of the $A_{F(1s)}/A_{C(1s)}$ area ratio as a measure of surface coverage is error-prone on carbon substrates because of the difficulty of distinguishing C(1s) signals from the molecular layer and the underlying substrate [6].

6.5: Structure of the Monolayer Films

As some alkenes can form polymers, angle resolved XPS can be utilised to provide evidence that the protecting overlayer has functionalised the surface in an organised fashion. In a randomly arranged film, both F(1s) and C(1s) photoelectrons have almost equal trajectories through the film so that photoelectrons ejected from either the CF_3 group or from the TFAAD alkyl chain will undergo similar amounts of inelastic scattering within the film itself. However, if the opposite is true and the film is produced systematically through the same surface-molecular interactions with the CF_3 groups at the exposed interface, then it would be expected that C(1s) photoelectrons ejected from the backbone of the molecules will be scattered more effectively than those of the fluorine atoms, and the observed F(1s)/C(1s) intensity ratio would increase as a function of electron takeoff angle with respect to the surface normal, especially for those electrons ejected close to the surface plane. The difference between these two different scenarios is shown in Figure 6.6 where the randomly arranged film (left) has nearly equal trajectories for photoelectrons compared to the organised film (right) which clearly shows a difference in scattering. As the current work only studied TFAAD protected polycrystalline samples at an angle of zero degrees between the electron take-off angle and the surface normal, calculations using data from these investigations gave a F(1s)/C(1s) intensity ratio of 0.19. This value agrees very well with values of the F(1s)/C(1s) intensity ratio calculated in previous studies if one extrapolates their data to a similar angle as the one studied here [20,22]. The previous work established that the intensity ratio increased approximately two fold as the electron take-off angle increased from 45° to 75° with respect to the surface normal

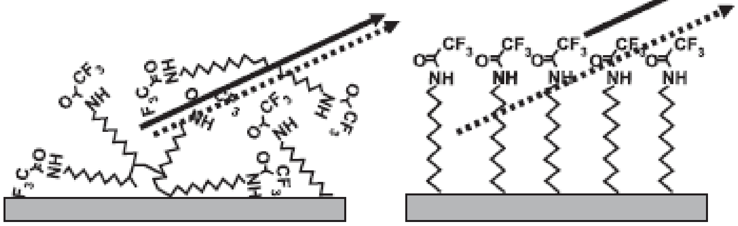

Figure 6.6: Comparison of electron ejection routes in a randomly organised (left) compared to orientated (right) polymerisation product [20].

This increased F/C ratio shows that the photoelectrons ejected from the C(1s) energy levels are selectively attenuated at larger angles, thereby demonstrating that the fluorine atoms terminate the TFAAD overlayer. Due to the observed behaviour of the intensity ratio as a function of angle, it was concluded that the photochemical functionalisation produces an oriented organic layer in which the C=C group reacts at the diamond surface. In the specific case of TFAAD, this leaves the protected amine group at the exposed surface, where it is accessible to further reactions after deprotection [20].

The high binding energy C(1s) peak at 294.3 eV is known to be a signature feature of the CF_3 group of the TFAAD protecting film and as such can be used as a measure of molecular density. Figure 6.7 details the area ratio of this high binding energy peak compared to the total C(1s) signal ($A_{294.3}/A_{C(1s)}$) as a function of photoelectron take-off angle. Plotted on the graph are data from the current work recorded at an angle of zero degrees relative to the surface normal along with an extrapolation of data from Ref. [21]. The graph shows a similar behaviour to that described above where the peak area ratio increases as a function of angle thereby

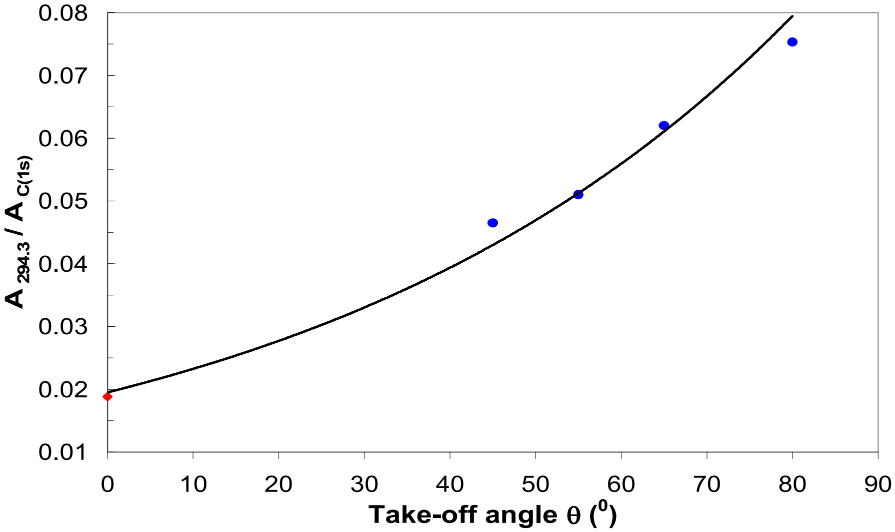

Figure 6.7: Area ratio of the high binding energy C(1s) peak at 294.3 eV (CF_3 group) relative to the total C(1s) area calculated using data from this work (◆) compared to those of [21] (●). The black line is a line of best fit extrapolated from the previous experiment.

confirming the original conclusion that the CF_3 groups are located at the exposed interface. The value calculated from the fitting parameters given in Table 6.1 gives $A_{294.3}/A_{C(1s)}$ ~ 0.02 and it is clear that data from the current work agrees with the trend discovered in the past investigation. From these values Nichols *et al* were able to determine a TFAAD molecular density of ~ 1.9 x 10^{14} moleculescm^{-2} [21]. The data presented here suggests that these samples would also have a molecular density within the same region. One must however cite the same argument as stated above in that the C(1s) signal cannot be separated between that of bulk diamond and the aliphatic chain and consequently any comparisons must be treated as a lower limit.

6.6: XPS of Amine Terminated Deprotected Diamond

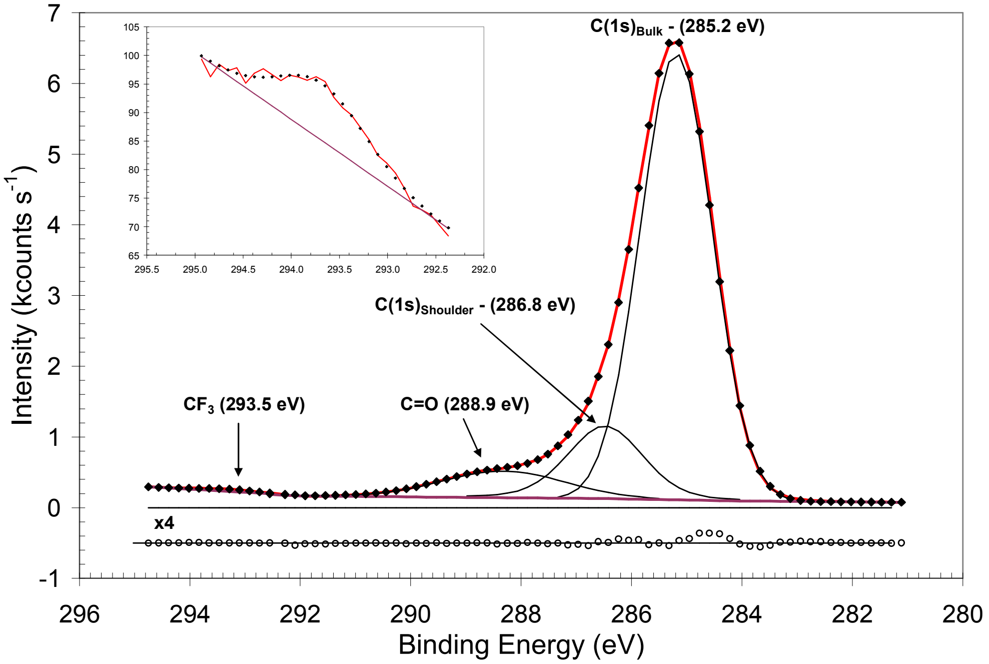

Figure 6.8 (a): Peak sum (◆), Shirley baseline correction (purple line) and constituent components (black curves) of the C(1s) peak (red line) along with residuals (○) of the fit. The high binding energy peak at 293.5 eV is expanded on the inset for clarity.

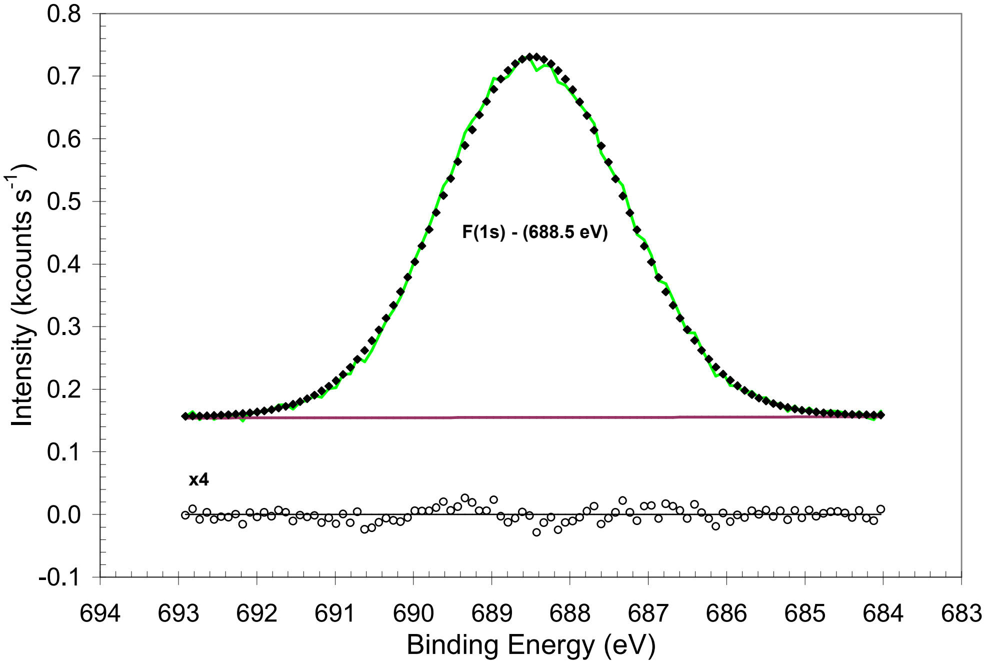

Figure 6.8 (b): Peak sum (◆), Shirley background (purple line) and residuals (○) of the high resolution spectrum of fluorine (green line).

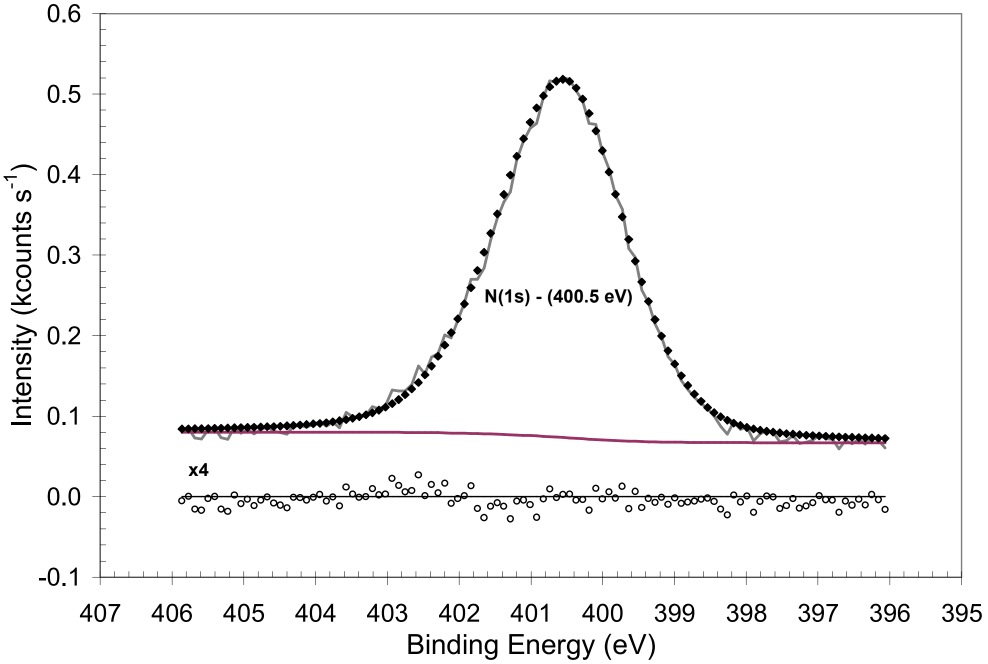

Figure 6.8 (c): Peak sum (◆), background (purple line) and residuals (○) of the N(1s) spectrum (grey line).

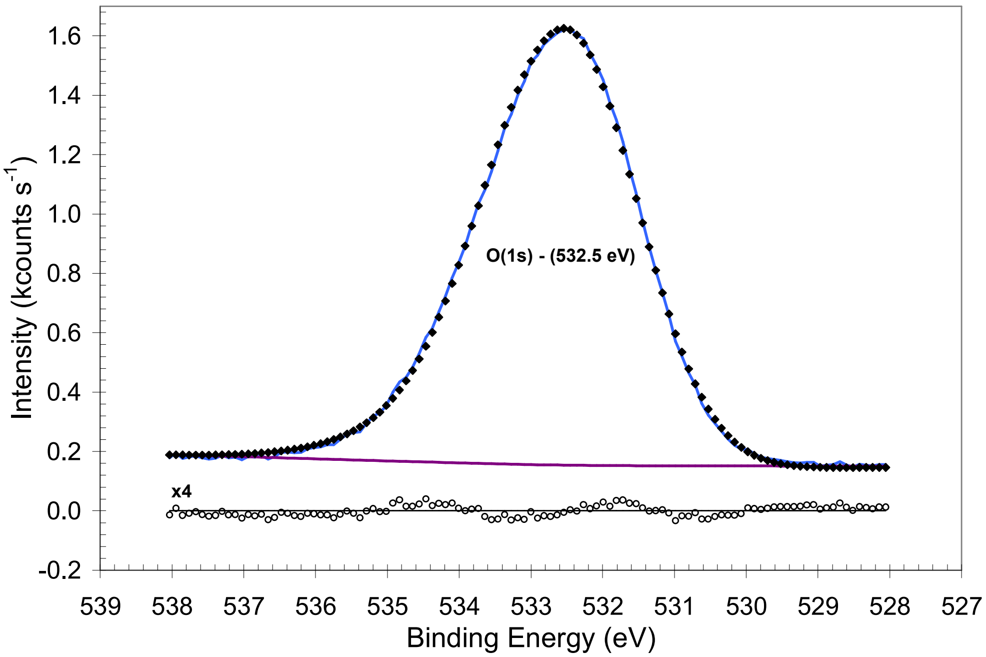

Figure 6.8 (d): XPS spectrum of oxygen (blue line), background correction (purple line), its fit (◆) and residuals (○).

Figures 6.8 (a) – (d) are the high resolution XPS spectra of the same sample shown in Figure 6.5 after deprotection to leave the diamond surface terminated with a free amine in preparation for covalent bonding with SSMCC. The graphs were scaled so that the main C(1s) peak had the same intensity as for the TFAAD protected sample so direct comparisons could be made. Figure 6.8 (a) is the high resolution XPS spectrum of carbon after deprotection and clearly shows a marked reduction in the area of the CF_3 group at 293.5 eV. Also shown is Table 6.2 in which the fitted components of each of the respective peaks in Figure 6.8 are given.

If a comparison is made between Tables 6.1 and 6.2, one immediately notes a clear and consistent downward shift in the binding energy of all peaks between 0.6-1.0 eV after deprotection. One would suspect since all external parameters have been kept constant and the same sample used in both experiments that this is the effect of removal of the strongly electron withdrawing fluorine cap of the TFAAD molecule [8,15]. It is also observed that all peaks apart from that belonging to fluorine become

Table 6.2: Fitted components of the characteristic XPS spectra originating from the deprotected amine terminated diamond sample.

Peak	Baseline	E_B (eV)	I (cs^{-1})	Area	% Area	FWHM (eV)	%G	$\Sigma\chi^2$
$C(1s)_B$	S + L	285.2	6301.8	12448	86.3	1.54	100	0.16
$C(1s)_S$		286.8	1027.5	1307	9.1	1.64	69	
C=O		288.8	376.8	637	4.4	2.04	93	
CF_3		293.5	30.1	39	0.3	1.15	100	
F(1s)	S + L	688.5	575.5	1672	100	2.73	100	0.02
N(1s)	S	400.5	445.0	1218	100	1.89	80	0.02
O(1s)	S + L	532.5	1471.0	4328	100	2.34	100	0.03

consistently sharper after deprotection if one studies the FWHM column. This possibly indicates that photoelectrons ejected from beneath the terminating CF_3 group undergo fewer inelastic scattering processes after removal of this cap thereby resulting in more defined characteristic XPS peaks. Furthermore, the increased presence of a Lorentzian contribution to some peaks after deprotection suggests that removal of the terminating group fundamentally modifies the electronic structure of the molecule as would be expected from a chemical process which involves fluorine, nitrogen and oxygen; three species who have very high electronegativities.

Prior to deprotection, the Fluorine (1s) peak area was 23.55% that of the total C(1s) peak signal as opposed to only 5.29% following this process while the F(1s) peak is also reduced to ~ 23% its original size indicating that deprotection has resulted in a major removal of > 65% of this species from the surface in agreement with previous studies [7,8,15,18]. This is further confirmed by the peak attributable to the CF_3 cap at high carbon binding energies which almost vanishes after deprotection to an area approximately 14.4% its original size [15].

Deprotection leaves the N(1s) intensity and peak area relatively unchanged at approximately 6% that of carbon meaning that the amine group is intact at the molecule/vacuum interface [7].

The deprotection process as outlined in the experimental section of this chapter would be expected to lead to sizeable reductions in the peak areas of both the O(1s) and C(1s) carbonyl peaks at 532.5 and 288.8 eV respectively. However, while this effect was observed to some extent in the case of the C=O peak reducing to ~ 45% its original area, it was not accompanied by a similar reduction in the O(1s) peak area which, indeed, slightly increases to 16.87% that of C(1s). Such an effect can be attributed to oxidation of unreacted C-H sites present at the surface prior to de-protection which have ultimately concealed the true effectiveness of the reaction [15].

6.7: RAS of Thiol-Modified ss-DNA Attached to Diamond

RA spectra were recorded before any modifications were made to the surface [Figure 6.1], after functionalisation with the TFAAD protecting group and also following deprotection to characterise the changes induced in the optical response of the substrate, if any, as a result of these processes. It must be noted that while all experiments involved in functionalisation, deprotection, tethering of DNA and

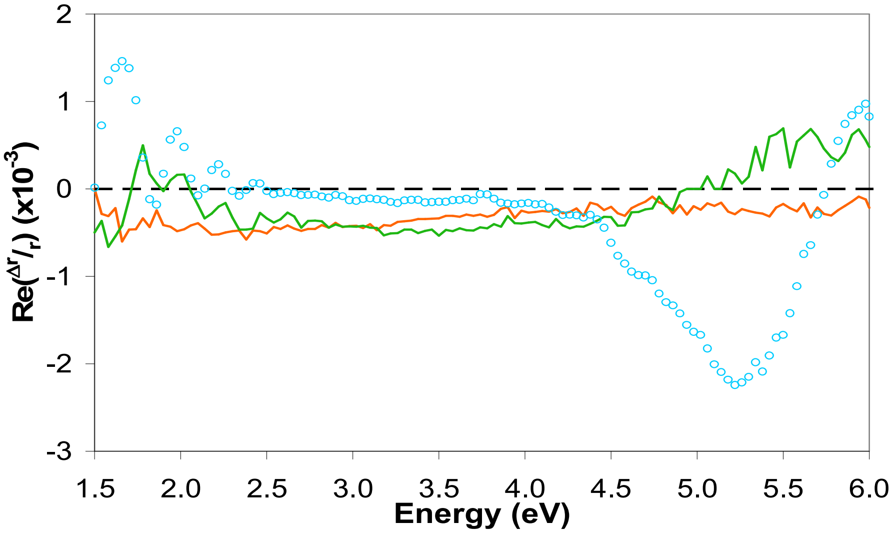

Figure 6.9: RA spectra of TFAAD protected diamond (green line), TFAAD de-protected diamond (orange line) and ss-DNA attached to diamond (○).

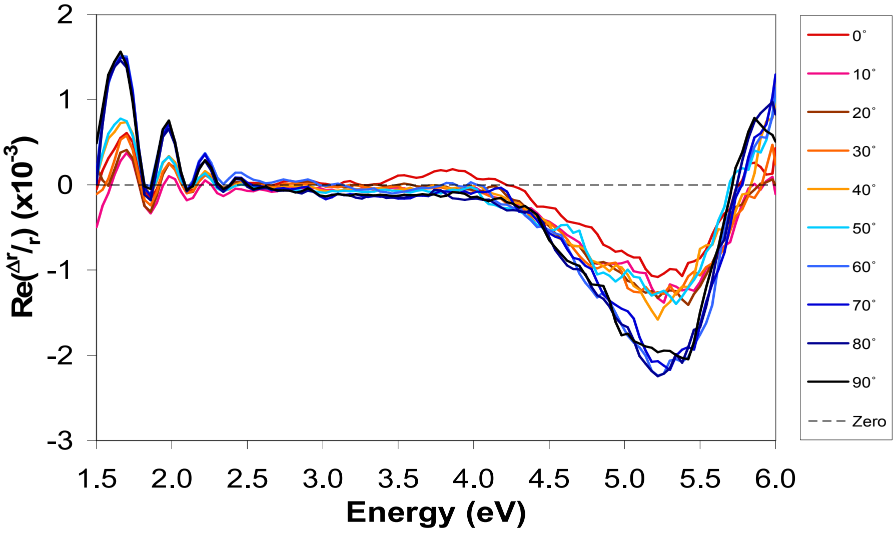

Figure 6.10: RA spectra of DNA attached to diamond as the sample is rotated about the axis of the incident light through 90˚.

hybridisation were conducted with the diamond substrate in a liquid environment, all RAS studies were carried out on a dry surface. As expected for an isotropic surface terminated with the TFAAD protecting group, the spectral profiles observed before treatment with ss-DNA were flat. This was also true for the amine terminated surface which produced a consistent RA baseline near to zero. This surface therefore provided a featureless background against which to assess the spectrum of DNA as shown in Figure 6.9.

After attachment of ss-DNA to the functionalised diamond surface, RA spectra were recorded and the changes induced by this process result in distinct peaks at approximately 5.25 eV accompanied by noticeable shoulders at 4.7 and 5.0 eV. It is clear from this graph that the changes induced in the RA profile of the system through the attachment of DNA are greater than those variations in the spectrum brought about during crystal preparation and as such can be considered to be the exclusive optical response of the biological molecule.

Figure 6.10 shows RA spectra of the ss-DNA as the sample was rotated about the axis of the incident light. Usually the RAS intensity follows a cos2θ dependence [12] as found previously for cytosine [11], adenine [Chapter 4] and DNA [9,10] on Au (110). The RA spectrum in Figure 6.10 does not show this angular dependence; instead there is a change in the intensity of the DNA feature with θ. The angular dependence of the RAS signal is important because it provides insight into the symmetry of the ss-DNA on the surface. The variation in RAS intensity with θ is easily explained since the substrate is polycrystalline and ss-DNA molecules are probably randomly arranged. If the centre of rotation is not perfectly aligned with the centre of the area illuminated in the RAS then a rotation will produce a variation in the number of molecules excited. The absence of a cos2θ dependence of the RAS is more informative since it places strong restrictions on the orientation of the dipole transitions that give rise to the RAS. The RAS signal will be dominated by transitions orientated in the plane of the DNA bases. A random arrangement of the directions of these transitions will lead to a cancellation of the RAS. Transitions orientated vertically to the surface will give zero RAS and those orientated parallel to the surface will give a cos2θ dependence. The only arrangement that would give the observed angular dependence is one in which the ss-DNA is tethered to the diamond via the amine group in a near vertical orientation with the individual bases in a chiral stacking formation. The individual strands would then form an equivalent twist at each location on the surface even if, as expected for a polycrystalline substrate, there is no ordering of these locations. This would explain why a RAS signal is obtained from a disordered surface and also the angular dependence of the signal. More importantly this would suggest that the DNA bases were exposed and able to hybridise with a homologous strand. A previous study found that ds-DNA bonded to diamond surfaces adopt an orientation with a tilt angle of ~ 35° to the surface plane [15], however the RAS results produced from this investigation using ss-DNA rule out such an orientation in this instance.

6.8: Detection of DNA Hybridisation

The integrity and directionality of the ss-DNA layer was tested by conducting a hybridisation experiment whereby a second oligonucleotide, homologous to the tethered DNA was added and hybridisation monitored using RAS. The results presented in Figure 6.11 show that the spectrum obtained for DNA bound to the diamond surface was similar to that presented in Figure 6.10. There was an increase in the signal intensity and a shift in peak position indicating that the DNA had hybridised since the peak at between 5.2 and 5.4 eV became larger with the response; changing from a value of approximately -1.7 x 10^{-3} to -3 x 10^{-3}, a near doubling in intensity. This conclusion was supported by the addition of 6 M urea, known to dissociate ds-DNA back to its constituent ss form, resulting in the intensity of the DNA peak reverting back to approximately -1.7 x 10^{-3}. This confirmed that the ordered ss-DNA layer was tethered in such a way as to allow access to the incoming probe and the near doubling of the signal intensity implies that nearly all the tethered DNA molecules were available for hybridisation. Consequently, the most favourable configuration to enable the vast

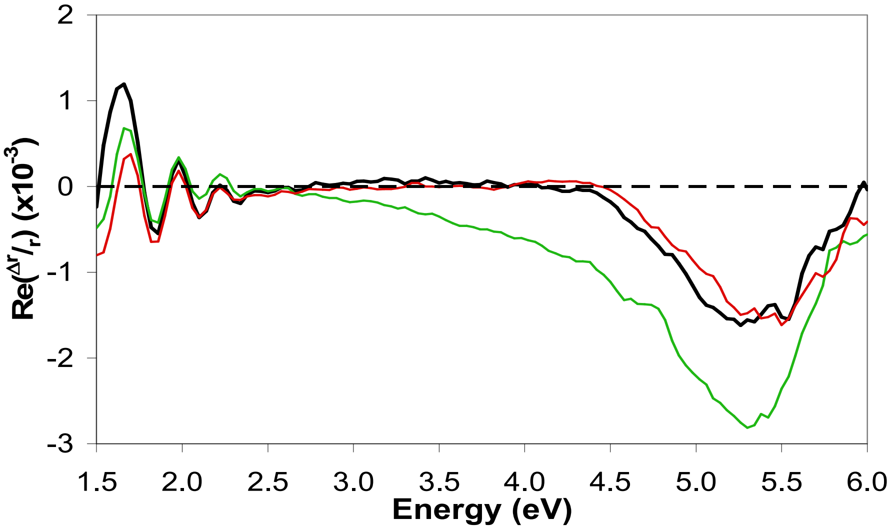

Figure 6.11: RA spectra of ss-DNA attached to diamond (black line), after hybridisation (green line) and after treating with urea (red line).

majority of tethered DNA molecules to hybridise would be for the DNA to be vertically orientated.

6.9: Summary

Polycrystalline diamond surfaces were functionalised with amine groups protected by trifluoroacetic acid groups in order to provide a regulated platform upon which Single stranded DNA molecules could be attached. RAS confirmed the isotropic nature of the thin film.

Thiolated oligonucleotides (target sequences) were reacted with the amine surface after deprotection of the protecting TFAAD overlayer. High resolution XPS spectra were analysed before and after deprotection and the resulting removal of > 65% of the protecting overlayer was confirmed.

Angular rotations of the ss-DNA/diamond interface showed no $\cos 2\theta$ dependence and only a small sensitivity to intensity as a function of angle and as such precluded the possibility that any other form of arrangement than chiral stacking was apparent. RAS analysis confirmed that the ss-DNA was tethered as up-standing molecules.

An oligonucleotide probe, homologous to the diamond-bound ss-DNA, was used to show the integrity of the tethered DNA by demonstrating that DNA hybridisation occurred.

6.10: References

[1] J. Lamartine, *Mater. Sci. Eng. C: Biomimetic Supramol. Syst.* **26**, 354 (2006)

[2] Y. Y. Wang, T. Prokein, M. Hinz, H. Seligern and W. A. Goedel, *Anal. Biochem.* **344**, 216 (2005)

[3] C. Debouck and P. N. Goodfellow, *Nat. Genet.* **21**, 48 (1999)

[4] T. Livache, E. Maillart, N. Lassalle, P. Mailley, B. Corso, P. Guedon, A. Roget and Y. Levy, *J. Pharm. Biomed. Anal.* **32**, 687 (2003)

[5] M.-L. Visnapuu, D. Duzdevich and E. C. Greene, *Mol. BioSyst.* **4**, 394 (2008)

[6] P. E. Colavita, B. Sun, K-Y. Tse and R. J. Hamers, *J. Am. Chem. Soc.* **129**, 13554 (2007)

[7] W. Yang, J. E. Butler, W. Cai, J. Carlisle, D. Gruen, T. Knickerbocker, J. N. Russell Jr., L. M. Smith and R. J. Hamers, *Nat. Mater.* **1**, 253 (2002)

[8] B. Sun, P. E. Colavita, H. Kim, M. Lockett, M. S. Marcus, L. M. Smith and R. J. Hamers, *Langmuir* **22**, 9598 (2006)

[9] M. C. Cuquerella, C. I. Smith, D. G. Fernig, C. Edwards and P. Weightman, *Langmuir* **23**, 2078 (2007)

[10] C. P. Mansley, C. I. Smith, M. C. Cuquerella, T. Farrell, D. G. Fernig, C. Edwards and P. Weightman, *Phys. Stat. Solidi C* **5**, 2582 (2008)

[11] P. Weightman, G. J. Dolan, C. I. Smith, M. C. Cuquerella, N. J. Almond, T. Farrell, D. G. Fernig, C. Edwards and D. S. Martin, *Phys. Rev. Lett.* **96**, 086102 (2006)

[12] P. Weightman, D. S. Martin, R. J. Cole and T. Farrell, *Rep. Prog. Phys.* **68**, 1251 (2005)

[13] R. LeParc, C. I. Smith, M. C. Cuquerella, R. L. Williams, D. G. Fernig, C. Edwards, D. S. Martin and P. Weightman, *Langmuir* **22,** 3413 (2006)

[14] M. Palummo, O. Pulci, R. Del Sole, A. Marina, M. Schwitters, S. R. Haines, K. H. Williams, D. S. Martin, P. Weightman and J. E. Butler, *Phys. Rev. Lett.* **94**, 087404 (2005)

[15] T. Knickerbocker, T. Strother, M. P. Schwartz, J. N. Russell Jr., J. E. Butler, L. M. Smith and R. J. Hamers, *Langmuir* **19**, 1938 (2003)

[16] C. E. Nebel, H. Uetsuka, B. Rezek, D. Shin, N. Tokuda and T. Nakamura, *Diamond & Related Materials* **16**, 1648 (2007)

[17] S. Wenmackers, S. D. Pop, K. Roodenko, V. Vermeeren, O. A. Williams, M.

Daenen, O. Douhéret, J. D'haen, A. Hardy, M. K. van Bael, K Hinrichs, C. Cobet, M. Vandeven, M. Ameloot, K. Haenen, L. Michiels, N. Esser and P. Wagner, *Langmuir* **24**, 7269 (2008)

[18] T. Strother, T. Knickerbocker, J. N. Russell Jr., J. E. Butler, L. M. Smith and R. J. Hamers, *Langmuir* **18**, 968 (2002)

[19] M. Lu, T. Knickerbocker, W. Cai, W. Yang, R. J. Hamers and L. M. Smith, *Biopolymers* **73**, 606 (2004)

[20] R. J. Hamers, J. E. Butler, T. Lasseter, B. M. Nichols, J. N. Russell Jr., K-Y. Tse and W. Yang, *Diamond & Related Materials* **14**, 661 (2005)

[21] B. M. Nichols, J. E. Butler, J. N. Russell Jr. and R. J. Hamers, *J. Phys. Chem. B* **109**, 20938 (2005)

[22] C. Nebel, D. Shin, B. Rezek, N. Tokuda, H. Uetsuka and H. Watanabe, *J. R. Soc. Interface* **4**, 439 (2007)

[23] X. Wang, P. E. Colavita, K. M. Metz, J. E. Butler and R. J. Hamers, *Langmuir* **23**, 11623 (2007)

[24] P. E. Colavita, J. E. Streifer, B. Sun, X. Wang, P. Warf and R. J. Hamers, *J. Phys. Chem. C* **112**, 5102 (2008)

[25] P. E. Colavita, B. Sun, X. Wang and R. J. Hamers, *J. Phys. Chem. C* **113**, 1526 (2009)

[26] B. M. Nichols, K. M. Metz, K-Y. Tse, J. E. Butler, J. N. Russell Jr. and R. J. Hamers, *J. Phys. Chem. B* **110**, 16535 (2006)

[27] R. J. Hamers, B. Sun and X. Wang, *Chemistry Department, University of Wisconsin-Madison, 1101 University Avenue Madison, Wisconsin 53706* and J. E. Butler, *Code 6174, Naval Research Laboratory, Washington, DC 20375*

[28] J. H. Scofield, *Journal of Electron Spectroscopy and Related Phenomena* **8**, 129 (1976)

[29] R. Hesse, P. Streubel and R. Szargan, *Surf. Int. Anal.* **39**, 381 (2007)

[30] D. A. Shirley, *Phys. Rev. B* **5**, 4709 (1972)

[31] D. R. Penn, *Journal of Electron Spectroscopy and Related Phenomena* **9**, 29 (1976)

[32] M. P.Seah, *Surf. Int. Anal.* **20**, 243 (1993)

Chapter 7: Conclusions

The conclusions drawn from this thesis are summarised and the possible direction of future work is also discussed

7.1: Summary of Findings

The key outcomes of the work undertaken in this thesis are outlined in the sections below.

7.1.1: The Au(110) Surface

The RA profile of Au(110) observed under electrolyte at an applied potential of 0.0 V has been found to be that of the inherently anisotropic (1x2) reconstruction due to its similarity to RA profiles of clean Au(110) in UHV where LEED confirmed the presence of such a surface structure. The sensitivity of RAS to the different reconstructions heralded by the variation of applied electrode potential into either the positive or negative potential regime has been proven. Characteristic modifications to the spectral profile independent of anion and pH allow the spectral signatures of the (1x1), (1x2) and (1x3) reconstructions to be assigned. Au(110) in 0.1 M H_2SO_4/Na_2SO_4 (pH 1.36), $NaClO_4/HClO_4$ (pH 1.18) and $NaClO_4$ (pH 6.14) electrolytes were simulated using the three-phase model and the expected sensitivity of the 2.5 eV feature to surface reconstruction due to the existence of the surface state, is quantitatively described through consistent changes to the 2nd transition used in the model; a transition centred on this region of the spectrum. In neutral pH the oxidation of the crystal surface occurred at 0.2 V lower than in acidic solutions in the absence of specific anion adsorption.

7.1.2: Adenine

The adsorption of adenine as a function of coverage established that the three most concentrated solutions gave rise to a saturating coverage on Au(110) while the least concentrated solution failed to produce this saturation. Nonetheless, a linear simulation showed that the orientation of the molecule on the surface was independent of the solution concentration and that the RAS observed from the surface following adsorption from the least concentrated adenine solution included contributions from regions of bare gold. Rotations of the crystal about the plane of polarisation of the incident light determined that the adsorption of adenine at saturation and sub-saturation coverage onto the Au(110) surface in phosphate buffer occurred with the long axis of the molecule coincident with those of the gold substrate. The similarity between the spectral profiles of adenine and AMP indicated that adsorption for both molecules occurred through sites common to the base; namely the NH_2 and possibly also the N(7) sites due to the presence of the phosphate group in AMP. The application of the three-phase model to adenine adsorbed on the Au(110) substrate required two additional transitions to those needed to represent the contribution of the Au(110) to capture the effects of molecular adsorption. These transitions were polarised in $[1\bar{1}0]$ directions at energies of approximately 4.40 and 5.55 eV. This means the molecules must align with the plane of the base normal to the surface and their long axes parallel to the $[1\bar{1}0]$ direction. This suggests that adenine forms base stacked layers the orientation of which is determined by the substrate. A simple analysis of the angle the molecule makes with the plane vertical to the surface was found to explain the intensity variation in the adenine transitions as a function of electrode potential though within large error boundaries. These studies also suggest that adenine does not adsorb at this interface in alkaline solutions. The positive charge on the N(3) site at pH 1.2 is likely to disrupt the π stacking interactions between molecules and is the likely explanation of the variation in spectral profile at this pH.

7.1.3: Decanethiol

The orientation of decanethiol was observed to be independent of surface coverage through systematic variations in the RA signal as saturation was reached coupled to the use of a simple linear addition which showed that it was possible to simulate the RA profile obtained at an intermediary stage of adsorption using a spectrum recorded at an earlier stage and that recoded at saturation coverage. Their relative contributions to the simulated profile were approximately 45% and 55%; values close to those that would be expected for a simulation of an RA profile recorded at half monolayer coverage if orientation were the same in both instances. Rotations of the Au(110) crystal after decanethiol adsorption in ethanol, air and finally phosphate buffer showed subtle but important changes to the spectral profile. As decanethiol SAMs are formed through a covalent gold/sulphur bond which is stable, these variations must be due to small orientational modifications to the hydrophobic alkyl backbone of the molecule which would be sensitive to changes in the external environment.

7.1.4: DNA on Diamond

RAS of both an unmodified and functionalised polycrystalline diamond surface were found to exhibit no anisotropy. This provided a base from which variations to the spectral profile of the surface after the attachment of thiol–modified ss-DNA could be directly attributed to the molecule. High resolution XPS established the integrity and bonding character of the protecting TFA group and also confirmed the removal of this acidic group following treatment with acid leaving a primary amine terminated surface ready for reaction with the ss-DNA. RAS of single stranded DNA adsorbed on a functionalised diamond substrate showed distinct differences from the RA profile of the functionalised diamond surface. Further the lack of a $\cos 2\theta$ dependence with rotations in the crystal plane determined that the only arrangement that would give the observed angular dependence is one in which the ss-DNA is tethered to the diamond via the amine group in a near vertical orientation with the individual bases in a chiral stacking formation. The individual strands would then form an equivalent twist at each location on the surface even if there is no ordering of these locations. This would explain why a RAS signal is obtained from a disordered surface and also the angular dependence of the signal. DNA hybridisation of the target sequence was confirmed using RAS which detected a near doubling in the signal intensity and a reduction to the intensity observed prior to hybridisation with the addition of urea; a substance known to dissociate hybridised DNA to its constituent strands thus confirming the orientation of the attached DNA strands.

7.2: Future work

The scope of this thesis is quite wide in that it includes detailed studies of the Au(110) crystal as a function of electrolyte and pH along with the effects of molecular adsorption on the optical response of the surface. Using these electrochemical studies in the future, one would hope that knowledge of the variations in surface reconstruction could underpin further understanding of adsorption kinetics such as whether the act of the molecule is to preserve reconstruction or promote the lifting of it. However, this involves a comprehensive understanding of the coupling between the dielectric constant of the substrate and the optical transitions of the subject molecule. This information is contained within the interfacial boundary defined in the three-phase model and as such requires a different theoretical approach.

The development of a coherent approach to investigations involving interfaces is also required. The formation of self assembled monolayers is incredibly important to the fabrication of bio-electronic devices and RAS has proven to be sensitive to subtle modifications to orientation dependent upon external environment and these investigations need to be further explored in conjunction with other surface sensitive optical probes.

While the conclusions of this work are based on interpretations of spectral profiles of the systems under investigation with reference to previous work, it is clear that one tool in particular would offer a great advantage in understanding the delicate forces at play in electrochemical studies of Au(110) and molecular adsorption onto this substrate: electrochemical STM. The details provided by such a technique would undoubtedly strengthen the interpretation of RA profiles if the two were used together in the context of the time-scale and detailed process of adsorption and its effects upon the surface structure. Such studies would have great benefits to investigations of fuel cells, drug delivery systems, new conducting devices and of course the bio-electronic interface.

Appendix

A.1: XPS of Amine Terminated TFAAD Deprotected Diamond (Part II)

A.1: XPS of Amine Terminated Deprotected Diamond (II)

These graphs are included to compare directly the deprotected sample shown in Chapter 6 with a sample already deprotected by collaborators in the USA. All spectra were recorded in the same XPS equipment as in Chapter 6 with the same pass energy, slit width and position and monochromatic Al K_α source of 1486.6 eV. Characterisation spectra were analysed by fitting raw data using XPSPEAK 4.1 after a baseline correction. Figure A.1 (a) shows the broadscan spectra of the deprotected sample from Chapter 6 and deprotected sample from the USA clearly highlighting the large reduction in the fluorine peaks. It is clear that the sample shows a remarkable similarity to that which was deprotected in Chapter 6. It also proves the high stability of these functionalised samples and the efficiency and accuracy of the deprotection process itself. All spectra are scaled so that the C(1s) peaks are of equal height.

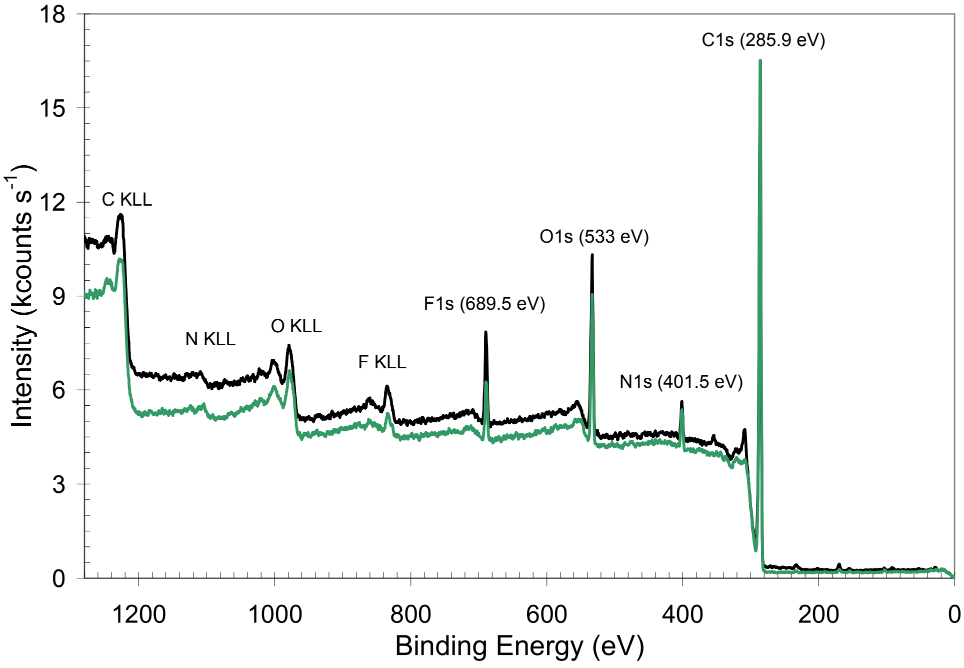

Figure A.1 (a): Deprotected sample from Chapter 5 (green line) and the USA sample (black line).

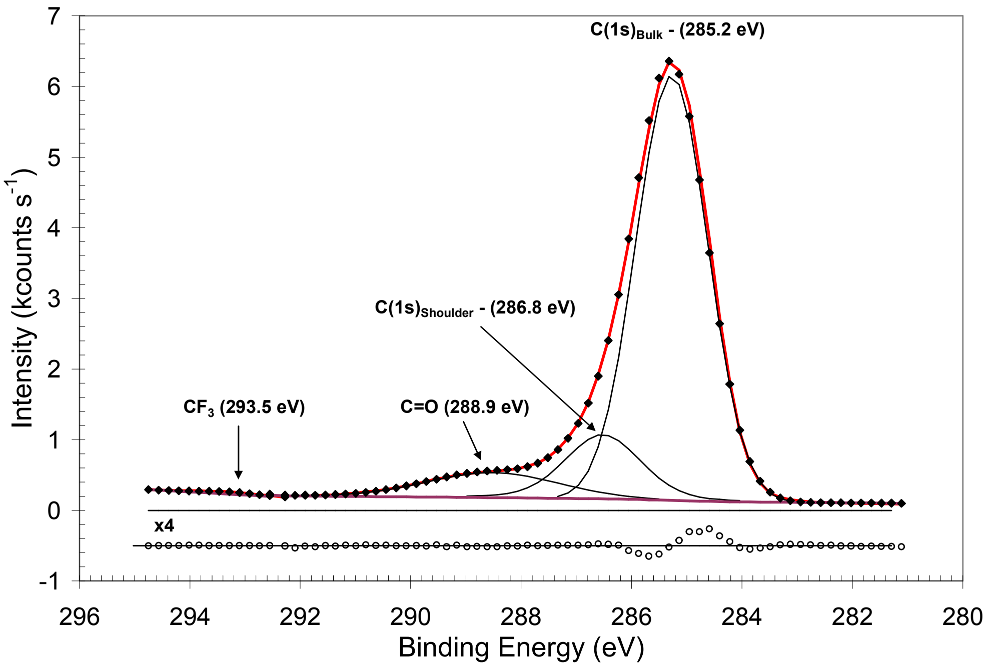

Figure A.1 (b): Peak sum (◆), Shirley baseline correction (purple line) and constituent components (black curves) of the C(1s) peak (red line) along with residuals (○) of the fit.

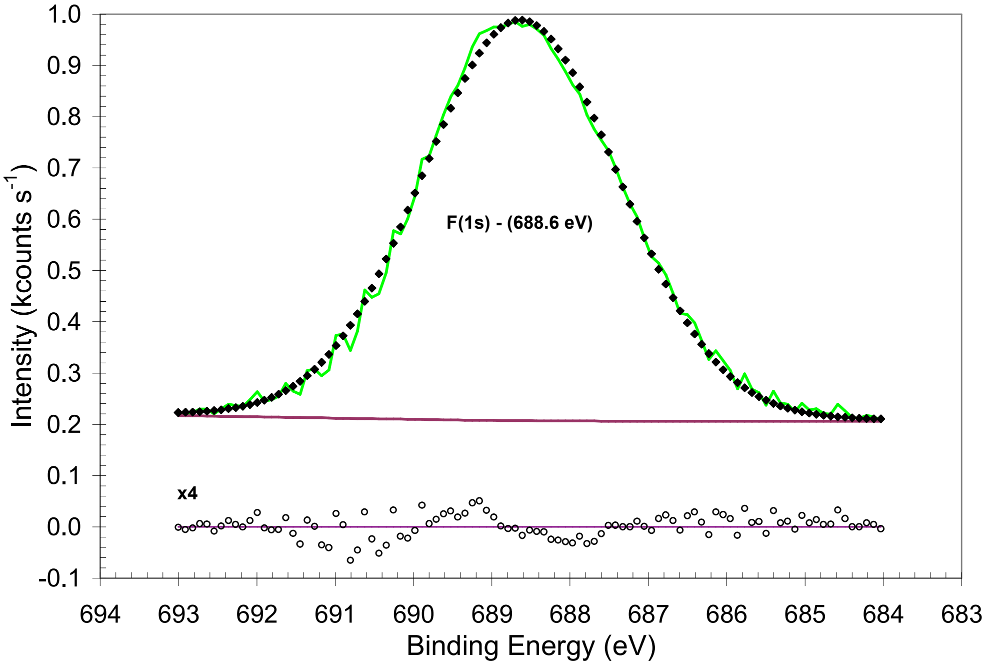

Figure A.1 (c): Peak sum (◆), Shirley background (purple line) and residuals (○) of the high resolution spectrum of fluorine (green line).

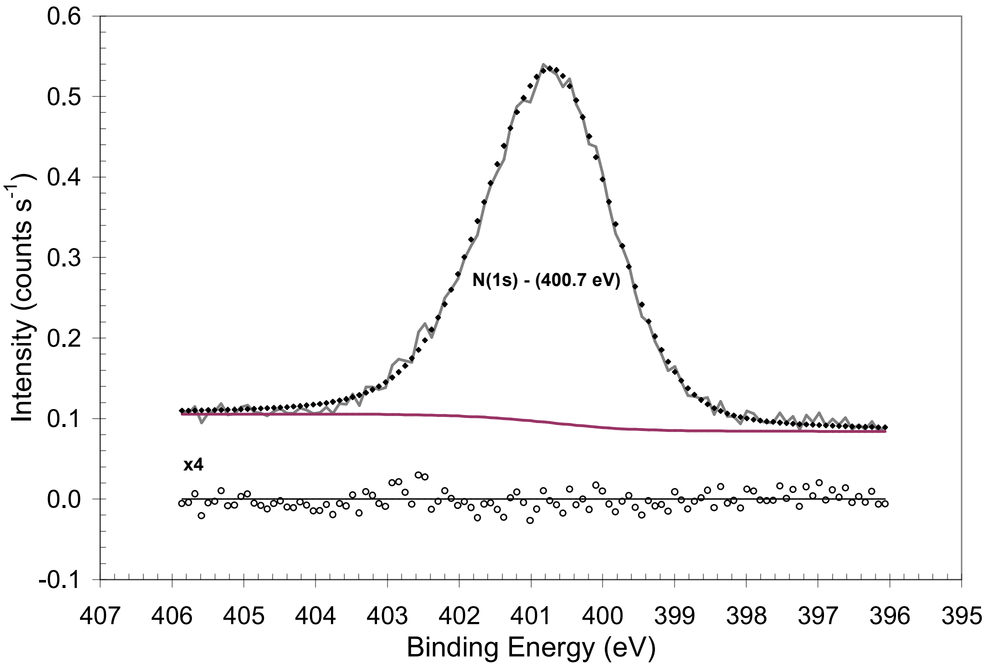

Figure A.1 (d): Peak sum (◆), background (purple line) and residuals (○) of the N(1s) spectrum (grey line).

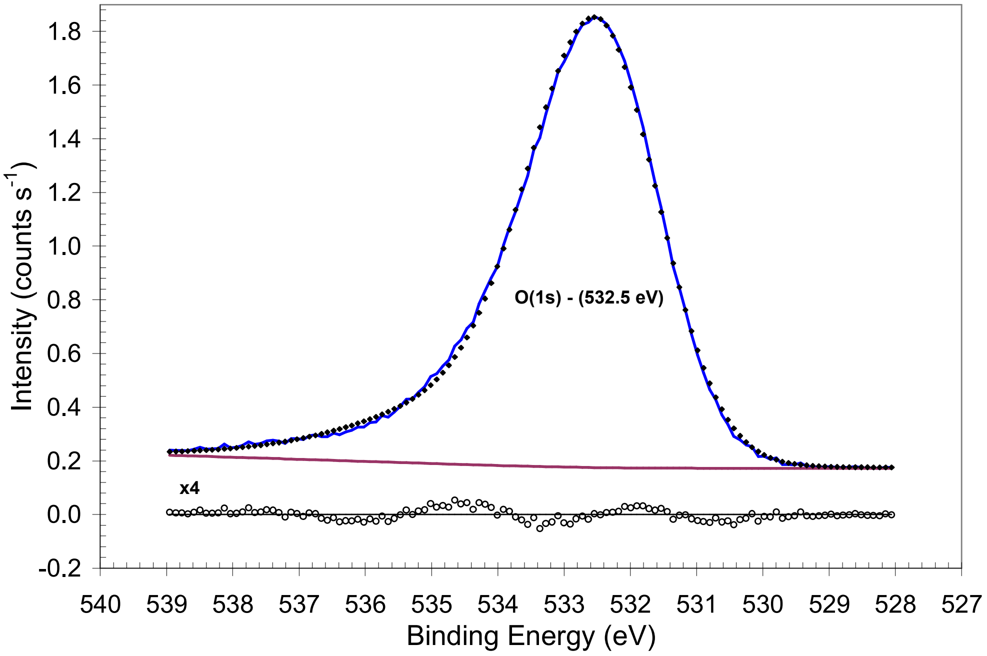

Figure A.1 (e): XPS spectrum of oxygen (blue line), background correction (purple line), its fit (◆) and residuals (○).

Table A.1.1: Fitted components of the characteristic XPS spectra originating from the deprotected amine terminated diamond sample sent from the USA.

Peak	Baseline	E_B (eV)	I (cs^{-1})	Area	% Area	FWHM (eV)	%G	$\Sigma\chi^2$
$C(1s)_B$	S + L	285.3	6359.6	9747.2	86.3	1.54	98	0.16
$C(1s)_S$		286.5	718.6	912.6	9.1	1.61	80	
C=O		288.5	315.3	532.8	4.4	2.81	100	
CF_3		293.7	26.4	34.1	0.3	1.06	100	
F(1s)	S + L	688.5	788.5	1869	100	2.797	95	0.04
N(1s)	S	400.7	445.0	1170	100	2.13	74	0.02
O(1s)	S + L	532.5	1693.0	5585	100	2.45	97	0.03

As there is no data from the protected sample, no comparisons can be made. However, inspection of the table above reveals extremely similar results to those obtained in Table 6.2. These values again confirm the accuracy of the functionalisation and deprotection process

Publications

Chapter 3

(1) Spectral Signatures of the Different Reconstructions of Au(110)
A. Bowfield, C. I. Smith, N. Almond, and P. Weightman
(*Manuscript in Preparation*)

Chapter 4

(2) Determination of the Structure of Adenine Monolayers Adsorbed at Au(110)/electrolyte Interfaces
C. I. Smith, A. Bowfield, G. J. Dolan, M. C. Cuquerella, C. P. Mansley, D. G. Fernig, C. Edwards and P. Weightman
The Journal of Chemical Physics **130**, 044702 (2009)

Chapter 4

(3) The Structure of Adenine Adsorbed at Sub-Saturation Coverage at Au(110)/Electrolyte Interfaces
A. Bowfield, C. I. Smith, G. J. Dolan, M. C. Cuquerella, C. P. Mansley and P. Weightman
e-Journal of Surface Science and Nanotechnology **7**, 225 (2009)

Chapter 4

(4) The Effect of pH Variation on the Adsorption of Adenine on Au(110)
A. Bowfield, C. I. Smith, G. J. Dolan, M. C. Cuquerella, C. P. Mansley and P. Weightman
(*Submitted*)

Chapter 5

(5) Reflection Anisotropy Spectroscopy of Decanethiol Adsorbed at Au(110)/liquid Interfaces
A. Bowfield, C. I. Smith, M. C. Cuquerella, T. Farrell, D. G. Fernig, C. Edwards and P. Weightman
physica status solidi (c) **5**, No. 8, 2600 (2008)

Chapter 6

(6) Detection of DNA Hybridisation on a Functionalised Diamond Surface
C. I. Smith, A. Bowfield, M. C. Cuquerella, C. P. Mansley, T. Farrell, P. Harrison, D. S. Martin, D. G. Fernig, C. Edwards, J. E. Butler, R. J. Hamers, B. Sun, X. Wang and P. Weightman
Euro Physics Letters **85**, 18006 (2009)

Other Publications

(7) A New UV Reflection Anisotropy Spectrometer and its Application to the Au(110) Electrolyte Surface
C. P. Mansley, T. Farrell, C. I. Smith, P. Harrison, A. Bowfield and P. Weightman
Journal of Physics D: Applied Physics **42**, 115303 (2009)

(8) Fluorination of Perovskite-Related Phases of Composition $SrFe_{1-x}Sn_xO_{3-\delta}$
F. J. Berry, A. F. Bowfield, F. C. Coomer, S. D. Jackson, E. A. Moore, P. R. Slater, M. F. Thomas, A. J. Wright and X. Ren
Journal of Physics: Condensed. Matter **21**, 256001 (2009)